12-8-2008

Timing and Characterization of the Change in the Redox State of Uranium in Precambrian Surface Environments: A Proxy for the Oxidation State of the Atmosphere

Gerald D. Pollack

TIMING AND CHARACTERIZATION OF THE CHANGE IN THE REDOX STATE OF URANIUM IN PRECAMBRIAN SURFACE ENVIRONMENTS: A PROXY FOR THE OXIDATION STATE OF THE ATMOSPHERE

by

GERALD D. POLLACK

Under the Direction of Eirik J. Krogstad and Andrey Bekker

ABSTRACT

The redox-sensitive geochemical behavior of uranium permits the use of Th/U ratios as a geochemical proxy for the oxidation state of the atmosphere and oceans during sedimentary processes. Due to the effects of post-depositional uranium mobility on Th/U ratios during events involving oxygenated fluids, direct measurements of Th/U ratios are often misleading, but the whole rock Pb isotope composition may be used to determine a sample's apparent time-integrated Th/U ratio (κ_a) and the timing associated with the onset of the U-Th-Pb geochemistry. Rare earth element (REE) concentrations were determined by isotope dilution mass spectrometry to evaluate the influence of multiple provenance components and potential mobility of Th, U, and Pb during post-depositional processes on the Th/U ratio.

The Pb isotope compositions and REE concentrations were determined for six Paleoproterozoic sedimentary sequences, which were the focus of previous studies involving the timing of the rise of atmospheric oxygen. The Mount McRae Shale, Huronian Supergroup, and Zaonezhskaya Formation have been interpreted as experiencing post-depositional alteration (perhaps associated with orogenic events) due to Pb-Pb ages that are younger than the likely depositional age and observed fractionation of REE in chondrite normalized REE patterns and interelement REE ratios (e.g. La/Nd, La/Yb, Eu/Eu*). Similar geochemical proxies have been interpreted as sedimentary geochemical features of the Timeball Hill Formation, Hotazel Formation, and Sengoma Argillite Formation. This study of Paleoproterozoic sedimentary units constrains the onset of U-Th decoupling, most likely due to the onset of oxidative weathering conditions, began by 2.32 Ga, the latest.

INDEX WORDS: Pb isotopes, Rare earth elements, Th/U ratios, Time-integrated, Atmospheric evolution, Oxygen content of the atmosphere, U-Th decoupling

TIMING AND CHARACTERIZATION OF THE CHANGE IN THE REDOX STATE OF URANIUM IN PRECAMBRIAN SURFACE ENVIRONMENTS: A PROXY FOR THE OXIDATION STATE OF THE ATMOSPHERE

by

GERALD D. POLLACK

A Dissertation Submitted in Partial Fulfillment of the Requirements for the Degree of

Doctor of Philosophy

in the College of Arts and Sciences

Georgia State University

2008

TIMING AND CHARACTERIZATION OF THE CHANGE IN THE REDOX STATE OF URANIUM IN PRECAMBRIAN SURFACE ENVIRONMENTS: A PROXY FOR THE OXIDATION STATE OF THE ATMOSPHERE

by

GERALD D. POLLACK

Committee Co-Chairs: Eirik J. Krogstad
Andrey Bekker

Committee: W. Crawford Elliott
Timothy La Tour

Electronic Version Approved:

Office of Graduate Studies
College of Arts and Sciences
Georgia State University
December 2008

DEDICATION

This dissertation is dedicated to my family. My strength and tenacity can be attributed to the constant support, advice and encouragement of my wife, Nikki. Without her I would have never refocused my career goals and would have never applied to the Ph.D. program. She has been my light during the darkest times of the past few years and continues to motivate me and challenge me to be my best. Additional motivation comes from my newborn daughter, Riley, who I think about constantly and cannot even begin to imagine life without. My dog, Jake, also deserves a mention here as late evening and early morning walks and moments of silliness helped me through some of the most difficult moments of this process. Additional support from my parents and mother- and father-in-law made this degree program end in success.

ACKNOWLEDGEMENTS

I wish to acknowledge the following people and organizations without which this degree program would have been much more difficult. First of all, I thank my primary advisor, Dr. Eirik J. Krogstad who taught me the necessary laboratory procedures and the intricacies of REE and the U-Th-Pb system interpretation that made this project possible. Dr. Krogstad's financial support made it possible to present this research at several professional meetings as well as purchase necessary laboratory supplies for geochemical analyses. I would also like to thank my secondary advisor Dr. Andrey Bekker for providing me with all of the samples used in this dissertation as well as his expertise in the evolution of atmospheric oxygen. Special thanks is given to Drs. Timothy LaTour and W. Crawford Elliott for serving as department chair and providing me with the opportunity to teach in the lecture setting and providing me with financial support throughout my tenure at Georgia State University. Additional appreciation of their reviews of my dissertation was greatly appreciated as they greatly improved this document. Dr. Russell Malchow instructed me about the standard operating conditions of the laboratory and operation of the ThermoFisher Scientific Element2 ICP-MS instrument. Lastly, I greatly appreciate the assistance of Ms. Tyra Hines and Ms. Basirat Lawal with navigating the university's bureaucracy.

TABLE OF CONTENTS

LIST OF TABLES

LIST OF FIGURES

1. INTRODUCTION

1.1 Background

1.1.1 Redox conditions of the Precambrian atmosphere

Early research into biochemical carbon and oxygen pathways suggested that the oxygen concentration of Earth's early atmosphere likely increased through time perhaps associated with the advent of photosynthesis. This putative increase in oxygen concentration was first investigated by geologists in the earliest part of the twentieth century through examination of the geochemistry of Archean and Paleoproterozoic sedimentary units (Cloud, 1968; MacGregor, 1927; Roscoe, 1969). Recently geologists have used redox-sensitive trace elements and their ratios (i.e. Fe/Al, U/Al, Mo/Al) and stable isotope compositions (notably $\delta^{13}C$, $\delta^{34}S$, $\delta^{33}S$ and $\delta^{56}Fe$) to explore the timing and nature of the rise of atmospheric oxygen concentrations (Anbar et al., 2007; Bau et al., 1999; Bekker et al., 2004; Bekker and Kaufman, 2007; Canfield et al., 2000; Farquhar et al., 2000; Holland, 1984; Karhu and Holland, 1996; Ohmoto et al., 2006; Ono et al., 2006; Rouxel et al., 2005). Many of these studies have concluded that the rise of atmospheric oxygen to levels greater than 10^{-5} of present atmospheric level (Pavlov and Kasting, 2002) occurred between 2.47 and 2.32 Ga (e.g. Bekker et al., 2004; for a different interpretation see Ohmoto et al., 2006). The rise of atmospheric oxygen and the associated environmental changes including the 2.22-2.1 Ga Lomagundi carbon isotope excursion in seawater composition were christened the 'Great Oxidation Event' (GOE; Holland, 2002). Because the timing of this event is now reasonably well constrained, research has focused on the relationship of this event with other environmental changes (e.g. Bekker et al., 2005; Bekker and Kaufman, 2007) and its effect on the ocean redox

state and initiation of oxidative continental weathering (e.g. Yang and Holland, 2002; Hannah et al., 2004; Scott et al., 2008). These studies have shown that during and subsequent to the rise of atmospheric oxygen, concentrations of redox-sensitive elements such as U, Mo, Re, and Os increased in organic-rich shales deposited under anoxic and, locally, euxinic conditions; however they did not reach comparable levels to their Phanerozoic analogues indicating weaker terrestrial flux of redox-sensitive elements released during oxidative continental weathering and/or more extensive anoxic and euxinic environments in the ocean.

1.1.2 Geochemistry

The differential reduction-oxidation (redox) behavior of elements yields the potential for elemental ratios to serve as useful proxies for paleoredox conditions. One such pair that is particularly useful in the assessment of the paleoredox conditions of sedimentary systems is Th and U. This utility originates from common oxidation of insoluble tetravalent U to highly soluble hexavalent UO_2^{2+} and UO_2^{2+} hydroxide ionic complexes at surface conditions (Drever, 1997). The redox behavior of U is important in evaluating modern anoxic basins (Anderson et al., 1989a; Anderson et al., 1989b; Barnes and Cochran, 1990; Barnes and Cochran, 1993; Cochran et al., 1986; Shaw et al., 1994; Swarenski et al., 1999) as well as microbial biologic processes (Abdelouas et al., 2000; Fredrickson et al., 2002; Lee et al., 2005; Lovley et al., 1991).

1.1.2.1 U-Th-Pb Systematics

The Th/U ratios in sediments deposited in modern oxidized environments are typically above the average upper continental crust ratio of 3.8 (Taylor and McLennan, 1985) and, normally, are well below this average ratio in sediments deposited in reducing environments due to decoupling of redox-sensitive U and invariant Th (Hemming and McLennan, 2001; Krogstad et al., 2004; McLennan and Taylor, 1980). However, post-depositional changes can significantly alter concentrations of redox-sensitive elements. As this dissertation demonstrates, the U-Th couple is particularly useful in constraining paleoredox conditions because ^{232}Th, ^{235}U, and ^{238}U are long-lived radionuclides, which decay to different Pb isotopes at known rates. It is therefore possible to determine time-integrated Th/U ratios as well as the age when the Th/U ratio was established through ages derived from the relative growth of radiogenic ^{207}Pb and radiogenic ^{206}Pb. These constraints are important because U is commonly mobilized during post-depositional processes (e.g., modern weathering). This direct approach to determining the age of redox transition is not possible with other redox-sensitive geochemical systems, with the exception of the Re-Os system. If this age is close to the age of sedimentation, the time-integrated Th/U ratio reflects the depositional Th/U ratio; otherwise it represents the time-integrated Th/U ratio of sediment since it was deposited.

Uranium has two common oxidation states (+4 and +6) resulting in distinctly different geochemical behaviors and affinities under different redox conditions. The effective radius of U in minerals is dependent upon the oxidation state and coordination number. The effective radius of U^{4+} in 8-fold coordination is 0.100 nm, whereas the effective radius of U^{6+} in 6-fold coordination is 0.073 nm (Shannon, 1976). Thorium has

only one common oxidation state (+4) and is usually found as a trace element in most mineral phases. The effective ionic radius of Th^{4+} in its most common 8-fold coordination is 0.105 nm (Shannon, 1976). U^{4+} and Th^{4+} have similar chemical properties (e.g. ionic charge, effective radius, and coordination number) making substitution of U and Th common under reducing conditions. Tetravalent U and Th are largely insoluble in water under surface conditions; therefore under reducing atmospheric conditions both thorium and uranium would be transported with detrital materials. The resulting sedimentary rocks should have Th/U ratios close to the average upper crustal value of 3.8 (Taylor and McLennan, 1985) if they were derived from a large homogenized continental provenance.

Thorium is usually transported adsorbed onto clays and organic compounds in water (Langmuir and Herman, 1980) and has short residence time of tens of years or less in the modern oceans (Nozaki et al., 1981; Taylor and McLennan, 1985). Thorium concentrations are often used to monitor rates of sediment accumulation and particle mixing due to its conservative geochemical behavior (Cochran et al., 1986). Therefore Th is an ideal proxy for monitoring the detrital input in sedimentary systems.

Under conditions where U^{4+} is oxidized to U^{6+}, U and Th behave dissimilarly. This is due to the high stability of U^{6+} as uranyl carbonate ionic complexes in oxygenated aqueous solutions (Langmuir, 1978). Starting with the rise in atmospheric oxygen and the development of oxidizing continental weathering conditions after 2.3 Ga (Bekker et al., 2004), uranium was likely delivered to the oceans as stable uranyl complexes dissolved in river waters. This translates to uranyl complexes dissolved in an oxygenated ocean that have a long residence time. In the modern oxygenated ocean, the residence

time of U is ~0.5 million years (Ku et al., 1977). The removal of dissolved U from oxygenated waters into anoxic sediments occurred at the redoxcline by abiotic and biologic U reduction (Anderson et al., 1989b; Barnes and Cochran, 1990; Cochran et al., 1986; Klinkhammer and Palmer, 1991; Lovley et al., 1991; McManus et al., 2006; Zheng et al., 2002). This results in variable Th/U ratios in reducing marine sediments found in an otherwise oxidized ocean. Variable Th/U ratios reflect a combination of factors including sedimentation rate, influx of detrital material with variable Th concentrations, organic carbon content, and position of the redoxcline in the water and sediment column. Post-depositional processes can alter Th/U as well as Th/Pb and U/Pb ratios mainly by removal of U and/or Pb from sediments since Th is largely immobile. However, U is only mobilized by oxygenated fluids, which are unlikely to occur in reducing sediments either during the diagenetic or metamorphic stage unless those sediments were flushed with a large external flux of oxidized fluids. Pb removal from rocks is not common, but is known to take place when large volumes of Cl-rich brines were flushed through the basin (Doe et al., 1983). Therefore, the most common case of U removal is when rocks are exhumed and eroded and thus exposed to oxidized groundwaters and weathering. In general, post-depositional alteration would tend to increase Th/U ratios.

Under reducing continental weathering conditions, such as those proposed for the early Archean, uranium was not quantitatively oxidized. Consequently, uranium was primarily delivered to the ocean with detrital materials (Figure 1.1a). The Th/U ratios of marine sediments deposited in contact with a reducing atmosphere should be representative of the average exposed continental crust. In oxidized sedimentary environments, chemically evolved sediments may contain less uranium and have higher

Th/U ratios compared with the average upper crustal value as uranium is preferentially kept in solution. In contrast, sediments deposited in anoxic basins connected to the otherwise oxygenated ocean (Figure 1.1b) have low Th/U ratios due to uranium reduction at or below the redoxcline and its delivery to the sediment-water interface with organic matter (Anderson et al., 1989a; Anderson et al., 1989b; Barnes and Cochran, 1990; Barnes and Cochran, 1993; McManus et al., 2005; McManus et al., 2006; Mo et al., 1973; Morford et al., 2001; Russell and Morford, 2001). This pattern of differential uranium enrichment results in variable apparent time-integrated Th/U ratios (κ_a) derived from Pb isotope compositions of shales with ages straddling the rise of atmospheric oxygen has been documented previously (Krogstad, 2004).

1.1.2.2 Rare Earth Element Geochemistry

The geochemical behavior of the 14 naturally occurring lanthanide elements (collectively known as the rare earth elements or REE) is analogous to Th and tetravalent U. The REE are rather insoluble in seawater, with residence times of only 50 to 600 years. Like Th, they are considered among the least mobile elements during weathering processes (Piper, 1974). The REE are also not commonly fractionated with respect to each other due to similarities in their 3+ oxidation state and systematic electron (f-shell) orbital filling (observed through limited variation in their ionic radius; 0.116 – 0.0977 pm). Exceptions exist, as Eu has both Eu^{2+} and Eu^{3+} oxidation states and Ce exists as Ce^{3+} and Ce^{4+} in nature. The redox-sensitive behavior of these two elements is quantified by normalization to the geometric mean of adjacent polyisotopic elements within the REE group and referred to as Eu- and Ce-anomalies, where Eu/Eu* =

$Eu_N/((Sm_N*Gd_N))^{0.5}$ and $Ce/Ce^* = Ce_N/(La_N^{2/3}*Nd_N^{1/3})$. Fractionation of the REE is observed in the estuarine environments between solutions and colloids (Sholkovitz and Szymczak, 2000; Sholkovitz, 1992), on the surface coating of suspended particles in the Sargasso Sea (Sholkovitz et al., 1994), and on the surface of ferromanganese nodules and crusts and hydrothermal precipitates (Cocherie et al., 1994; Mills et al., 2001; Mitra et al., 1994; Sherrill et al., 1999); in all cases LREE were preferentially removed and solutions were HREE-enriched. LREE depletion is also observed in the ca. 3.0 Ga Buhwa shales of Zimbabwe, where the LREE (along with Pb) were mobilized during diagenesis and basin closure by Cl-rich brines (Krogstad et al., 2004). Furthermore, it has been suggested that REE are mobile during diagenesis in reducing pore waters although it has no impact on bulk sediment chemistry (Elderfield and Sholkovitz, 1987) except for shales hosting phosphatic concretions that develop depletion in MREE accompanied by MREE enrichment in phosphatic concretions (Shields and Stille, 2001; Kidder et al., 2003).

The REE behave conservatively during weathering processes and are transported to the oceans mainly with fine-grained detrital particles (Taylor and McLennan, 1985). The REE budget in clastic sediments is therefore dominated by detrital rather than aqueous or diagenetic components. The REE are largely immobile under most common sedimentary, diagenetic and metamorphic processes due to their low solubility (Awwiller, 1994; Bierlein, 1995; McLennan, 1989; Taylor et al., 1986) except for sediments with more than 5% P_2O_5 (Kidder et al., 2003). These attributes make REE concentration data essential to provenance studies and assessment of post-depositional alteration.

1.1.2.3 Th-U-REE Compatibility

The similarity in geochemical behavior between the REE and Th (in particular La and Th) has been previously noted (McLennan et al., 1980); no previous study has discussed a similar analogue for U^{4+}. The similarity of La and Th has been successfully applied in a variety of geological applications (Bhatia and Crook, 1986; McLennan et al., 1980; Rudnick et al., 1985; Taylor and McLennan, 1985), including the recognition of Th mobilization under granulite facies metamorphic conditions (Rudnick et al., 1985). Additional evidence for their association is La substitution for Th in common Th-rich minerals such as monazite (Langmuir and Herman, 1980).

This association of La and Th can be also extended to evaluate a REE proxy for U. Because Th and U have similar geochemical behavior in the tetravalent state, it would be reasonable to assume that the REE proxy for U^{4+} should be as different from La as Th^{4+} is from U^{4+}. The ionic potential (ionic charge/ionic radius) of Th is 4.76% less than that of U, which can be used to select an appropriate proxy for U. Nd fits this description with respect to La, as both La and Nd are found as trivalent cations in nature with the ionic potential of La being 4.40% less than that of Nd. Because the behavior of these REE under a variety of conditions is well known, the La/Nd ratios should be comparable to Th/U ratios under reducing conditions. Therefore La/Nd ratios combined with time-integrated Th/U ratios inferred from Pb isotope data could provide additional information to constrain the oxidation state of U during sedimentary processes.

Although the association of La and Th is well documented, chemical properties of several other REE make them potentially more appropriate proxies for Th. A charge difference exists between the trivalent REE and Th^{4+}, but the similarities in ionic radii

make these elements comparable with Th. The ionic radius of Gd^{3+} (0.1053 nm) suggests that Gd is more suitable for substitution with Th^{4+} (0.105 nm) than La^{3+} (0.116 nm) on the sole property of ionic radius. Similarly, Er^{3+} (0.1004 nm) is likely to substitute for tetravalent U (0.100 nm). Based on ionic potentials, Er is a better proxy for U as the relative difference in ionic potentials between Gd and Er is 4.65%, which is closely comparable to the 4.76% relative difference between Th and U. These similarities suggest that La/Nd and Gd/Er ratios are the best proxies for the Th/U ratio of the unweathered source materials. Therefore, a comparison of time-integrated Th/U ratios and La/Nd or Gd/Er ratios should yield important information whether variations in time-integrated Th/U ratio reflect redox behavior of U during sedimentary processes or heterogeneous sources in the provenance.

1.1.3 Application of Pb isotopes and REE systematics to resolve between redox decoupling of U from Th and multiple provenance sources

1.1.3.1 Pb Isotope Ratio Interpretations

Traditionally, Pb isotope data have been used to determine the radiometric age of igneous and sedimentary rocks through the evaluation of the U-Pb system with $^{207}Pb/^{204}Pb$ and $^{206}Pb/^{204}Pb$ data. Establishing that the U-Pb whole rock system has remained chemically closed since deposition is essential to the evaluation of original (depositional) Th/U, as post-depositional alteration to the whole rock geochemistry would significantly affect the data interpretation. Therefore, determination of Pb-Pb isochron ages or, when scattered, the approximate slope (errorchron) ages, must be done to evaluate the timing of the establishment of U/Pb ratios. In addition to providing radiometric ages, Pb isotope compositions can yield important information regarding the

Th-Pb geochemical system through changes in $^{208}Pb/^{204}Pb$ ratios. The comparison of $^{206}Pb/^{204}Pb$ and $^{208}Pb/^{204}Pb$ data can be used to evaluate time-integrated Th/U ratios (Faure, 1986). The growth of uranogenic Pb would be reflected by changes in $^{206}Pb/^{204}Pb$ ratios and therefore, horizontal variations on the $^{206}Pb/^{204}Pb$ vs. $^{208}Pb/^{204}Pb$ diagram (Figure 1.2). In contrast, thorogenic Pb growth affects $^{208}Pb/^{204}Pb$ ratios and introduces vertical variations on this diagram. A combination of both processes results in the evolution of Pb isotopes along a slope that is a function of the depositional Th/U ratio.

Graphically, the growth starts at an initial Pb isotope composition. Because the solubility of Pb in seawater and basinal brines is very low and similar to that of the REE (Carpenter et al., 1974; Sverjensky, 1984; Taylor and McLennan, 1985), the initial Pb isotope composition of clastic sedimentary rocks is determined by the provenance composition. Post-depositional processes are unlikely to alter the Pb isotope composition of the rock other than through the radioactive decay of U and Th, due to low Pb solubility. The initial Pb isotope composition can be modeled using an appropriate Pb isotope evolution model and a constrained age for sedimentation. Rays can be constructed from the model initial Pb isotope composition through the Pb isotope composition measured for each sample. The slope of these rays can then be used to calculate the apparent time-integrated Th/U ratio that would have resulted in the present Pb isotopic composition of each sample. In the absence of oxidative weathering, the slopes of these rays do not vary significantly (Krogstad, 2004; Krogstad et al., 2004). On the other hand, ray slopes with greater variability than that of the source rocks may indicate decoupling of U from Th during oxidative weathering.

The apparent time-integrated $^{232}Th/^{238}U$ ratio since sedimentation is referred to here as the average model κ (κ_a). Thorogenic and uranogenic Pb isotopes evolved in a variety of reservoirs with distinct κ values until the sediment was deposited. The value of κ_a can be calculated using the measured $^{206}Pb/^{204}Pb$ and $^{208}Pb/^{204}Pb$ ratios, the decay constants for each parent nuclide, and model initial $^{208}Pb/^{204}Pb$ and $^{206}Pb/^{204}Pb$ ratios. The model initial ratios for this study have been determined from the lead isotope evolution model for the continental crust of Kramers and Tolstikhin (1997), however the choice of model Pb isotope composition is not so critical for the calculation of κ_a values. Selection of this Pb isotope evolution model is based on the model's realistic handling of uranium cycling in oxidized weathering environments after 2.0 Ga. The time-integrated Th/U can be calculated using the following equation derived from the decay equations for ^{238}U and ^{232}Th and simplified according to l'Hôpital's rule, such that:

$$\kappa_a = \frac{\lambda_{238}}{\lambda_{232}} \times \frac{(^{208}Pb/^{204}Pb)_m - (^{208}Pb/^{204}Pb)_i}{(^{206}Pb/^{204}Pb)_m - (^{206}Pb/^{204}Pb)_i}$$

, where the subscript 'i' stands for the model initial value, 'm' for the measured value. The isotopic composition of naturally occurring uranium and thorium are such that today ^{238}U comprises 99.27% of all U and ^{232}Th is essentially 100% of natural Th; therefore dividing values of κ_a by 0.9927 can be used to calculate Th/U ratios.

The accuracy of these κ_a ratios is somewhat dependent upon the model initial ratios used in the calculation. Optimally, "true" initial Pb isotope ratios should be determined through measurement of the Pb isotopic composition of potassium feldspars from the actual provenance. Direct measurement of uranium and thorium concentrations in sedimentary rocks to calculate Th/U ratios would not generally help to resolve this issue, as uranium is highly susceptible to remobilization during post-depositional

processes (e.g. metamorphism and modern weathering). These processes would produce erroneously high Th/U ratios as uranium is preferentially mobilized and removed from the rock, thereby propagating errors into any models using these ratios.

1.1.3.2 REE Pattern Interpretation

Variations in calculated κ_a values could be the result of multiple sources rather than redox conditions; therefore determining the composition and variability of detrital sources in the provenance is essential to this study. Isotope dilution mass spectrometry (IDMS) provides accurate and precise measurements of REE concentrations required to constrain sedimentary provenance and the redox conditions present at the time of sediment deposition. Due to natural variations observed in the absolute concentrations of the REE (e.g. the Oddo-Harkins Effect), REE concentrations are usually normalized to a related material or composite of materials. In order to preserve the accuracy and precision obtained through IDMS, the normalizing concentrations should also be measured by IDMS. Two patterns that are similar in morphology may indicate that they were derived from a single provenance component or multiple but well homogenized components. Parallel patterns that vary in normalized concentrations can be explained through the incorporation of variable fractions of minerals in which REE are incompatible (e.g. quartz). Differences in pattern shape could be attributed to variable fractions of common rock-forming and accessory minerals that readily incorporate REE (e.g. apatite, plagioclase, and monazite) indicating incompletely homogenized provenance or multiple detrital sources (Gromet and Silver, 1983; Hogan and Sinha, 1991; Stern and Hanson, 1991; Taylor and McLennan, 1985).

1.2 Dissertation Layout

The interpretation of geochemical analyses of approximately 70 drill core samples of Paleoproterozoic organic-rich and -poor shales as well as banded iron and manganese formations (and their metamorphosed equivalents) obtained from Dr. Andrey Bekker form the essence of this Ph.D. dissertation. Specifically, this study uses rock samples of shales from the 2.5 Ga Mount McRae Shale, Hamersley Province, Western Australia, ca. 2.3 Ga Timeball Hill Formations, South Africa, ca. 2.2 Ga Sengoma Argillite Formation, Botswana, and ca. 2.1 Ga Zaonezhskaya Formation, lower Ludikovian Series, Karelia, Russia as a proxy for organic-rich sedimentary rocks from the Paleoproterozoic Era. In addition to the organic-rich shales mentioned above, organic-poor shales from the ca. 2.4 Ga Huronian Supergroup, Ontario, Canada as well as banded iron and manganese formation samples from the 2.22 Ga Hotazel Formation, South Africa have been analyzed to monitor organic-poor environments as well as chemically precipitated rocks. The formation of black shales and banded iron-formations (BIFs) is well studied, as they are known to be economic resources due to the enrichment of many rare elements (Isley, 1995; Wignall, 1994).

The following chapters will focus on the different lithologic units individually and will be organized in chronologic order from the oldest to the youngest and address the geologic setting, geochemical data, and interpretation of the data from each. Finally a summary of discussion topics and conclusions will be provided to summarize the findings of this study. Pb isotope ratio and REE concentration data from the ca. 2.5 Ga Mount McRae Shale (Chapter 2) is interpreted as showing a potential disruption to the radiogenic growth of Pb isotopes at approximately 400 Ma, coinciding with the initiation

of tectonic basin development in the adjacent Canning Basin. This disruption may have been caused by the introduction of additional U and/or Pb via dewatering of rocks in the Canning Basin. The geochemical data from samples from the ca. 2.4 Ga Huronian Supergroup (Chapter 3) are interpreted such that the Pb isotope ratio derived Th/U ratio (κ_a) may not be indicative of redox conditions prevalent in the atmosphere during provenance material weathering. The variation in κ_a for these rocks may be related to potential provenance heterogeneity, as suggested by REE patterns, and/or disruption to Pb isotope growth as suggested by Pb-Pb errorchron ages. The interpretation of whole-rock REE patterns from organic-rich shales from the Upper Zaonezhskaya Formation (Chapter 7) supports the model that the provenance of these sedimentary rocks are not homogeneous and therefore the calculated κ_a ratio may be indicative of source characteristics rather than redox conditions during weathering.

The interpretation of Pb isotope ratios and REE patterns from at least two other Paleoproterozoic sedimentary sequences do not support post-depositional disturbance to whole rock geochemistry nor do they show significant differences in source characteristics. The geochemical data from organic-rich shales from the 2.32 Ga Timeball Hill Formation (Chapter 4) are likely indicative of homogenous source geochemistry and therefore the κ_a ratios reflect oxidative weathering conditions. Similarly, the Pb isotope ratio data have been used to calculate κ_a ratios for ten shale samples from the Sengoma Argillite Formation and are interpreted as being indicative of redox conditions during weathering (Chapter 6).

Although Pb isotope ratios were not determined for BIF and manganese formation samples from the Hotazel Formation, REE patterns and Ce-anomalies are indicative of

oxidized conditions in the marine environment at 2.22 Ga (Chapter 5). The interpretation of the REE data is consistent with the behavior of REE in the oceans being similar to that observed in modern marine environments. The interpretation of κ_a ratios is suggestive of the onset of oxidative weathering of uranium by 2.32 Ga, at the latest, where the interpretation of REE data suggests that the oxidative cycling of cerium in the ocean had begun by 2.22 Ga the latest.

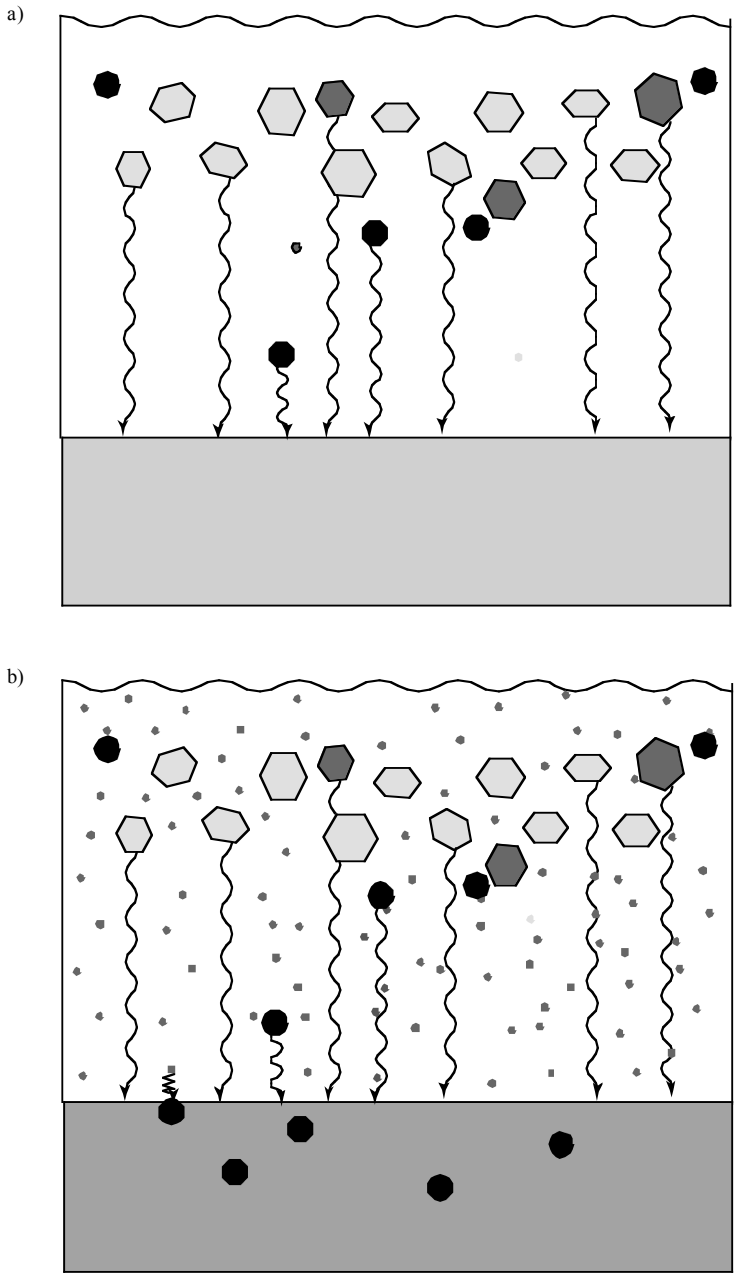

Figure 1.1 Characterization of the aqueous geochemistry of thorium and uranium under (A) reducing and (B) oxidative weathering conditions. The hexagonal shapes represent detrital minerals whereas the circular symbols represent dissolved constituents. The light grey symbols represent materials that are thorium-rich, whereas the dark grey symbols correspond to uranium-rich materials. The black circles signify the presence of organic matter. Note the darker grey shade of the substrate under oxidizing weathering conditions as the concentration of uranium is increased by the reductive precipitation of uranium onto organic matter.

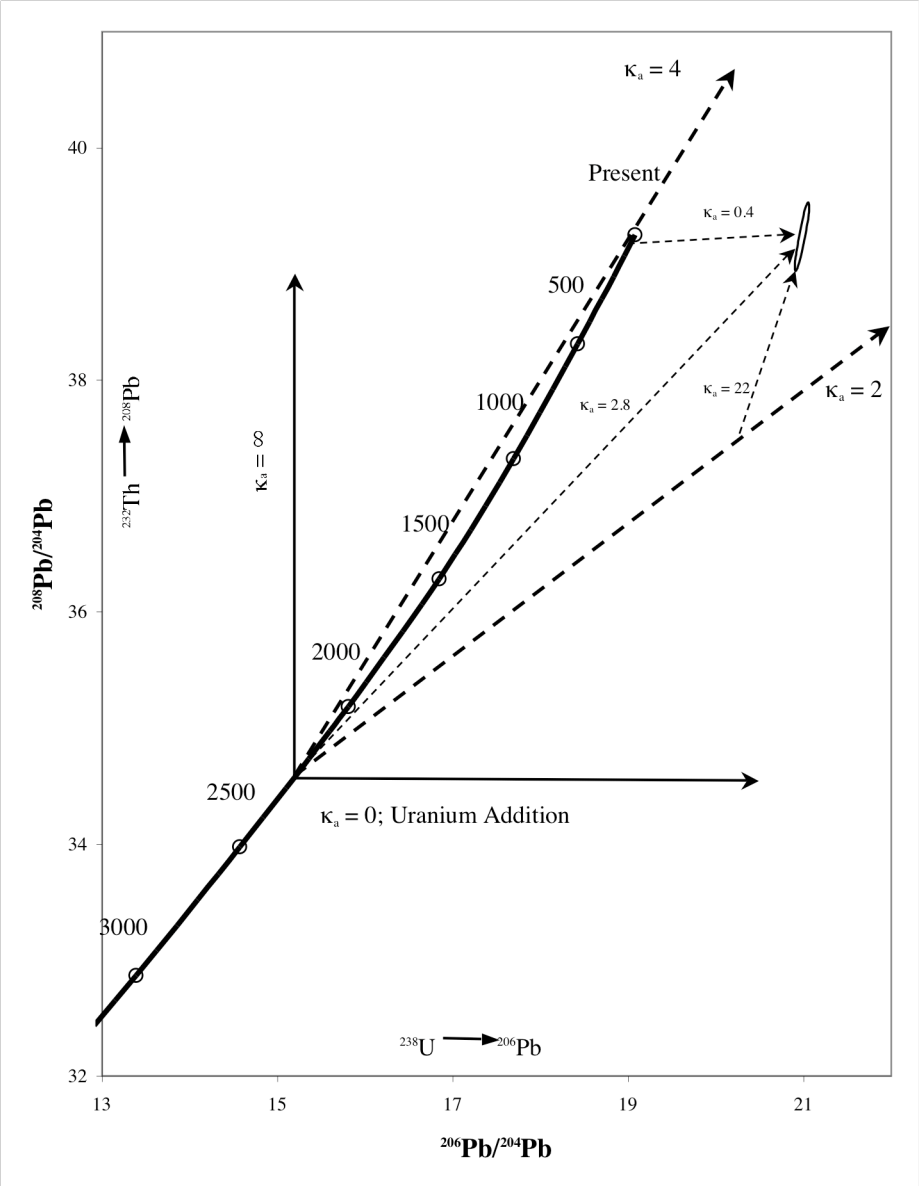

Figure 1.2 Hypothetical uranogenic and thorogenic Pb isotope growth and possible interpretations. The model Pb isotope growth curve is provided as a solid curvilinear feature with ages noted for millions of years before present. Also provided are Pb isotope growth arrays (dashed lines) for several different values of κ_a. Note that although single stage Pb isotope growth starting at 2.2 Ga with a κ_a of 2.8 can result in the final Pb isotope composition, so can a two-stage growth of $\kappa_a = 4$ from 2200 Ma until 100 ka followed by growth with a $\kappa_a = 0.4$ from 100 ka until present. Discrimination of the timing of Pb isotope growth is possible through evaluating a uranogenic Pb isotope ratio plot.

2. THE 2.5 GA MOUNT MCRAE SHALE, HAMERSLEY GROUP, WESTERN AUSTRALIA

2.1 Geologic Setting

The early Archean rocks of the Yilgarn Craton and Pilbara Craton and the younger rocks deposited in superimposed basins dominate the geology of Western Australia (Figure 2.1). The Hamersley Basin formed on the Pilbara Craton during the later part of the Archean Eon and contains volcano-sedimentary units of the Mount Bruce Supergroup deposited between ~2.5 Ga (Anbar et al., 2007; Glikson and Vickers, 2007; Rasmussen et al., 2005; Trendall, 1990). The Hamersley Group is the middle of three stratigraphic units that comprise the Mt. Bruce Supergroup and is interpreted as being deposited in a deep marine basin (Hassler, 1993). These sedimentary rocks were subjected to prehnite-pumpellyite, and locally greenschist, facies metamorphic conditions (Blake, 1984; Blake and Barley, 1992). The Mount McRae Shale is a well-characterized organic-rich shale formation within the Hamersley Group (Kakegawa et al., 1999). The depositional age of the Mount McRae Shale has been determined by direct radiometric Re-Os dating of whole-rock drill core samples of the Mount McRae Shale (2501 ± 8.2 Ma; Anbar et al., 2007) and U-Pb dating of zircon (2504 ± 5 Ma; Rasmussen et al., 2005). The Mount McRae Shale is only about 60 meters thick and contains organic-rich shales which overlie the Mt. Sylvia Formation and underlie iron formations.

Samples were taken from two short exploration drill holes in Perth, Western Australia by the Rio Tinto Iron Ore Company. The drill cores (WLT-02 and WLT-10) were drilled through the Dales Gorge Iron Formation and a short distance into the Mount McRae Shale. The upper part of the Mount McRae Shale recovered from the drill cores was deeply weathered and oxidized with no remaining organic material. Consequently,

the samples selected for this study were stratigraphically below this oxidized zone and did not show any visible signs of alteration. Samples were collected from both cores and assigned sample numbers based on the core and depth of collection. Samples were then powdered for use in this geochemical study using a high strength steel stamp mill and shatterbox.

2.2 Results

2.2.1 Whole Rock Pb Isotope Ratios

Whole-rock Pb isotope data from the drill core samples obtained in this study are presented in Table 2.1. Uranogenic Pb isotope ratios ($^{207}Pb/^{204}Pb$ and $^{206}Pb/^{204}Pb$) for the eleven whole-rock samples as well as model Pb isotope growth curves representing single-stage Pb isotope evolution from a μ=8, κ=3.9 reservoir (calculated from primordial Pb isotope ratios and T_1 of 4.57 Ga), a two-stage Pb isotope evolution model (Stacey and Kramers, 1975), as well as the lead isotope growth model of Kramers and Tolstikhin (1997) are displayed in Figure 2.2. Although the Kramers and Tolstikhin model is preferred for modeling surficial environments, the other models are commonly used and therefore have been provided to display the slight differences between these models. Using the Pb isotopic composition from these models at 2.5 Ga, the shale samples have μ_2 values ranging from 4.9 to 14.8. The Pb isotopic ratios of the samples plot as a positively correlated array with a best-fit slope of 0.155 ± 0.054, which corresponds to a growth age of 2402 ± 590 Ma to present (MSWD = 16). This age cannot be considered an isochron age, as arrays are required to have less scatter (MSWD < 1.5) to be

considered as a true isochron. This slope age however falls within the range of previously determined ages for the Mount McRae Shale.

Pb isotope ratios plotted on a $^{206}Pb/^{204}Pb$ vs. $^{208}Pb/^{204}Pb$ diagram (Figure 2.3) reveal a scattered array of points with a positive slope. Using the model Pb isotope ratios corresponding to the accepted age of sedimentation as the initial Pb isotope composition, κ_a ranges from 3.33 to 2.14, with an average value of 2.80. These values (even the maximum value) are well below the average Th/U ratio of Post-Archean shales (3.8 from Taylor and McLennan, 1985) and the model Th/U ratio for sedimentary rocks at 2.5 Ga (3.86 from Kramers and Tolstikhin, 1997).

2.2.2 Leached Sample Pb Ratios

Two samples (WLT-02; 145.9 m and WLT-10; 381.0 m) were selected for step-wise acid leaching (Table 2.2; Figures 2.4 and 2.5). The step-wise acid leaching of the more radiogenic sample (WLT-02; 145.9 m; Figure 2.4a) resulted in two of the leach steps (L2 and L3) having very low concentrations of Pb. The lack of Pb isotope ratio data for these two leach steps does not indicate a flawed methodology (as demonstrated through Pb isotope ratio data for these leach steps from other samples), but rather a lack of Pb liberated by these acid digestions. The first (L1) and last (R) leach steps have Pb isotope compositions such that the Pb liberated by leaching is in equilibrium with the Pb isotopic composition of the whole rock. The leach steps and whole-rock Pb isotope composition of this sample display a linear array with a slope of 0.11 (± 0.55) corresponding to Pb isotope growth from 1719 ± 9500 Ma to present on a $^{206}Pb/^{204}Pb$ vs. $^{207}Pb/^{204}Pb$ diagram (MSWD = 6.7). These leach steps define a linear array on a

$^{206}Pb/^{204}Pb$ vs. $^{208}Pb/^{204}Pb$ diagram (Figure 2.4b) with corresponding model κ_a values ranging from 2.35 to 3.89, which is inclusive of the whole rock κ_a ratio (3.25), calculated using model Pb initial ratios based on the Kramers and Tolstikhin model (1997).

The field of Pb isotopic compositions of the leach steps and residue of the less radiogenic sample (WLT-10; 381.0 m; Figure 2.5) enclose the isotopic composition of the whole rock, implying that the whole rock is represented by its leach components and residue. The leach steps and whole-rock Pb isotope composition define a linear array with a slope of 0.146 ± 0.076 corresponding to Pb growth from 2297 ± 900 Ma to present on a $^{206}Pb/^{204}Pb$ vs. $^{207}Pb/^{204}Pb$ diagram (Figure 2.5a; MSWD = 3.2). On a $^{206}Pb/^{204}Pb$ vs. $^{208}Pb/^{204}Pb$ diagram (Figure 2.5b), the leach steps and whole rock Pb isotopic composition define a linear array corresponding to model κ_a values ranging from 2.04 to 2.81, inclusive of the whole rock κ_a ratio (2.29).

An approximation of the whole rock Pb isotope composition can be made by multiplying the relative signal intensity from mass spectrometry of each leach step by the Pb isotope ratios of those leach steps and summing the derived values (Table 2.3). When this calculated whole rock Pb isotope composition is compared to the measured whole rock Pb isotope composition, agreement for all isotope ratios (< 1.9% relative difference) is observed, further supporting system equilibrium and reducing the possibility that resistant phases remained undigested after leaching.

2.2.3 REE Concentrations

REE concentration data obtained during this study are presented in Table 2.4 along with a new analysis of REE abundances for United States Geological Survey

standard SCo-1 (Cody Shale) for reference. Chondrite-normalized REE patterns (Figure 2.6) are similar in all samples, displaying concave downward patterns with light REE (LREE) enrichment ($La_N/Yb_N = 11.83 \pm 3.60$). The heavy REE (HREE) display little observable fractionation (average $Dy_N/Yb_N = 1.01 \pm 0.14$). Anomalous behavior of Eu and Ce results from the susceptibility of these elements to variable oxidation states during high and low temperature hydrothermal fluxes (Gao and Wedepohl, 1995) and variable redox conditions (DeBaar, 1991 and sources within). This phenomenon is quantified by Eu- and Ce-anomalies (see Section 1.1.2.2). Chondrite-normalized REE patterns display negative Eu-anomalies ($Eu/Eu^* = 0.746 \pm 0.065$) and with both slightly negative and positive Ce-anomalies ($Ce/Ce^* = 0.985 \pm 0.085$). REE concentrations are generally lower than PAAS with greater fractionation in the HREE and slight PAAS-normalized negative Ce-anomalies ($Ce/Ce^* = 0.922 \pm 0.080$) and pronounced positive Eu-anomalies ($Eu/Eu^* = 1.12 \pm 0.10$).

Sample normalized REE patterns can accentuate small differences in REE concentrations amongst samples from the same suite. The sample chosen for normalization was the sample having the greatest REE concentration (WLT-02, 146.4m). In sample normalized REE patterns (Figure 2.7), some notable variations do exist although all variations are within 40% of the concentration of the normalizing sample. All sample-normalized patterns display a positive Ce-anomaly ($Ce/Ce^* = 1.10 \pm 0.034$) and have HREE fractionation (average $Gd_{SN}/Yb_{SN} = 0.900 \pm 0.174$).

2.3 Discussion

Interpretation of the comparative Pb isotope composition diagrams and REE patterns provide insights into the behavior of the U-Th-Pb system within the Mount McRae Shale. The age associated with the onset of Pb isotope growth (2402 ± 590 Ma) is close to that previously determined for the Mount McRae Shale. This provides evidence that Pb isotope growth was initiated during sedimentary processes and that κ_a values might represent the time-integrated Th/U ratio associated with sedimentary events (κ_a). If this is true, and the concentration of Th is conservative over the same time, the values of κ_a would be associated with an addition of up to 41% excess uranium. The relative consistency of the REE patterns and interelement REE ratios (La/Nd, Ce/Ce*, and Eu/Eu* 2σ = 8.64%, 8.65%, 8.64% respectively) may also be interpreted as an indication that post-depositional processes did not alter the geochemistry of these samples. This excess uranium could be the result of oxidative weathering of continental crust liberating U as dissolved ions as early as 2.5 Ga. This model requires little additional interpretation, but upon close inspection the Pb isotope ratios and REE patterns suggest that another model may better explain the data.

Despite the lack of visible evidence of post-depositional alteration in these samples, geochemical evidence suggests potential disruption to the U-Th-Pb system, which can be modeled using uranogenic Pb isotope ratios ($^{206}Pb/^{204}Pb$ and $^{207}Pb/^{204}Pb$). The near linear array that is present on the whole-rock uranogenic Pb isotope diagram (Figure 2.2) appears to be branched. This observed branching may be further explored by identifying samples as members of a steeper (older) array or a more gently sloping (younger) array based on their Pb isotope composition. Although the division of the

samples into two groups is suggested by the Pb isotope ratios, interelement REE ratios do not support this. Therefore any disturbance to the U-Th-Pb geochemistry of the Mount McRae Shale must be low temperature in nature or alternatively the result of source mixing.

In the most conservative estimate, the gently sloping array may be composed of just the two samples that lie off to the right of the major array (WLT-10, 379.9m and 383.8m). The remaining samples would then define a stepper array than that originally proposed for all of the samples. This division is not clearly evident from REE patterns but may be the result of uranium mobility, which is often not associated with REE mobility.

Using the new proposed groupings, the steeper array has far less scatter (MSWD = 2.3) with a slope of 0.1869 (± 0.022) corresponding to Pb isotope growth from 2715 ± 190 Ma to present (Figure 2.8). Because this model proposes a disruption to the growth of Pb isotopes, it is unlikely that Pb isotope growth continued unchanged from the initial U/Pb until present. Using the previously determined Re-Os radiometric age of 2501.1 ± 8.2 Ma (Anbar et al., 2007) as a model for the onset of Pb growth and the slope of the 9-point array (0.1869), the age associated with the end of Pb growth is 461.5 ± 446.5 Ma. The statistical analysis of κ_a values also change when considering the $^{206}Pb/^{204}Pb$ and $^{208}Pb/^{204}Pb$ ratios of the samples that define the steeper array (Figure 2.9). The κ_a of this refined grouping of samples averages 2.88 ± 0.23 (2σ). This indicates that despite removing two samples from the group, the overall average κ_a does not change much but the variation decreases significantly. Although the interpretation of the Pb isotope ratio data from the steeper array provides the basis for this model, it is important not to neglect

the other two samples but rather interpret the significance (if any) of their Pb isotope composition.

The two points that have been identified as potential outliers define a line on both Pb isotope ratio plots (per geometry) and the slopes of these lines can be interpreted but much caution is to be used. A line constructed by connecting the two remaining points on a $^{206}Pb/^{204}Pb$ vs. $^{207}Pb/^{204}Pb$ diagram has a slightly positive slope (0.012). This slope however is too shallow from which any meaningful age can be calculated regardless of the time constraints imposed on the calculation. Similarly these points have two different κ_a values (2.77 and 2.14), which define a line with a negative slope on a $^{206}Pb/^{204}Pb$ vs. $^{208}Pb/^{204}Pb$ diagram. The shallow slope and variable values of κ_a for the Pb isotope ratios of these samples require that they were altered since deposition and/or had different initial U/Pb ratios, perhaps multiple times. Because the Pb isotope ratios of all of the remaining samples do not show variations in initial U/Pb ratios it is more likely that the Pb isotope ratios were altered during post-depositional processes. These interpretations based on this model bring into serious doubt the suitability of these rocks for use in paleoredox studies.

The variation observed in Pb isotope ratio analyses of the step-wise acid leaching procedure, also suggests that the U/Pb ratios may have been reset during post-depositional processes. The Pb-Pb slope ages of the leach sequences are not equal (1719 ± 9500 Ma and 2297 ± 900 Ma) however because each sample set has large uncertainties the ages fall within the error of the other. This is not an entirely valid perspective as the younger age has errors that permit its interpretation as material predating the origins of the Solar System. The older age may prove more helpful but suggests a Paleoproterozoic

disturbance, which is not observed in the diagram of whole rock Pb isotope ratios. Additionally, both samples would be classified as coming from the steep array, implying that the steep array is the result of geochemical happenstance rather than geochemical preservation since 2.5 Ga.

The model suggesting that the Pb isotope ratios have been reset or altered since deposition can be further evaluated with the more robust REE geochemical system. The variable morphologies of the chondrite-normalized REE patterns (Figure 2.6) for selected samples of the Mount McRae Shale also support the hypothesis of post-depositional alteration of the whole rock geochemistry. Although ancient post-depositional oxidative weathering could explain the distribution of uranogenic Pb isotope ratios, chondrite normalized REE patterns should be unaltered by this type of alteration (Condie et al., 1995; Duddy, 1980; Nesbitt and Markovics, 1997). Absolute differences in REE concentration should not be used to interpret different provenance components as variable concentrations of mineral phases in which the REE are incompatible (e.g., quartz) are common among sedimentary strata of single formations (Taylor and McLennan, 1985). Therefore it is often better to quantify the observed differences in pattern morphology through interelement REE ratios (e.g. La_N/Yb_N, La_N/Sm_N, Eu/Eu*). Although all samples display LREE-enriched concave upward REE patterns common to shales, the overall slope of the pattern ($La_N/Yb_N = 11.9 \pm 3.63$ 2σ) is steeper than most shales. More significantly, the differences in morphology cannot be simply modeled by the addition or subtraction of a common rock-forming mineral but are rather complex indicating that either the provenance of these samples was not consistent or the REE were remobilized during a post-depositional event.

Due to the lack of high precision Sm and Nd isotope ratio data, this REE redistribution event cannot be dated by direct radiometric methods, and may be distinct from the event that disturbed the U-Th-Pb system. However because it can be generally assumed that the REE are less mobile than U under oxidizing conditions of geochemical alteration, the U-Th-Pb system should provide a record of two disturbances if they were distinct events. Because the distribution of whole rock Pb isotope compositions can be explained by one disturbance, the need exists to explain one post-depositional event capable of disturbing U-Th-Pb and REE geochemistry.

The timing of this event may be related to the age associated with the branching of the uranogenic Pb isotope growth (ca. 460 Ma) which is similar to that associated with the early stages of tectonism associated with the Alice Springs Orogeny. Although majority of tectonic stress during Alice Springs Orogeny was centered well to the east of the Hamersley Basin, extension associated with the event resulted in the Middle Paleozoic development of the adjacent Canning Basin. This time period also encompass the age range determined for the disruption in radiogenic Pb isotope growth. It can therefore be suggested that the tectonic development of the nearby Canning Basin resulted in the alteration of the geochemistry of the Mount McRae Shale. The presence of alteration phenomena recorded in both the Pb isotope ratios and the REE concentration that coincide with the timing of a proximal tectonic event suggests that these events are related. It is therefore likely that some of the paleoredox indicators of oxidative conditions recorded by the time-integrated Th/U ratios were not of sedimentary origin but rather were altered by oxidizing fluids or other metamorphic conditions during the Canning Basin tectonic event.

The Pb isotope ratios of the samples used in this study have been interpreted as an indication of U enrichment during sedimentation or post-depositional events, but the data may also be explained solely through the presence of multiple detrital sources of U-Th-Pb and the REE. In this model, the variations observed in time-integrated Th/U ratios result from the admixture of sediment sources with variable Th/U ratios. The observed variation of Pb isotopic compositions of the whole rocks studied can be used to constrain the number of sediment sources and their Pb isotopic ratios. Pb isotope ratios plotted on a $^{206}Pb/^{204}Pb$ vs. $^{208}Pb/^{204}Pb$ diagram, reveal a minimum of two sources, one with κ_a of 2.14 and the other with a κ_a of 3.33. The distribution of chondrite-normalized REE patterns suggests that a minimum of two sources (one with a $La_{CN}/Yb_{CN} = 12.3$ and the other 6.85) is required to explain the differing degrees of LREE enrichment. An additional source is required to explain the more subtle Eu-anomaly observed in WLT-10; 387.4m. Although only two sources are needed to explain the variation in Th/U ratios, the branched appearance of Pb isotope ratios plotted on a $^{206}Pb/^{204}Pb$ vs. $^{207}Pb/^{204}Pb$ diagram requires a minimum of three sources with different U/Pb ratios. Because the geochemical characteristics of each source are not necessarily covariant, a minimum of four sources must have been present in order to explain the total variation in geochemistry by source mixing alone. It is more likely that bimodal source mixing resulted in the variation in interelement REE ratios and post-depositional alteration of the U-Th-Pb system of the suite is responsible for the variation in κ_a ratios.

Regardless of the hypothesis, it is clear that using geochemical proxies in samples of the Mount McRae Shale for paleoenvironmental studies is inappropriate. Models that attempt to explain the rise of atmospheric concentrations of oxygen through geochemical

proxies are perhaps the most impacted by this revelation, especially if they use samples from the Mount McRae Shale or other sedimentary rocks from the Hamersley Basin. The recent paper by Anbar et al. (2007) uses the geochemistry of drill core samples from the Mount McRae Shale to assert that oxygen levels rose to a level capable of oxidizing Mo and Re while leaving the U cycle unchanged. This study was careful to explore several potential explanations for variable trace element ratios and even provided geochronological context for the geochemical data in an attempt to "verify that metal abundances were unaffected by remobilization." Despite the authors' careful treatment of the data and treatment of other potential explanations of the data, the possibility of multiple provenance components with variable trace element ratios was not considered. The trace element (and Al) concentration data of Anbar et al. (2007) could be explained by the influx of sediment produced by the exhumation and weathering of a sulfide-rich rock unit (with high concentrations of Re and Mo) within the drainage basin of the depositional basin in which the Mount McRae Shale was deposited. An investigation of the distribution of the REE within these rocks would provide resolution to the proposal that the influx of geochemically distinct sediment could explain the variations in Re/Os, Re/Al, and Mo/Al ratios. Additional work must still be done to preclude this provenance-based model from further contention.

2.4 Conclusions

It is obvious from the geochemical data presented, that the geochemical composition of the Mount McRae Shale does not permit the use of this stratigraphic unit for meaningful interpretation of paleoenvironmental conditions without extensive

supporting geochemical data to verify that the distribution of geochemical data is not the result of either post-depositional processes or multiple provenance components. Trace element concentration data is particularly susceptible to misinterpretation as there are few geochemical systems that combine the utility of providing temporal context to the establishment of element ratios used as paleoredox proxies. Future studies with the expressed purpose of trying to evaluate the paleoredox conditions associated with deposition must take all measures to eliminate the potential for non-redox related explanations for geochemical variations. These measures include:

1) Extensive characterization of the redox related changes within geochemical system(s) being considered. These changes should be obvious and distinguishable such as the less variable Th/U ratio characteristic of igneous rocks not subjected to the oxidation of U (3.8) and the highly variable Th/U ratio characteristic of oxidized sources.

2) Geochronological verification that the geochemical proxy was unaffected by post-depositional redistribution of the elements through radiometric ages determined for a redox sensitive system (i.e., U-Th-Pb, Re-Os).

3) Ensuring that the geochemical variations are not related to changes in the geochemical nature of the detrital sources through the evaluation of REE patterns and other geochemical proxies that have the potential to reveal provenance mixing and variability.

This study evaluates the redox-sensitive decoupling of U from Th under oxidizing conditions through evaluation of time-integrated Th/U ratios (κ_a) and the U-Th-Pb

geochemical system. The interpretation of Pb isotope ratios allows for the temporal evaluation of the establishment of these redox-sensitive ratios through Pb-Pb slope ages. If the calculated slope age corresponds to the age of sedimentation it is interpreted that the κ_a is representative of the Th/U ratio established during the sedimentary process and can be used as an indicator of redox conditions prevalent during weathering, transportation, and deposition.

The evaluation of the geochemistry in samples of the Mount McRae Shale indicates that the calculated values of κ_a are not representative of the Th/U ratio during the sedimentary process at ca. 2.5 Ga. Uranogenic Pb isotope ratio plots and chondrite-normalized REE patterns are interpreted as recording a disturbance to the U-Th-Pb system at 460 Ma and source variability within the Mount McRae Shale. This raises the issue of the robustness of other geochemical paleoredox indicators during geochemical disturbances and the effect of multiple sources on the interpretation of paleoredox conditions. Therefore it is inappropriate to interpret the low and variable values of κ_a in the context of an indicator of paleoredox conditions. Rather it is likely that these values represent the redistribution of trace elements during a post-depositional disturbance. The variation in REE patterns can be interpreted as representing an admixture of distinct provenance components for the Mount McRae Shale. Although this study fails to provide additional constraints to the rise of atmospheric oxygen concentrations, it demonstrates the effectiveness of the U-Th-Pb system in determining appropriate stratigraphic units for paleoredox studies. Additionally, it introduces suspicion to previous studies that have claim to have found geochemical evidence of local oxygen

oases or “whiffs” of atmospheric oxygen in multiple geochemical proxies from several sedimentary units that predate the Great Oxidation Event.

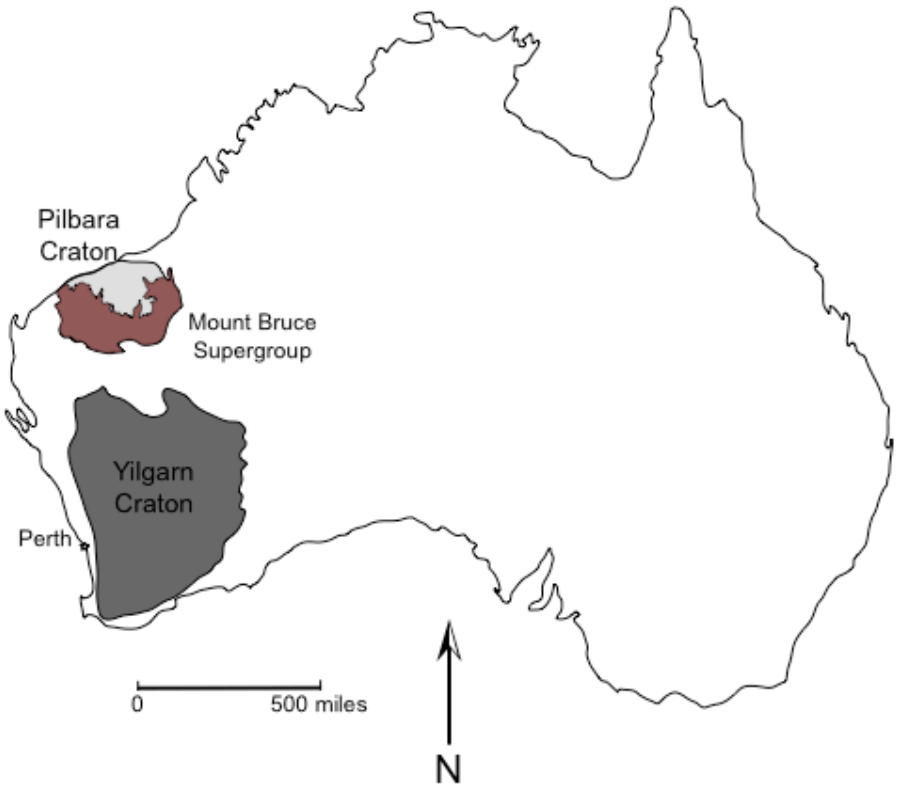

Figure 2.1 Generalized geologic map of Western Australia. The extent of the Pilbara and Yilgarn Cratons as well as the distribution of rocks in the Mount Bruce Supergroup are displayed. Also shown is the location of Perth for reference.

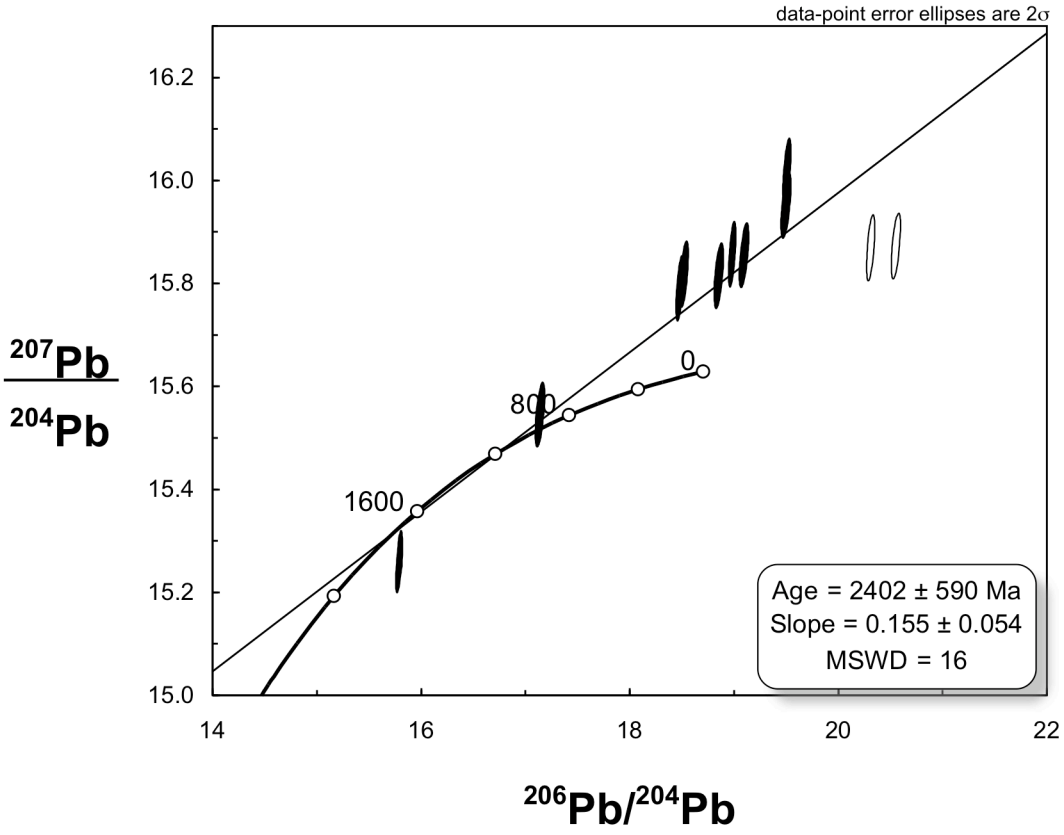

Figure 2.2 $^{206}Pb/^{204}Pb$ vs. $^{207}Pb/^{204}Pb$ isotope ratio diagram for the whole rock shale samples of the Mount McRae Shale. The Pb isotope growth curve shown is based on the Pb isotope growth model of Kramers and Tolstikhin (1997). Model Pb isotope ratios for several ages are provided for reference. The slope of the total array of points corresponds to a Pb-Pb slope age of 2402 ± 590 Ma, which agrees with the 2501 ± 1.8 Ma Re-Os radiometric age for sedimentary pyrite (Anbar et al., 2007). The Y-shape of the points indicates that uranium was likely mobilized after deposition. Hollow symbols indicate samples that appear to have experienced U mobilization (see text).

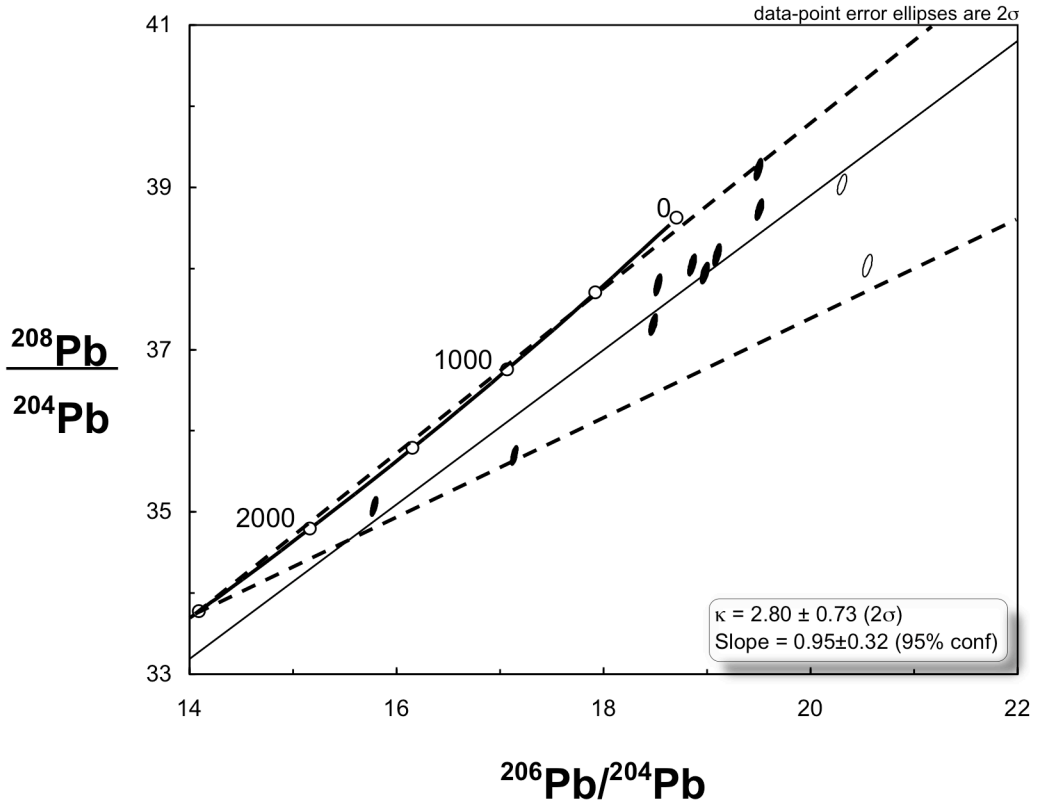

Figure 2.3 $^{206}Pb/^{204}Pb$ and $^{208}Pb/^{204}Pb$ isotope data for the whole rock shale samples of the Mount McRae Shale. The growth curve shown represents the Pb isotope growth model of Kramers and Tolstikhin (1997). Samples that appear to display disrupted U/Pb ratios are left hollow. Model Pb isotope values for several ages are provided for reference with the apex of the two dashed rays representing the model Pb isotope value at 2501 Ma. The observed dispersion may result from variable Th/U ratios present in the sediments during deposition or from post-depositional redistribution of isotopes in the U-Th-Pb system.

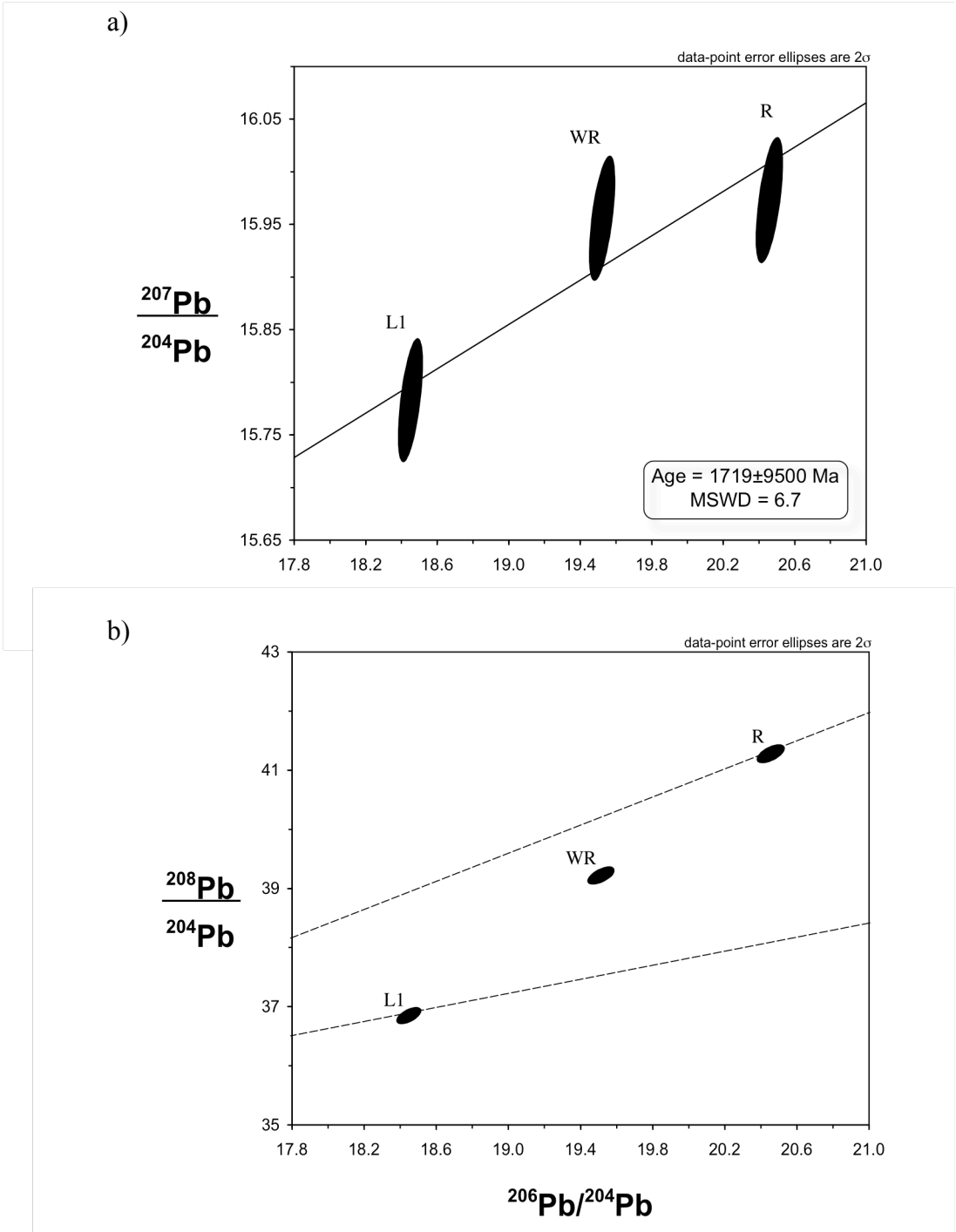

Figure 2.4 Pb isotope ratio plots from acid leaching of sample WLT-02; 145.9 m. The isotope ratio of the whole rock and each leach step is labeled. These isotope ratio diagrams show that the whole rock is in equilibrium with the leached mineral phases. The young age associated with the slope of the array on a $^{206}Pb/^{204}Pb$ vs. $^{207}Pb/^{204}Pb$ plot (a) has a high degree of error due to the lack of variation in Pb isotope ratios.

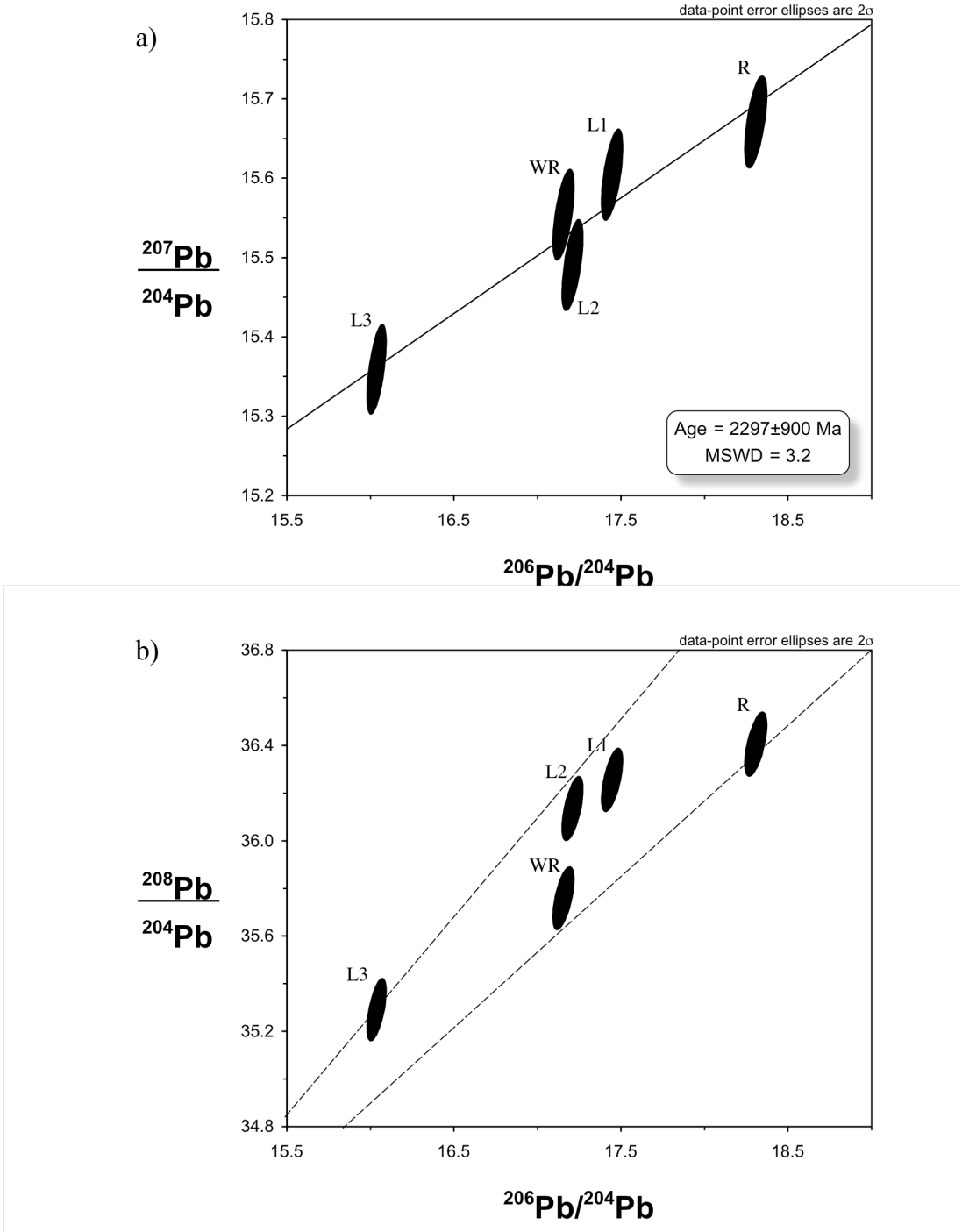

Figure 2.5 Pb isotope ratio plots from acid leaching of sample WLT-10; 381.0 m. The isotope ratio of the whole rock and each leach step is labeled. These isotope ratio diagrams show that the whole rock is in equilibrium with the leached mineral phases. The age associated with the slope of the array on a $^{206}Pb/^{204}Pb$ vs. $^{207}Pb/^{204}Pb$ plot (a) is coincident with previous age determinations for the Mount McRae Shale and may be indicative of an "unaltered" sample.

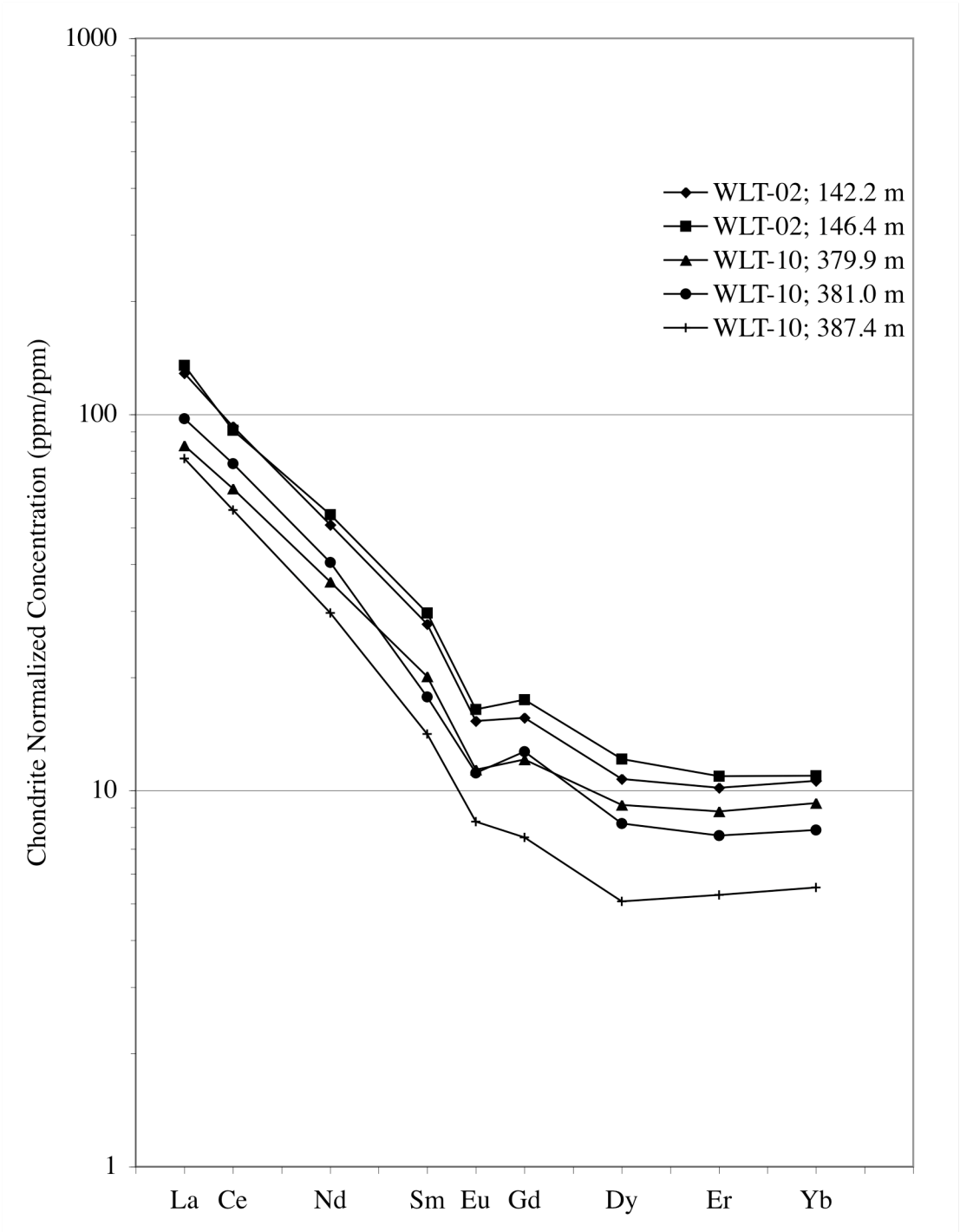

Figure 2.6 Chondrite-normalized REE patterns of the shale samples of the Mount McRae Shale. These patterns were determined by ID-ICP-MS, so the errors of the individual points are smaller than the symbols used. The different morphologies observed in these patterns indicate multiple provenance components for the detrital fraction of the Mount McRae Shale.

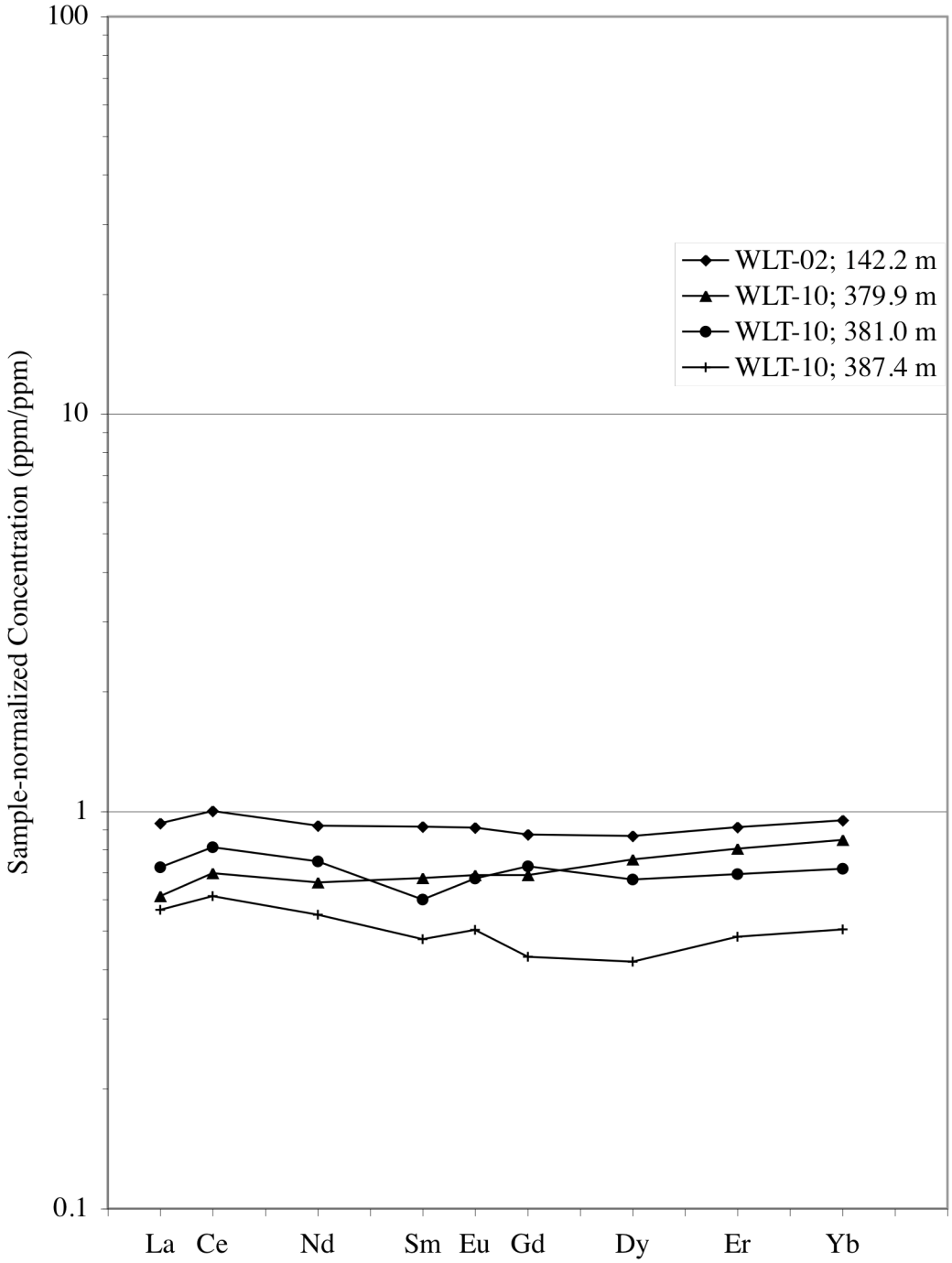

Figure 2.7 Sample-normalized REE patterns of the shale samples of the Mount McRae Shale. Sample REE concentrations are normalized to those from sample WLT-02; 146.4m, the sample with the highest REE concentration. The geochemically variable provenance suggested by chondrite-normalized REE patterns is supported by sample-normalized REE patterns, which show significant fractionation between analyzed samples.

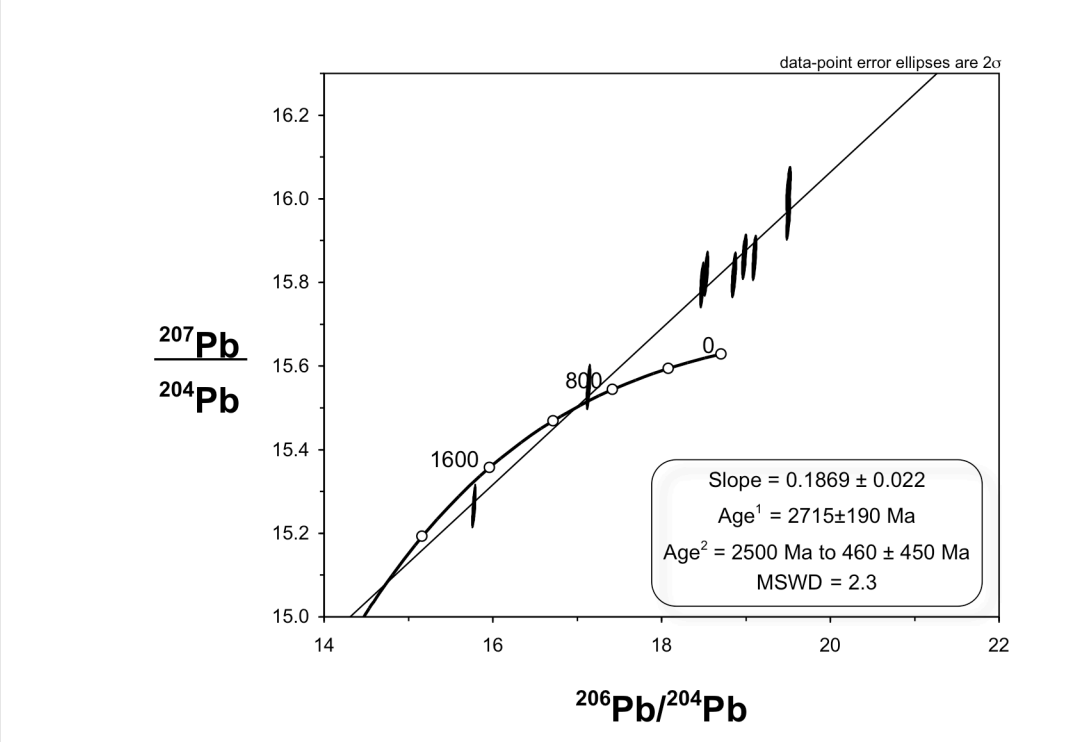

Figure 2.8 $^{206}Pb/^{204}Pb$ vs. $^{207}Pb/^{204}Pb$ isotope ratio diagram for selected whole rock samples of the Mount McRae Shale. Age^1 is the age associated with the initiation of Pb isotope growth assuming no disruption to the system. Age^2 is the age that corresponds to the end of Pb isotope growth based on Pb isotope growth starting at the previously determined age for the Mount McRae Shale (Anbar et al., 2007).

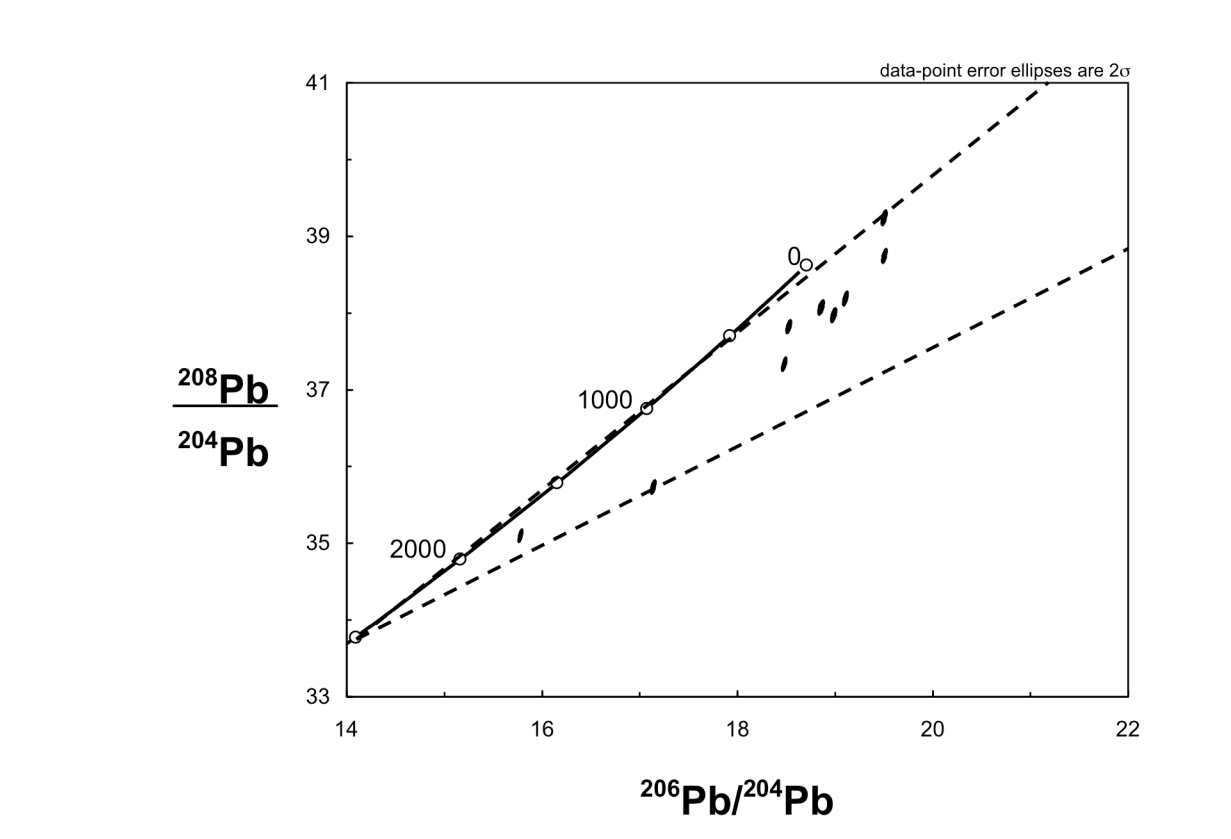

Figure 2.9 $^{206}Pb/^{204}Pb$ vs. $^{208}Pb/^{204}Pb$ isotope ratio diagram for selected whole rock samples of the Mount McRae Shale. Although the average κ_a value of these samples (2.80) is not much different than the average κ_a of all the samples, the variation is much less. The isotope ratios display a near linear relationship which may be an indication of unaltered κ_a ratios.

Table 2.1 Whole rock Pb isotope compositions and values of κ_a for the Mount McRae Shale

Sample and Drill core	$^{206}Pb/^{204}Pb$	$^{207}Pb/^{204}Pb$	$^{208}Pb/^{204}Pb$	κ_a
2.5 Ga Mount McRae Shale				
WLT-02				
142.2m	18.55	15.82	37.84	2.99
145.9m	19.52	15.96	39.24	3.25
146.4m	18.88	15.82	38.08	2.95
147.3m	18.50	15.80	37.35	2.70
147.5m	19.00	15.86	37.98	2.81
148.0m	19.12	15.86	38.20	2.88
148.1m	19.52	16.02	38.75	2.98
WLT-10				
379.9m	20.57	15.88	38.07	2.21
381.0m	17.16	15.56	35.76	2.29
383.8m	20.33	15.87	39.06	2.76
387.4m	15.81	15.27	35.14	2.86

Table 2.2 Pb isotope compositions for the step-wise leaching of shales from the Mount McRae Shale

Sample and Drill core	$^{206}Pb/^{204}Pb$	$^{207}Pb/^{204}Pb$	$^{208}Pb/^{204}Pb$
2.5 Ga Mount McRae Shale			
WLT-02; 145.9 m			
L1	18.46	15.79	36.89
R	20.45	15.97	41.27
WR	19.52	15.96	39.24
WLT-10; 381.0 m			
L1	17.45	15.60	36.26
L2	17.22	15.49	36.14
L3	16.05	15.36	35.30
R	18.31	15.67	36.41
WR	17.16	15.56	35.76

Leaching was done according to steps L1 (1 mL 0.1M HBr, ~1h), L2 (1 mL 4M HBr, ~1 hr), L3 (1 mL 50:50 HCl:HNO_3), R (HF and HNO_3)

Leaching of sample WLT-02; 145.9 m produced negligible amounts of Pb in steps L2 and L3; data was not reported

Table 2.3 Relative proportion of Pb associated with each leach step for two shales from the Mount McRae Shale

Sample and Drill core	Counts per Second (cps)					
	^{204}Pb	^{206}Pb	^{207}Pb	^{208}Pb	Total	Percentage
WLT-02; 145.9 m						
L1	5.46E+07	1.01E+09	8.59E+08	2.01E+09	3.93E+09	62.9%
R	2.95E+07	6.01E+08	4.69E+08	1.21E+09	2.31E+09	37.1%
		$^{206}Pb/^{204}Pb$	$^{207}Pb/^{204}Pb$	$^{208}Pb/^{204}Pb$		
Calculated Whole Rock		19.20	15.86	38.51		
Measured Whole Rock		19.52	15.96	39.24		
WLT-10; 381.0 m						
L1	3.54E+05	6.03E+06	5.40E+06	1.25E+07	2.43E+07	1.7%
L2	1.63E+07	2.80E+08	2.52E+08	5.87E+08	1.14E+09	78.8%
L3	4.04E+06	6.47E+07	6.20E+07	1.42E+08	2.73E+08	18.9%
R	1.32E+05	2.26E+06	1.93E+06	4.48E+06	8.80E+06	0.6%
		$^{206}Pb/^{204}Pb$	$^{207}Pb/^{204}Pb$	$^{208}Pb/^{204}Pb$		
Calculated Whole Rock		17.01	15.47	35.98		
Measured Whole Rock		17.16	15.56	35.76		

Table 2.4 REE concentrations for samples of the Mount McRae Shale

	WLT-02; 145.9 m	WLT-02; 145.9 m (1)	WLT-02; 145.9 m (2)	WLT-02; 146.4 m	WLT-10; 379.9 m	WLT-10; 381.0 m	WLT-10; 387.4 m	Sco-1
La	40.6	40.5	40.7	42.5	26.0	30.7	24.0	42.2
Ce	75.7	75.3	76.1	74.4	52.0	60.5	45.6	56.0
Nd	30.5	30.5	30.6	32.6	21.6	24.4	17.9	25.7
Sm	5.34	5.31	5.38	5.74	3.90	3.44	2.74	5.03
Eu	1.11	1.10	1.12	1.20	0.827	0.811	0.602	1.09
Gd	4.06	4.04	4.08	4.56	3.16	3.32	1.96	4.38
Dy	3.51	3.50	3.51	3.97	3.00	2.68	1.66	4.05
Er	2.17	2.16	2.19	2.34	1.88	1.63	1.13	2.39
Yb	2.22	2.21	2.22	2.29	1.94	1.65	1.16	2.29
LaN/SmN	4.63	4.64	4.61	4.51	4.06	5.44	5.35	5.11
GdN/YbN	1.47	1.47	1.47	1.60	1.30	1.62	1.36	1.54
LaN/YbN	12.1	12.1	12.1	12.2	8.83	12.3	13.7	12.2
Ce/Ce*	0.984	0.980	0.988	0.917	1.02	1.02	1.00	0.751
Eu/Eu*	0.736	0.735	0.737	0.723	0.728	0.741	0.802	0.720

Sample WLT-02; 145.9 m was replicated to evaluate reproducibility

3. THE CA. 2.4 GA HURONIAN SUPERGROUP, ONTARIO, CANADA

3.1 Geological Setting

The geology of the early Paleoproterozoic Huronian Supergroup is well studied due to the relative easy access and great outcrop exposures along the north shore of Lake Huron, Ontario, Canada (Figure 3.1). The siliciclastic rocks of the lower Huronian Supergroup overlie the basal mafic volcanic rocks of the Huronian Supergroup and the Archean basement rocks (Young et al., 2001; Bekker and Kaufman, 2007). Due to the lack of interbedded volcanic units within the sedimentary succession, the age of the Huronian Supergroup has not been well established. Radiometric ages for the volcanic rocks and the Murray and Creighton granites constrain the age of the base of the Huronian Supergroup between 2.49 and 2.42 Ga (Krogh et al., 1984; Krogh et al., 1996; Smith, 2002). The 2217±1.6 Ma Nipissing sills and dikes (Andrews, et al., 1986) cross cut the entire sedimentary sequence, providing a minimum age constraint to the Huronian Supergroup. The rocks of the Huronian Supergroup were subjected to sub-greenschist to lower greenschist facies metamorphism during the 1.85 – 1.80 Ga Penokean Orogeny and alkali metamorphism at about 1.7 Ga (Card, 1978; Fedo et al., 1995). In addition to disturbing the distribution of alkali elements, the ca. 1.7 Ga metasomatic event disturbed the Pb isotope system (McLennan et al., 2000).

The McKim and Pecors formations are siliciclastic units in the middle of the lower Huronian Supergroup separated by the glacial diamictites of the Ramsay Lake Formation, with the McKim Formation underlying the Ramsay Lake Formation (Figure 3.2). Fine-grained, organic-poor (TOC < 0.1%) portions of the McKim and Pecors formations were sampled from the Kerr–McGee Corp. 156-1 drill core drilled in 1969 in

Beange Township (46°27'56" N, 82°43'15" W; Fig. 3.1) and stored in Sault Ste. Marie by the Ontario Geological Survey. In this drill core, the McKim Formation is considerably thicker than the Pecors Formation, although in other areas the opposite is true. The McKim and Pecors formations were deposited in a shallow water environment above wave base on the strand and offshore areas of braided deltas in a rift basin possibly connected with an ocean to the east (Fralick et al., 1989; Young et al., 2001; Zolnai et al., 1984). Additionally, paleocurrent indicators for the lower Huronian sandstones, facies analysis, and isopach maps have been interpreted as suggesting that the depositional surface sloped towards the southeast (Fralick et al, 1989). The high CIA (chemical index of alteration) values of the McKim Formation suggest that the source materials were well weathered under potentially warm and humid conditions (Nesbitt and Young, 1982).

3.2 Results

3.2.1 Whole rock Pb isotope compositions

Whole rock Pb isotope ratio data for twelve argillite samples from the McKim and Pecors formations (six samples from each formation) are presented in Table 3.1. Uranogenic Pb isotope ratios for all of the samples and the model Pb growth curve of Stacey and Kramers (1975) are plotted in Figure 3.3. The argillite samples have μ_2 values ranging from 1.55 to 60.0, using the $^{206}Pb/^{204}Pb$ and $^{207}Pb/^{204}Pb$ ratios from the Kramers and Tolstikhin model (K&T97) at 2.4 Ga. The six samples from the Pecors Formation are represented by this total variation in μ_2, whereas those samples from the McKim Formation display less variable μ_2 values (6.03 to 18.1). The Pb isotope ratios of all of the samples plot as a positively correlated array with a best-fit slope of 0.109 (±

0.010), which corresponds to a period of radiogenic Pb isotope growth in these rocks from 1778 ± 170 Ma to present (MSWD = 115). Although this age cannot be considered an isochron age (as indicated by the high MSWD; MSWD > 1.5), it is likely that this age has significance (the age of the Penokean Orogeny is 1.85-1.80 Ga and the age of alkali metasomatism in the region is 1.7 Ga). When the samples are separated into groups by formation, the samples from the McKim Formation (Figure 3.4a) define a slope of 0.077 ± 0.032, which corresponds to the growth of radiogenic Pb isotopes from 1114 ± 820 Ma to present (MSWD = 27). The Pb isotope ratios of the Pecors Formation samples (Figure 3.4b) define an array with a slope of 0.1123 ± 0.0044, which corresponds to radiogenic Pb isotope growth from 1836 ± 71 Ma to present (MSWD = 10.9).

A $^{206}Pb/^{204}Pb$ vs. $^{208}Pb/^{204}Pb$ plot of the Pb isotope ratios from all of the samples (Figure 3.5) shows a positively correlated array with much scatter (MSWD = 1318). Using the model Pb isotope ratios from the K&T97 Pb isotope growth model that correspond to the early Paleoproterozoic age of sedimentation (ca. 2.4 Ga), model time-integrated Th/U ratios (κ_a) range from 1.01 to 3.00 for all samples from the Huronian Supergroup with an average ratio of 2.34. Pb isotope ratios of the samples from the McKim Formation (Figure 3.6a) correspond to κ_a ratios that vary from 1.01 to 2.34 and average 1.91. Pb isotope ratios of the Pecors Formation samples (Figure 3.6b) correspond to κ_a ratios that vary from 2.44 to 3.00 and average 2.76. The κ_a ratios of samples from the McKim Formation are lower than any of the samples from the Pecors Formation, which allows for the discrimination of two groups within the samples based on formation. Regardless of the formation, all κ_a ratios are well below the model Th/U ratio (3.86) for the "erosion mix" from K&T97 at 2.4 Ga.

3.2.2 Sequential acid leaching

Two samples (one from each stratigraphic unit) were selected for step-wise acid leaching and processed for Pb isotope ratio analysis (Table 3.2). The sample from the McKim Formation (5141') was selected on the basis of it having the lowest whole rock κ_a ratio (1.01). Acid leaching of this sample resulted in isotope ratio data from all of the leaching steps with 57.3% of the Pb liberated by dilute (0.1M) HBr and 33.7% of the Pb liberated by stronger (4M) HBr (Table 3.3). A plot of uranogenic Pb isotope ratios (Figure 3.7a) displays a field of scattered points that are not arranged in an organized manner. The slope of a best-fit line through these data corresponds to a Pb isotope growth age from 5344 ± 11000 Ma to present. This age is not realistic and has no relationship to the age of sedimentary or post-depositional events, but may be indicative of post-depositional redistribution of U and/or Pb. Pb isotope ratios from the leach steps and whole-rock define a positively correlated array on a $^{206}Pb/^{204}Pb$ vs. $^{208}Pb/^{204}Pb$ plot (Figure 3.7b), however due to the nature of U/Pb behavior it may be assumed that κ_a values are not indicative of U-Th-Pb systematics during depositional conditions.

The step-wise acid leaching of the Pecors Formation sample (4798'; Figure 3.8) resulted in Pb isotope ratios from three out of the four leach steps, with the third leach step containing insufficient concentrations of Pb to produce Pb isotope ratio data. The leach steps and whole-rock Pb isotope composition of this sample display a positively sloped array (slope = 0.113 ± 0.031) on a $^{206}Pb/^{204}Pb$ vs. $^{207}Pb/^{204}Pb$ plot (Figure 3.8a). The slope corresponds to the start of radiogenic Pb isotope growth at 1855 ± 490 Ma ending at present day (MSWD = 46). Pb isotope ratios from the leach steps and whole-

rock also define a positively correlated array on a $^{206}Pb/^{204}Pb$ vs. $^{208}Pb/^{204}Pb$ plot (Figure 3.8b), with the points representing κ_a values ranging from 2.12 to 3.18, encompassing the whole rock value of 2.86. Although the κ_a values may suggest that the whole rock Pb isotope composition is in equilibrium with the leach steps, the Pb isotope ratios of the leach steps are higher than the corresponding ratio of the whole rock, indicating that equilibrium may not have been achieved.

3.2.3 REE Concentrations

The REE concentrations of four samples from the Huronian Supergroup (three from the McKim Fm. and one from the Pecors Fm., including the two samples selected for acid leaching) were determined by isotope dilution mass spectrometry (Table 3.4). Chondrite-normalized REE patterns (Figure 3.9) are variable for the samples, with all samples displaying LREE enrichment over the HREE ($La_N/Yb_N = 8.57 \pm 8.91$, 2σ). The patterns display more consistent LREE fractionation ($La_N/Sm_N = 3.87 \pm 0.97$) when compared to the fractionation of the HREE ($Gd_N/Yb_N = 1.60 \pm 1.23$). The anomalous behavior of Eu, a potential geochemical indicator of Proterozoic systematics, is poorly represented in two of the McKim Formation samples (5057' and 4862'; Eu/Eu* = 1.00 and 0.98 respectively) whereas the other two samples have pronounced Eu-anomalies (Eu/Eu* = 0.72 and 0.74). These two samples display chondrite-normalized REE patterns typical of post-Archean shales (PAAS). Despite the differences observed in sample morphology and Eu-anomalies, all samples lack the presence of a Ce-anomaly ($Ce/Ce^* = 0.99 \pm 0.07$).

3.3 Discussion

Previous studies of the Huronian Supergroup have revealed that the whole rock geochemistry has been altered by alkali metasomatism and lower greenschist facies metamorphism (Card, 1978; Fedo et al., 1995; McLennan et al., 2000). McLennan et al. (2000) concluded that the U-Pb isotope systematics of sedimentary rocks of the Lower Huronian Supergroup was disturbed "at or shortly after the time of sedimentation" (2.0 – 2.2 Ga) based on the regression of uranogenic Pb isotope ratios. Specific ages of 2170 ± 58 Ma and 2212 ± 92 Ma are presented (Table 2 of McLennan et al., 2000) for the McKim and Pecors formations respectively. The authors attribute this disturbance to diagenetic processes because the age is "close to or slightly younger than sedimentation." Additionally, the authors of this study proposed that the samples of the McKim and Pecors Formations with low $^{206}Pb/^{204}Pb$ ratios (< 30) had their U/Pb ratios altered by mechanisms that solely resulted in uranium gain, whereas with those samples with high $^{206}Pb/^{204}Pb$ ratios (>30) experienced "significant" lead loss based on their interpretation of μ and κ. The calculated κ for these samples range from 2 to 4, which is close to the upper crustal average of 3.8 (Taylor and McLennan, 1985). The interpretation of Pb isotope ratio and REE concentration data for samples from the same sedimentary rock units in the Lower Huronian Supergroup presented within this dissertation do not support this earlier conclusion.

3.3.1 Interpretation of Geochemical Data from the McKim Formation

The evaluation of uranogenic Pb isotope ratios, μ, κ_a, and REE patterns for shales of the McKim Formation can reveal significant information regarding behavior of the U-Th-Pb system. The age associated with the onset of radiogenic Pb isotope growth using

the Stacey-Kramers model (1114 ± 820 Ma) does not coincide with the age constraints for the deposition of the sediments of the Huronian Supergroup (2.49 Ga – 2.22 Ga). Additionally, the 1114 ± 820 Ma Pb-Pb age range does not agree with the Pb-Pb age previously reported for the McKim Formation (2170 ± 58 Ma). This difference is unlikely explained by the local geology of the areas from which the sedimentary rocks were sampled, because the samples from this study were collected farther away from the 1.7 Ga igneous intrusions and the ca. 1.0 Ga Grenville Front when compared to the sample locations used by McLennan et al. (2000). The corresponding κ_a values for shales from the McKim Formation are interpreted as being unrelated to the oxidation state of the atmosphere during deposition, because the Pb-Pb age range is not within error of the depositional age. Instead the range of Pb-Pb ages is interpreted as indicative of source variability and a Penokean post-depositional disruption to the U-Pb isotope system.

Calculating κ_a ratios using the model initial Pb isotope ratios at 1100 Ma from the K&T97 model is inappropriate, because this calculation results in an unrealistic negative κ_a ratio (-0.799) for the deepest sample (5141'). Calculations using the Stacey-Kramers Pb isotope growth model (Stacey and Kramers, 1975) also result in negative values for κ_a. Therefore it is unrealistic to model the initial Pb isotope ratios for this sample using the K&T97 model at 1100 Ma.

3.3.2 Interpretation of geochemical data from the Pecors Formation

The Pb isotope compositions of the samples from the Pecors Formation are associated with a Pb-Pb age of 1836 ± 71 Ma (MSWD = 10.9), which is not coincident with the previously established age constraints for the deposition of the Huronian

Supergroup (2.49 – 2.22 Ga). This is interpreted as an indication that the observed variation in κ_a ratios for shales from the Pecors Formation is not related to changes in the atmospheric oxidation state at ca. 2.4 Ga but may reflect the redox conditions of metasomatism associated with the Late Paleoproterozoic Penokean Orogeny. The κ_a ratios for Pecors Formation samples range from 2.44 to 3.00 and average 2.76 using the initial Pb isotope ratio composition at 2400 Ma from the erosion mix of the K&T97 model. The κ_a ratio represents the time integrated growth of radiogenic Pb isotopes related to the depositional Th/U ratio from 2.4 Ga until 1.8 Ga and then a partially disturbed Th/U ratio from 1.8 Ga until present. This disruption is realized through the presence of a range of Pb-Pb ages that do not include the depositional age. The erosion mix of the K&T97 model attempts to model the oxidation of surficial environments through variable κ values, however at 2.4 Ga the model κ (3.86) is well above those calculated using the K&T97 model (2.44 – 3.00). The loss of uranium is consistent with the samples being organic-poor and having oxidizing metasomatic fluids leach the uranium from the samples.

3.3.3 Comparison to a previous interpretation of Pb isotope data from the Lower Huronian Supergroup

Similarities between chondrite-normalized REE patterns of the shale samples from the McKim and Pecors formations (Figure 3.9 and from McLennan et al., 1979; 2000), allow for the interpretation of other geochemical data as one comprehensive group. They also bracket the Ramsay Lake glaciation, which is a potential indicator of oxidative atmospheric chemistry (Bekker et al., 2005). The Pb-Pb age for the entire

group of twelve samples (1778 ± 170 Ma) is significantly younger than that observed by McLennan et al. (2000) and displays variable κ_a values that range from 0.397 to 2.94 (average = 2.12). The K&T97 model utilizes a κ value of 3.86 for its erosion mix component at 2.4 Ga. This implies that all samples have experienced a gain of uranium, with the lowest percentage of uranium gain at 31%. As this interpretation is model-dependent, an independent evaluation of the Pb isotope ratios is necessary. This is especially true as Th/U ratios are not solely dependent upon redox conditions but may be altered by variable amounts of trace mineral phases or the mixing of provenance materials. In an attempt to evaluate the potential contribution of these factors to the κ_a, it is necessary to compare REE patterns and REE interelement ratios.

The chondrite-normalized REE patterns for the samples of the Lower Huronian Supergroup (Figure 3.9) show three distinct patterns, which display similar distributions of the LREE ($La_N/Sm_N = 3.87 \pm 0.97$) but vary considerably in the HREE distribution ($Gd_N/Yb_N = 1.60 \pm 1.23$). When normalized to the sample with the lowest concentration of REE (5141'; $\sum$REE = 103.5 ppm), the differential behavior of the HREE becomes more obvious (Figure 3.10). The sample-normalized REE patterns are indicative of variable amounts of garnet in the samples from 5057 and 5141 feet deep. This is not likely due to variable amounts of detrital garnet as the mineral is not stable in the weathering environment. More likely, the variability of sample-normalized REE patterns is suggestive of the variable nature of the source materials. The shared geochemical affinity of Th and the REE for incorporation in a similar set of minerals (e.g. apatite, allanite, zircon, and monazite) allows for the comparison of La/Nd and Gd/Er ratios and κ_a in an attempt to evaluate the contribution of multiple provenance components on the

whole-rock REE patterns and Pb isotope ratios (See section 1.1.2.3).

The average La/Nd ratio for samples of the Lower Huronian Supergroup is 1.19 with a relative variation (2σ) of 13.8% and the average value of κ_a is 2.05 with a relative variation of 74.34%. The relatively small variation in La/Nd ratios is indicative of a homogenous source for the LREE within these samples, a potential indication of a common provenance for these samples. The observed relative variation of κ_a values is much greater than that of the La/Nd ratios, which is a strong indicator that the observed κ_a values are not related to variations in source geochemistry or the addition or subtraction of trace minerals but rather were established during the post-depositional geochemical alteration of the sediments. Additionally, the measured La/Nd or κ_a ratios for the samples can not be explained by trace mineral addition to the sample with the highest κ_a (Figure 3.11).

The potential for the addition or subtraction of garnet from the samples of the McKim formation was suggested by the sample normalized REE patterns (Figure 3.10). The La/Nd and κ_a ratio of the sample from 5141' depth is such that the ratios may be the result of an addition of 3% garnet to the sample from 4862' depth, but mixing any proportion of garnet to the sample from 5057' depth will only result in lower La/Nd ratios than that determined for the sample from 5141' depth (Figure 3.11). Due to the enrichment of HREE in garnet, the addition/subtraction of garnet may be better characterized by evaluating covariation in HREE ratios (Gd/Er ratios) and κ_a rather than La/Nd ratio variations. Although similar relative variations exist in the Gd/Er ratios (77.5%) and κ_a ratios (75.2%) for these samples, the comparison of Gd/Er and κ_a ratios in these samples (Figure 3.12) reveals that there is no apparent connection between HREE

variation observed in the REE patterns and the variation in κ_a ratios. In fact the curvilinear expression of mixing values for garnet and the sample with the highest κ_a does not explain any of the Gd/Er or κ_a ratios determined for these samples. The lack of covariation between La/Nd or Gd/Er ratios and κ_a ratios is suggestive that the observed variation in each ratio is caused by unrelated phenomena. It is therefore possible that the "garnet-like" sample-normalized REE pattern is the result of additional garnet in the provenance of this sample but that later metasomatic fluids may have disturbed the U-Th-Pb system leaving the REE unaltered. Pb isotope evidence of this early garnet metasomatism is not preserved in these samples.

3.4 Conclusions

The Pb isotope ratios and REE concentrations of the sedimentary rocks of the Lower Huronian Supergroup not allow for simple interpretation of the apparent time-integrated Th/U ratio (κ_a). The geochemical evidence presented in this chapter is indicative of post-depositional alteration of Pb isotope ratios and, potentially, REE fractionation. According to the least complicated interpretation of the Pb isotope and REE concentration data:

(1) The fine-grained detrital sedimentary rocks of the Lower Huronian Supergroup experienced at least one post-depositional event that altered the geochemistry of the rocks. This event likely occurred at about 1.8 Ga and resulted in the alteration of κ_a ratios by metasomatic fluids.

(2) As much as 450% "excess uranium" may have been added to the rock, but the interpretation of redox conditions associated with this alteration

event are model-dependent; regardless of the model used all of the samples experienced the addition of uranium. Although now organic-poor, sedimentary organic carbon in the rocks may have caused the precipitation of uranium from uraniferous oxidizing fluids that flowed through the rock. The organic carbon may have been oxidized and removed as carbonate complexes.

(3) Variable addition of different source materials (trace minerals and sedimentary source end members) cannot explain the variation observed in κ_a ratios. This does not prohibit the interpretation of κ_a ratios in the context of redox conditions associated with the post-depositional alteration event.

(4) The previous interpretation of U-Th-Pb systematics in the Huronian Supergroup (McLennan et al., 2000) did not conduct a comprehensive REE study. Consequently, their interpretation of the disruption of the U-Th-Pb system is subject to reconsideration. Despite the similarity in sample location and stratigraphic units studied, the previous study did not see evidence of a later disruption to the U-Th-Pb system instead favoring a diagenetic alteration of the sedimentary rocks. If this was the case for the samples in this study, the subsequent ca. 1.8 Ga metasomatic event has overprinted the geochemical signature of this earlier event.

Although this part of this study was ineffective in providing constraints on the oxidative weathering of uranium at about 2.4 Ga, it is a useful exercise in exploring the implications of Pb isotope ratios and REE patterns. Also, this part of the study illustrates

the importance of obtaining high precision REE concentration data along with Pb isotope ratio data, as relying on the Pb isotope data alone does not evaluate the contribution of multiple provenance materials effectively. Lastly, it introduces further concern for using direct measurements of Th/U ratios as a measurement for the redox conditions present during continental weathering, as Th/U ratios would be unable to reveal timing associated with their establishment (in this case at least 250 million years after deposition).

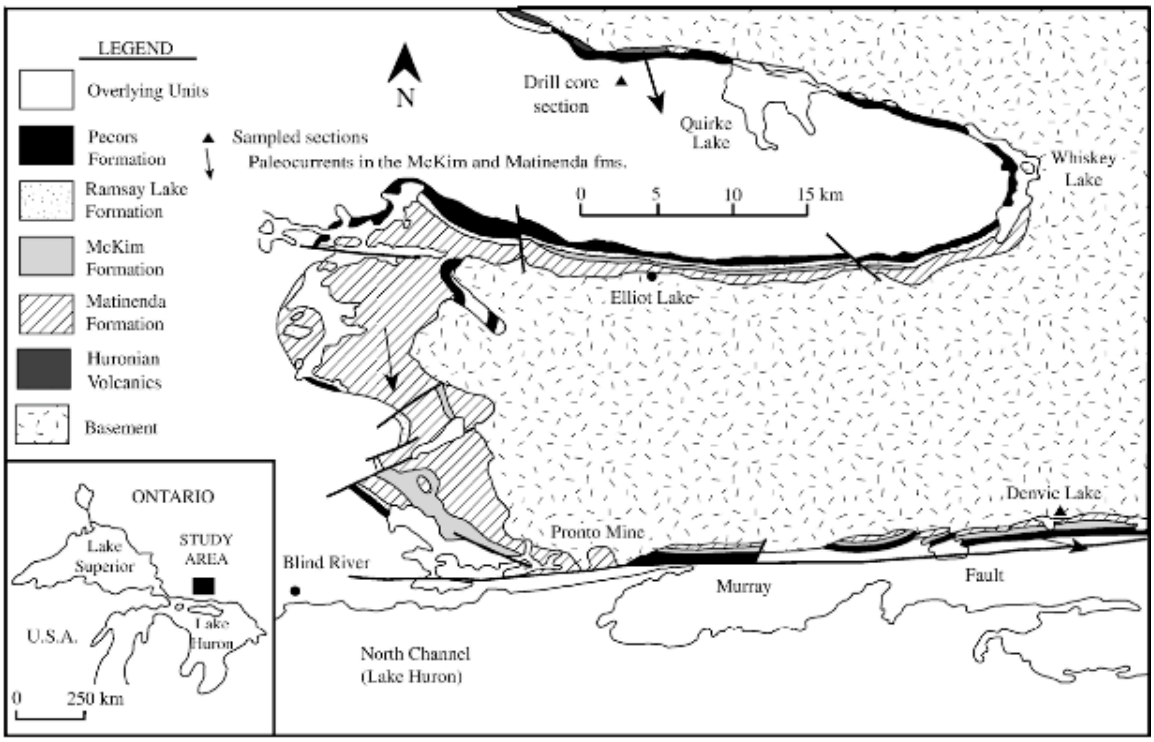

Figure 3.1 Simplified map of the Quirke Lake area, Ontario, Canada. The location of the Kerr–McGee Corp. 156-1 drill core is shown (from Bekker and Kaufman, 2007). Paleocurrents in the lower part of the Huronian Supergroup indicate the slope during deposition towards the south–southeast.

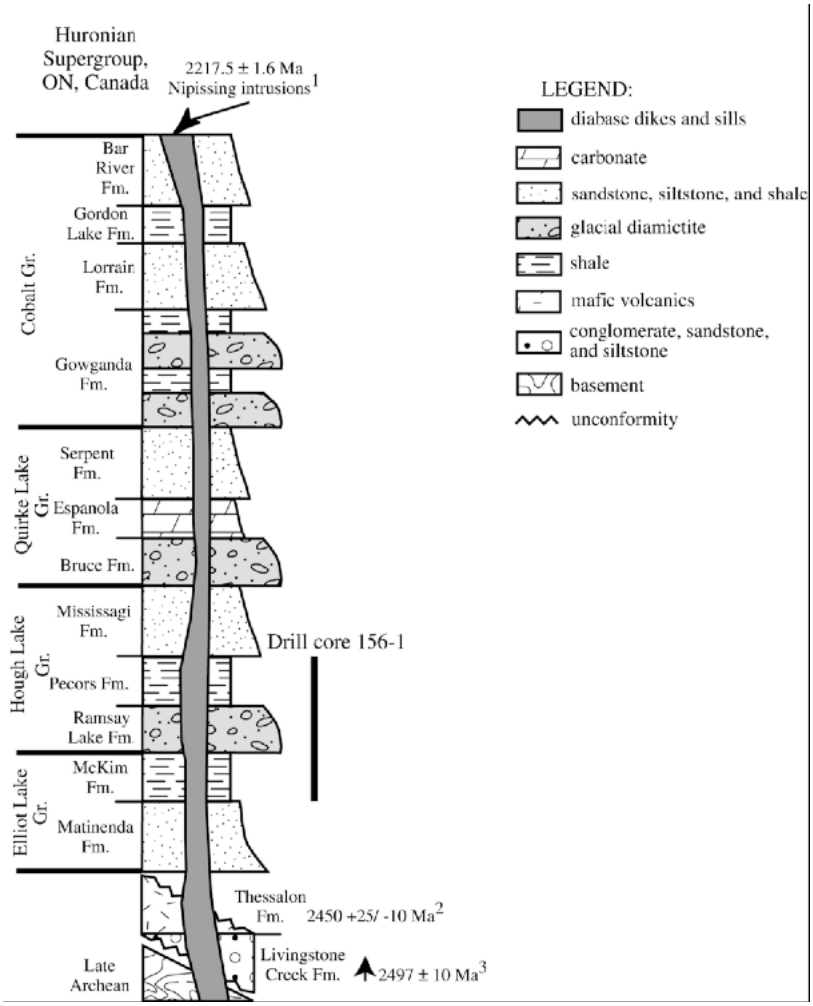

Figure 3.2 Lithostratigraphy of the Huronian Supergroup. Stratigraphic column of the Huronian Supergroup in the western part of the outcrop belt, Ontario, Canada with a vertical bar that shows the stratigraphic interval sampled by the drill core (modified from Bekker and Kaufman, 2007). References to age constraints: 1 — Andrews et al., 1986; 2 — Krogh et al., 1984; 3 — Rainbird and Davis, 2006. Age with an arrow pointing up indicates detrital zircon age (maximum age of deposition).

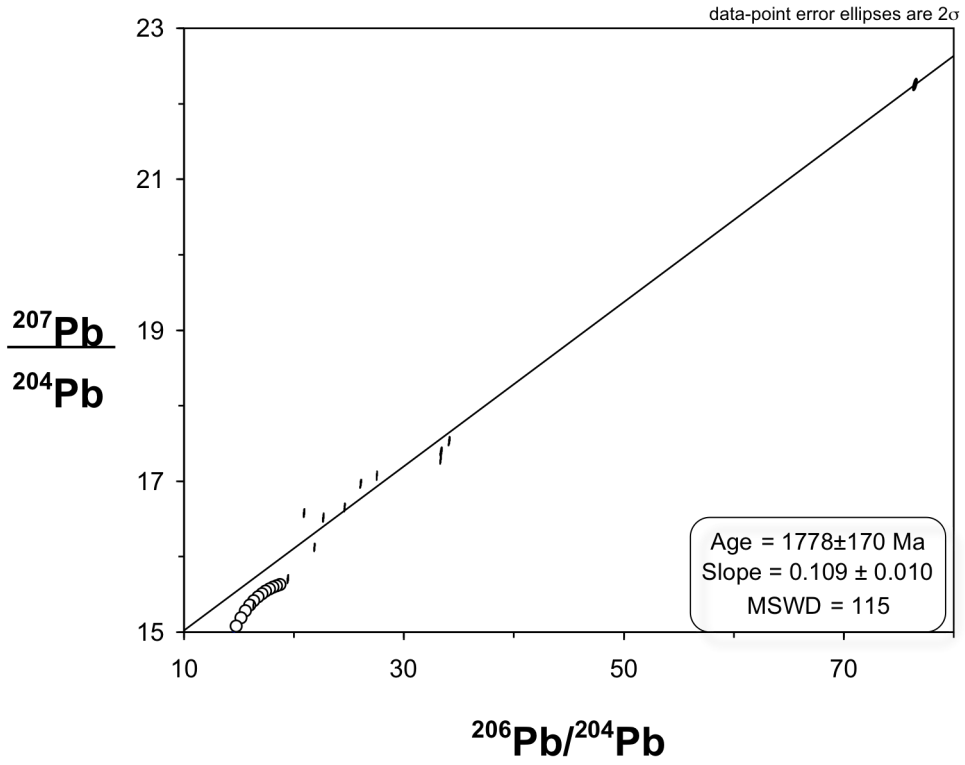

Figure 3.3 $^{206}Pb/^{204}Pb$ vs. $^{207}Pb/^{204}Pb$ isotope ratio diagram for the whole rock shale samples of the lower Huronian Supergroup. The Pb isotope growth curve shown is based on the Pb isotope growth model of Stacey and Kramers (1975). The slope of the array of points corresponds to a Pb-Pb age of 1778 ± 170 Ma, which is considerably younger than the age constraints for deposition (2.22 – 2.49 Ga). The Pb-Pb age represents the timing associated with the establishment of the U/Pb ratio, which likely reflects uranium mobilization during a ca. 1.7 Ga metasomatic event.

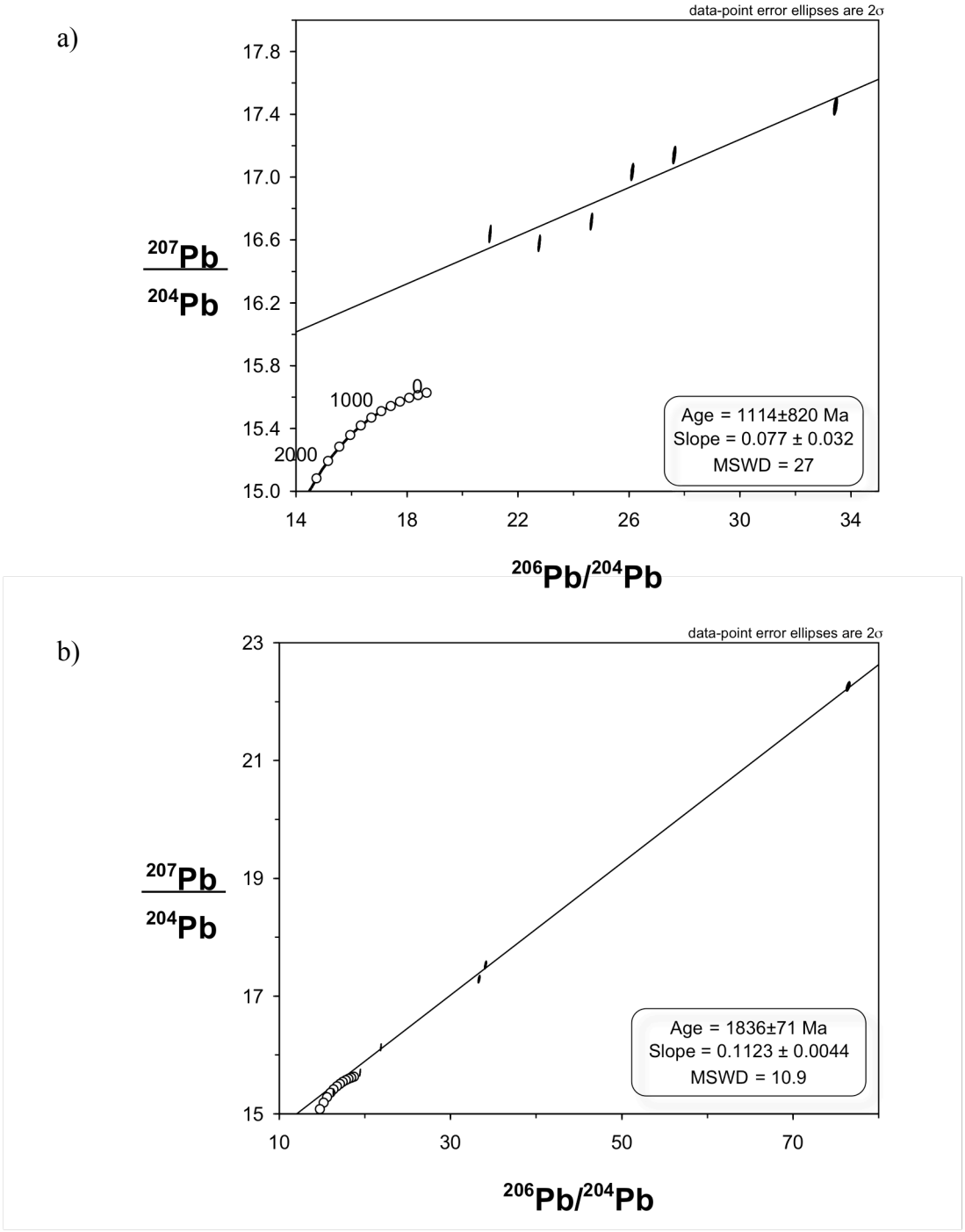

Figure 3.4 $^{206}Pb/^{204}Pb$ vs. $^{207}Pb/^{204}Pb$ isotope ratio diagram for the whole rock shale samples of the (a) McKim and (b) Pecors formations. The Pb isotope growth curves shown are based on the Pb isotope growth model of Stacey and Kramers (1975). The Pb-Pb ages of both formations (1114 ± 820 Ma and 1836 ± 71 Ma) are much younger than the age constraints for deposition (2.22 – 2.49 Ga). These relatively young ages likely represent the age of one post-depositional event at ca. 1.7 Ga that resulted in the redistribution of uranium.

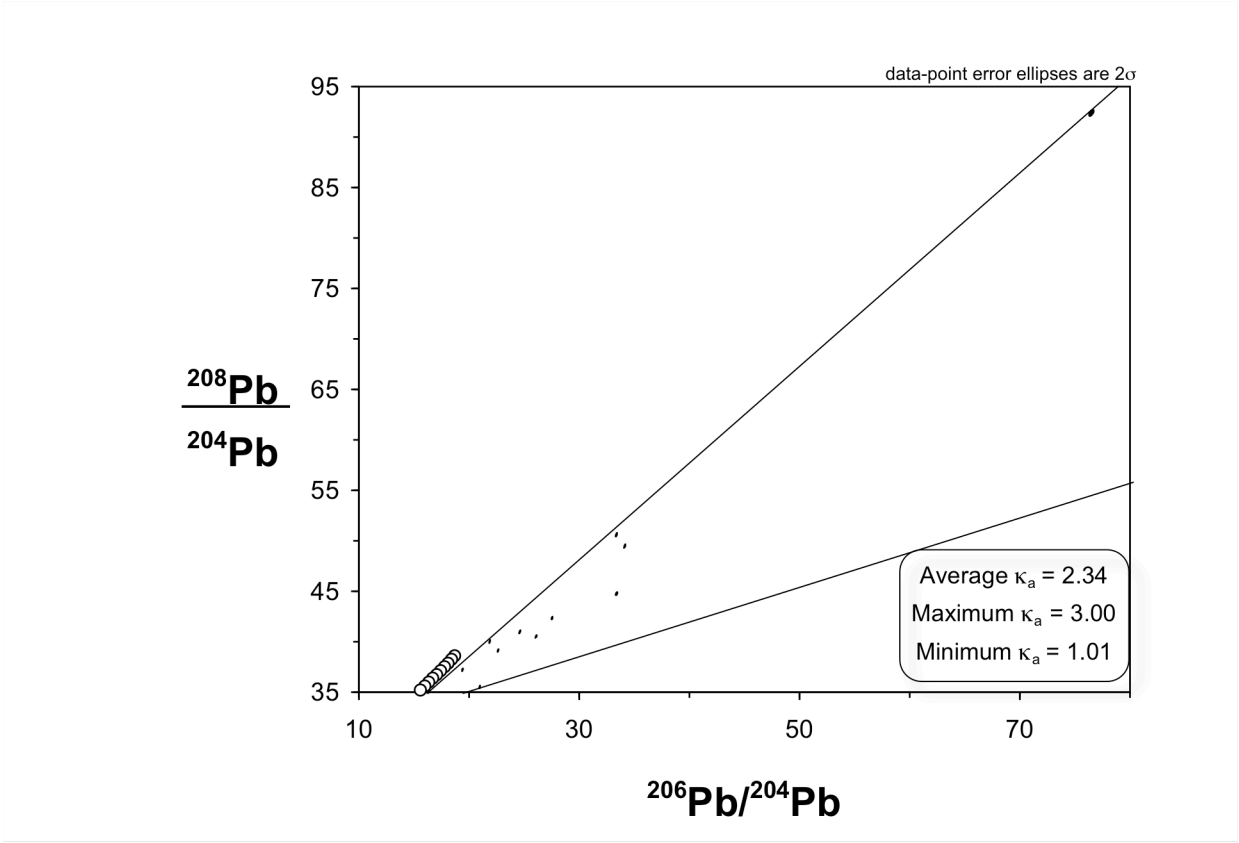

Figure 3.5 $^{206}Pb/^{204}Pb$ vs. $^{208}Pb/^{204}Pb$ isotope ratio diagram for the whole rock shale samples of the lower Huronian Supergroup. The growth curve shown represents the Pb isotope growth model of Stacey and Kramers (1975). Rays are constructed from the model Pb isotope composition at 2.4 Ga and extend to Pb isotope compositions of samples with the highest and lowest apparent time-integrated Th/U ratios (κ_a). Variations in κ_a ratios may result from variable Th/U ratios present in the provenance of these rocks or post-depositional redistribution of the U-Th-Pb system.

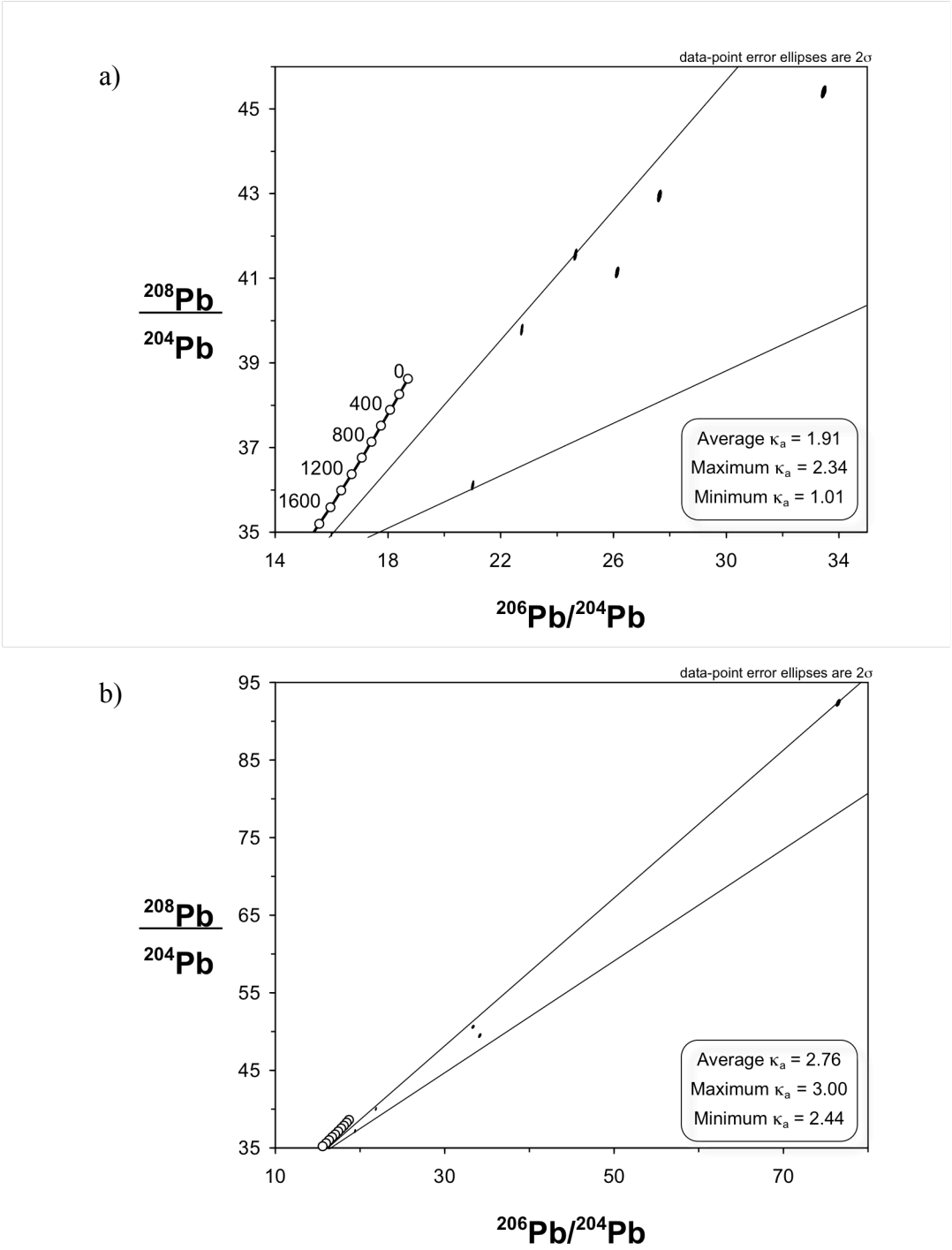

Figure 3.6 $^{206}Pb/^{204}Pb$ vs. $^{208}Pb/^{204}Pb$ isotope ratio diagram for the whole rock shale samples of the (a) McKim and (b) Pecors formations. The growth curve shown represents the Pb isotope growth model of Stacey and Kramers (1975). Rays are constructed from the model Pb isotope composition at 2.4 Ga and extend to Pb isotope compositions of samples with the highest and lowest κ_a ratios from each formation. The range of κ_a ratios from each formation do not overlap indicating two distinct post-depositional events or the evolution of redox conditions during the Ramsay Lake glaciation.

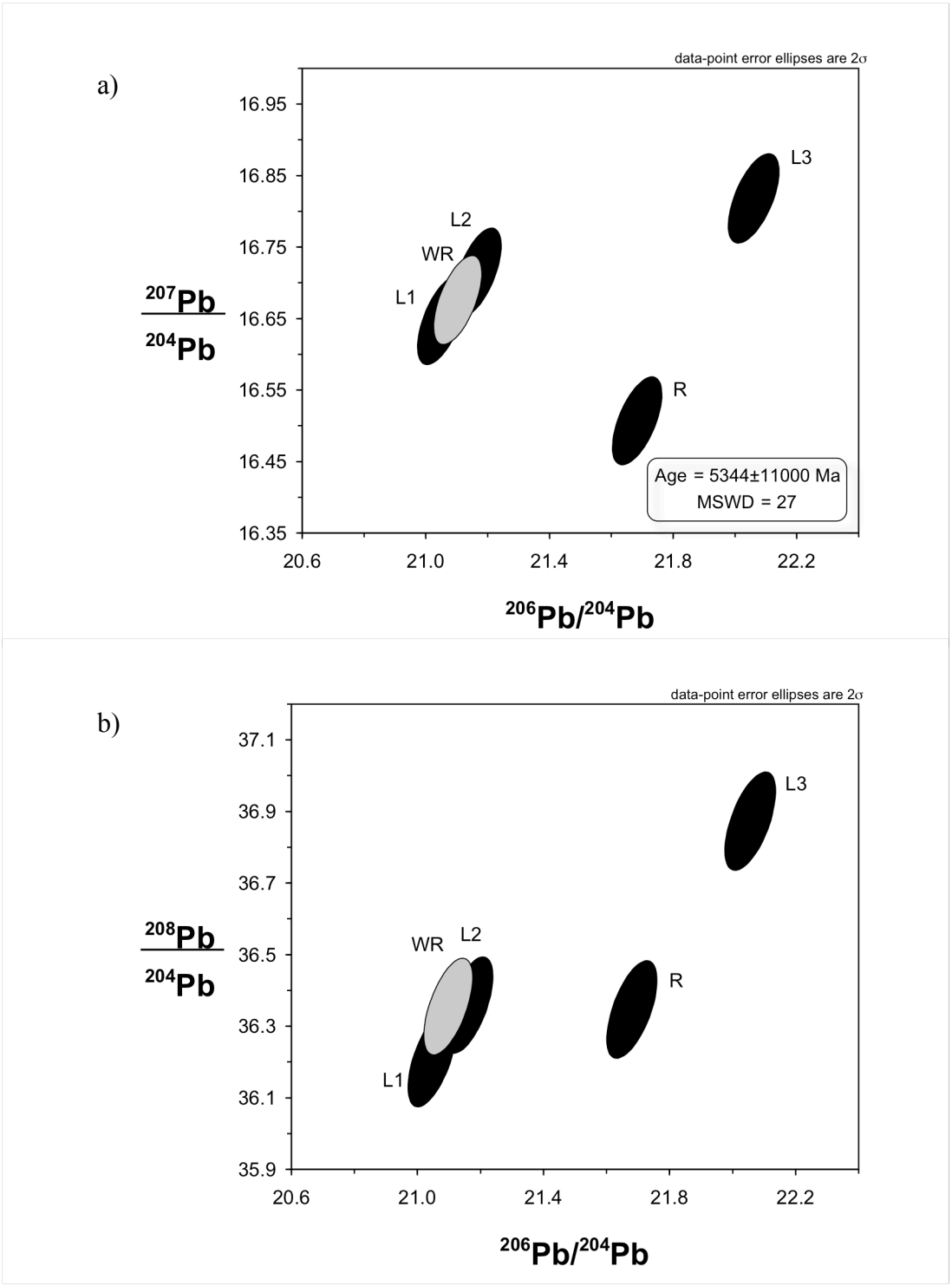

Figure 3.7 Pb isotope ratio plots from sequential acid leaching of a sample from the McKim Formation (5141'). This diagram shows a geologically meaningless age for the establishment of the U/Pb ratio (5344 ± 11000 Ma). The age predates the formation of the solar system and therefore the κ_a ratios are not calculated. It likely indicates that the rock was subjected to post-depositional redistribution of uranium and/or lead. The gray symbol signifies the Pb isotope composition of the whole rock.

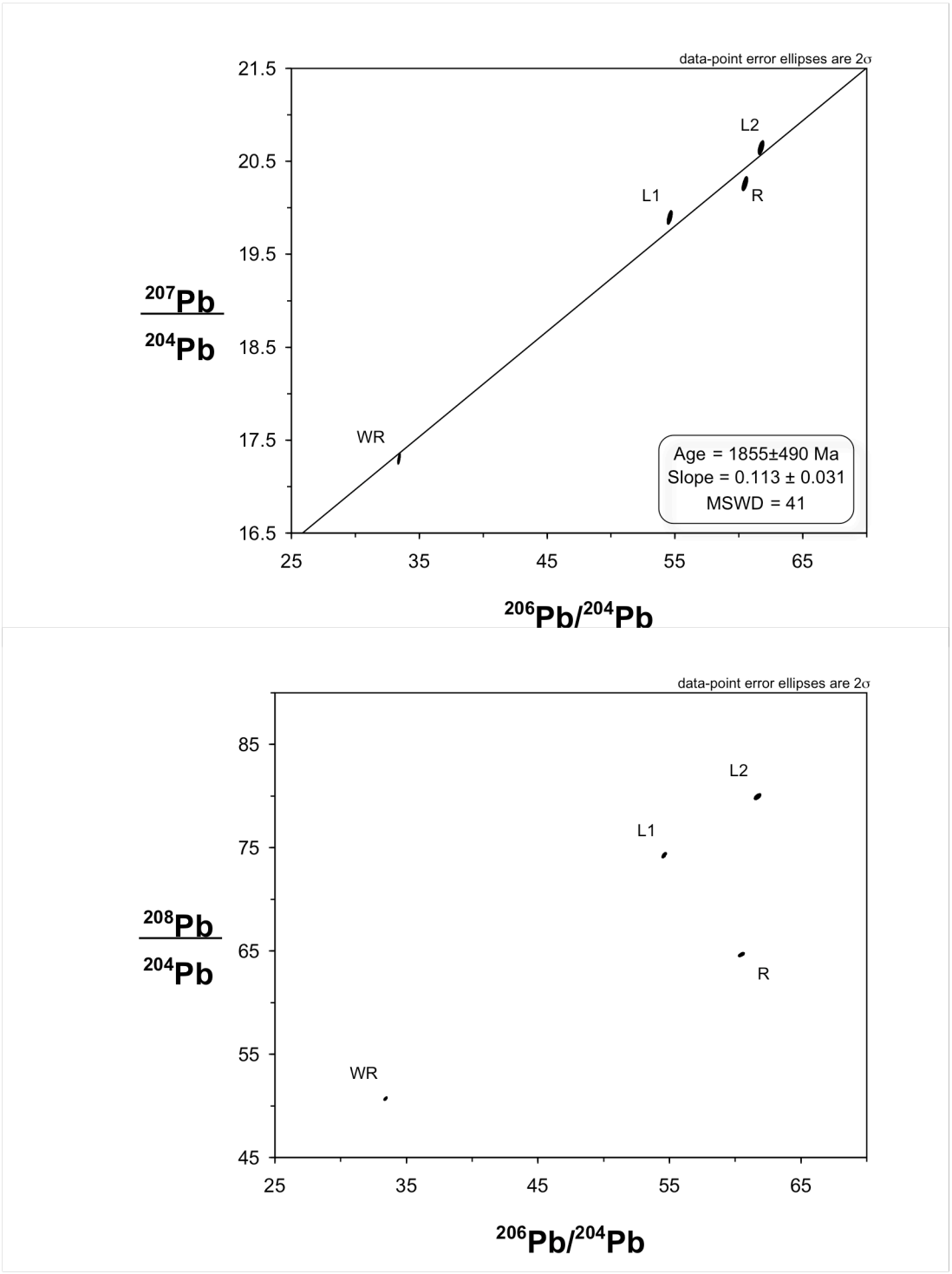

Figure 3.8 Pb isotope ratio plots from sequential acid leaching of a sample from the Pecors Formation (4798'). The slope of the array of uranogenic Pb isotope ratios (a) corresponds with an age of Pb isotope growth from 1855 ± 490 Ma. The uncertainty of the Pb-Pb age results in slight overlap with the constraints for the depositional age (2.49 – 2.22 Ga). The κ_a ratios (b) are based on the Kramers and Tolstikhin (1997) model at 1800 Ma. It is likely that the rock was subjected to post-depositional redistribution of uranium and/or lead.

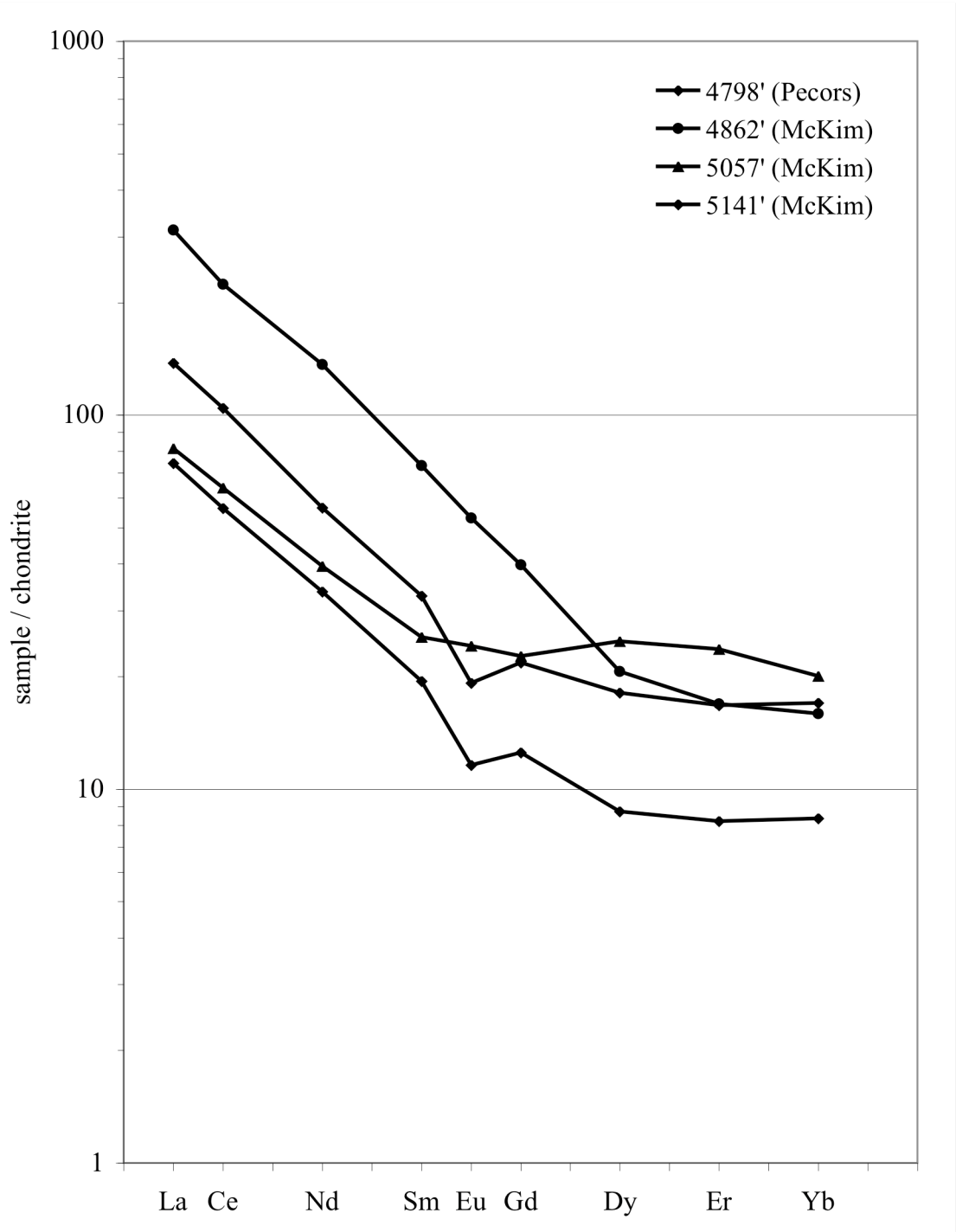

Figure 3.9 Chondrite-normalized REE patterns for four samples from the lower Huronian Supergroup. Although all samples show LREE enrichment relative to the HREE and have similar La/Sm ratios, the distribution of the HREE is variable. This may suggest multiple provenance materials or post-depositional redistribution of the REE. Because the REE are relatively immobile under low to medium grade metamorphic conditions that affected these rocks, it is more likely that REE distribution was source controlled.

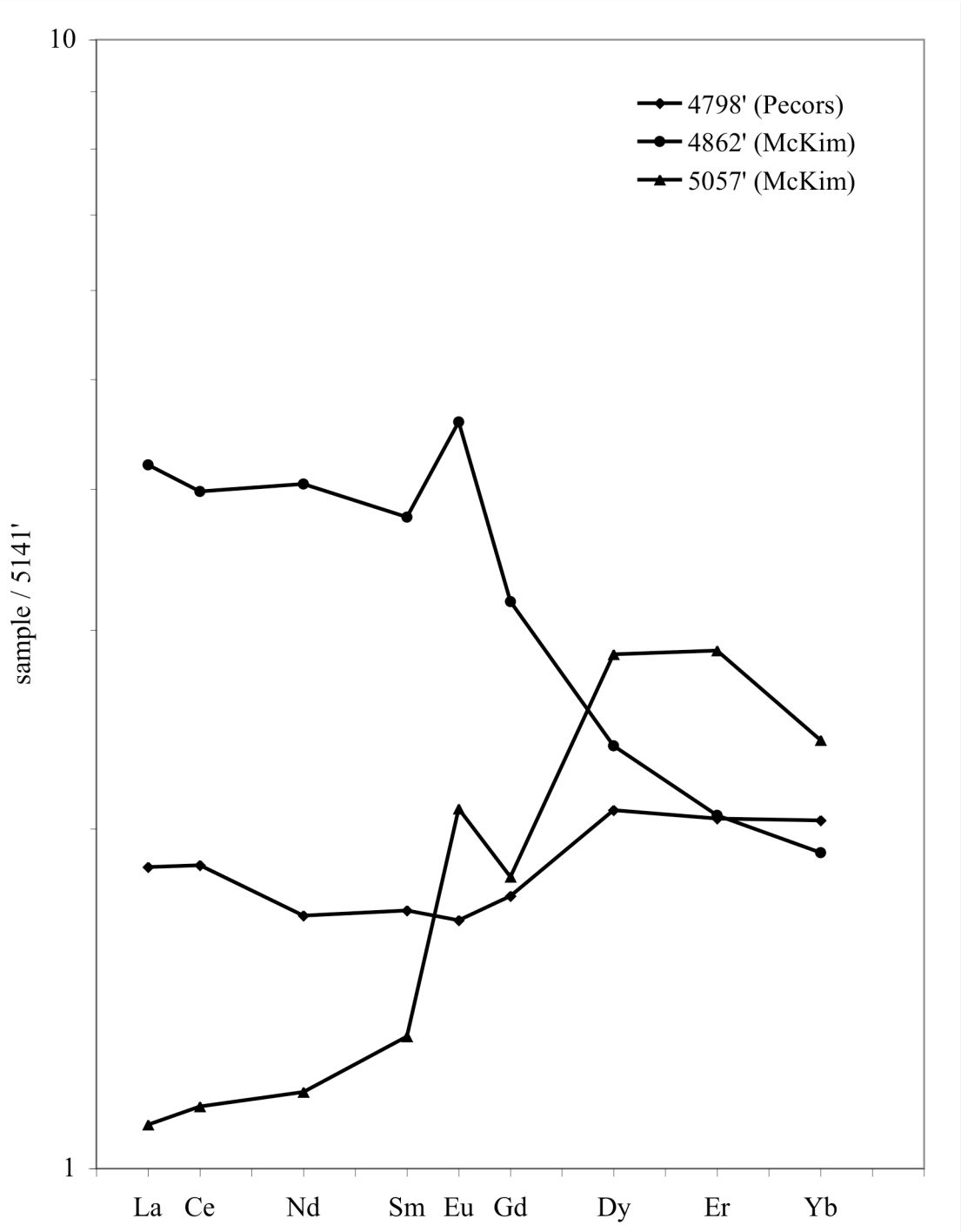

Figure 3.10 Sample-normalized REE patterns for three samples from the lower Huronian Supergroup. These REE patterns serve to enhance similarities in LREE fractionation between the samples (notice the flat portion of the REE pattern between La and Nd). The differences in HREE fractionation are also magnified using this technique (notice the variation in slope and shape of the pattern between Gd and Yb). Because minerals with REE patterns similar to those displayed here are not stable in the weathering environment, these patterns are likely indications of post-depositional processes.

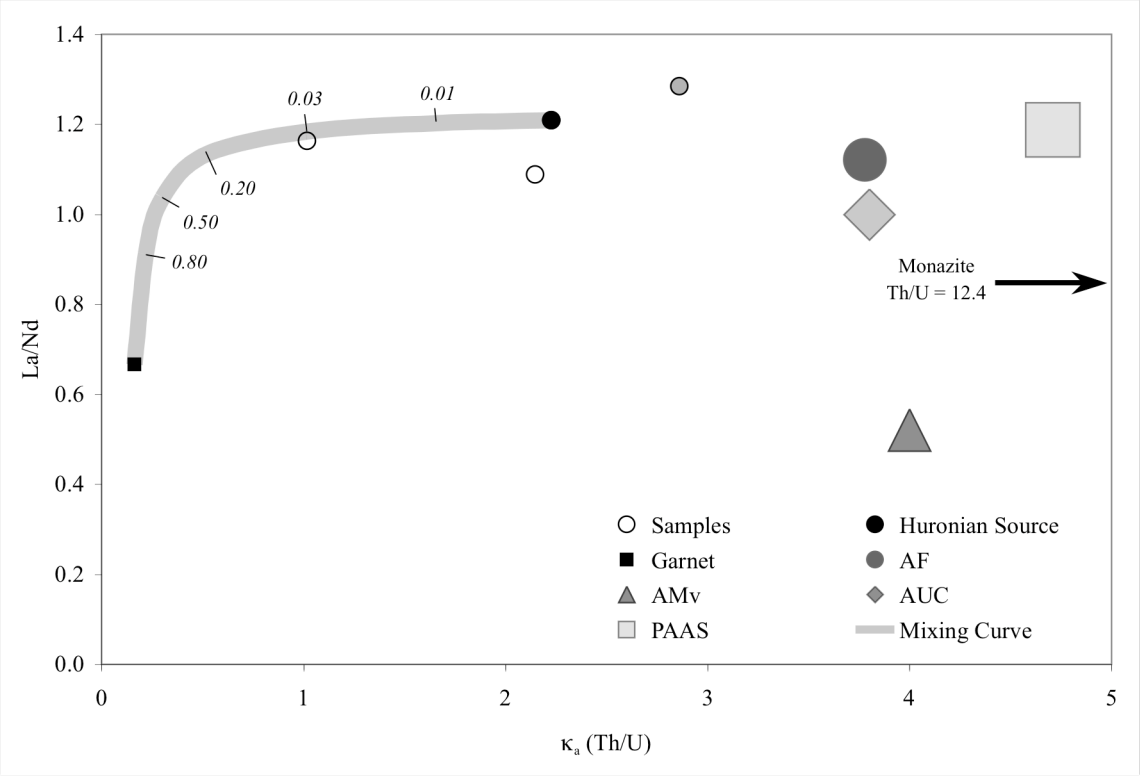

Figure 3.11 Diagram comparing variations in κ_a and La/Nd ratios for four samples of the lower Huronian Supergroup. Note that the "Huronian Source" is the sample from the McKim Formation with the highest κ_a although the sample from the Pecors Formation (small gray circle) has a higher κ_a ratio. Sample geochemistries can not be explained by simple bimodal mixing of potential source materials and trace minerals or proposed end members (AMv = Archean Mafic volcanics; AF = Archean Felsic rocks; AUC = Archean Upper Crust; PAAS = Post-Archean average Australian Shale, from Taylor and McLennan, 1985).

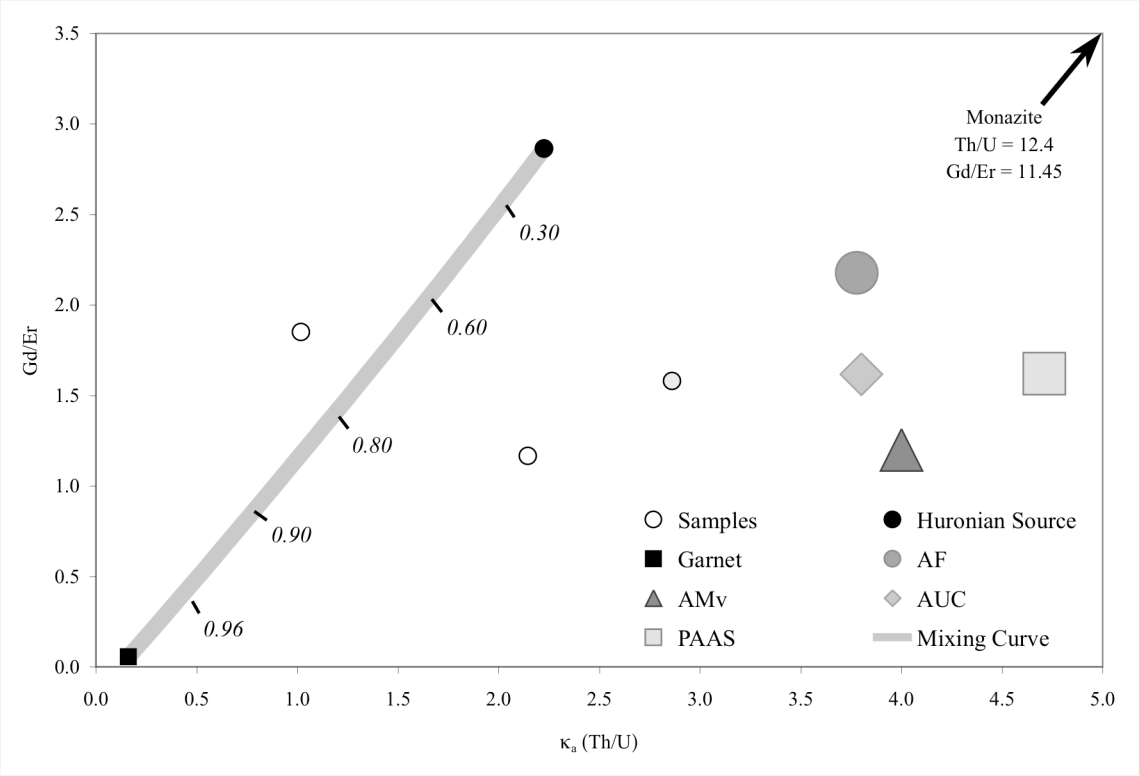

Figure 3.12 Diagram comparing variations in κ_a and Gd/Er ratios for four samples of the lower Huronian Supergroup. The relative variation observed in both ratios is similar, however the data lack covariation of these ratios. Additionally, the observed variation is not explained by the mixing of trace minerals or model sedimentary end members (abbreviations are identical to those used in Figure 3.11). It is therefore likely that two separate events (one sedimentary and one metamorphic) caused the redistribution of the REE and the U-Th-Pb system.

Table 3.1 Whole rock Pb isotope compositions and κ_a values for shale samples of the ca. 2.4 Ga lower Huronian Supergroup

Sample	$^{206}Pb/^{204}Pb$	$^{206}Pb/^{204}Pb$	$^{206}Pb/^{204}Pb$	κ_a
McKim Formation				
5141'	21.05	16.65	36.22	1.01
5121'	26.19	17.04	41.19	1.92
5097'	27.70	17.15	42.96	2.13
5057'	33.54	17.45	45.39	1.87
4871'	24.71	16.73	41.60	2.34
4862'	22.81	16.59	39.85	2.21
Pecors Formation				
4798'	33.49	17.35	51.13	2.84
4771'	76.75	22.25	92.31	2.94
4733'	34.27	17.59	50.02	2.55
4599'	22.00	16.20	40.65	2.81
4510'	19.54	15.79	37.89	2.44
4449'	16.43	15.45	35.75	3.00

Table 3.2 Pb isotope compositions from sequential acid leaching of two samples from the ca. 2.4 Ga lower Huronian Supergroup

Leach Step	$^{206}Pb/^{204}Pb$	$^{206}Pb/^{204}Pb$	$^{206}Pb/^{204}Pb$
McKim Formation			
5141'			
L1	21.10	16.68	36.36
L2	21.16	16.72	36.37
L3	22.06	16.82	36.88
R	21.68	16.51	36.36
WR	21.05	16.65	36.22
Pecors Formation			
4798'			
L1	54.73	19.91	74.40
L2	61.88	20.65	79.98
L3	--	--	--
R	60.63	20.26	64.92
WR	33.49	17.35	51.13

Leaching was done according to the steps in Section 1.2.2.
The L3 leach step in sample 4798' resulted in low Pb concentrations and no reliable Pb isotope ratio data

Table 3.3 Relative proportion of Pb liberated by sequential acid leaching of two samples from the ca. 2.4 Ga lower Huronian Supergroup

Leach Step	Counts per second (cps)					
	^{204}Pb	^{206}Pb	^{207}Pb	^{208}Pb	Total	Percentage
McKim Formation						
5141'						
L1	4.62E+07	9.74E+08	7.69E+08	1.68E+09	3.47E+09	57.3%
L2	2.72E+07	5.75E+08	4.53E+08	9.86E+08	2.04E+09	33.7%
L3	2.89E+06	6.34E+07	4.83E+07	1.06E+08	2.21E+08	3.65%
R	2.51E+06	5.42E+07	4.12E+07	9.07E+07	3.21E+08	5.30%
		$^{206}Pb/^{204}Pb$	$^{207}Pb/^{204}Pb$	$^{208}Pb/^{204}Pb$		
Calculated Whole Rock		21.19	16.69	36.38		
Measured Whole Rock		21.05	16.65	36.22		
Pecors Formation						
4798'	^{204}Pb	^{206}Pb	^{207}Pb	^{208}Pb	Total	Percentage
L1	1.59E+06	8.65E+07	3.13E+07	1.17E+08	2.37E+08	33.8%
L2	1.74E+06	1.07E+08	3.54E+07	1.37E+08	2.81E+08	40.2%
R	1.25E+06	7.52E+07	2.50E+07	8.02E+07	1.82E+08	26.0%
		$^{206}Pb/^{204}Pb$	$^{207}Pb/^{204}Pb$	$^{208}Pb/^{204}Pb$		
Calculated Whole Rock		59.14	20.30	74.18		
Measured Whole Rock		33.49	17.35	51.13		

Table 3.4 REE concentrations of four whole rock shale samples from the Huronian Supergroup

Sample Depth	5141'	5057'	4862'	4798'
Formation	McKim	McKim	McKim	Pecors
La	23.4	25.7	98.5	43.4
Ce	46.1	52.3	183	85.6
Nd	20.3	23.8	82.1	34.0
Sm	3.77	4.93	14.2	6.37
Eu	0.844	1.76	3.87	1.40
Gd	3.27	5.92	10.4	5.69
Dy	2.86	8.16	6.77	5.93
Er	1.76	5.07	3.62	3.59
Yb	1.75	4.20	3.34	3.56
La_N/Yb_N	8.84	3.19	14.06	8.04
La_N/Sm_N	3.79	3.17	4.22	4.15
Gd_N/Yb_N	1.50	1.13	2.50	1.28
Ce/Ce*	0.988	1.00	0.948	1.03
Eu/Eu*	0.743	1.00	0.983	0.718

Note: La/Nd and Gd/Er ratios used in Figures 3.11 and 3.12 are not normalized

4. The 2.32 Ga Timeball Hill Formation, Transvaal Basin, South Africa

4.1 Geological Setting

Organic-rich shales from the Timeball Hill Formation of the Pretoria Group, South Africa (Figures 4.1 and 4.2), contain geochemical evidence associated with the rise in atmospheric oxygen (Bekker et al., 2004; Dorland, 1999; Hannah et al., 2004). The underlying units (and correlative units), with the exception of the Rooihoogte Formation, contain geochemical evidence of a reducing atmosphere (Cameron, 1982; England et al., 2002; Farquhar et al., 2000; Bau et al., 1998; Beukes and Klein, 1990; Strauss, 2002). A Re-Os isochron age of 2316 ± 7 Ma has been determined for synsedimentary – early diagenetic pyrites contained in both formations (Hannah et al., 2004). This isochron age and geochemical evidence has been widely cited as evidence that the Great Oxidation Event started by 2.32 Ga, at the latest (Barley et al., 2005; Canfield, 2005; Frei et al., 2008; Kaufman et al., 2007; Kump et al., 2008; Papineau et al., 2007; Rouxel et al., 2005; Scott et al, 2008).

Based on detailed studies of the sedimentology, the Timeball Hill Formation was deposited in the deltaic part of a basin open to the ocean on the southwest (Coetzee, 2002; Visser, 1972; Eriksson, 1973; Eriksson and Reczko, 1998). The studied samples were collected from drill core EBA-2, which was drilled by Gold Fields Ltd in the Potchefstroom area (in the western part of the Transvaal Basin), and is currently in storage at the Geological Survey of South Africa (Figure 4.1). Volcanic contributions to the Pretoria Group are uncommon and found only in the extreme southwestern part of the basin, about 27 km from the sampled drill core, where the 5-m-thick Bushy Bend Lava occurs within the upper Rooihoogte Formation (Coetzee, 2002). The shales of the

Timeball Hill Formation were deposited between two glacial diamictites, which are considered correlative with the middle and the upper of three glacial diamictites in the early Paleoproterozoic Huronian Supergroup, Ontario, Canada (Bekker et al., 2001; see Figure 3.2). The shales of the Timeball Hill Formation have been affected by lower greenschist facies metamorphism (Coetzee, 2002).

4.2 Results

4.2.1 Whole rock Pb isotope compositions

Whole rock Pb isotope compositions for eleven organic-rich shale samples from the Timeball Hill Formations are presented in Table 4.1. These data are plotted on comparative Pb isotope ratio diagrams ($^{206}Pb/^{204}Pb$ vs. $^{207}Pb/^{204}Pb$; Figure 4.3 and $^{206}Pb/^{204}Pb$ vs. $^{208}Pb/^{204}Pb$; Figure 4.4) in an effort to constrain the timing associated with the establishment of apparent time-integrated $^{238}U/^{204}Pb$ ratios (μ_a) and apparent time-integrated Th/U ratios (κ_a). The shale samples have μ_2 values that range from 3.75 to 13.41 with an average value of 10.08, using the $^{206}Pb/^{204}Pb$ and $^{207}Pb/^{204}Pb$ ratios from the Kramers and Tolstikhin model (K&T97) at 2.3 Ga. The uranogenic Pb isotope ratios of the samples display a positively correlated array of points on a $^{206}Pb/^{204}Pb$ vs. $^{207}Pb/^{204}Pb$ diagram (Figure 4.3), which is associated with a best-fit line having a slope of 0.120 ± 0.025 (MSWD = 7.6). This slope corresponds to radiogenic Pb isotope growth from 1962 ± 360 Ma to present. This age is within error of previously reported Re-Os isochron age (2317 ± 7 Ma) for sedimentary pyrite grains from the Rooihoogte-Timeball Hill Formations. Because the MSWD is greater than 1.5, the Pb isotope growth age (Pb-Pb age) is not considered an isochron age but may still have significance to the temporal

establishment of the μ_2 ($^{238}U/^{204}Pb$) and κ_a ratios.

A positively sloped array is displayed through a comparison of thorogenic and uranogenic Pb isotope ratios on a $^{206}Pb/^{204}Pb$ vs. $^{208}Pb/^{204}Pb$ diagram (Figure 4.4). Calculated κ_a ratios for samples from the Timeball Hill Formation range from 2.17 to 2.98 with an average of 2.65, using the K&T97 model Pb isotope ratios for an 'erosion mix' at 2.3 Ga. The alternative use of "initial" Pb isotope ratios associated with the K&T97 erosion mix at an age of 1.9 Ga should be avoided as the range of Pb-Pb ages permits the interpretation of a 2.3 Ga depositional establishment of the U-Th-Pb system. The κ_a ratios are well below the upper crustal average Th/U ratio of 3.8 (Taylor and McLennan, 1985) and the κ ratio predicted by the K&T97 model for 2.3 Ga, regardless of the model for determining the "initial" Pb isotope ratios.

4.2.2 Sequential acid leaching

Two samples (EBA2/37 and EBA2/42) with minimum and maximum κ_a (Table 4.2) were selected for step-wise acid leaching and then analyzed for their Pb isotope composition. Sequential acid leaching of the sample with the lowest κ_a (EBA2/37) resulted in isotope ratio data (Figure 4.5; Table 4.3) for all of the leach steps with 23.8% of the Pb liberated by dilute (0.1M) HBr (L1), 14.3% of the Pb liberated by stronger (4M) HBr (L2), 54.2% of the Pb liberated by a mixture of concentrated HCl and HNO_3 (L3), and only 7.7% of the Pb liberated by concentrated HF and HNO_3 (R). A plot of uranogenic Pb isotope ratios (Figure 4.5a) displays a field of scattered points that are not arranged in an organized manner. The slope of a best-fit line (0.094 ± 0.036) through these data corresponds to a Pb isotope growth age from 1501 ± 720 Ma to present with a

MSWD of 6.6. The Pb isotope ratio data from whole rock and stepwise leaching digestion for the same sample define a linear array on a $^{208}Pb/^{204}Pb$ vs. $^{206}Pb/^{204}Pb$ diagram (Figure 4.5b) with κ_a values ranging from 1.61 to 2.34, calculated using model Pb initial ratios based on the K&T97 model at 2.3 Ga.

The step-wise acid leaching of the sample with the highest κ_a ratio (EBA2/42) resulted in Pb isotope ratios for all of the leach steps (Figure 4.6; Table 4.3). The majority of the Pb (52.6%) was liberated by a 1:1 mixture of ultra-pure concentrated HCl and HNO_3 (L3), with 33.7% of the Pb liberated by a 4M HBr solution (L2). A plot of uranogenic Pb isotope ratios (Figure 4.6a) displays a positively sloped array with a slope (0.133 ± 0.067) that corresponds to radiogenic Pb growth from 2133 ± 880 Ma to present. As with the other best-fit slopes in this study, the MSWD is greater than 1.5 ((MSWD = 6.5) eliminating the possibility of this age being considered as an isochron age. Although this age is not an isochron age it likely represents the age of deposition or that of diagenesis because it is within error of the whole rock Pb-Pb age (1962 ± 360 Ma) and the previously published Re-Os sedimentary pyrite age (2317 ± 7 Ma). Applying the K&T model initial Pb isotope ratios at 2.3 Ga the κ_a ranges from 2.29 to 3.66 with an average of 3.07, which is very similar to that of the whole rock (3.01).

4.2.3 REE Concentrations

Highly precise REE concentrations of ten shale samples from the Timeball Hill Formation (EBA2/16 was not evaluated for its REE concentrations) were determined by isotope dilution mass spectrometry in an effort to evaluate provenance heterogeneity (Table 4.4). Three of the samples (EBA2/18, EBA2/24, EBA2/37) have La concentration

data as the La separation was calibrated while samples were run. Therefore whereas interelement REE ratios utilizing La (e.g. La_N/Yb_N, La_N/Sm_N, La/Nd, etc.) have been used in previous chapters (and will be again used in subsequent chapters) they will be substituted with Ce-based ratios in this chapter. All samples display concave upwards chondrite-normalized REE patterns (Figure 4.7) with LREE enrichment (Ce_N/Yb_N = 7.10 ± 1.92, 2σ) and negative Eu-anomalies (0.648 ± 0.0948, 2σ). The patterns display more consistent and pronounced LREE fractionation (Ce_N/Sm_N = 3.06 ± 0.297) when compared to the fractionation of the HREE (Gd_N/Yb_N = 1.48 ± 0.170). Overall REE concentrations are generally greater than in PAAS (Nd concentrations in Sengoma shales are typically 65.7 times chondritic values whereas PAAS Nd concentrations are 54 times chondritic values).

4.3 Discussion

The age associated with the ancient establishment of U/Pb ratios using the Stacey-Kramers model (1962 ± 360 Ma) is barely coincident with the Re-Os age for sedimentary pyrites from the same rock unit (2317 ± 7 Ma). The overlap of these ages reduces the likelihood that post-sedimentary processes affected geochemical data and potential redox indicators, however the geochemical data should not be interpreted without further discretion. but should be only accepted once other geochemical proxies of post-sedimentary alteration have been considered.

4.3.1 Interpretation of sequential acid leaching

The mobilization and addition of post-sedimentary Pb from within the Timeball

Hill Formation provides one potential mechanism by which the whole rock Pb-Pb age may not be affected, but may be recognized through evaluating the Pb isotope ratios revealed by sequential acid leaching. The whole rock Pb isotope compositions of the two samples chosen for Pb leaching (EBA2/37 and EBA2/42) are very similar to one another. The sequential acid leaching of EBA2/42 reveals that 52.6% of the Pb liberated during leaching was released during the L3 leach step. Similarly, 54.2% of the Pb liberated during leaching of EBA2/37 was released during the L3 leach step. Additionally, the Pb isotope composition of both samples' L3 step proved to be the least radiogenic (i.e. L3 has the lowest ratios). Despite the similarities in whole rock Pb isotope composition, contribution of Pb in L3, and the Pb isotope composition of L3, the samples reveal two very different Pb-Pb ages.

The Pb-Pb age of EBA2/42 (2133 ± 880 Ma) agrees well with the whole rock Pb-Pb age (1962 ± 360 Ma) and the sedimentary age of the Timeball Hill Formation (2317 ± 7 Ma), whereas the Pb-Pb age for EBA2/37 (1501 ± 720 Ma) is suggestive of a post-depositional disturbance to the U-Th-Pb isotopic system. This difference in age can be eliminated using the full extent of the age ranges. Therefore further interpretations based on the Pb-Pb age ranges of these leaches and whole-rock samples are speculative.

4.3.2 Interpretation of REE patterns

The chondrite-normalized REE patterns of the organic-rich shales from the Timeball Hill Formation display similar patterns with LREE enrichment (Figure 4.7). Similarities in REE patterns can be attributed to (1) a single provenance component, or (2) different provenance components whose detrital contributions were well mixed before

transport and deposition and can be quantified through relative variations in interelement REE ratios (e.g. Ce_N/Yb_N, Ce_N/Sm_N, etc.). The low calculated relative variation in Ce_N/Sm_N (9.71%, 2σ) is a strong indication that processes capable of LREE fractionation were not prevalent or acted on these samples uniformly. Similarly, the calculated relative variation in Sm_N/Gd_N ratios (14.4%, 2σ) and Gd_N/Yb_N ratios (11.5%, 2σ) are interpreted as the result of the relative insignificance of processes capable of MREE fractionation. Further exploration of REE fractionation processes and trace mineral controls on the REE budget of these samples can be evaluated through a comparison of interelement REE ratios and Th/U ratios.

The geochemical similarities between Th and the REE suggest that La/Nd and Gd/Er ratios are good proxies for Th/U ratios under reducing conditions (Section 1.1.2.3). As mentioned above (Section 4.2.3), La concentrations were determined for only three samples rendering the interpretation of La/Nd ratios highly limited. Additionally, using Ce/Nd ratios might represent changes in redox behavior of Ce, which greatly reduces the utility of the Ce/Nd ratio for comparison purposes. The comparison of Gd/Er ratios and κ_a ratios can reveal the potential impact of source and trace element mixing on κ_a ratios (Figure 4.8). Interpretation of the Gd/Er and κ_a ratios does not explain the distribution of Timeball Hill shale data through mixing of the modeled sedimentary end members (e.g. AF, AMv, etc.). Similarly, the distribution of the Gd/Er and κ_a ratios is not explained by variability or simple addition of zircon or monazite to the sample with the highest κ_a during sedimentary or post-sedimentary processes. The Th-U-REE geochemistry of apatite is highly variable, therefore prohibitive of modeling trace element ratio mixing using an average composition apatite.

The relative variations observed in Gd/Er and κ_a ratios are not related to simple bimodal mixing of two end members and therefore is suggestive of a common source with slight geochemical heterogeneity or multiple well-mixed sources. Because the impact of sedimentary source mixing and post-sedimentary processes fails to explain the total variation in κ_a ratios and the Pb-Pb age associated with Pb isotope growth is within error of the previously determined sedimentary age of the Timeball Hill Formation, it is likely that the variation in k_a ratios is a function of the oxidation state of the atmosphere. The average κ_a ratio from the organic-rich shales of the Timeball Hill Formation (2.65) is well below the upper crustal average Th/U ratio (3.8; Taylor and McLennan, 1985) and the model Th/U ratio of detrital materials at 2.3 Ga (3.86; erosion mix of K&T97) indicative of uranium addition. The range of κ_a ratios (2.17 – 2.98) correlates to the addition of between 78.1% and 29.5% uranium with an average of 47.5% additional uranium. The slightly younger age may represent the influence of diagenetic processes on the U-Th-Pb, however the addition of uranium in the digenetic environment still requires a plentiful source of uranium in its oxidized uranyl form.

4.4 Conclusions

The Pb isotope ratios and REE concentrations allow for the interpretation of the apparent time-integrated Th/U ratio (κ_a) of the organic-rich fine-grained sedimentary rocks of the Timeball Hill Formation, in the context of the redox conditions of surficial weathering 2.3 billion years ago. There is no evidence that variable contributions of trace minerals can explain the observed variation in REE patterns and κ_a ratios. The geochemical evidence presented in this chapter is indicative of slight variations in

provenance geochemistry that does not fully explain the total observed variation in κ_a ratios. According to the least complicated interpretation of the Pb isotope and REE concentration data:

(1) The Pb-Pb age of the organic-rich shale samples of the Timeball Hill Formation is within error of the previously determined Re-Os isochron age for sedimentary pyrite from the same unit. Therefore it is unlikely that the U-Th-Pb system has been significantly disturbed since sedimentation at ca. 2.3 Ga.

(2) Variable Pb-Pb ages revealed by sequential acid leaching of EBA2/37 and EBA2/42 are explained by inaccurate Pb isotope ratios for the R leach step for sample EBA2/37.

(3) Slight differences in chondrite- and sample-normalized REE patterns suggest that the source materials were not significantly variable and were well homogenized.

(4) The calculated relative variation in interelement REE ratios is insufficient to explain the observed variation in κ_a ratios. Therefore the variation in κ_a ratios is not related to the mixing of sources or the differential contributions of REE- and U-enriched trace minerals.

(4) As much as 78.1% “excess uranium” may have been added to the rock during the sedimentary process. Organic carbon in the rocks may have caused the precipitation of uranium from uraniferous surface water that reacted with the rock during deposition or diagenesis.

(5) The previous study of sulfur isotope systematics in pyrite grains from

> the Timeball Hill Formation (Bekker et al., 2004) concluded that these organic-rich sediments were deposited during a time when the atmosphere was oxygenated. This study supports this conclusion with evidence of oxidative weathering observed in time-integrated Th/U ratios.

This part of the study shows how interpretation of the redox state of the weathering environment can be made through careful analysis of multiple geochemical proxies. Pb isotope ratio data supports the presence of a closed U-Th-Pb system since deposition however only when these data are interpreted along with REE concentration data, the potential influence of heterogeneous source components, differential trace mineral contributions, and fractionation processes can be dismissed as trivial.

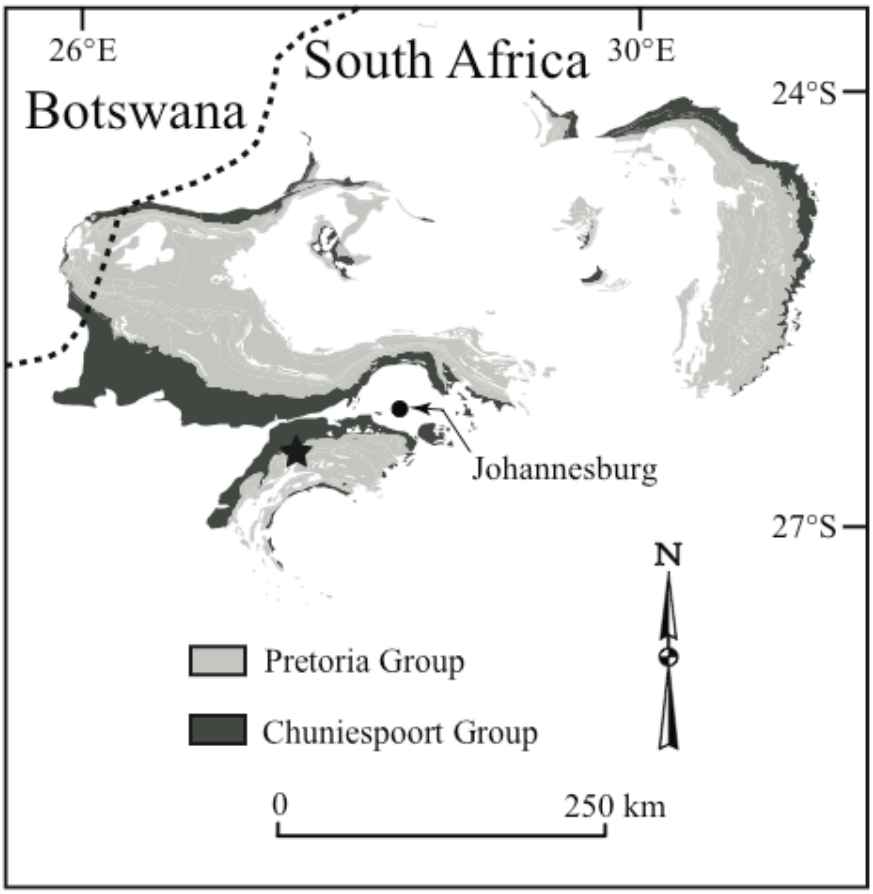

Figure 4.1 Map of early Paleoproterozoic sedimentary sequences of the Transvaal Basin, South Africa. The black star southwest of Johannesburg indicates the location of drill core EBA2 (modified from Hannah et al., 2004).

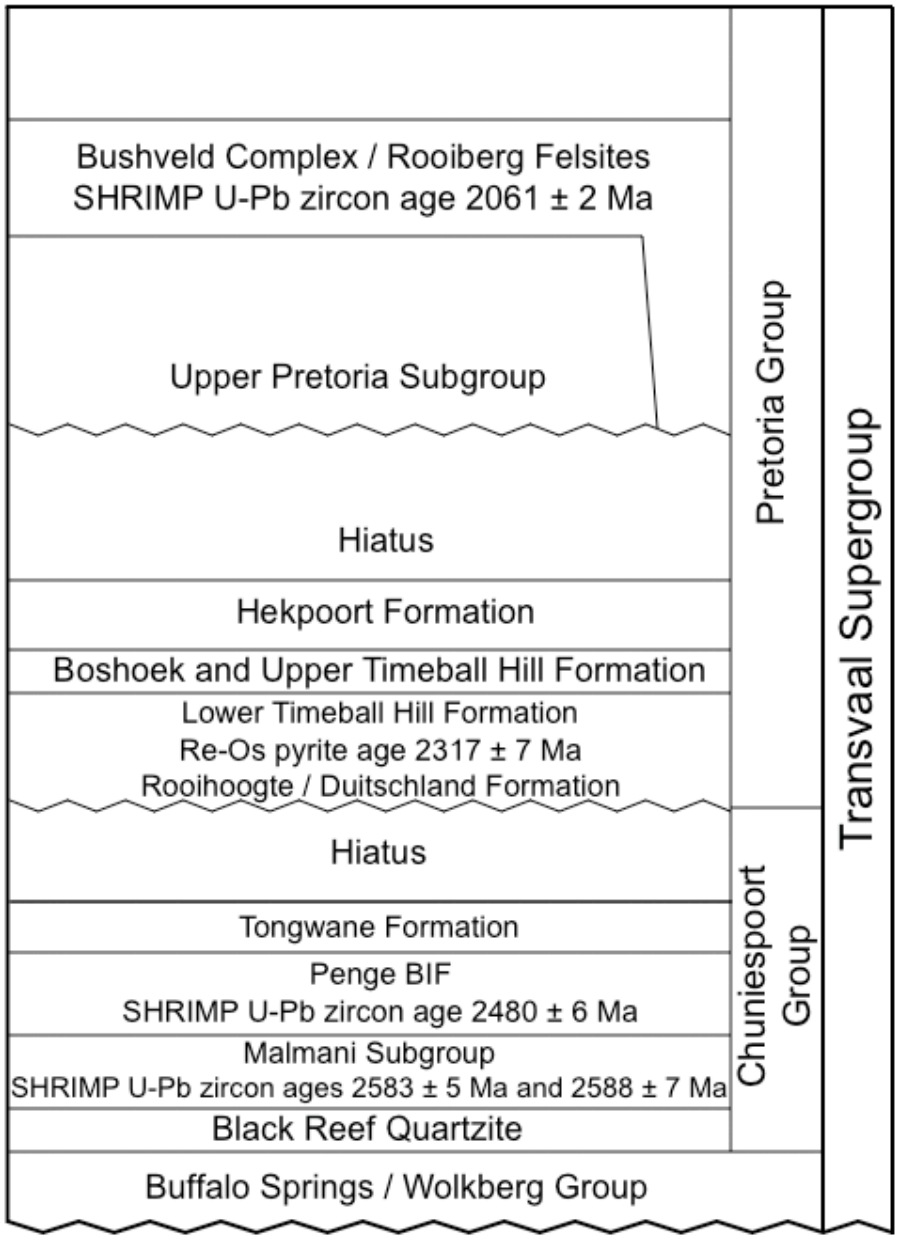

Figure 4.2 Stratigraphy of the Transvaal Supergroup as exposed in the Transvaal Basin. The Re–Os age for the Rooihoogte-Lower Timeball Hill formations is from (Hannah et al., 2004); see Bekker et al., (2004) for references to other ages. BIF=banded iron formation; SHRIMP=sensitive high-resolution ion micro-probe (modified from Bekker et al., 2001).

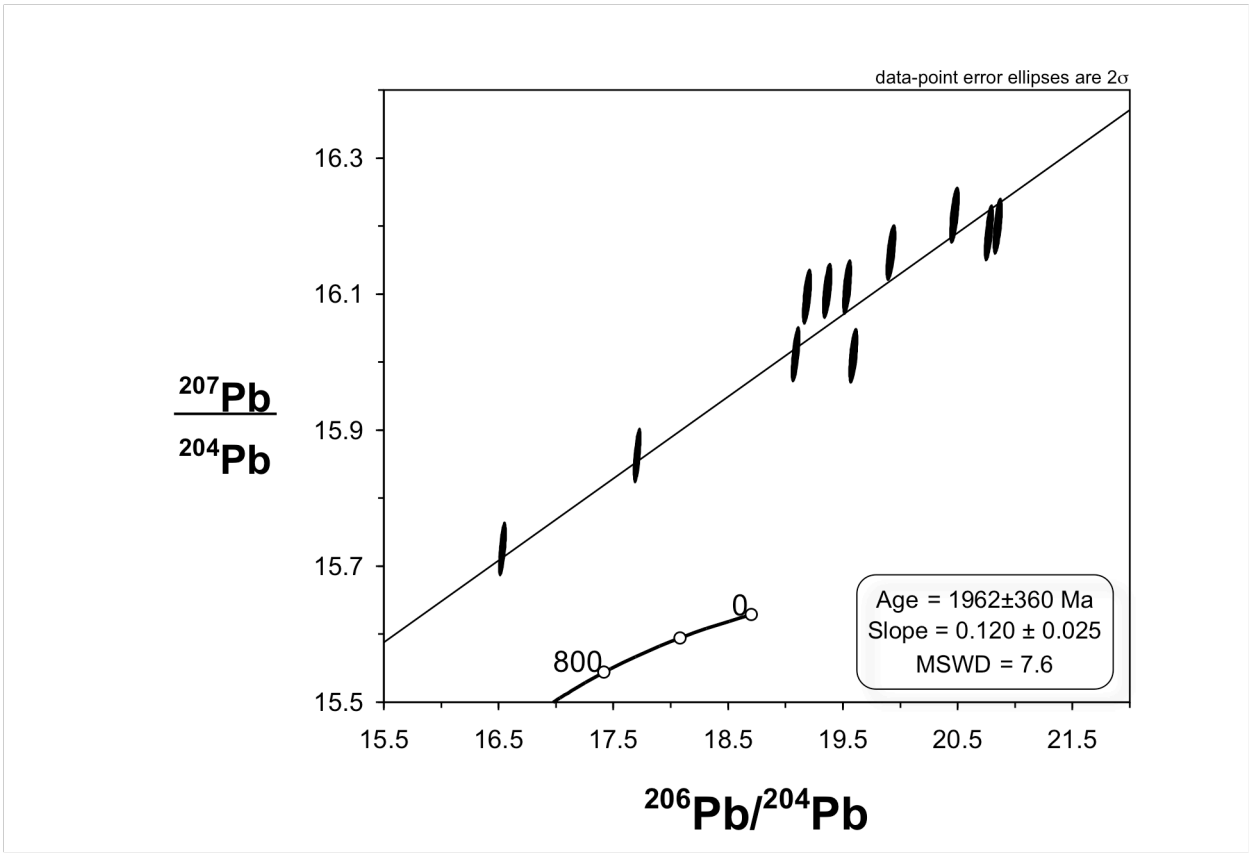

Figure 4.3 $^{206}Pb/^{204}Pb$ vs. $^{207}Pb/^{204}Pb$ isotope ratio diagram for the whole rock shale samples of the Timeball Hill Formation. The Pb isotope growth curve shown is based on the Pb isotope growth model of Stacey and Kramers (1975). The Pb-Pb age of the samples (1962 ± 360 Ma) is within error of the depositional age (2.32 Ga). The overlapping ages are an indication that U/Pb ratios are undisturbed since deposition and that κ_a ratio reflect sedimentary redox conditions.

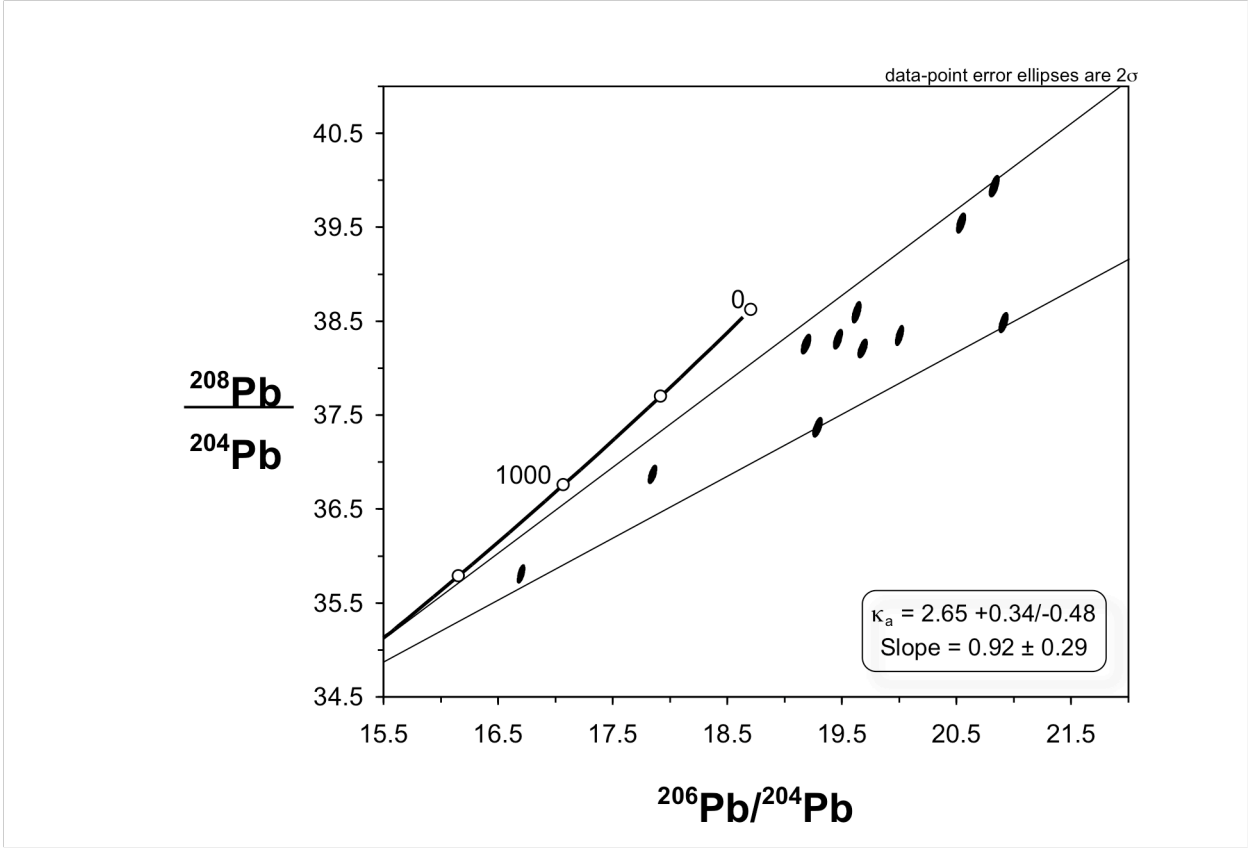

Figure 4.4 $^{206}Pb/^{204}Pb$ vs. $^{208}Pb/^{204}Pb$ isotope ratio diagram for the whole rock shale samples of the Timeball Hill Formation. The Pb isotope growth curve shown is based on the Pb isotope growth model of Stacey and Kramers (1975). Rays are constructed from the model Pb isotope composition at 2.3 Ga and extend to Pb isotope compositions of samples with the highest and lowest apparent time-integrated Th/U ratios (κ_a). Variations in κ_a ratios result from the redox decoupling of U from Th or variable Th/U ratios present in the provenance of these rocks.

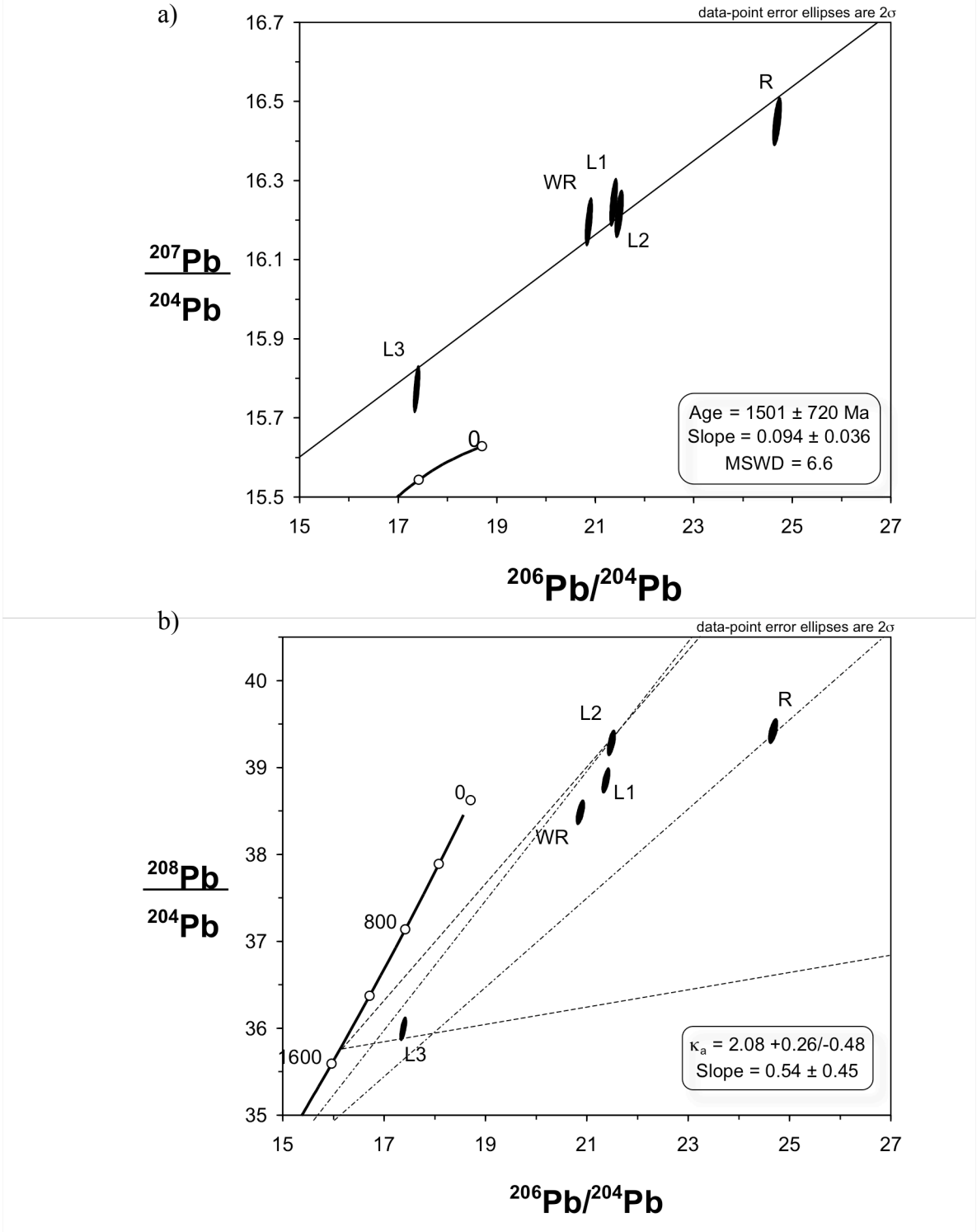

Figure 4.5 Pb isotope ratio plots for acid leaching of EBA2/37. The Pb-Pb age associated with the slope of uranogenic Pb isotope ratios (a) is significantly younger than the 2.32 Ga depositional age. Using the young Pb-Pb age results in much lower values of κ_a (dashed lines in b) compared to using a 2.3 Ga age (dash-dot lines in b) and may indicate a disturbance that redistributed uranium, however there is no indication of this in other proxies.

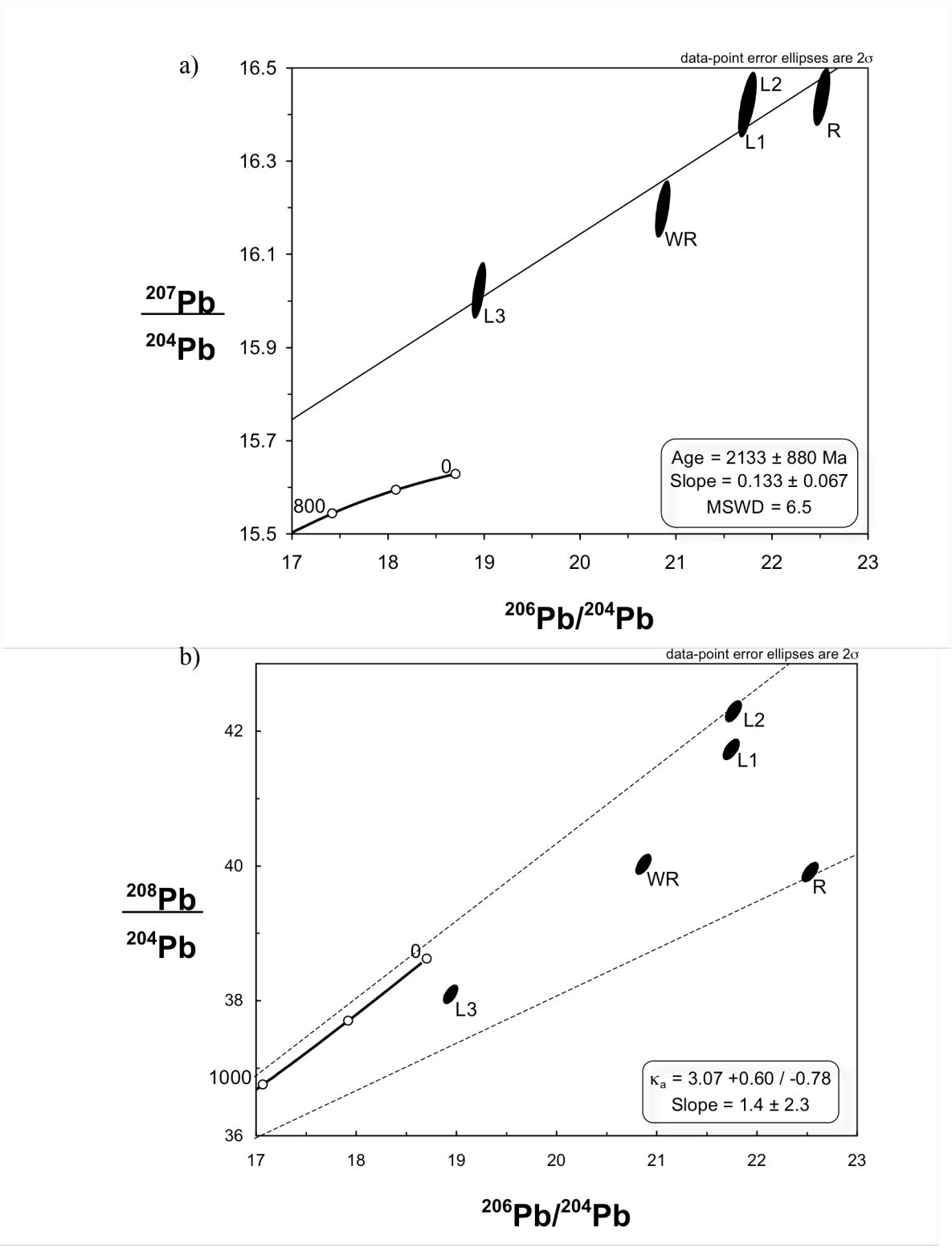

Figure 4.6 Pb isotope ratio plots for acid leaching of EBA2/42. The Pb-Pb age associated with the slope of uranogenic Pb isotope ratios (a) is within error of the 2.32 Ga depositional age. The antiquity of κ_a ratios (b) is evidence that U-Th decoupling is the result of ancient oxidative weathering conditions at 2.3 Ga.

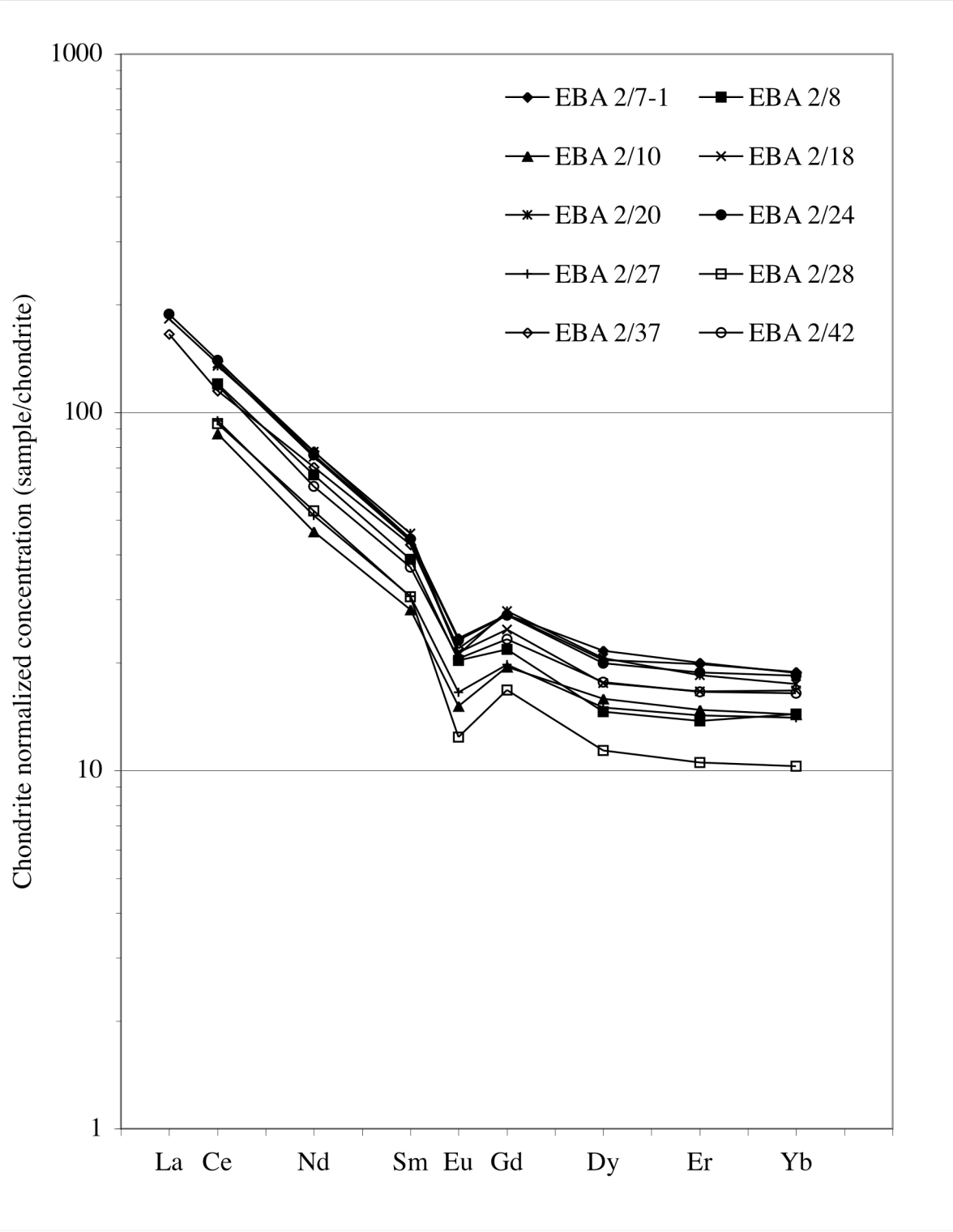

Figure 4.7 Chondrite-normalized REE patterns of the shale samples of the Timeball Hill Formation. The patterns are similar to one another indicating a common provenance for all samples. These similarities can be quantified through interelement REE ratios, such as Ce_N/Sm_N.

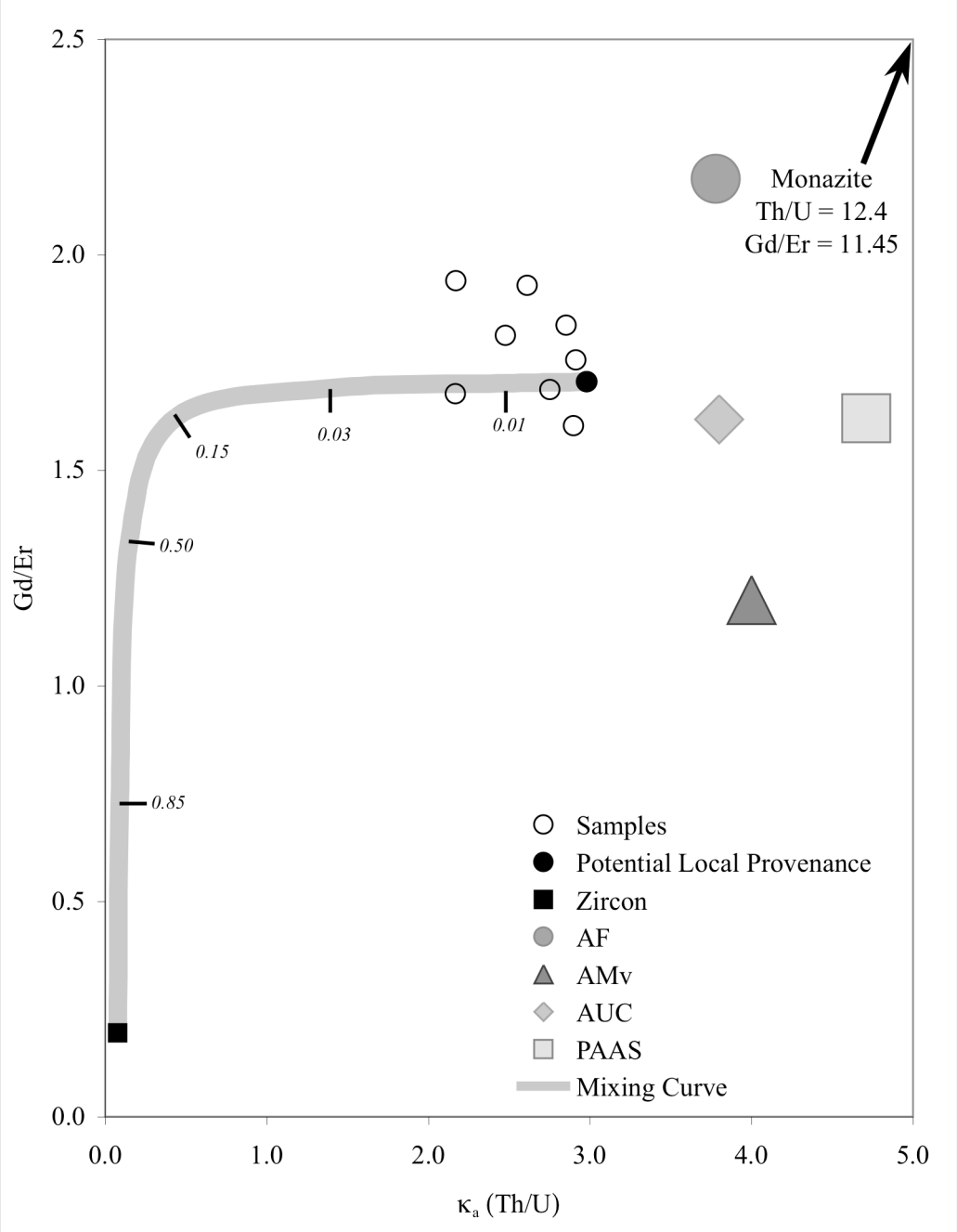

Figure 4.8 Gd/Er ratios and κ_a ratios for organic-rich shales of the Timeball Hill Formation. The REE geochemistry and κ_a ratios of shales from the Timeball Hill Formation does not support mixing of multiple detrital sources or differential concentrations of trace minerals as an underlying factor for variations in κ_a values. The sample with the highest κ_a ratio value is used as the potential local provenance source in sedimentary mixing with zircon. Errors for data points from the Timeball Hill Formation are 1.0% for Gd/Er ratios and 2.3% for κ_a ratio values. Errors for the data from Taylor and McLennan (1985) are estimated at 5% for both Th/U and Gd/Er ratios.

Table 4.1 Whole-rock Pb isotope compositions and κ_a values for shales of the Timeball Hill Formation

Sample	$^{206}Pb/^{204}Pb$	$^{207}Pb/^{204}Pb$	$^{208}Pb/^{204}Pb$	κ_a	Depth
EBA2/7	19.68	16.01	38.22	2.56	1327.70 - 1327.80 m
EBA2/8	16.72	15.73	35.84	2.61	1327.80 - 1327.90 m
EBA2/10	19.19	16.02	38.27	2.90	1328.00 - 1328.10 m
EBA2/16	17.86	15.87	36.89	2.73	1328.60 - 1328.70 m
EBA2/18	20.00	16.16	38.36	2.48	1328.80 - 1328.90 m
EBA2/20	19.63	16.11	38.61	2.85	1329.00 - 1329.10 m
EBA2/24	20.54	16.22	39.54	2.91	1329.40 - 1329.50 m
EBA2/27	19.47	16.11	38.32	2.75	1329.70 - 1329.80 m
EBA2/28	19.29	16.10	37.39	2.17	1329.80 - 1329.90 m
EBA2/37	20.90	16.20	38.50	2.17	1333.70 - 1333.80 m
EBA2/42	20.83	16.19	39.93	2.98	1330.20 - 1330.40 m

Table 4.2 Pb isotope composition of the stepwise acid leaching of shales from the Timeball Hill Formation

Sample	$^{206}Pb/^{204}Pb$	$^{207}Pb/^{204}Pb$	$^{208}Pb/^{204}Pb$	κ_a
EBA2/37				
L1	21.41	16.25	38.86	2.17
L2	21.52	16.22	39.29	2.34
L3	17.40	15.78	36.04	2.12
R	24.73	16.45	39.42	1.61
WR	20.90	16.20	38.50	2.17
EBA2/42				
L1	21.76	16.41	41.73	3.41
L2	21.78	16.43	42.29	3.66
L3	18.96	16.03	38.13	2.96
R	22.54	16.44	39.92	2.29
WR	20.83	16.19	39.93	2.98

The following acids and times were used during leaching experiments: step L1 (1 mL 0.1M HBr, ~1h), L2 (1 mL 4M HBr, ~1 hr), L3 (1 mL 50:50 HCl:HNO_3), R (HF and HNO_3)

Table 4.3 Relative proportion of Pb liberated by sequential acid leaching of two shale samples from the ca. 2.3 Ga Timeball Hill Formation

Leach Step	Counts per second (cps)					
	^{204}Pb	^{206}Pb	^{207}Pb	^{208}Pb	Total	Percentage
EBA2/37						
L1	2.15E+06	4.59E+07	3.48E+07	8.33E+07	1.66E+08	23.8%
L2	1.28E+06	2.75E+07	2.07E+07	5.02E+07	9.97E+07	14.3%
L3	5.39E+06	9.37E+07	8.48E+07	1.94E+08	3.78E+08	54.16%
R	6.61E+05	1.63E+07	1.08E+07	2.60E+07	5.38E+07	7.72%
		$^{206}Pb/^{204}Pb$	$^{207}Pb/^{204}Pb$	$^{208}Pb/^{204}Pb$		
Calculated Whole Rock		19.51	16.01	37.44		
Measured Whole Rock		20.90	16.20	38.50		
EBA2/42	^{204}Pb	^{206}Pb	^{207}Pb	^{208}Pb	Total	Percentage
L1	7.50E+05	1.61E+07	1.22E+07	3.09E+07	5.99E+07	3.0%
L2	8.38E+06	1.81E+08	1.37E+08	3.52E+08	6.78E+08	33.7%
L3	1.43E+07	2.71E+08	2.29E+08	5.44E+08	1.06E+09	52.59%
R	2.71E+06	6.08E+07	4.43E+07	1.08E+08	2.16E+08	10.72%
		$^{206}Pb/^{204}Pb$	$^{207}Pb/^{204}Pb$	$^{208}Pb/^{204}Pb$		
Calculated Whole Rock		20.38	16.22	39.83		
Measured Whole Rock		20.83	16.19	39.93		

Table 4.4 REE concentrations for organic-rich shale samples of the Timeball Hill Formation (in ppm)

	EBA 2/7	EBA 2/8	EBA 2/10	EBA 2/18	EBA 2/20	EBA 2/24	EBA 2/27	EBA 2/28	EBA 2/37	EBA 2/42
La	--	--	--	57.5	--	59.3	--	--	52.2	--
Ce	113	97.6	70.8	111	110	114	76.9	75.6	93.5	96.6
Nd	46.5	40.0	27.7	44.9	46.3	45.5	30.8	31.7	42.0	37.0
Sm	8.53	7.47	5.40	8.40	8.80	8.52	5.88	5.87	8.22	7.09
Eu	1.69	1.47	1.09	1.54	1.52	1.67	1.19	0.896	1.58	1.48
Gd	7.05	5.65	5.05	6.42	7.22	7.03	5.12	4.35	7.07	6.02
Dy	7.01	4.74	5.15	5.71	6.70	6.48	4.87	3.69	6.61	5.73
Er	4.25	2.93	3.15	3.54	3.93	4.00	3.03	2.24	4.22	3.53
Yb	3.89	2.99	2.98	3.48	3.63	3.82	2.92	2.14	3.92	3.42
Ce_N/Sm_N	3.12	3.09	3.10	3.13	2.94	3.15	3.09	3.04	2.69	3.22
Gd_N/Yb_N	1.45	1.52	1.36	1.48	1.60	1.48	1.41	1.63	1.45	1.41
Ce_N/Yb_N	7.41	8.34	6.07	8.18	7.74	7.60	6.75	9.05	6.10	7.22
Ce/Ce*	--	--	--	1.01	--	1.00	--	--	0.923	--
Eu/Eu*	0.673	0.697	0.647	0.649	0.589	0.666	0.671	0.548	0.642	0.701

5.1 Background

5.1.1 Geological Setting

Samples of banded iron formation (BIF) and manganese formation (MnF) from the ca. 2.22 Ga Hotazel Formation of the Paleoproterozoic Transvaal Supergroup in the Griqualand West structural basin of South Africa were collected from drill core G664 from the Mamatwan Mine in the Kalahari Manganese Field (Figures 5.1 and 5.2). In the Griqualand West structural basin, the Transvaal Supergroup is composed of the Ghaap Group, primarily comprised of chemically precipitated sedimentary rocks, and the Postmasburg Group, comprised of two unconformity-bound sequences of mixed volcanic and chemically precipitated rocks (Button, 1973a). The base of the Postmasburg Group is marked by a regional unconformity upon which the glacial diamictite of the Makganyene Formation is deposited. This diamictite is correlative to the basal diamictite of the Rooihoogte Formation of the Pretoria Group in the Transvaal structural basin (Eriksson et al., 1995; Eriksson and Reczko, 1995). Directly overlying the Makganyene Formation is a series of andesitic basalt and basalt flows, collectively known as the Ongeluk Formation. The Ongeluk and Hekpoort Lavas of the Transvaal structural basin are correlative units based on both lithostratigraphic and geochronologic age determinations (Cornell et al., 1996; Eriksson and Reczko, 1995).

The Hotazel Formation conformably overlies the Ongeluk Lava, which provides a maximum age constraint of 2222 ± 13 Ma (Cornell et al., 1996). The minimum age is constrained by the 2.061 Ga Rooiberg Felsites and Bushveld Complex (Buick et al., 2001; Dorland, 2004; Walraven, 1997), however this constraint is subject to stratigraphic correlations being correct, as these rocks are not found in the Griqualand West structural

basin. The Hotazel Formation is comprised of three laminated Mn ore units interbedded with iron formation and lutite. This formation has been the focus of many studies in economic geology due to its importance as the major Mn ore-bearing unit in the Kalahari Manganese Field of the Northern Cape Province, the largest land-based Mn resource (Gutzmer and Beukes, 1997; Roy, 2000; Tsikos and Moore, 1998). The dolomites of the Mooidraai Formation overlie the Hotazel Formation and mark the top of the lower unconformity-bound sequence of the Postmasburg Group.

In the Mamatwan Mine, the preserved section of the Hotazel Formation is comprised of a lower BIF, the "lower manganese ore body", various lutite layers, and an upper BIF and overlain by the Tertiary Kalahari Formation (Nel et al., 1986). The Hotazel Formation was sampled from various depths via drill core G664, which was drilled by SAMANCOR in the Mamatwan Mine. The section of the Hotazel Formation sampled in drill core G664 is approximately 98 meters thick with ~44 meters of primary manganese formation overlain by ~49 meters of lutite and 5 meters of BIF. The depth from which samples included in this study were sampled and description of the lithology is noted in Table 5.1.

5.1.2 REE concentrations in modern seawater

The REE are considered nearly insoluble and often have concentrations on the order of picomoles/kg or parts per quadrillion (ppq) in modern seawater (German and Elderfield, 1990b; Greaves et al., 1989). Due to the overall low concentrations of the REE in seawater, it is of great importance to use high precision analytical techniques under low REE blank conditions that can be accomplished through isotope dilution mass spectrometry (IDMS). Several previous studies that have determined the concentration of

REE in seawater have recognized the advantages of using IDMS as well as chemical separation techniques (Elderfield and Greaves, 1983; Greaves et al., 1989; Piepgras et al., 1979). Regardless of the chemical analyses performed, proper chemical separations are necessary to ensure that isobaric interferences do not obscure the REE concentrations. Therefore measurements of REE concentrations in modern seawater have employed isotope dilution mass spectrometry, because it has been demonstrated that this method produces highly precise and accurate data (Greaves et al., 1989). IDMS employs the principle of isotopic spiking and uses the isotope dilution equation to calculate highly precise and accurate concentration data. The high quality of this data allows for meaningful interpretation of igneous processes as well as sedimentary provenance and post-depositional processes (Gleason et al., 2000; Hanson, 1980; Krogstad et al., 2004; Lev et al., 1999; McLennan, 1989; Ohr et al., 1994; Taylor and McLennan, 1985).

The major advantage of the isotope dilution method is the production of high precision data with accuracies traceable through the isotopic tracer to gravimetric standard solutions. It is not possible to obtain high precision data using the standard addition technique utilized in other laboratories, as there are no rock standards that have been analyzed for monoisotopic element concentrations (e.g. Mn, Pr, Tb, Ho, Tm) with methods traceable to gravimetric standard solutions. Additional support for the precision of this method is derived from the consistency of interelement ratios for USGS standard BHVO-1 (better than 1% on all element ratios other than those involving La and Ce, 2σ). Replicate mass spectrometry of BHVO-1 yield average concentration errors of 0.62% (2σ) for elements except La. The observed variations in element concentrations and interelement ratios for samples are therefore likely due to a combination of variable

proportions of mineral phases in which REE are present in incompatible phases (i.e. the quartz effect), mineral phases in which REE are compatible (i.e. the nugget effect), and weighing error.

Previous studies (Bertram and Elderfield, 1993; Elderfield and Greaves, 1982; Elderfield et al., 1988; German and Elderfield, 1990b; German et al., 1995; Greaves et al., 1989; Greaves et al., 1991; Klinkhammer et al., 1994; Mitra et al., 1994; Piepgras and Jacobsen, 1992; Sholkovitz et al., 1994; Sholkovitz and Schneider, 1991; Westerlund and Öhman, 1992) have shown that REE concentrations do not vary significantly from ocean to ocean (Table 5.2). It has become conventional to evaluate REE patterns of natural waters normalized against shale rather than chondrite to eliminate the influence of variable amounts of detrital sediment on the interpretation of REE distribution. The shale-normalized (in this case a shale sample selected from the Sengoma Argillite Formation) pattern of modern seawater displays a negative Ce-anomaly, positive Eu-anomaly, and overall heavy rare earth element (HREE) enrichment (Figure 5.3). Normalized interelement ratios vary significantly (45% 2σ) despite the observed similarities in REE patterns, which are interpreted as being effected by different contributions of REE from detrital sediment sources and/or hydrothermal input into each ocean basin.

5.1.3 Previous Work

The overall low REE concentration in chemically precipitated sedimentary rocks (limestone, dolomite, and BIF) is well documented (Alexander et al., 2008; Bau and Dulski, 1992; Bau and Dulski, 1996; Bau et al., 1997; Bau and Möller, 1993; Bolhar et

al., 2004; Derry and Jacobsen, 1990; Dymek and Klein, 1998; Frei et al., 2008; Fryer, 1977; Kamber and Webb, 2001; Kato et al., 1998; Shields and Stille, 2001; Spier et al., 2007; Veizer et al., 1992a; Veizer et al., 1989; Veizer et al., 1992b; Yamamoto et al., 2004). No previous studies have used the isotope dilution technique to analyze the concentration of REE in BIFs, despite the number of these studies and the low abundances of REE. Instead REE concentrations are typically determined using external standards with ICP-MS resulting in reported 10% errors. As mentioned above (Section 5.2.2) the typical concentrations for the REE are on the order of a few parts per million or less with shallow slopes on chondrite-normalized REE patterns (La/Yb_{CN} = ~3.1). Of particular interest to this study are the specifics of the REE concentrations as they pertain to banded iron formations and manganese formations.

In contrast, detrital material typically has REE concentrations 10 to 100 times that found in chemically precipitated sediments. Therefore the REE concentration of chemically precipitated sediments can be overwhelmed by the introduction of detrital material. It is therefore important to evaluate the contribution of detrital material to the overall concentration of chemically precipitated sedimentary rocks. This can be accomplished through normalization of REE concentration data to that of related detrital materials.

5.2 Results

The data obtained for this study (Table 5.3) have very low errors compared to data obtained by ICP-MS without chemical separation of the REE, spark source mass spectrometry (SSMS), or instrumental neutron activation analysis (INAA). The

concentration data presented here by ID-HR-ICP-MS have precision of 4% (2σ) errors as calculated using replicate analyses of different aliquots of the same rock powders. Analyses of REE concentrations by ICP-MS, SSMS, and INAA analyses often have minimum precision of 10% or greater (2σ). More important than the reproducibility of a single element concentration is the ability to precisely and accurately replicate interelement ratios. These ratios are used far more often in the interpretation of REE data and therefore must be of the highest quality to validate their interpretations. The maximum reproducibility of all REE interelement ratios is 4% (2σ) with key ratios (Gd_N/Yb_N and Eu/Eu*) having 2σ precisions of 1.3% and 1.5% respectively. The unusually high errors may be associated with sample heterogeneity at such a scale that replicate analyses of the same sample powder have different concentrations of U-Th-Pb-REE enriched minerals (i.e. "the nugget effect"). Other similar circumstances may also result in high errors in the data however weighing errors and poor isotope tracer (spike) calibration are more common explanations for poor reproducibility of REE data. Therefore many of the fine structures observed in these individual REE patterns would be rendered unresolved by other methods and sample normalized patterns would be impossible to interpret due to the compounded errors.

An example of a fine structure in REE patterns that is often unresolved by those using data determined by ICP-MS and INAA techniques due to the low precision of these data is the tetrad effect. The tetrad effect is the representation of increased geochemical stability in REE with one-quarter, half, three-quarter, and completely filled 4f electron shells, which is manifested as kinked REE patterns when using IDMS (Akagi et al., 1994; Masuda and Ikeuchi, 1979; Masuda et al., 1987). These 4f electron shell configurations

are found between Nd and Pm (one-quarter filled), at Gd (half-filled), between Ho and Er (three-quarters filled), and at Lu (completely filled) and may be expressed as kinked REE patterns associated with increased stability of Nd, Gd, Er, and Lu ionic complexes. These kinks are most apparent in natural waters and rocks that experienced extensive interaction with these waters (e.g., pegmatites, chemical sediments). Due to redox controls on the concentration of Ce and Eu and that Lu concentrations were not measured in this study, evaluation of the tetrad effect must be done by looking for kinks in the REE patterns near Er. These kinks in the HREE portion of shale-normalized REE patterns of seawater are clearly visible as concave upward kinks at Er (Figure 5.3). These concave downward kinks at Er are also noticeable in chondrite and shale normalized REE patterns of BIF and MnF samples from the Hotazel Formation (Figures 5.4 and 5.8).

High precision data is essential when the intention is to evaluate the relative behavior of the REE in paleoenvironmental conditions. The analytical methods used in this study are significantly more precise than those used to determine REE concentrations of other geologically related materials. Therefore when interpreting the data obtained in this study, previously determined low precision data (e.g. North American Shale Composite, NASC and Post-Archean Average Australian Shale, PAAS; of Gromet et al. (1984) and Taylor and McLennan (1985), respectively) are inadequate for normalization and only serve to devalue the quality of the data. In the case of the Artic Ocean, REE concentrations have not been determined by IDMS and ICP-MS data were used in this study.

5.2.1 Timeball Hill Formation

Ten organic-rich shale samples of the 2.32 Ga Timeball Hill Formation as well as ten organic-rich shale samples from the ca. 2.1 Sengoma Argillite Formation were analyzed for their REE concentration (Tables 4.4 and 6.3). The total concentration of REE in the Timeball Hill Formation samples is higher than that in the Sengoma Argillite Formation. Direct comparison of REE concentrations is often not appropriate because the quartz effect may result in profound variations in the overall concentration of the REE in each sample. Additionally, the Oddo-Harkins rule asserts that elements with an even number of protons have greater concentrations than their odd-numbered proton neighbors in natural substances. Therefore the concentration of Eu in shale is 19% that of Sm concentrations and 23% that of Gd concentrations and the same relative Eu depletions in chondrites are 38% and 28%, respectively. In this chapter, REE concentrations for samples are normalized to either chondritic or shale values depending upon the most commonly used normalizing factor for the corresponding lithology applied in the literature. Therefore REE concentrations of shale samples from the Timeball Hill and Sengoma Argillite Formations are normalized to chondritic values. Similarly after the REE signature of shales from the Pretoria Group has been established, the samples of BIF and manganese formation are normalized to appropriate shale values. Visual assessment of REE concentration data is simplified through the use of normalized REE patterns. In order to properly evaluate the REE geochemistry of these sedimentary units, sample REE concentrations were normalized to IDMS chondritic values (Masuda et al., 1973) divided by 1.20 to correct for volatilization during meteoritic processes and IDMS shale values from this paper.

Chondrite-normalized REE patterns of the shale samples from the Timeball Hill Formation (Figure 4.7) are subparallel to one another and have concave upwards shapes, typical of shales (Taylor and McLennan, 1985). These patterns are further characterized by pronounced LREE enrichment (Ce_{CN}/Yb_{CN} = 7.45 ± 1.92, 2σ) and negative Eu-anomalies (Eu/Eu* = 0.648 ± 0.095). These patterns also lack the presence of well-defined Ce-anomalies (Ce/Ce* = 0.978 ± 0.095).

5.2.2 Hotazel Formation

REE concentration data of the 17 samples from the Fe-rich and Mn-rich portions of the Hotazel Formation are presented in Table 5.2. The average total concentration of the REE in the Hotazel Formation is consistent with that reported by other REE studies of BIFs (∑REE = 15.2 ppm). In accordance to the selection criteria discussed above, REE concentrations are normalized to chondritic values for the purpose of comparison. Chondrite-normalized REE patterns for the samples are shown in Figure 5.4, which display LREE enrichment (La_{CN}/Yb_{CN} = 4.60 ± 2.58 2σ) with pronounced negative Ce-anomalies Ce/Ce* = 0.674 ± 0.166) and Eu-anomalies (Eu/Eu* = 0.705 ± 0.071). Greater fractionation of the LREE (La_{CN}/Sm_{CN} = 4.92 ± 1.06) compared to the HREE (Gd_{CN}/Yb_{CN} = 0.895 ± 0.419) is apparent in the overall REE pattern having a J-shaped morphology.

Due to the variation in major element geochemistry, samples were classified as BIF or Mn-formation (MnF). Although the REE patterns of these samples do not vary greatly, it is necessary to treat the different classes as separate groups, as the origins of each of these lithologies are different. In order to quantify the effect of variable genetic processes, the REE concentration of each sample was normalized by one sample in the

suite (Hanson, 1980; 1989). Seven of the seventeen collected samples have been identified as BIF, whereas the others have been identified as primarily MnF.

5.2.2.1 Iron Formation Samples

The REE concentration of the BIF samples is highly variable with a low average total REE concentration ($\sum$REE = 11.4 ± 7.84 ppm). The chondrite-normalized REE patterns of these BIF samples (Figure 5.5a) display less overall enrichment of LREE with respect to HREE (La_{CN}/Yb_{CN} = 3.95 ± 1.14) compared to the total suite of samples from the Hotazel Formation. Samples of Hotazel BIF have slightly greater LREE fractionation (La_{CN}/Sm_{CN} = 5.16 ± 0.57) compared to the average for all analyzed samples of the Hotazel Formation, although the relative variation of values is similar. Samples characterized as BIF have more pronounced and consistent HREE fractionation (Gd_{CN}/Yb_{CN} = 0.757 ± 0.120), compared to the entire suite. Ce-anomalies for the BIF samples are less pronounced and have reduced relative variability (Ce/Ce* = 0.701 ± 0.081), whereas Eu-anomalies are more pronounced (Eu/Eu* = 0.683 ± 0.047) and have lower relative variability. The reduction in relative variability in all key interelement ratios indicates that BIF samples represent a distinct statistical group different from that of the MnF samples. In order to evaluate the effect of genetic processes and detrital input on the REE patterns, samples concentrations were normalized to one sample of each lithology. Sample H42 was selected for normalization of the BIF samples due to it having the lowest concentration of total REE.

Iron-formation (H42) sample normalized REE patterns are presented in Figure 5.6a. The benefit of plotting these parameters is the ability to directly compare the REE patterns of potentially related samples. All samples display a slight negative Eu-anomaly

(Eu/Eu* = 0.891) although the degree to which the Eu depletion is observed is variable (11.6% 2σ). Despite the consistency of the Eu-anomalies, the other key interelement ratios (Ce/Ce*, La/Yb, La/Sm, Gd/Yb) for these samples all have higher variability (>20%). Most samples show a greater LREE enrichment compared to that in H42 (La_{H42}/Yb_{H42} = 1.70 ± 0.83; La_{H42}/Sm_{H42} = 1.12 ± 0.25). The most obvious variations exist in Ce-anomalies (Ce/Ce* = 0.997 ± 0.251). Modeling and explanation of these observed variations will be addressed below (Section 5.4.3 and 5.4.4).

5.2.2.2 Manganese Formation Samples

The REE concentration of the MnF samples is highly variable with a slightly higher average total REE concentration (∑REE = 17.9 ± 12.1 ppm). The chondrite-normalized REE patterns of these samples (Figure 5.5b) display some variability in LREE enrichment (La_{CN}/Yb_{CN} = 5.05 ± 1.24). Chondrite-normalized REE patterns of Hotazel MnF samples show less LREE fractionation compared to the average for all analyzed samples of the Hotazel Formation (La_{CN}/Sm_{CN} = 4.75 ± 0.45), with little HREE fractionation (Gd_{CN}/Yb_{CN} = 0.992 ± 0.208). This results in steeper overall patterns, as the HREE enrichment observed in the BIF samples is largely absent. As was done for the BIF samples, the sample of the MnF with the lowest total concentration of REE (10.8 ppm; H30) was selected for normalization to evaluate the relative changes observed in REE concentrations.

Sample-normalized (H30) REE patterns of primary manganese formation samples are presented in Figure 5.6b. The H30-normalized REE concentrations vary over one order of magnitude amplifying any slight variations in REE concentrations. The overall variability of the REE patterns make it impossible to draw any generalized statement

regarding chemical parameters of the MnF samples. These deviations may represent significant genetic differences or changes in provenance as samples with low concentrations are particularly susceptible to these effects. Due to the subtrivial calculated blank/sample ratios (less than 1:2800) for this technique it is unlikely that the observed differences are the result of a blank effect.

5.3 Discussion

5.3.1 Using REE data from shales of the Pretoria Group for normalization

Chondritic REE concentrations are used for normalizing a variety of materials, as these data are thought to approximate bulk earth chemistry. Although these values are appropriate for characterizing the REE patterns of igneous rocks, interpretation of chondrite-normalized REE patterns for most sedimentary rocks is complicated as these rocks are at least two stages removed from their origins in the bulk Earth (one associated with an igneous precursor and a second associated with sedimentary processes). The effects of individual processes within each stage are difficult to resolve. Therefore an ideal alternative to normalizing sedimentary REE values to chondritic values is to normalize them to a similar, common sedimentary material such as shale. Previous studies have used composites and average REE concentration data of shales for normalization (i.e. PAAS and NASC). Despite the acceptance of this method in the scientific community, their application to this study would result in decreased accuracy of the resultant normalized REE patterns, due to the less precise methods for REE analyses used in these studies. The comparatively high errors associated with using REE concentrations determined by ICP-MS without the use of isotope dilution and chemical

separation methods for normalization are supported by the inconsistency of REE patterns that use one shale sample to normalize associated rocks.

Through simple visual interpretation of chondrite-normalized REE pattern morphologies and interelement ratios, it has been shown that the REE behavior in the BIF samples of the Hotazel Formation is predictable. The REE concentration data for one of these samples (H38) was normalized to REE concentration data from several different shale samples from the Mozaan Group of eastern South Africa and Swaziland determined by ICP-MS (Alexander et al., 2008). The resultant Mozaan shale (Ms)-normalized REE patterns of sample H38 are highly irreproducible (Figure 5.7). These highly variable REE patterns likely reflect the low precision and accuracy of Mozaan shale REE concentrations (2σ = 168%) and interelement REE ratios (2σ = 65.2%). This reproducibility is far worse than the errors (±5%) reported in the study of the Mozaan shales indicating that these errors were grossly underestimated and are likely only counting statistics on an ion beam for a single measurement. In order to show the effectiveness of the isotope dilution method for producing high quality data, the same exercise is repeated with IDMS REE data for the shale samples from the Sengoma Argillite Formation (Chapter 6).

The Sengoma Argillite Formation shale (SAF)-normalized REE patterns of H38 show strong similarities from one shale sample to the next (Figure 5.8). These similarities can be quantified using the same geochemical parameters as before. The reproducibility of all SAF-normalized concentrations (2σ = 28.5%) is 5.9 times as consistent as that for the Ms-normalized concentrations. More important than the concentration of individual elements is the reproducibility of interelement ratios for the

SAF-normalized REE patterns (2σ = 15.9%), which is 25% of that for the Ms-normalized ratios. Based on this comparison of data quality, IDMS REE concentration data for one of the shale samples of the Sengoma Argillite Formation that shows a near average value for interelement ratios (Strat2; 224.87 m) was selected for normalization of the REE data from the Hotazel Formation.

5.3.2 Shale-normalized REE patterns for the Hotazel Formation

The complex morphology of the chondrite-normalized REE patterns for the chemical sedimentary rocks of the Hotazel formation make interpretation of these patterns difficult. One possible reason for the observed complexity is the presence of a fine-grained detrital sediment component. The resultant REE pattern would have the combined features of a chemical sediment and shale. Due to greater REE concentrations in shales, the detrital flux would overwhelm the chemically precipitated flux to the REE budget of the sedimentary rock. In order to evaluate the input of detrital REE, the REE data for the chemical sedimentary rocks (both BIF and MnF) of the Hotazel Formation were normalized to a shale sample from the Sengoma Argillite Formation (Strat2; 224.87 m) (Figure 5.9).

The shale-normalized REE patterns for all of the samples from the Hotazel Formation display a pronounced HREE enrichment and significant negative Ce-anomalies. REE fractionation for the Hotazel Formation results in HREE enrichment ($La_{SN}/Yb_{SN} = 0.434 \pm 0.244$, 2σ). The differential stability of aqueous REE ionic complexes is noted for modern seawater (Brookins, 1989; Byrne and Kim, 1990; Cantrell and Byrne, 1987; Lee and Byrne, 1993), which results in LREE depletion in modern chemical sediments (Haley et al., 2005; Sholkovitz and Shen, 1995). The LREE

depletion observed in shale-normalized REE patterns of the Hotazel Formation permits the interpretation that the ca. 2.22 Ga seawater from which the chemical sediments of the Hotazel Formation were precipitated also displayed this increased stability of aqueous LREE ionic complexes. Minimal fractionation of the LREE is observed in the samples (La_{SN}/Sm_{SN} = 1.08 ± 0.23) whereas fractionation of the HREE is more pronounced (Gd_{SN}/Yb_{SN} = 0.604 ± 0.283). All samples show negative Ce-anomalies (Ce/Ce* = 0.730 ± 0.180) and all but one (H43; Eu/Eu* = 0.946) display positive Eu-anomalies (Eu/Eu* = 1.11 ± 0.11). The consistency of these shale-normalized patterns is further displayed, as there is no apparent preferential fractionation of the LREE or HREE. The overall consistency of these factors (especially interelement ratios) indicates that no significant genetic differences exist between samples, however evaluation of these parameters for each lithology provides a more complete assessment.

The shale-normalized REE patterns of these BIF samples (Figure 5.9a) display some overall variability but remain similar to modern seawater with an overall enrichment of HREE with respect to LREE (La_{SN}/Yb_{SN} = 0.372 ± 0.216). Samples of Hotazel BIF have slightly greater LREE fractionation compared to the average for all analyzed samples of the Hotazel Formation (La_{SN}/Sm_{SN} = 1.13 ± 0.25), although the relative variation of values is similar. Samples characterized as BIF have more pronounced and consistent HREE fractionation (Gd_{SN}/Yb_{SN} = 0.511 ± 0.162), compared to the average of all samples. The steepness of the shale-normalized REE patterns of BIF samples between Gd and Dy is noteworthy, indicating a strong fractionation of these two very similar elements (Gd_{SN}/Dy_{SN} = 0.789 ± 0.101).

When normalized to the same shale sample, all MnF samples (Figure 5.9b) exhibit HREE-enriched REE patterns (La_{SN}/Yb_{SN} = 0.477 ± 0.233; Gd_{SN}/Yb_{SN} = 0.670 ± 0.281) with flat LREE portions (La_{SN}/Sm_{SN} = 1.04 ± 0.20). The lack of pronounced LREE enrichment is further supported by shale-normalized Nd/Sm ratios that are near unity (Nd_{SN}/Sm_{SN} = 0.985 ± 0.098). The presence of consistent positive Eu-anomalies in all MnF samples (Eu/Eu* = 1.13 ± 0.04) is interesting considering that Eu-anomalies observed in the BIF samples are only slightly less pronounced but far less consistent (Eu/Eu* = 1.07 ± 0.15), which might reflect variable hydrothermal contributions to the total marine REE budget.

5.3.3 Comparison of shale-normalized Hotazel Formation and seawater REE patterns

The REE concentrations of seawater samples from four out of the five modern oceans (Pacific, Atlantic, Indian, and Southern) have previously been established by IDMS (German and Elderfield, 1990b; German et al., 1995; Piepgras and Jacobsen, 1992; Sholkovitz and Schneider, 1991). REE concentration data for the Arctic Ocean was determined by ICP-MS without use of chemical separation or isotopic tracer (5-15% precision, Westerlund and Öhman, 1992). Average REE concentrations for each ocean were calculated from the REE concentration data from these studies. The weighted average of REE concentrations for the various oceans was compiled as REE concentrations for the World Ocean. The weight of each ocean was determined by the percentage of the total volume of water in the world's ocean present in the specific ocean basin. The REE concentrations for the World Ocean as well as those for each ocean were normalized to shale (Figure 5.3).

A comparison of the shale-normalized REE patterns for modern seawater (Figure 5.3) and chemical sediments from the Hotazel Formation (Figure 5.8) indicates a visual similarity. In an effort to further resolve this visual resemblance, interelement ratios of the World Ocean and the chemical sediments of the Hotazel Formation were compared. The shale-normalized REE patterns for samples of the Hotazel Formation display enrichment of the HREE (La_{SN}/Yb_{SN} = 0.434; Gd_{SN}/Yb_{SN} = 0.604) with very gently sloping LREE portions (La_{SN}/Sm_{SN} = 1.08). The negative Ce-anomalies and slight Eu-anomalies also characterize these REE patterns (Ce/Ce* = 0.730; Eu/Eu* = 1.11). The flatness of the REE pattern between Nd and Sm is another feature that is distinctive of these patterns (Nd_{SN}/Sm_{SN} = 0.999).

The diagnostic interelement ratios provided above for the chemical sediments of the Hotazel Formation are similar to those of modern seawater. The shale-normalized REE patterns for modern seawater exhibit HREE enrichment (La_{SN}/Yb_{SN} = 0.372; Gd_{SN}/Yb_{SN} = 0.581) with nearly flat LREE portions of the pattern (La_{SN}/Sm_{SN} = 1.04). The Nd/Sm ratio for modern seawater shows no considerable enrichment over that of shale from the Sengoma Argillite Formation (Nd_{SN}/Sm_{SN} = 0.991). The other distinguishing geochemical characteristics of modern seawater are the presence of negative yet variable Ce-anomalies and slightly positive Eu-anomalies (Ce/Ce* = 0.154; Eu/Eu* = 1.07). The key interelement ratios of the calculated World Ocean are within the variations of both BIF and MnF samples with the exception of Ce-anomalies.

Shale normalized Ce-anomalies for modern seawater are negative for each ocean basin however the magnitude of the anomaly varies significantly from the Atlantic Ocean (Ce/Ce* = 0.404) to the Pacific Ocean (Ce/Ce* = 0.0834). A comparison of modern

seawater samples has shown that this difference may reflect the time-integrated redox conditions of the water mass (German and Elderfield, 1990a). The same study revealed two other criteria that must be met before interpreting the Ce-anomaly with any confidence. The first of these criteria is the Ce anomaly of the mineral phases must be related to that of the seawater in a predictable manner. Second, diagenetic alteration of the Ce anomaly must be assessed with interpretation of those samples showing any alteration rendered inappropriate.

These criteria must first be considered for the Hotazel Formation before the Ce-anomaly data can be interpreted as an indicator of paleoredox conditions. The second criterion can be addressed more simply than the first because the alteration of the samples can be evaluated through REE distributions. The lack of observed dispersion in the REE patterns of the Hotazel Formation indicates that these samples have not experienced metamorphic conditions associated with REE redistribution. Mineralogical evidence shows that the chemical sedimentary rocks of the Hotazel Formation found in Mamatwan Mine are primarily comprised of braunite ($Mn^{2+}Mn^{3+}_6SiO_{12}$), hausmannite ($Mn^{2+}Mn^{3+}_2O_4$), kutnahorite ($Ca(Mn,Mg,Fe)(CO_3)_2$), rhodochrosite ($MnCO_3$), hematite (Fe_2O_3) and calcite ($CaCO_3$) with minor amounts of jacobsite ($MnFe^{3+}_2O_4$). Diagenetic to very low grade metamorphic conditions are responsible for this Mn ore mineral assemblage (Nel et al., 1986).

In order to assess the first criterion, the partitioning coefficient of the minerals present in the samples must be calculated or experimentally determined. A first-order consideration suggests that Ce^{4+} is incompatible in the structures of the common minerals due to a charge imbalance and the large ionic radius for this cation compared to that of

Mn, Ca, Fe, and Mg in octahedral coordination. The trivalent REE are largely incompatible in all of the minerals under consideration but this is not due to charge imbalance but rather the large ionic radii (0.1032 to 0.0861 nm) relative to those of Mn and Fe (IR = 0.058 and 0.055 nm, respectively). Lastly we consider the compatibility of Eu^{2+} in these mineral structures, although Eu-anomalies in sedimentary rocks are not generally considered to be indicative of surficial weathering conditions but rather are inherited from precursors or the temperature of hydrothermal sources (Gao and Wedepohl, 1995; Taylor and McLennan, 1985). Divalent Eu and Ca should exhibit some compatibility due to similarities in ionic charge and coordination number. Despite these chemical similarities, the large relative difference in ionic radii (17%) and the overall depletion of Eu in seawater renders the contribution of this substitution insignificant. It would therefore be expected that the mineral assemblage found in the Hotazel Formation would have a flat seawater normalized pattern, indicative of the lack of preferential partitioning of the REE into these minerals.

5.4 Conclusions

The need exists for an increased number of high precision geochemical standards against which samples can be normalized. The currently used geochemical standards are too often inappropriate to use as they represent materials that have neither temporal nor spatial relationship to the studied materials. The utility of high precision REE data obtained by IDMS has been demonstrated as analyses performed by other techniques would not be able to resolve the intricate details of REE patterns or might produce false

associations. Therefore it was necessary to use the high precision REE data for shales from the Pretoria Group for normalization.

Evaluation of shale-normalized REE interelement ratios and patterns reveal the distinction between samples of BIF and MnF from the Hotazel Formation. By treating the samples of the Hotazel Formation as two separate groups based on their major element geochemistry, the relative range of each key interelement ratio decreases indicating that these two groups are geochemically distinct. The variations within the sample-normalized REE patterns of BIF samples can be modeled as being the result of an addition of 10% shale to a component that mimics seawater (e.g. chemical precipitate). The differences in absolute concentrations between the most REE depleted and enriched samples can be modeled dilution by quartz. The minor differences observed in sample-normalized REE patterns of the MnF samples are too inconsistent to model properly.

Additionally, shale-normalized REE patterns display a remarkable similarity between the REE patterns of the chemical sedimentary rocks of the Hotazel Formation and those of modern seawater. This similarity is supported by significant correlations between shale-normalized interelement ratios of modern seawater and the chemically precipitated sedimentary rocks of the Hotazel Formation. This is interpreted as the preservation of 2.22 Ga seawater chemistry within the chemically precipitated rocks of the Hotazel Formation. The only interelement ratio that differs significantly between modern and Paleoproterozoic seawater is the Ce-anomaly. This serves as a record of a significant change in the redox chemistry of Ce between 2.22 Ga and the present, due to subsequent rises in atmospheric oxygen concentrations after 2.22 Ga.

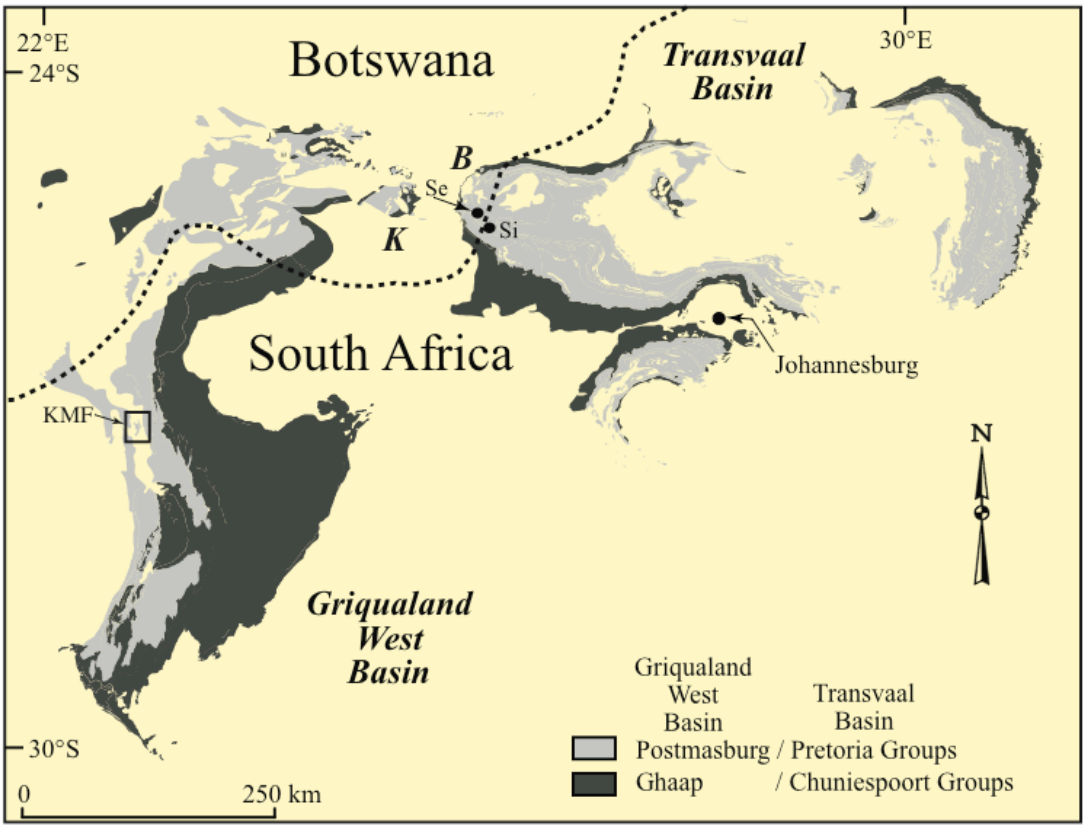

Figure 5.1 Map showing the distribution of early Paleoproterozoic sedimentary successions in the Transvaal and Griqualand West structural basins. The rock units found in both structural basins were deposited in the same depositional basin before structural deformation. Note the location of the Kalahari Manganese Field (KMF) with respect to the rocks discussed from the Transvaal Basin. Chuniespoort (dark grey) and Pretoria (light grey) groups in the Transvaal structural basin and Ghaap (dark grey) and Postmasburg (light grey) groups in the Griqualand West structural basin of South Africa taken from the digital 1:1,000,000 geology maps of South Africa and Botswana with the additional information from the digital 1:2,500,000 map of sub-Kalahari formations. Similar color patterns are also used to label the correlative units in the Bushveld (B) and Kanye (K) structural basins, Botswana. (Modified from Bekker et al., 2008)

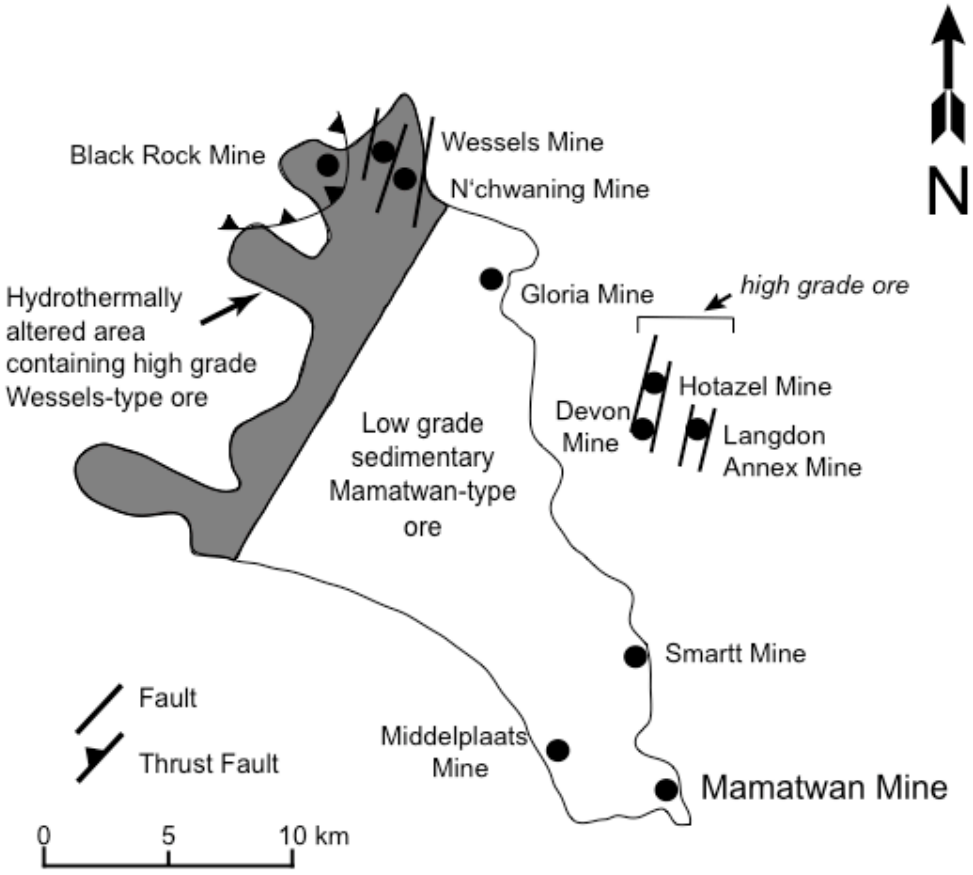

Figure 5.2 A generalized map of the Kalahari Manganese Field. Hotazel Formation manganese and iron formation samples used in this study were collected from drillcore G644 drilled in the Mamatwan Mine.

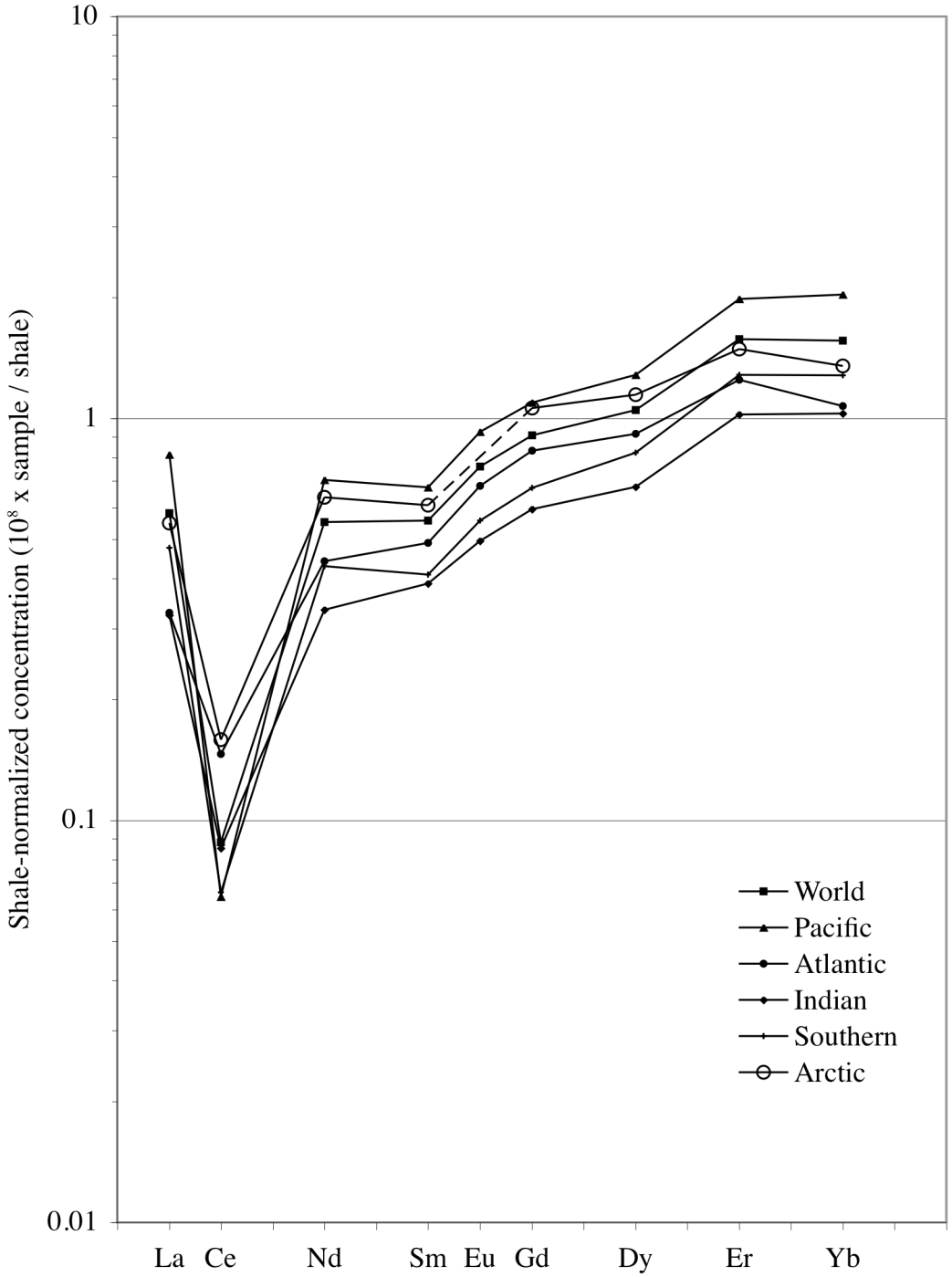

Figure 5.3 Shale-normalized REE patterns of averaged concentration data from all modern oceans. Note that there is no data for Eu concentrations in the Arctic Ocean, as concentrations were below detection limits in this study (Westerlund and Öhman, 1992). Data determined by IDMS were used when available (solid symbols). When IDMS data was not available, data with the lowest errors was used (hollow symbols). The patterns are very similar to one another rendering a weighted average of all samples to represent the "World Ocean".

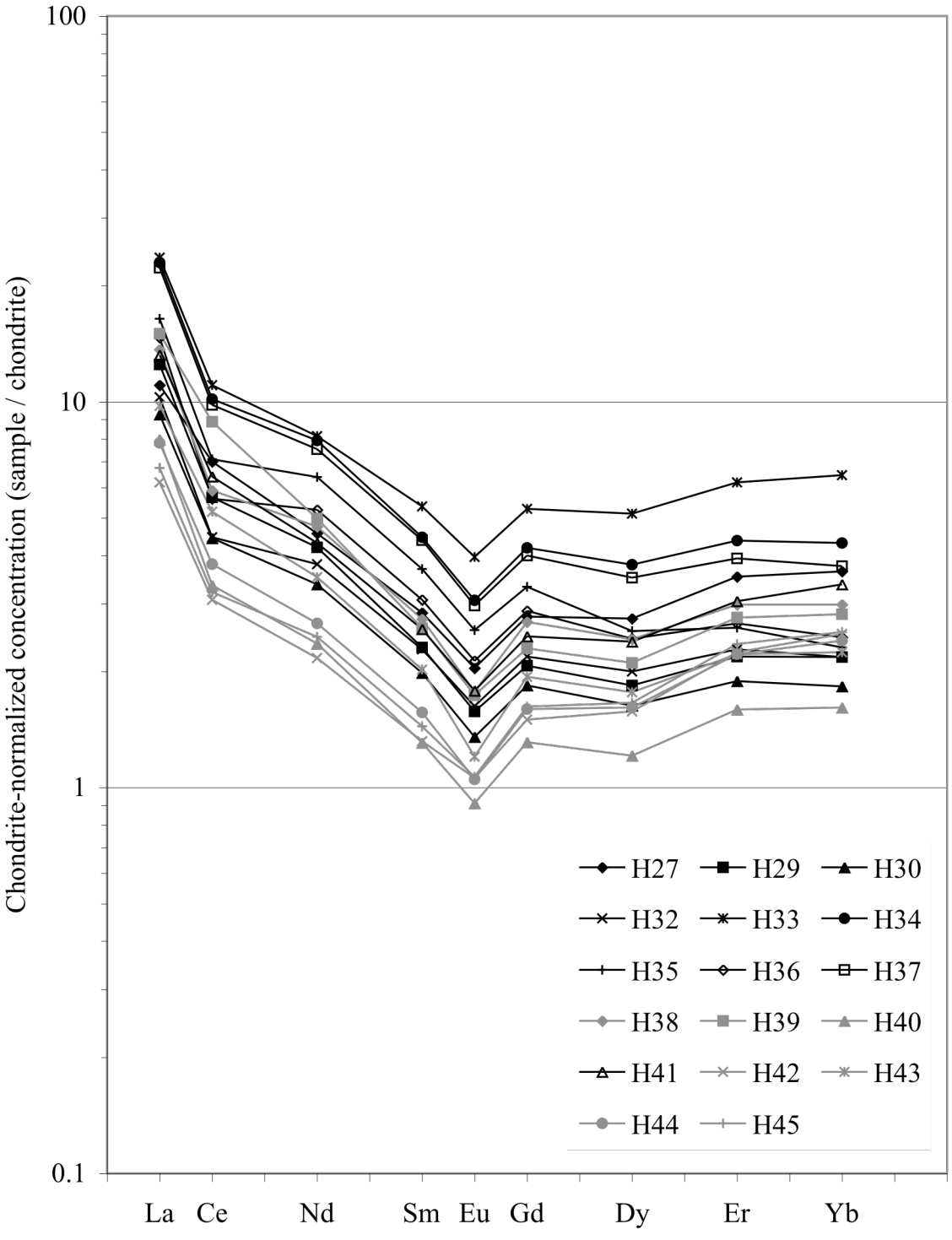

Figure 5.4 Chondrite-normalized REE patterns for all samples of the Hotazel Formation. These patterns were determined by HR-ICP-IDMS (high resolution inductively coupled plasma isotope dilution mass spectrometry), rendering the total analytical errors of each data point smaller than the symbol. The patterns of BIF samples (black symbols) show slightly higher REE concentrations compared to the MnF samples (grey symbols).

a)

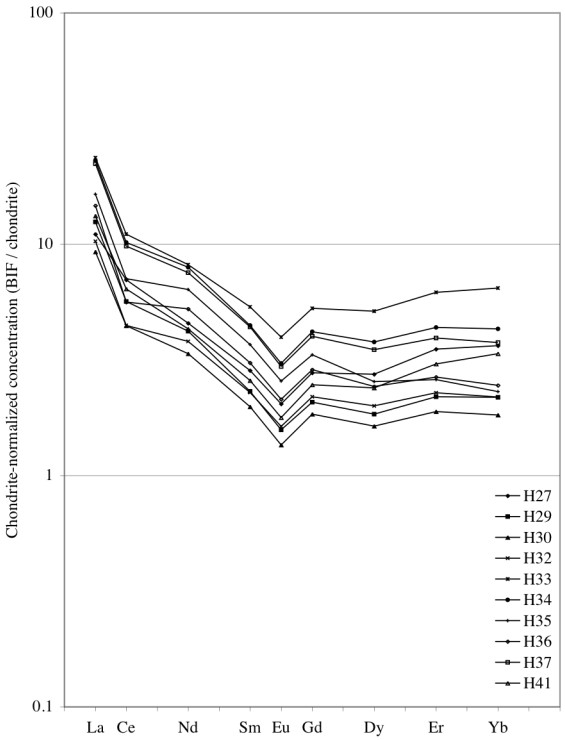

b)

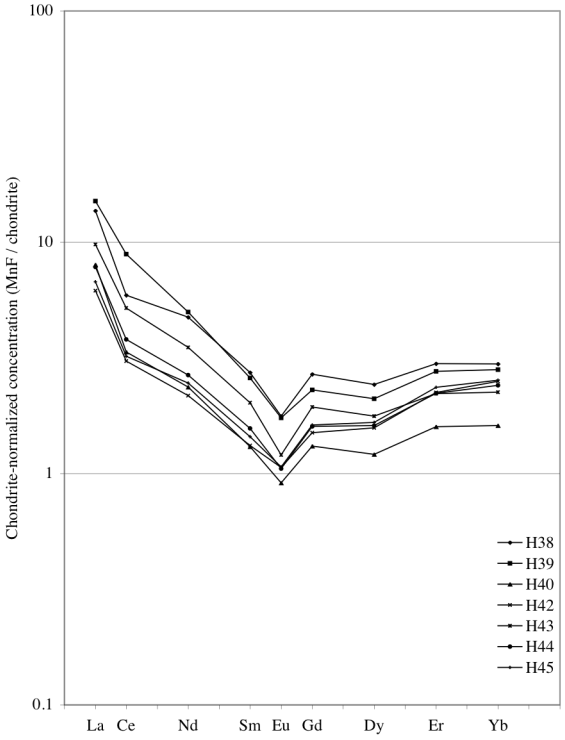

Figure 5.5 Chondrite-normalized REE patterns of the (a) BIF and (b) MnF samples of the Hotazel Formation. The BIF sample patterns have slightly higher REE concentrations and noticeably deeper Ce-anomalies when compared to the MnF patterns.

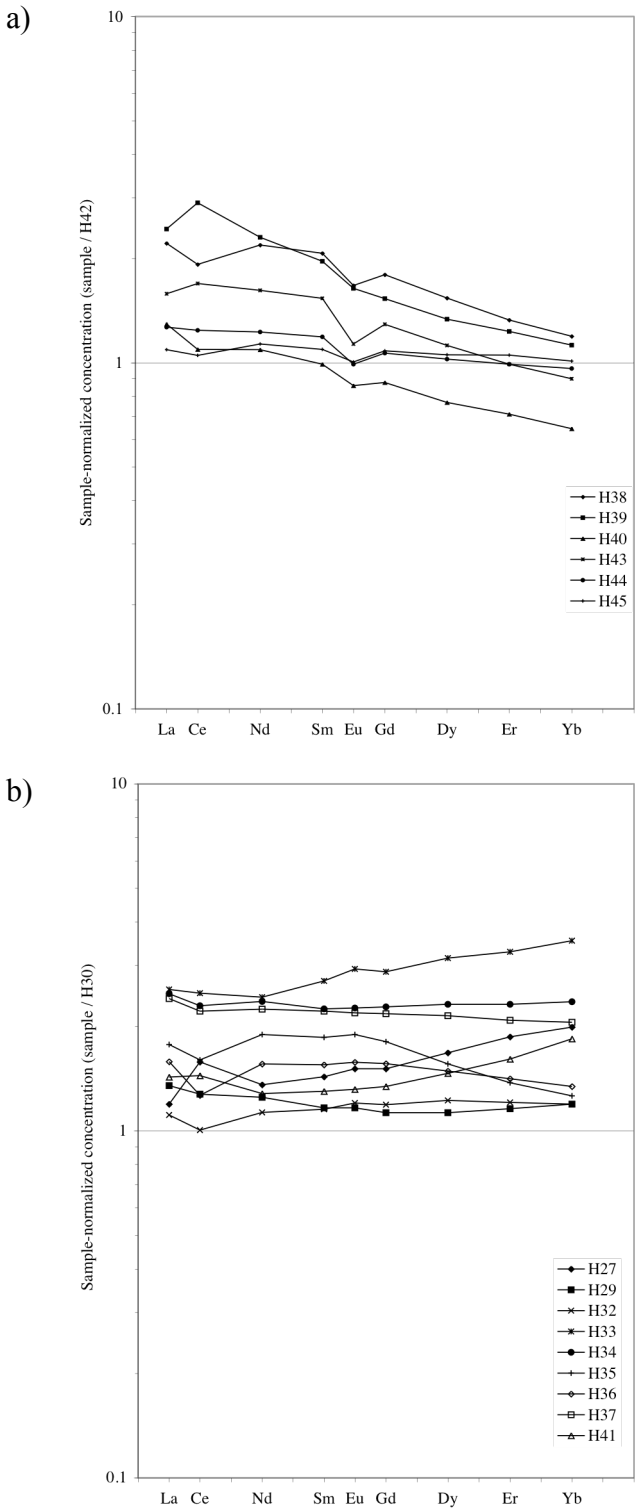

Figure 5.6 Sample-normalized REE patterns of the chemical sedimentary rock samples of the Hotazel Formation. (a) H42-normalized REE patterns of the BIF samples are similar to one another indicating that REE modeling can resolve the minor differences observed. (b) H30-normalized REE patterns of the MnF samples do not share a common morphology indicating that multiple different processes are responsible for these patterns.

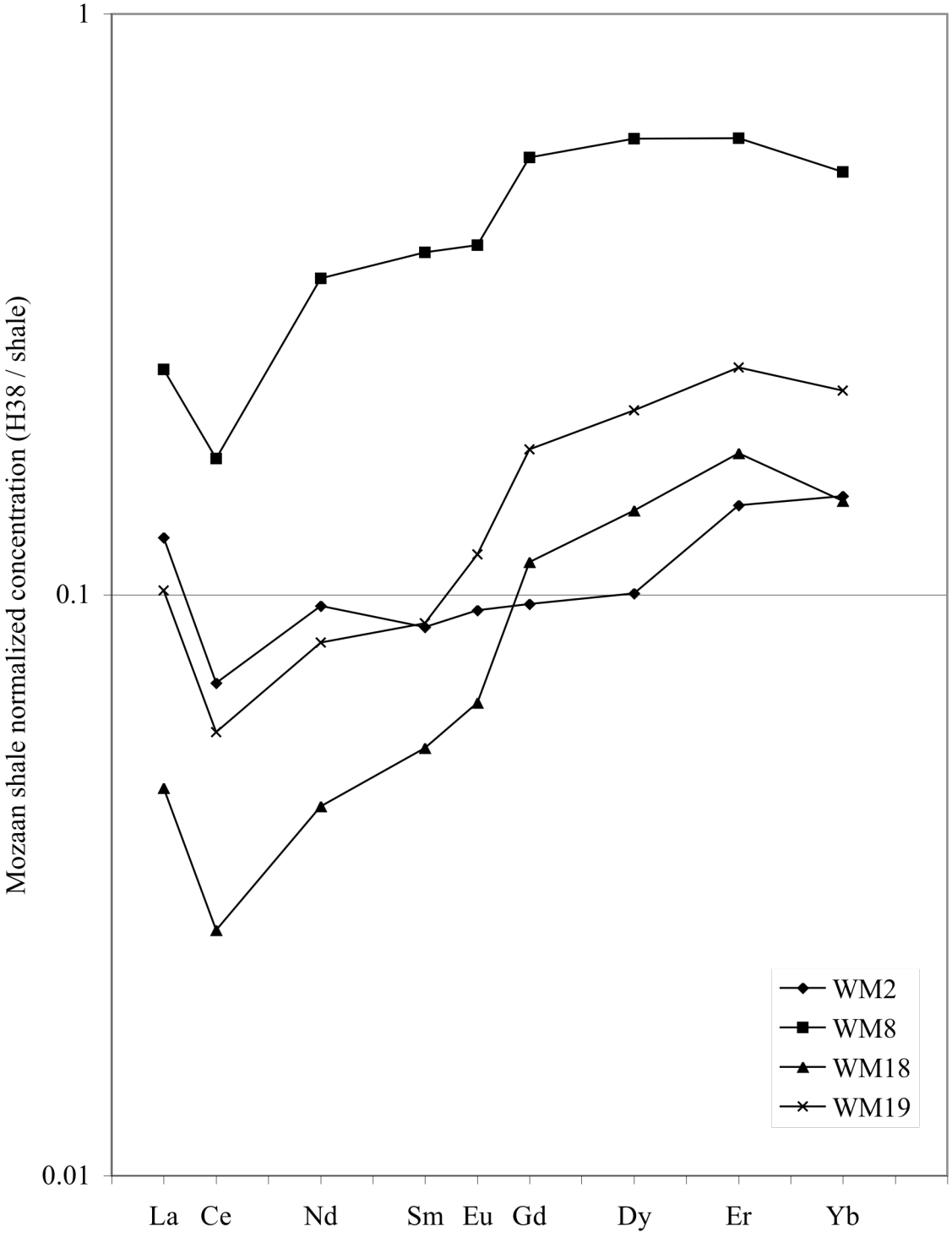

Figure 5.7 Mozaan Group shale-normalized REE patterns of H38. Four shales of the ca. 2.9 Ga Mozaan Group of eastern South Africa were used for normalization. In general these patterns are highly variable displaying HREE enrichment and Ce-anomalies but fine structures due to LREE fractionation and Eu-anomalies are inconsistent. Compare these shale-normalized REE patterns to those normalized to shales from the Sengoma Argillite Formation.

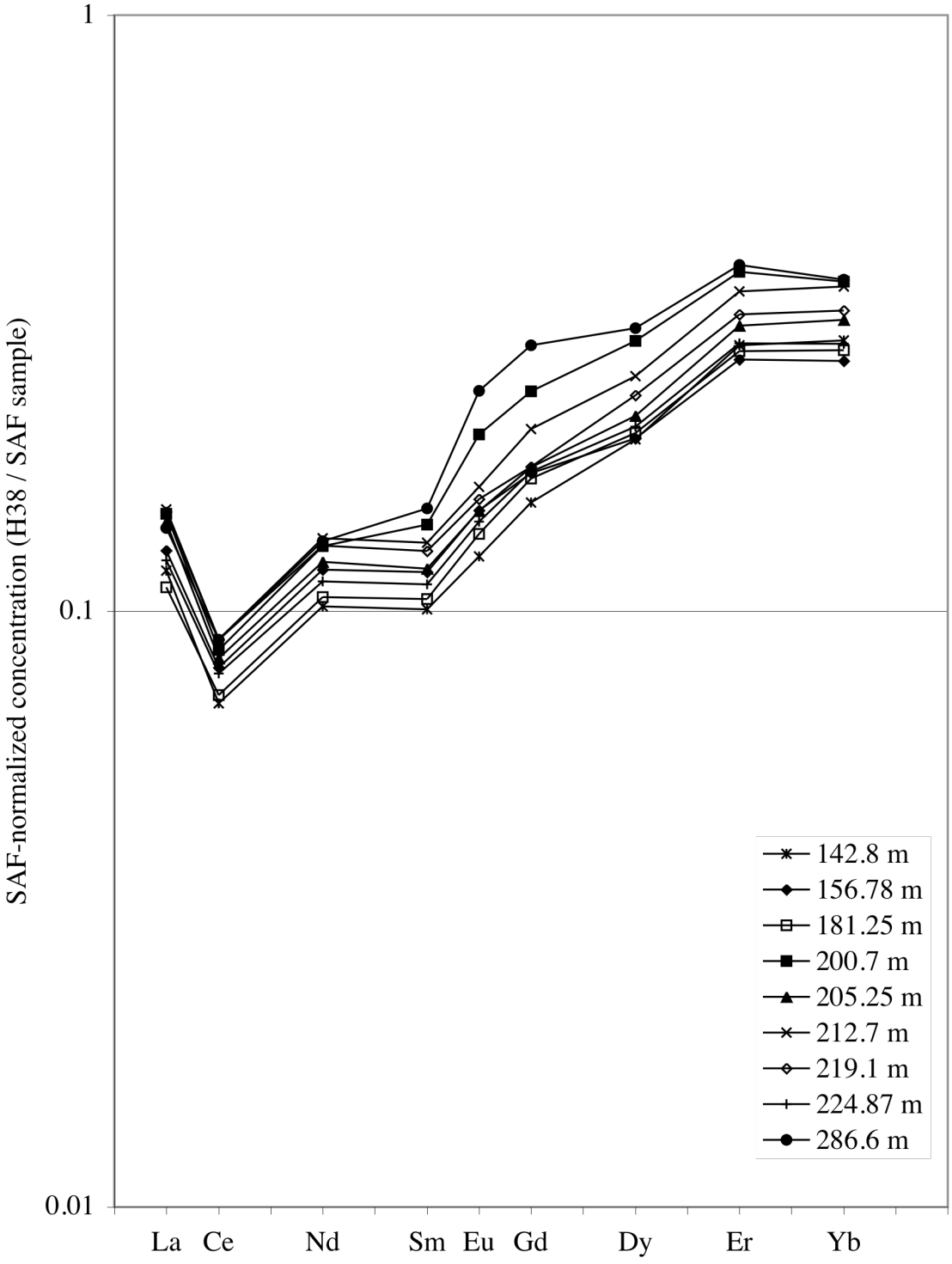

Figure 5.8 Sengoma Argillite Formation shale-normalized REE patterns of sample H38. These consistent REE patterns display HREE enrichment and Ce-anomalies like those in Figure 5.7, however are far more consistent. The consistency of La_N/Sm_N, Nd_N/Sm_N, and Eu-anomalies is attributable to the low degree of error on individual REE concentrations and covariation of REE concentrations.

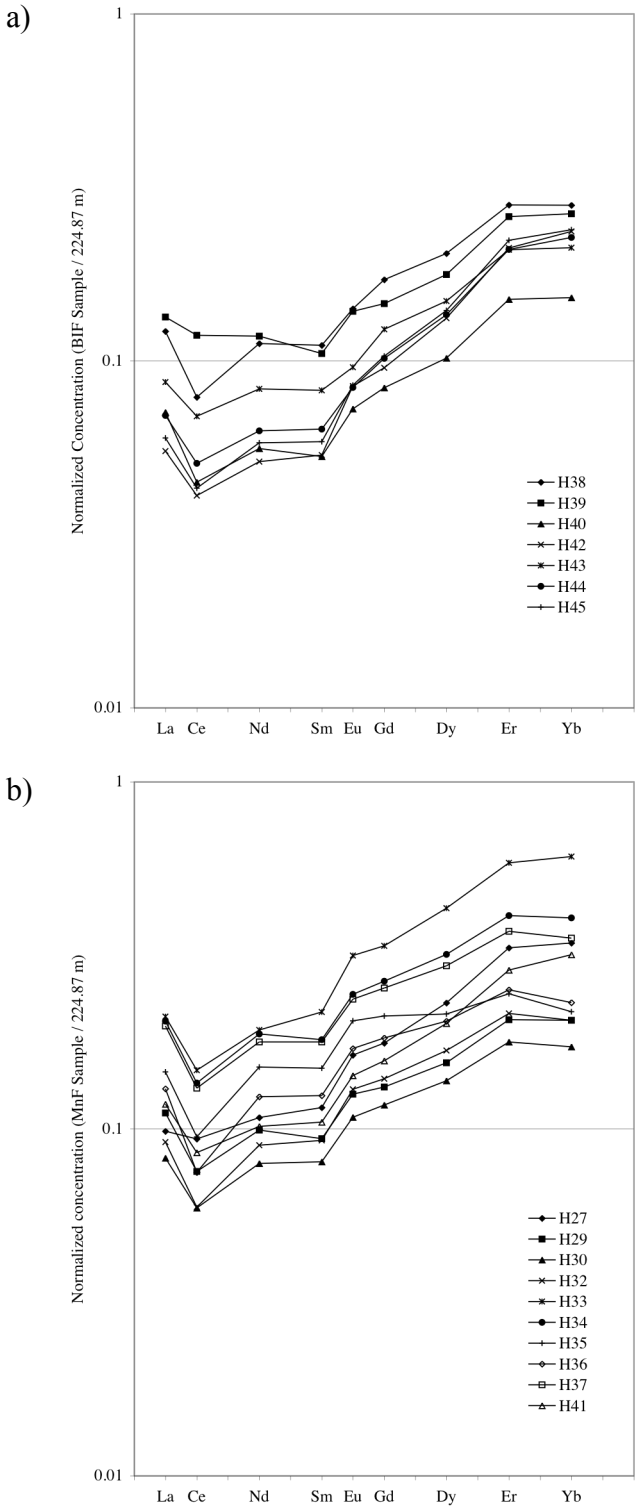

Figure 5.9 Shale-normalized REE patterns of (a) BIF and (b) MnF samples of the Hotazel Formation. These patterns show enrichment of the HREE over that of stratigraphically bracketing shale samples. The overall patterns are similar to modern seawater and may represent the chemistry of the Paleoproterozoic Ocean.

Table 5.1 Descriptions of BIF and manganese-rich samples of the Hotazel Formation

Sample #	Depth (m)	Sample Description
H27	155.4	Lower Mn Body; Section L; center of length of section
H29	152.6	Lower Mn Body; Middle of Section B
H30	149.25	Lower Mn Body; N Layer
H32	146	Center of Lower Mn Body; Middle of C Layer
H33	140.9	Lower Mn Body; Middle of M layer
H34	137.9	Lower Mn body; Top of Z layer
H35	128.7	Lower Mn body; Middle of Y layer
H36	120.7	Lower Mn body; Middle of X layer
H37	111.9	Very top of the lower Mn ore body; Top of V layer
H38	110.3	Above lower Mn body; BIF/Lutite
H39	99.8	Above lower Mn body; greenalite layer
H40	97.9	Above lower Mn body; BIF/greenalite
H41	83.4	Bottom of upper Mn body
H42	63.2	BIF
H43	63.3	BIF
H44	56.9	BIF with stromatolite-like texture
H45	58.4	BIF with stromatolitic layering

Sections/Layers originally defined by Nel et al., 1986.

Table 5.2 REE concentrations (in ppq) for modern seawater from each ocean basin determined by IDMS and a composite 'World Ocean'

	Pacific[1]	Atlantic[2]	Indian[3]	Arctic[4]	Southern[5]	World Ocean
La	0.287	0.116	0.115	0.194	0.169	0.206
Ce	0.0393	0.0892	0.0520	0.0968	0.0404	0.0537
Nd	0.178	0.112	0.085	0.161	0.109	0.140
Sm	0.0319	0.0232	0.0184	0.0288	0.0193	0.0264
Eu	0.00838	0.00615	0.00449	n/a	0.00504	0.00687
Gd	0.0446	0.0338	0.0242	0.0432	0.0273	0.0369
Dy	0.0496	0.0353	0.0261	0.0442	0.0317	0.0405
Er	0.0448	0.0282	0.0231	0.0336	0.0290	0.0356
Yb	0.0449	0.0237	0.0227	0.0298	0.0282	0.0345
∑REE	0.729	0.468	0.370	0.632	0.459	0.580

[1] data from Piepgras and Jacobsen (1992)

[2] data from Sholkovitz and Schneider (1991)

[3] data from German and Elderfield (1990)

[4] IDMS unavailable for the Arctic Ocean, ICP-MS data from (Westerlund and Öhman, 1992)

[5] data from German et al. (1995)

Table 5.3 REE concentrations for BIF and manganese-rich samples of the Hotazel Formation

	H27	H29	H30	H32	H33	H34	H35[a]	H35-1	H35-2	H35-3	H36	H37[a]	H37-1	H37-2
La	3.48	3.94	2.92	3.24	7.45	7.24	5.17	5.02	n/a	5.32	4.62	7.01	n/a	7.01
Ce	5.70	4.60	3.61	3.62	8.99	8.26	5.77	5.10	6.32	5.89	4.56	7.98	7.51	8.45
Nd	2.72	2.51	2.01	2.27	4.87	4.74	3.81	3.61	3.87	3.93	3.13	4.50	4.40	4.59
Sm	0.545	0.444	0.381	0.439	1.03	0.855	0.707	0.689	0.736	0.698	0.590	0.842	0.823	0.861
Eu	0.147	0.114	0.098	0.118	0.286	0.221	0.185	0.181	0.190	0.184	0.154	0.214	0.210	0.218
Gd	0.719	0.537	0.476	0.567	1.37	1.08	0.860	0.837	0.867	0.875	0.743	1.03	1.01	1.06
Dy	0.891	0.599	0.531	0.649	1.67	1.23	0.827	0.809	0.842	0.831	0.789	1.138	1.120	1.16
Er	0.750	0.466	0.402	0.486	1.32	0.930	0.553	0.543	0.562	0.554	0.568	0.838	0.827	0.848
Yb	0.757	0.453	0.380	0.453	1.34	0.895	0.480	0.470	0.489	0.480	0.510	0.781	0.765	0.798
La_N/Sm_N	3.89	5.41	4.67	4.50	4.42	5.16	4.46	4.44	n/a	4.65	4.77	5.08	n/a	4.96
Gd_N/Yb_N	0.763	0.950	1.01	1.00	0.818	0.973	1.44	1.43	1.42	1.47	1.17	1.06	1.06	1.06
La_N/Yb_N	3.04	5.73	5.07	4.72	3.66	5.34	7.12	7.05	n/a	7.33	5.98	5.93	n/a	5.80
Ce/Ce*	0.851	0.651	0.671	0.604	0.667	0.630	0.593	0.544	n/a	0.587	0.540	0.633	n/a	0.665
Eu/Eu*	0.727	0.721	0.709	0.728	0.744	0.708	0.733	0.738	0.733	0.728	0.718	0.708	0.709	0.706

[a] Average of listed replicate analyses

n/a Not Analyzed

Table 5.3 cont.

	H38[a]	H38-1	H38-2	H39	H40	H41[a]	H41-1	H41-2	H42	H43	H44	H45
La	4.30	n/a	4.30	4.74	2.52	4.17	n/a	4.17	1.95	3.08	2.46	2.12
Ce	4.79	4.842	4.74	7.21	2.72	5.20	5.14	5.27	2.49	4.22	3.09	2.61
Nd	2.83	2.80	2.87	2.98	1.41	2.57	2.51	2.63	1.29	2.10	1.59	1.47
Sm	0.524	0.520	0.529	0.497	0.251	0.495	0.490	0.499	0.253	0.389	0.301	0.277
Eu	0.128	0.126	0.130	0.126	0.066	0.129	0.129	0.128	0.077	0.087	0.076	0.077
Gd	0.697	0.684	0.710	0.594	0.340	0.639	0.630	0.649	0.388	0.501	0.414	0.420
Dy	0.787	0.780	0.794	0.684	0.393	0.778	0.761	0.794	0.512	0.574	0.524	0.540
Er	0.635	0.623	0.647	0.588	0.339	0.647	0.633	0.661	0.478	0.472	0.473	0.502
Yb	0.620	0.609	0.631	0.585	0.336	0.700	0.685	0.715	0.520	0.467	0.500	0.526
La_N/Sm_N	5.00	n/a	4.96	5.81	6.11	5.14	n/a	5.09	4.68	4.82	4.99	4.68
Gd_N/Yb_N	0.903	0.902	0.903	0.816	0.814	0.733	0.738	0.729	0.599	0.862	0.664	0.641
La_N/Yb_N	4.59	n/a	4.51	5.35	4.95	3.93	n/a	3.85	2.47	4.35	3.25	2.66
Ce/Ce*	0.613	n/a	0.604	0.852	0.629	0.703	n/a	0.707	0.703	0.747	0.696	0.668
Eu/Eu*	0.653	0.653	0.654	0.713	0.695	0.707	0.716	0.697	0.754	0.607	0.664	0.698

[a] Average of listed replicate analyses

n/a Not Analyzed

6. THE CA. 2.15 GA SENGOMA ARGILLITE FORMATION, BUSHVELD BASIN, BOTSWANA

6.1 Regional Geology and Stratigraphy of the Sengoma Argillite Formation

In this study we examine the Pb isotope compositions and REE concentrations of organic-rich shales from the ca. 2.15 Ga Sengoma Argillite Formation of the Paleoproterozoic Segwagwa Group of Botswana (Figures 6.1 and 6.2), sandwiched between carbonates with highly positive carbon isotope values corresponding to the 2.22-2.1 Ga Lomagundi carbon isotope excursion in seawater composition (Bekker et al., 2008). The Sengoma Argillite Formation was deposited in the Bushveld structural basin and is correlative with the Silverton Formation of the Pretoria Group in the Transvaal structural basin of South Africa (Bekker et al., 2008; Key, 1983). Both structural basins were once parts of the same open-marine epicontinental depositional basin.

The age of the formation is bracketed by the underlying ca. 2.22 Ga Hekpoort Lava and the overlying or intruding 2.061 Ga Rooiberg Felsites and Bushveld Complex, respectively (Buick et al., 2001; Dorland, 2004; Walraven, 1997). Further indirect age constraints might be inferred from the ca. 2.14–2.12 Ga U–Pb ages of authigenic metamorphic monazite in metashales, metasiltstones, and quartzites of the Chuniespoort Group and the older Central Rand Group of the Witwatersrand Supergroup of South Africa likely reflecting recently recognized tectonic event in the Transvaal structural basin after deposition of the Silverton Formation (Rasmussen et al., 2007; Bekker et al., 2008). Combined these age constraints suggest that the Sengoma Argillite Formation was deposited during the 2.22–2.1 Ga Lomagundi carbon isotope excursion and most likely shortly before the 2.14–2.12 Ga tectonic event. We therefore assume a ca. 2.15 Ga age for deposition of the Sengoma Argillite Formation.

The deltaic to offshore marine Silverton Formation is sandwiched between shallow-marine tidally-influenced quartz sandstones of the Daspoort and Magaliesberg formations (Button, 1973b; Fig. 1). The lower contact with the Daspoort Formation is sharp whereas the upper contact with the Magaliesberg Formation is gradational. The formation is divided by a basalt unit into two thick units of shales and siltstones with minor chert and carbonate layers.

The samples for this study were collected from the drill core Strat2 drilled approximately 7 km southwest of Ramotswa, Botswana and are identified by their depth. In this area, the Sengoma Argillite Formation is between 500 and 700 meters thick. The drillcore Strat2, stored at the Geological Survey of Botswana, consists of two upward-shallowing cycles with organic-rich pyriferous shales in the lower part of the cycles deposited in a prodelta setting above wave base and hematite-rich sandstones at the top of the cycles deposited on a delta plain (Bekker et al., 2008). Veins with carbonates, quartz, migrated solidified pyrobitumen, and remobilized sulfides locally occur but were avoided in this study.

The Sengoma Argillite Formation experienced metamorphic conditions no greater than greenschist facies. Previous paleocurrent studies of sandstones in the underlying Daspoort and overlying Magaliesberg formations have concluded that the likely transport of sediments was to the south and southeast in our study area (Button, 1975; Eriksson and Reczko, 1995), however, the sediments were most likely derived from the Archean Kaapvaal craton (Wronkiewicz and Condie, 1990).

6.2. Results

6.2.1 Whole-rock Pb Isotope Ratios

Whole-rock Pb isotope ratio data are presented in Table 6.1. Pb isotope ratios for whole-rock samples and a model Pb isotope growth curve (Kramers and Tolstikhin, 1997) are shown on a $^{207}Pb/^{204}Pb$ vs. $^{206}Pb/^{204}Pb$ diagram (Figure 6.3). Using the Pb isotope composition of the Kramers and Tolstikhin model at 2.15 Ga, the samples have time-integrated $^{238}U/^{204}Pb$ ratios (μ) ranging from 11.2 to 21.9. The Pb isotopic compositions of the samples show a nearly linear positive correlation with a best-fit slope of 0.159 +0.027/-0.037, which corresponds to a growth age of 2448 +260/-450 Ma to present (MSWD = 3.9). This age cannot be considered an isochron age, as the samples plot with too much scatter to produce a true isochron characterized by MSWD < 1.5. The variability in Pb isotope composition may be the result of source heterogeneity and/or post-depositional open system behavior. The depositional age of the Sengoma Argillite Formation (ca. 2.15 Ga) falls within the range of uncertainty for the growth age, suggesting that uranogenic Pb isotope growth started approximately at the time of sedimentation or shortly thereafter.

Thorogenic Pb isotope compositions plot as a moderately clustered field with $^{206}Pb/^{204}Pb$ variation exceeding that observed in $^{208}Pb/^{204}Pb$ ratios on a $^{208}Pb/^{204}Pb$ vs. $^{206}Pb/^{204}Pb$ plot (Figure 6.4). This trend shows that there are significant differences in the second-stage U/Pb ratios of these samples, as well as subtle differences in the second-stage Th/Pb ratios. Using the 2150 Ma age and the corresponding model initial Pb isotope composition, calculated κ_a values range from 3.67 to 1.77 with an average value

of 2.63 (±1.23; 2σ)[1]. Unfortunately the initial Pb isotope compositions for the provenance of the Sengoma Argillite Formation could not be independently defined since the studied shale samples are fine-grained, making feldspar separation and identification from the whole-rock samples impossible. Because Th is considered conservative during sedimentary and post-depositional processes, these κ_a values correspond to a potential addition of 55 ± 38% (1σ) excess uranium relative to that expected for the average upper crustal Th/U ratio of 3.86 predicted by the Kramers and Tolstikhin model (1997) and well below the average Th/U ratio for post-Archean Australian shale samples (4.71) from Taylor and McLennan (1985). Consequently, in order to eliminate the possibility that variations in the Th/U ratio are attributable to different mixing ratios of materials from multiple sedimentary sources, careful analysis of REE patterns is necessary.

6.2.2 Leach step Pb isotope compositions

Samples from 142.8 m and 200.7 m depths were selected for step-wise acid leaching (Table 2; Figures 6.5 and 6.6). The step-wise acid leaching of the more radiogenic sample from 200.7 m depth and whole-rock Pb isotope composition of this sample display a linear array with a slope of 0.136 (± 0.035) corresponding to Pb isotope growth from 2180 ± 450 Ma to present on a $^{207}Pb/^{204}Pb$ vs. $^{206}Pb/^{204}Pb$ diagram (MSWD = 5.0; Figure 6.5a). The whole rock data and leach steps for the same sample define a

[1] In most cases, like those of the whole-rock analyses of the shales from the Sengoma Argillite Formation, the choice of model Pb isotope composition is not important for the calculation of κ_a values. For samples in this study the κ_a ranges from 3.67 to 1.77 with an average of 2.63 for the Kramers and Tolstikhin (1997) model. The κ range (3.50 to 1.89) and average (2.64) do not change appreciably when using a single stage model with μ_1=8 and κ_1=3.9, values that simulate bulk Earth chemistry. The present Pb isotope values for the whole Earth composition predicted by these two models are dramatically different; however the models predict similar values for the Paleoproterozoic Era.

linear array on a $^{208}Pb/^{204}Pb$ vs. $^{206}Pb/^{204}Pb$ diagram (Figure 6.5b) with κ_a values ranging from 1.30 to 1.99, calculated using model Pb initial ratios based on the Kramers and Tolstikhin model (1997).

The step-wise acid leaching of the sample from 142.8 m depth (Figure 6.6) resulted in reliable Pb isotope ratio data for the first three leach steps, however the residual step (concentrated HF and HNO_3) did not yield a sufficiently high concentration of Pb to obtain reliable Pb isotope ratio data. The leach steps (L1, L2, and L3) and whole-rock Pb isotope composition define a linear array with a slope of 0.133 ± 0.022 corresponding to Pb growth from 2136 ± 290 Ma to present on a $^{207}Pb/^{204}Pb$ vs. $^{206}Pb/^{204}Pb$ diagram (MSWD = 1.18; Figure 8a). On a $^{208}Pb/^{204}Pb$ vs. $^{206}Pb/^{204}Pb$ diagram (Figure 8b), the leach steps and whole rock Pb isotope composition define a linear array corresponding to κ_a values ranging from 4.32 to 5.28.

The field of Pb isotope compositions of the first three leach steps of the sample from 142.8 m depth fails to enclose the isotope composition of the whole rock, requiring an unanalyzed component being present within the residual material. This may be due to heterogeneity in the powder, with the leached aliquot having a slightly less radiogenic composition than the aliquot used for whole-rock analysis.

6.2.3 REE data

REE concentration data for the ten shale samples are presented in Table 6.3 and chondrite-normalized REE patterns for these samples are shown in Figure 6.7. The chondrite-normalized REE patterns are similar for all samples, displaying subparallel concave upward patterns with light REE (LREE) enrichment (La_N/Yb_N = 7.76 ± 1.50,

2σ), typical of shale. All but one sample display negative Eu-anomalies (Eu/Eu* = 0.627 +0.058/-0.029) while the sample from 173.67 m depth has no appreciable Eu-anomaly (Eu/Eu* = 0.980). All samples have slightly negative Ce-anomalies (Ce/Ce* = 0.959 ± 0.058, 2σ) and overall REE concentrations are generally lower than in PAAS (Nd concentrations in Sengoma shales are typically 40.5 times chondritic values whereas PAAS Nd concentrations are 54 times chondritic values). The difference between the most and the least REE-enriched samples can be easily explained by variable amounts of quartz (±15 %) diluting the overall concentration of REE. This is supported by consistently negative Eu anomalies and by interelement ratios that do not change significantly; La/Yb, Gd/Er, and Sm/Dy ratios vary from 5.5 to 8.3% relative to average ratio values.

6.3 Discussion

6.3.1 Implications from U-Th-REE data

Due to the similar geochemical behavior of Th and the REE and the similar set of minerals (e.g., apatite, zircon and monazite) that dominates both the REE and U-Th budgets in most rocks (Gromet and Silver, 1983; Hogan and Sinha, 1991; Stern and Hanson, 1991; Taylor and McLennan, 1985), comparison between interelement ratios of REE and Th/U (or κ_a) values allows for the evaluation of geochemical behavior of U and Th. Since La and Gd have similar geochemical behavior to Th, and Nd and Er are good proxies for U^{4+} as discussed above, the comparison of κ_a and La/Nd or Gd/Er ratios can be helpful to discriminate between redox processes and heterogeneity in composition of the source area. Plots of κ_a values versus La/Nd ratios (Figure 6.8) and Gd/Er ratios

(Figure 6.9) provide the means for the evaluation of provenance heterogeneity and redox conditions during deposition, which may be responsible for the decoupling of U from Th. The shale samples from the Sengoma Argillite Formation have La/Nd ratios that vary 7.76% (2σ) relative to the average La/Nd value (1.37) and Gd/Er ratios that vary 16.5% (2σ) relative to the average Gd/Er value (1.82). This differs significantly from the relatively high variability of κ_a ratios, which vary 46.0% (2σ) relative to the average κ_a value of 2.63 and show no relationship to either La/Nd or Gd/Er values.

The distribution of data points in Figures 6.8 and 6.9 suggest that the interelement ratios are not simply due to an admixture of U-Th-REE-enriched mineral phases. The La/Nd and κ_a values alone could be explained by the admixture of between 0.52% and 3.0% zircon to a source having a similar Th/U ratio to PAAS (4.71) but slightly greater LREE enrichment (La/Nd ≈ 1.4). Similarly, the Gd/Er and κ_a values alone could be related to the mixing of a source with a similar Th/U ratio to PAAS but slightly greater MREE enrichment (Gd/Er ≈ 1.8) with zircon in the same proportion. The geochemical characteristics of this PAAS-like source are similar to some evolved granites.

Although interelement ratios allow the admixture of zircon and crustal materials, Pb isotope compositions of sequential acid leach steps (Figure 6.6) suggest that the addition of zircon is not responsible for the low κ_a values observed. The zircon addition would require the Pb isotope composition of the leaching steps to become sequentially more enriched with uranogenic Pb (^{206}Pb and ^{207}Pb) and less enriched with thorogenic Pb (^{208}Pb) as more zircon is dissolved. The final leach step when the residue was attacked with a mixture of HF and HNO_3 acids should have the lowest κ_a value as its Pb composition would be expected to have a very high ^{206}Pb/^{204}Pb ratio with

correspondingly low $^{208}Pb/^{204}Pb$ ratio. This is not observed in the Pb isotope compositions of the sequential acid leach steps (Figures 6.5b and 6.6b). The lack of the isotopic signature of a high μ, low κ phase being dissolved during leaching renders the simple zircon admixture hypothesis unlikely.

Although binary mixing of shale and zircon is not likely, based on the Pb isotope data (Figures 6.7b and 6.8b), interelement ratios and Pb isotope compositions may result from trimodal mixing between the Archean mafic volcanics, Archean felsic rocks, and a source with low κ_a, La/Nd > 1.2, and Gd/Er > 1.4. The geochemical characteristics of this potential source are uncommon for crustal rocks, but are similar to those of rare, highly evolved granitic rocks, topaz rhyolites and granites (Christiansen et al., 1983; Hudson and Arth, 1983). Other remarkable features of REE patterns from these rare, high-F rocks include deep negative Eu anomalies (Eu/Eu* < 0.2) and flat REE patterns ($La_N/Yb_N < 3$). These are completely different from those of the REE patterns of the Sengoma Argillite Formation and, therefore, it is highly unlikely that a component similar to topaz rhyolites or granites existed in the provenance of these rocks.

The small range in REE interelement ratios of shales from the Sengoma Argillite Formation suggests that there was only one source for the sediments or that admixtures of multiple sources were well homogenized. Therefore it is very likely that the Th/U ratios of the samples were established by either a homogeneous single source or well mixed sources during deposition. In suites in which the REE patterns and REE interelement ratios are more variable, it is more likely that the range of Th/U ratios would reflect variable sources of detrital material.

6.3.2 Comparison to Archean and Paleoproterozoic record

A comparison with the REE concentrations and κ_a values in Archean sedimentary rocks, which were deposited before the rise in atmospheric oxygen, can be potentially useful to address the variability in La/Nd and Gd/Er ratios in shale samples from the Sengoma Argillite Formation. Pb isotope compositions and REE concentrations have been previously determined for the shales of the ca. 3.05 Ga Buhwa Greenstone Belt in Zimbabwe (Fedo et al., 1996; Krogstad et al., 2004). The authors concluded based on the Pb isotope compositions and REE concentrations that the lack in variability of the time-integrated Th/U ratios ($\kappa_a = 3.04 \pm 0.23$; 1σ) was due to reducing surface conditions during deposition. Additionally, "excess uranium" was not indicated by the κ_a value, as it is close to the Archean average upper crustal Th/U ratio.

Unfortunately, there are no other Archean or Paleoproterozoic datasets currently available in the literature that include both Pb isotope ratios and high precision REE concentration data. However, several other published studies reported Pb isotope compositions for Archean and Paleoproterozoic shales. Pb isotope ratio data for the ca. 3.8 Ga turbiditic shale from the Isua supracrustal belt, Greenland (Rosing and Frei, 2004) lie tightly arrayed about a line with a κ_a value of 3.17 ± 0.37 (1σ) on a $^{206}Pb/^{204}Pb$ – $^{208}Pb/^{204}Pb$ diagram, which is consistent with the data for shales from the ca. 3.05 Ga Buhwa greenstone belt (Figure 6.10). Two Paleoproterozoic pelitic suites are available that bracket the age of the Sengoma Argillite Formation. The shale suite from the older ca. 2.5-2.22 Ga Huronian Supergroup, Ontario, Canada that bracket the rise of atmospheric oxygen (Bekker and Kaufman, 2007) has a κ_a values of 2.59 ± 0.47 (1σ); whereas the shale samples from the younger ca. 1.8-1.7 Ga metasediments of

southwestern USA have κ_a values of 3.02 ± 1.45 (1σ) (McLennan et al., 1995; 2000). The variability of κ_a values increases with the decreasing age in these three Paleoproterozoic datasets in a marked contrast to Archean datasets that show low variability about the upper crustal κ_a value. The contrasting Archean and Paleoproterozoic Th/U ratios in pelitic samples were earlier related to the different compositions of the upper continental crust in the Archean and Paleoproterozoic (McLennan et al., 1995). Considering close temporal coincidence between the rise in atmospheric oxygen (e.g. Bekker et al., 2004) and the dramatic change in κ_a values of pelitic suites, it seems more likely that the later change reflects decoupling between U and Th in surface processes in response to initiation of oxidative continental weathering.

The rise of atmospheric oxygen led to dramatic changes in sedimentary environments related to oxidative continental weathering and redox cycling as evidenced by 1) the appearance of the first red beds, copper stratiform deposits, sedimentary manganese deposits with pronounced negative Ce anomaly, and oxidized paleosols; 2) a rise in seawater sulfate content; 3) an increase in the content of redox-sensitive elements in organic-rich shales; 4) the disappearance of uraninite-, siderite- and pyrite-containing placer deposits from the rock record; 5) an increase in ferric-to-ferrous ratio in shales; 6) the disappearance of non-mass dependent fractionation of S isotopes from the rock record (see Bekker and Kaufman, 2007 for discussion and references). The inferred redox-driven decoupling of Th and U is therefore consistent with other environmental proxies in Paleoproterozoic sedimentary environments and indicates that oxidative continental weathering was already intense during the GOE.

Although the timing for the rise of atmospheric oxygen is reasonably well established now, the tempo of this change remains debated. The views are divided between a) transient oxygenation events before the GOE (Anbar et al., 2007; Kaufman et al., 2007; Ono et al., 2006; Ohmoto et al., 2006); b) gradual rise of atmospheric oxygen through the Paleoproterozoic (e.g. Cloud, 1968; Murakami and Yokota, 2008; Wille et al., 2007); or c) stepwise, abrupt changes in the atmospheric redox state coupled to climatic changes (e.g. Bekker and Kaufman, 2007). Pb isotope composition of shales provides a new proxy for the atmospheric redox state that can be widely applied to Archean and Paleoproterozoic successions to test between these models. A survey of Pb isotope compositions combined with high precision REE analyses of Archean and Paleoproterozoic shales and chemical precipitates straddling the GOE might unravel the tempo of the rise in atmospheric oxygen and constrain the role of redox processes in the Archean surface environments before the oxygenation of the atmosphere.

6.4 Conclusions

The Pb isotope compositions of organic-rich shales from the ca. 2.15 Ga Sengoma Argillite Formation of Botswana were used to calculate time-integrated Th/U ratios (κ_a) and interpret the presence of uranium enrichment. The process responsible for uranium enrichment can then be further characterized through comparison to other geochemical proxies for Th-U behavior such as La/Nd and Gd/Er ratios and high precision REE patterns. In order to calculate the time-integrated Th/U ratios from the Pb isotope compositions, model initial Pb isotope compositions associated with the age of

sedimentation were used. Based on the Pb isotope systematics, the calculated low κ_a values were interpreted as being established during or shortly after sedimentation.

Variations in κ_a values do not occur among the ca. 3.05 Ga shales of the Buhwa Greenstone Belt, Zimbabwe (Krogstad et al., 2004). However, variable and low κ_a values are typical for the shales of the ca. 2.15 Ga Sengoma Argillite Formation, Botswana. These Th/U variations are not accompanied by concomitant variations in interelement ratios among the REE implying that either uranium was added to or thorium was removed from these rocks. The consistency of the chondrite-normalized REE patterns, make it also highly unlikely that multiple sources in the provenance were responsible for this apparent uranium enrichment. Comparison of La/Nd and Gd/Er ratios with κ_a values allows for the interpretation that small amounts (<3%) of zircon were added to a shale with PAAS-like geochemical characteristics, however Pb isotope composition of acid leach steps make this interpretation unlikely. Trimodal mixing involving the Archean mafic volcanics, Archean felsic rocks, and a source similar to rare, highly evolved rocks such as topaz rhyolites and granites would be required to explain the variation in κ_a values; however REE patterns make this hypothesis equally as unlikely. Based on these geochemical indicators, uranium enrichment in these shales is most likely the result of uranium liberation during oxidative weathering of the continental crust at ca. 2.15 Ga and subsequent adsorption onto authigenic mineral phases (e.g. Fe-oxides) and organic complexes in the ocean.

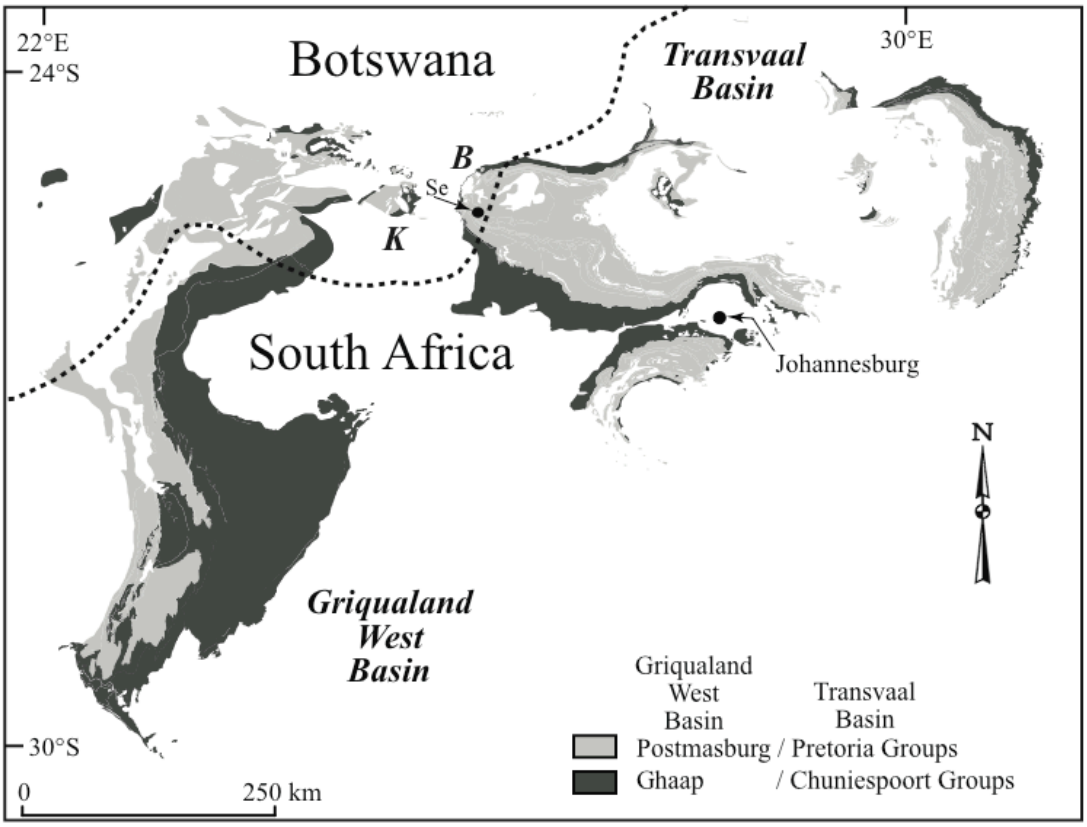

Figure 6.1 Schematic map of the late Archean and early Paleoproterozoic sedimentary successions of South Africa. Outcrop and sub-Kalahari sand distribution of the Chuniespoort (dark grey) and Pretoria (light grey) groups in the Transvaal structural basin and Ghaap (dark grey) and Postmasburg (light grey) groups in the Griqualand West structural basin of South Africa taken from the digital 1:1,000,000 geology maps of South Africa and Botswana with the additional information from the digital 1:2,500,000 map of sub-Kalahari formations (after Bekker et al., 2008). Similar color patterns are also used to label the correlative units in the Bushveld (B) and Kanye (K) structural basins, Botswana. All these structural basins used to belong to the same depositional basin. 'Se' points to the location of the drillcore Strat2 in Botswana from which black shales were sampled for this study.

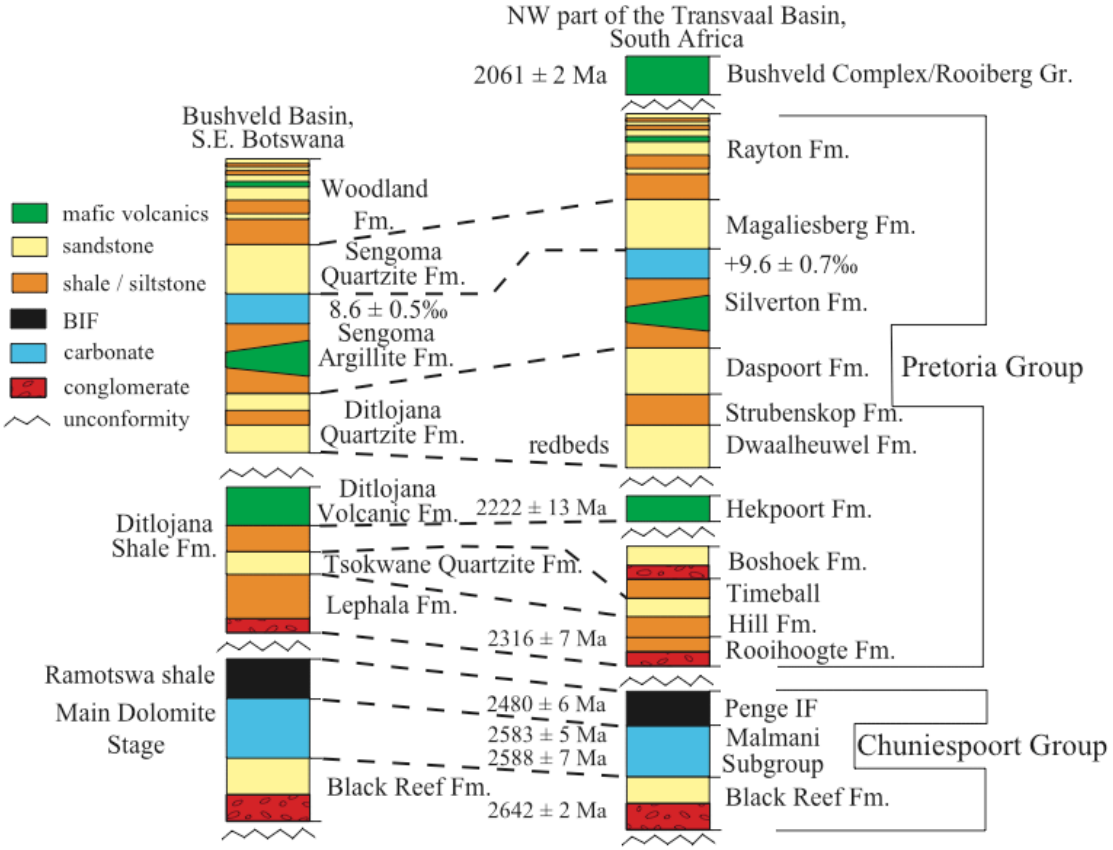

Figure 6.2 Stratigraphic comparison chart showing correlative units of the Transvaal Supergroup in the Bushveld and Transvaal basins. The locations of the Bushveld Basin and the can be found on Figure 6.1. Note that the age of the Hekpoort Formation is inferred based on the correlation with the Ongeluk Andesite of the Griqualand West basin and its whole rock Pb-Pb age (Bekker et al., 2008).

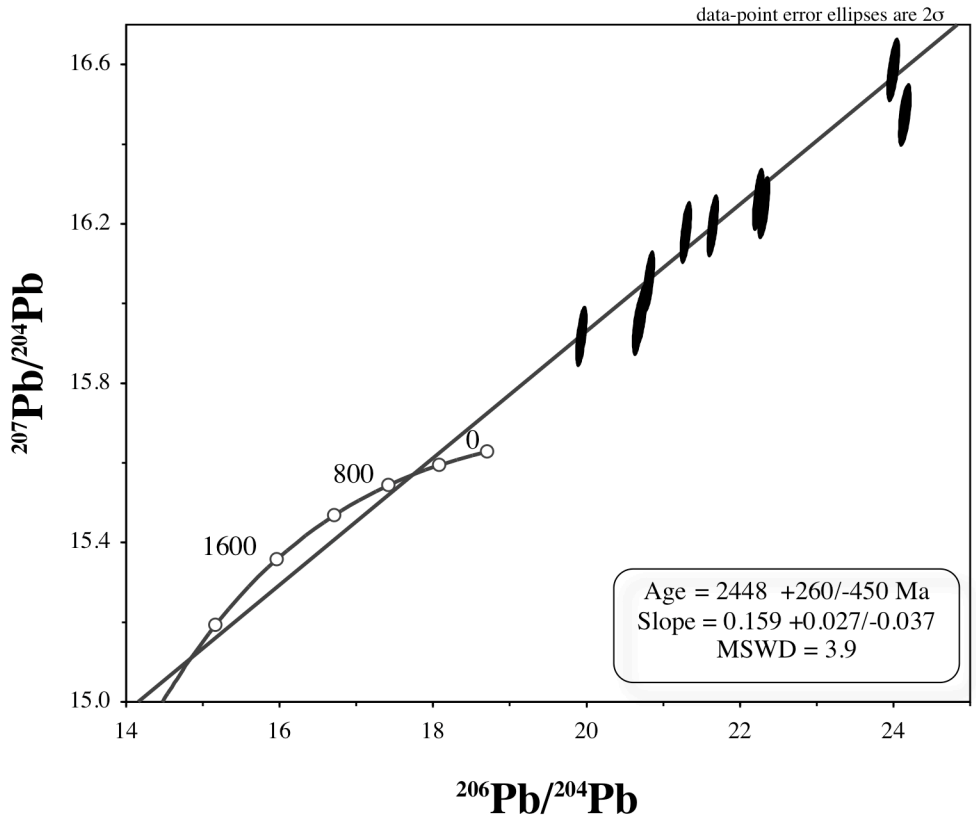

Figure 6.3 $^{206}Pb/^{204}Pb$ and $^{207}Pb/^{204}Pb$ isotope ratio diagram for whole rock shale samples of the Sengoma Argillite Formation. The Pb isotope growth curve shown is based on the Pb isotope growth model of Kramers and Tolstikhin (1997). Several ages for model values of the Pb isotope ratios are provided for reference. The slope of the array of the Sengoma Argillite Formation data points corresponds to an age of 2.45 Ga, although the depositional age was between 2.2 and 2.1 Ga. The near linear relationship of these points indicates that uranium was not likely mobilized after deposition.

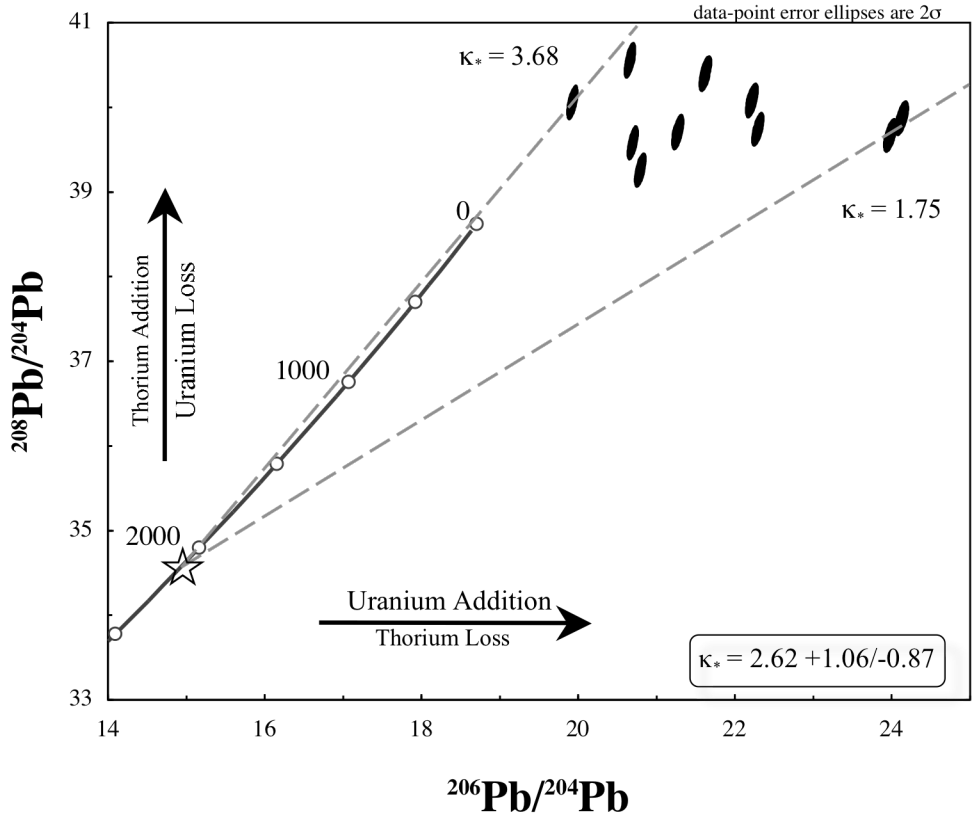

Figure 6.4 $^{206}Pb/^{204}Pb$ and $^{208}Pb/^{204}Pb$ isotope ratio diagram for whole rock shale samples of the Sengoma Argillite Formation. The diagram shows the relationship between thorogenic and uranogenic Pb isotopes. The Pb isotope ratio growth curve shown in this figure represents the Pb isotope growth model of Kramers and Tolstikhin (1997). Several ages are provided for reference for model Pb isotope values with the star representing the model Pb isotope value at 2100 Ma. The observed variability results from variable Th/U ratios present in the sediments at the time of deposition or shortly thereafter. This interpretation is based on the age for the slope of the Pb-Pb array in Figure 5, which suggests closed system behavior of the U/Pb system since 2448 +260/-450 Ma ago, therefore implying closed system behavior for the Th/Pb system since the same time. Arrows indicate the vectors for exclusively uranogenic (horizontal) and thorogenic (vertical) lead isotope evolution since divergence from the model source during deposition.

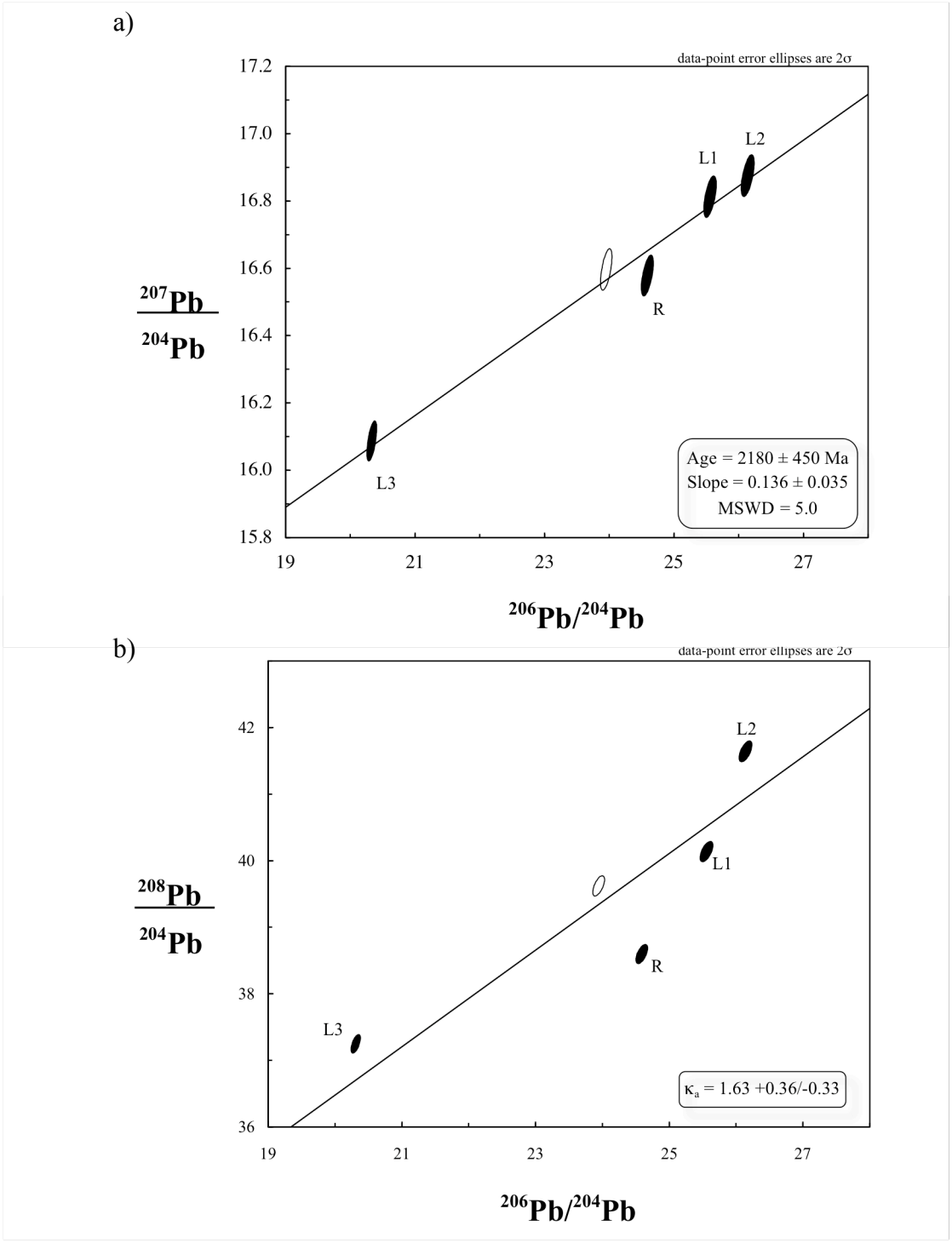

Figure 6.5 Pb isotope composition of the sequential acid leach steps for sample 200.7 m. The leaches and residue from this sample define a slope in Figure 7a that is nearly identical to the slope defined by the whole rock data. The calculated slope from the model initial Pb isotope ratios to each leach step in Figure 7b is characterized by slightly variable κ (Th/U) values, which is a function of the sites from which Pb was released by leaching. The Pb isotope ratios of the residual leach step (R) are not consistent with the derivation of radiogenic Pb from a low κ mineral phase (e.g. zircon), eliminating the possibility that the whole rock Pb isotope composition is controlled by zircon.

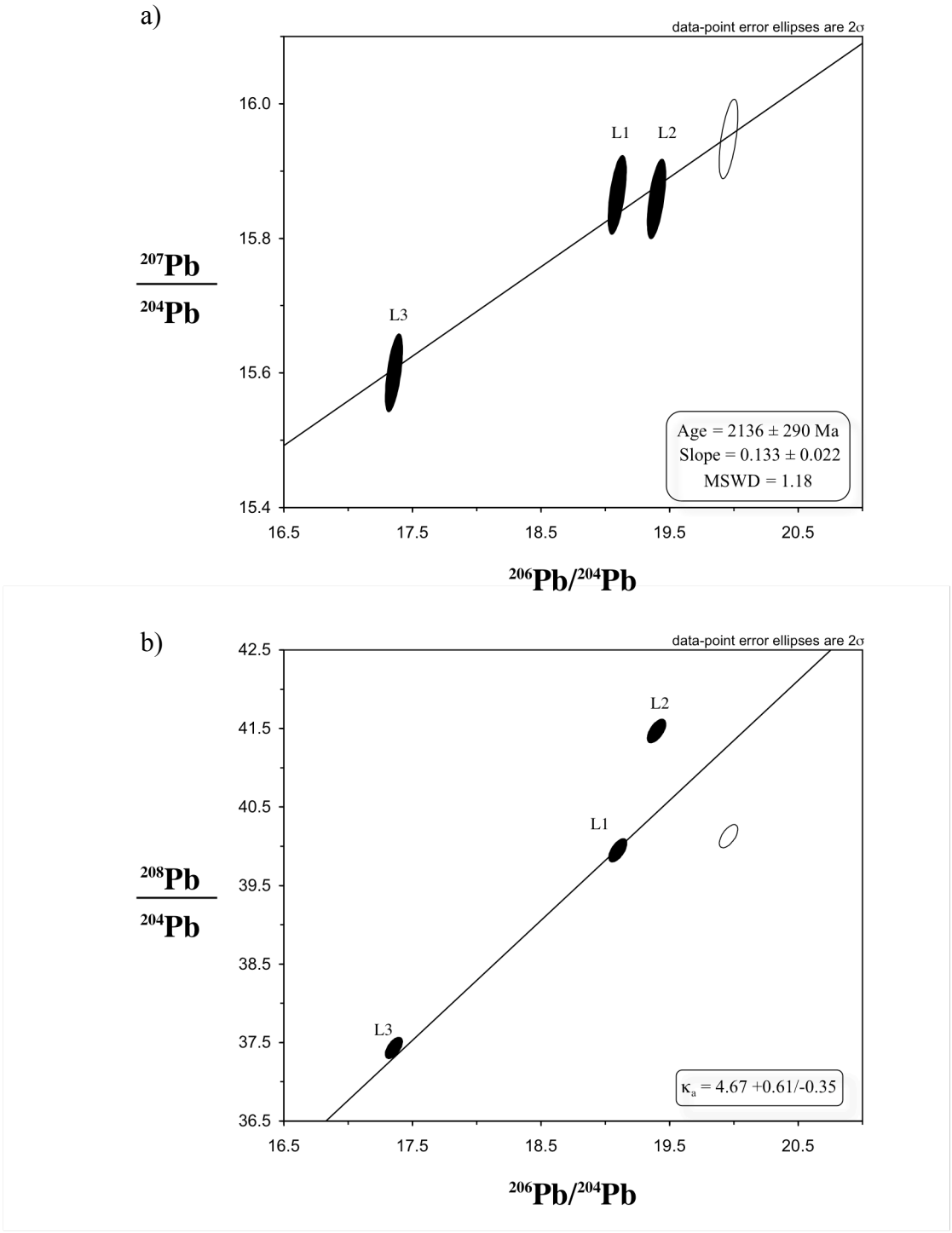

Figure 6.6 Pb isotope composition of the sequential acid leach steps for sample 142.8 m. The Pb isotope compositions of the leach steps do not delimit the Pb isotope composition of the whole rock, indicative of sample heterogeneity. The low Pb content in the residual leach step (R) is indicative of absence in the residue of minerals with high Pb contents. The slope of the array and the corresponding starting age of radiogenic Pb growth in Figure 8a indicate that the heterogeneity of the sample is not related to multiple stages of uranogenic Pb growth. Similarly, the calculated κ values for each leach step based on Figure 8b are distinct but all are consistently higher than that of the whole-rock.

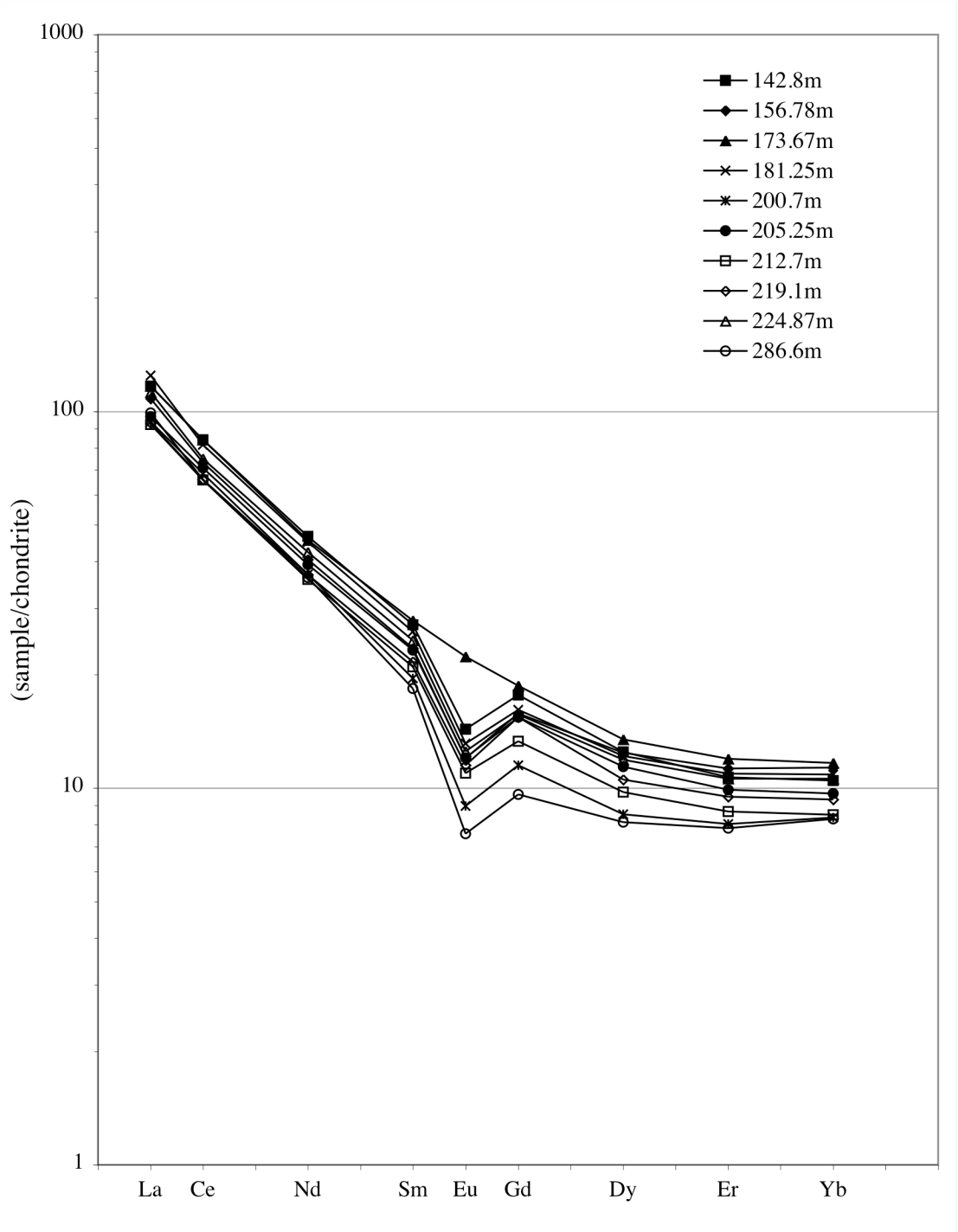

Figure 6.7 Chondrite-normalized REE patterns for shale samples of the Sengoma Argillite Formation. These patterns were determined by HR-ICP-IDMS (high resolution inductively coupled plasma isotope dilution mass spectrometry), rendering the total analytical errors of each data point smaller than the symbol. The patterns are very similar to one another indicating a common provenance for all samples. The only exception to similar REE patterns is the lack of a Eu-anomaly in sample 173.67 m, despite the overall pattern having the same morphology as the other samples. This may be the result of a minor contribution of feldspar above that observed in the other samples.

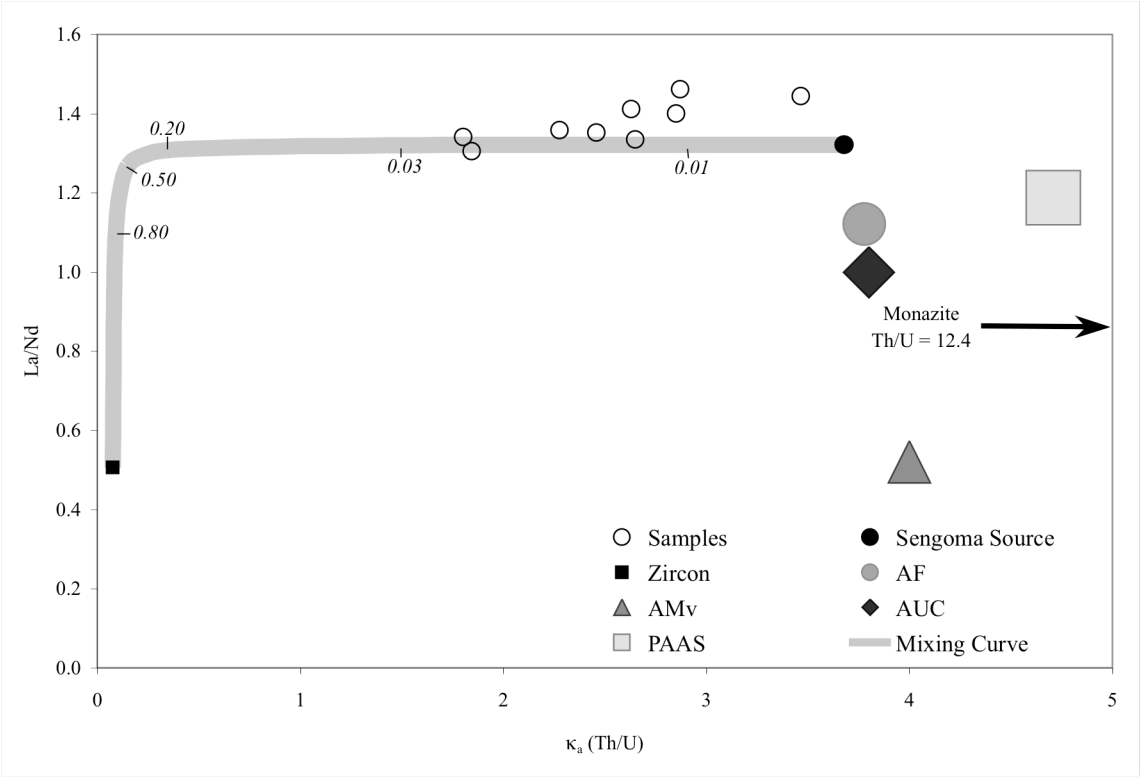

Figure 6.8 Plot of κ_a values and La/Nd ratios for shale samples of the Sengoma Argillite Formation. The Th/U ratios of several potential end members for sedimentary mixing are also plotted. Although some of the data support zircon addition as a mechanism of explaining the variable κ_a values, the Pb isotope ratios for the residue of sequential acid leaching (R in Figure 7b) do not support this interpretation. The simplest explanation for the Pb isotope values of the samples from the Sengoma Argillite Formation is the decoupling of U from Th during oxidative weathering (see text for further discussion). The samples of the Sengoma Argillite Formation are displayed as open circles whereas the end member compositions are labeled and shown as shaded symbols (AMv = Archean Mafic Volcanics, AF = Archean Felsic Rocks, AUC = Archean Upper Crust, PAAS = Post-Archean Australian Average Shale of Taylor and McLennan, 1985). Errors for the analyses of the samples of the Sengoma Argillite Formation are 1.0% for La/Nd ratios and 4.2% for κ_a values. Errors for the Th/U and La/Nd data from Taylor and McLennan (1985) are estimated at 5% for both ratios.

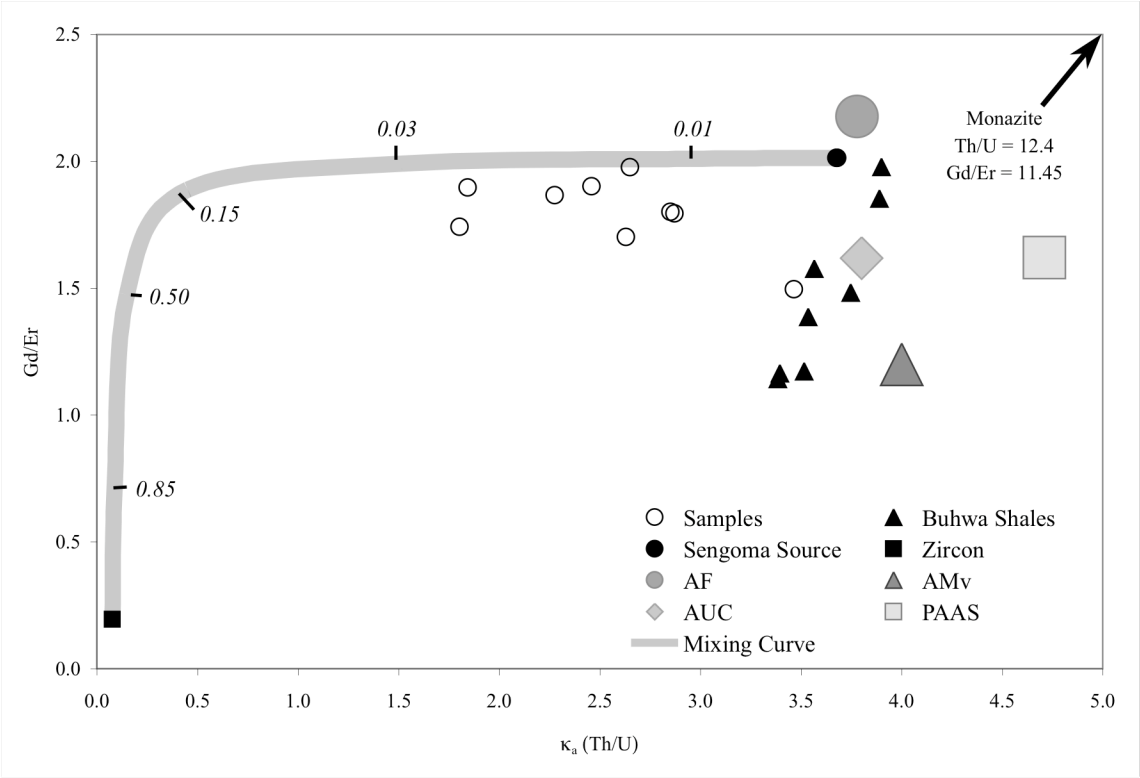

Figure 6.9. κ_a vs. Gd/Er ratio plot for shale samples of the Sengoma Argillite Formation. The relationship between Gd/Er ratios and κ_a values might reflect multiple detrital sources, post-depositional alteration, or decoupling of U from Th by redox processes. The variation in Gd/Er ratios for the Buhwa shales was explained by post-depositional processes altering REE concentrations and interelement ratios but not affecting κ_a values. In contrast, the REE geochemistry of shales from the Sengoma Argillite Formation does not support multiple detrital sources or post-depositional alteration as an underlying factor for variations in κ_a values. The most likely explanation therefore is that uranium was added to the sediments during deposition via redox processes resulting in "excess uranium". Errors for data points from the Sengoma Argillite Formation are 1.0% for Gd/Er ratios and 4.2% for κ_a values. Errors for the data from Taylor and McLennan (1985) are estimated at 5% for both Th/U and Gd/Er ratios. See Figure 6.8 for the legend.

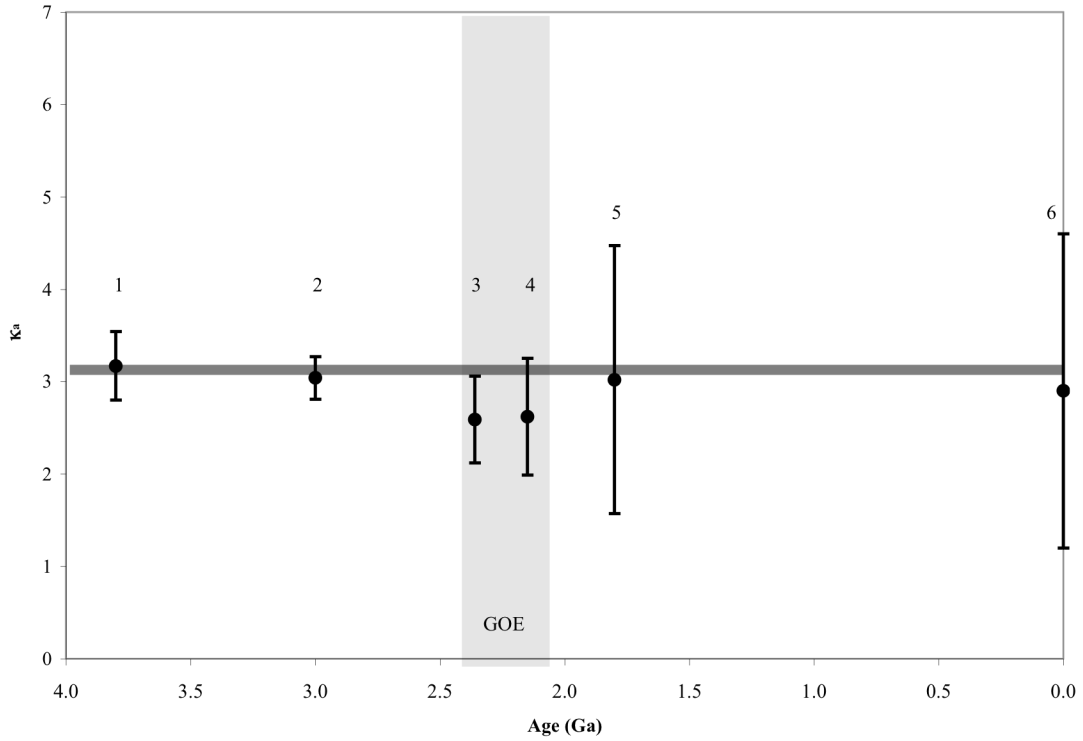

Figure 6.10 κ_a values for selected shale suites deposited throughout geologic time. The sample suites used in this plot come from the (1) ca. 3.8 Ga Isua Supracrustal belt, Greenland (Rosing and Frei, 2004), (2) ca. 3.05 Ga Buhwa shales, Buhwa greenstone belt, Zimbabwe (Krogstad et al., 2004), (3) ca. 2.4 Ga Huronian Supergroup, Ontario, Canada (McLennan et al., 2000), (4) ca. 2.15 Ga Sengoma Argillite Formation, Botswana (this study), (5) ca. 1.8 Ga Hondo Group, southwestern USA (McLennan et al., 1995), and (6) modern turbiditic muds (Hemming and McLennan, 2001). The κ_a value for the average marine shale (3.2; Turekian and Wedepohl, 1961) is shown by grey horizontal line for reference. The κ_a values for all suites are close to that for the average marine shale. Notably, Archean suites show little variations from this value, whereas starting as early as ca. 2.4 Ga, but definitely by ca. 2.15 Ga, shale suites show increased variation in κ_a values. This increased variation is likely due to the initiation of oxidative continental weathering by ca. 2.15 Ga, at the latest.

Table 6.1. Pb isotope compositions for the Sengoma Argillite Formation

Sample (depth)	$^{206}Pb/^{204}Pb$	$^{207}Pb/^{204}Pb$	$^{208}Pb/^{204}Pb$	κ_a
142.8 m	19.92	15.92	40.1	3.68
156.78 m	20.79	16.06	39.3	2.59
173.67 m	22.22	16.26	40.1	2.42
181.25 m	20.68	15.97	39.6	2.84
200.7 m	23.98	16.59	39.7	1.75
205.25 m	24.13	16.47	39.9	1.80
212.7 m	22.29	16.24	39.7	2.23
219.1 m	21.27	16.18	39.7	2.61
224.87 m	21.62	16.19	40.4	2.82
286.6 m	20.65	15.95	40.6	3.46

Table 6.2. Pb isotope composition of the stepwise acid leaching experiments

Sample Depth	$^{206}Pb/^{204}Pb$	$^{207}Pb/^{204}Pb$	$^{208}Pb/^{204}Pb$	κ_a
200.7 m				
L1	25.26	16.62	39.65	1.54
L2	26.14	16.87	41.62	1.99
L3	20.32	16.07	37.26	1.56
R	24.50	16.51	38.44	1.25
200.7 m - Replicate				
L1	25.91	17.00	40.67	1.75
L2	26.18	16.88	41.65	1.99
L3	20.39	16.11	37.39	1.62
R	24.73	16.65	38.85	1.35
WR	23.98	16.59	39.66	1.77
142.8 m				
L1	19.11	15.87	39.96	4.41
L2	19.40	15.86	41.47	5.28
L3	17.37	15.60	37.46	4.32
R	--	--	--	--
WR	19.92	15.92	40.05	3.67

The following acids and times were used during leaching experiments: step L1 (1 mL 0.1M HBr, ~1h), L2 (1 mL 4M HBr, ~1 hr), L3 (1 mL 50:50 HCl:HNO_3), R (HF and HNO_3)

Leaching of sample 142.8 m produced a negligible amount of Pb in step R; data are not reported

Table 6.3. REE concentrations for organic-rich shale samples of the Sengoma Argillite Formation (in ppm)

	142.8 m	156.78 m	173.67 m	181.25 m	200.7 m	205.25 m	212.7 m	219.1 m	224.87 m	286.6 m
La	36.8	34.1	36.8	39.3	29.6	30.5	29.1	29.4	35.4	31.2
Ce	68.4	59.6	68.3	66.2	55.6	57.5	53.4	53.5	60.9	53.5
Nd	27.8	24.1	27.2	26.9	22.0	23.4	21.4	22.0	25.3	21.6
Sm	5.21	4.51	5.34	5.00	3.75	4.46	4.03	4.16	4.73	3.52
Eu	1.04	0.866	1.61	0.949	0.647	0.869	0.791	0.830	0.904	0.547
Gd	4.58	4.09	4.85	4.18	2.98	4.00	3.45	3.99	4.07	2.49
Er	4.06	4.04	4.37	3.95	2.77	3.70	3.17	3.42	3.86	2.64
Dy	2.27	2.4	2.55	2.33	1.71	2.11	1.85	2.02	2.26	1.67
Yb	2.18	2.36	2.43	2.26	1.74	2.01	1.77	1.94	2.21	1.72
La_N/Sm_N	4.31	4.61	4.19	4.78	4.80	4.18	4.40	4.30	4.56	5.40
Gd_N/Yb_N	1.69	1.39	1.60	1.48	1.38	1.60	1.56	1.65	1.48	1.16
La_N/Yb_N	8.04	9.56	7.19	7.49	8.19	7.31	7.73	7.07	7.07	7.95
Ce/Ce*	0.98	0.94	0.98	0.92	0.99	0.99	0.98	0.96	0.92	0.93
Eu/Eu*	0.65	0.62	0.98	0.64	0.60	0.64	0.66	0.63	0.64	0.57

7. THE CA. 2.0 GA ZAONEZHSKAYA FORMATION, LOWER LUDIKOVIAN SERIES, KARELIA, RUSSIA

7.1 Geologic Setting

In this chapter we examine the utility of Pb isotope compositions and REE concentrations in evaluating the rise of oxidative weathering during the deposition of the ca. 2.0 Ga upper Zaonezhskaya Formation of the Karelian Supergroup, Karelia, Russia (Figures 7.1 and 7.2). The Precambrian rocks of Karelia have been studied extensively with many of the studies being written in non-English sources, however the regional and local geology of Karelia is derived from several English language sources that cite these other sources (Melezhik et al., 1999; Melezhik et al., 2004; Ojakangas et al., 2001). The Karelian Supergroup is composed of a turbidite-dominated upper sequence and an arenite-dominated lower sequence unconformably deposited upon Archean granitoids and gneisses and (Ojakangas et al., 2001). The rocks of the Karelian Supergroup are divided into four informal unconformity-bound groups (Sariolian, Jatulian, Ludikovian, and Kalevian) of metasedimentary and metavolcanic rocks. The Ludikovian Series is comprised of basaltic tuffs, organic matter-rich shales, and cherts (lower Zaonezhskaya and upper Zaonezhskaya formations) and basalts with intercalated gabbro sills (Suisarskaya Formation) (Melezhik et al., 1999; Melezhik et al., 2004; Ojakangas et al., 2001).

Samples of organic matter-rich siltstones and mudstones were collected from drill cores C-19, C-25, C-34, C-159, C-207, and C-5190 from various depths within the upper Zaonezhskaya Formation, in the Lake Onega area of northwestern Russia (Table 7.1). In this area, rocks rich in organic matter comprise approximately 30% of the overall thickness of the upper Zaonezhskaya Formation, which is approximately 600 meters

thick. Drill holes C-19, C-25, C-34, and C-207 were drilled in the Maksovo shungite deposit northwest of Tolvuya, Russia (Figure 7.1). The remaining samples for this study were collected from drill core C-5190 drilled southeast of Padma, Karelia. Samples were given an identification number (e.g. UZF-1) based on the drill core number and depth sampled (Table 7.1). The lithologies represented by the Zaonezhskaya Formation are representative of deposition on a marine platform. Specifically, the geology of organic-rich layers (high C_{org}/S ratios, elevated C_{org} and S concentrations, and carbonate concretions) has been interpreted as representative of sediments deposited in a swampy, brackish, non-euxinic lagoon (Melezhik et al., 1999).

The upper Zaonezhskaya Formation overlies the Jatulian carbonates that record the 2.22 – 2.1 Ga positive carbon isotope excursion (Karhu, 1993; Karhu and Holland, 1996; Melezhik et al., 1997). A lower age constraint is provided by a gabbro intrusion from the overlying Suisarskaya Formation is dated by the Sm-Nd isochron method at 1980 ± 27 Ma (Pukhtel et al., 1992). These constraints result in a depositional age of approximately 2.0 Ga for the Zaonezhskaya Formation. The Paleoproterozoic rocks of the Lake Onega area were deformed by greenschist facies regional metamorphism during the ca. 1.8 Ga Svecofennian Orogeny.

7.2 Results

7.2.1 Whole rock Pb isotope compositions

Whole rock Pb isotope ratio data for twelve organic-rich shale samples from the upper Zaonezhskaya Formation are presented in Table 7.2. Uranogenic Pb isotope ratios for all of the samples and the model Pb growth curve of Stacey and Kramers (1975) are

plotted in Figure 7.3. The Pb isotope ratios of all of the samples plot as a positively correlated array with a best-fit slope of 0.108 (± 0.014), which corresponds to a period of radiogenic Pb isotope growth in these rocks from 1774 ± 230 Ma to present (MSWD = 51). The maximum Pb-Pb age (2004 Ma) is within error of the proposed sedimentary age of the unit (ca. 2.0 Ga; Melezhik et al., 1999) indicating that the U/Pb ratio may have been established during sedimentary processes and post-depositional processes (e.g. the Svecofennian Orogeny) did not redistribute U/Pb. The argillite samples have model time-integrated $^{238}U/^{204}Pb$ ratios (μ_a ratios) ranging from 7.26 to 59.8, using the $^{206}Pb/^{204}Pb$ and $^{207}Pb/^{204}Pb$ ratios from the Kramers and Tolstikhin model (K&T97) at 2.0 Ga. An alternative interpretation of the Pb-Pb age concludes that this age may have significance as the age of disruption to the U-Pb geochemical system during the 1.8 Ga Svecofennian Orogeny. The argillite samples have μ_a ratios ranging from 7.98 to 74.3, using the model initial $^{206}Pb/^{204}Pb$ and $^{207}Pb/^{204}Pb$ ratios from the Kramers and Tolstikhin model (K&T97) at 1.8 Ga. Because the age of the Svecofennian Orogeny is closer to the average Pb-Pb age (1774 Ma), the preferred interpretation involves a disruption to the U-Pb system at 1.8 Ga. The interpretation of radiometric age significance will be further evaluated through sequential acid leaching, REE concentrations, and interelement ratio plots.

A $^{206}Pb/^{204}Pb$ vs. $^{208}Pb/^{204}Pb$ plot of the Pb isotope ratios from all of the samples (Figure 7.4) shows a positively correlated array with greater relative variation in the $^{206}Pb/^{204}Pb$ ratio as compared to that of the $^{208}Pb/^{204}Pb$ ratio. Using the model initial Pb isotope ratios from the K&T97 Pb isotope growth model at 2.0 Ga (the age of sedimentation), model apparent time-integrated Th/U ratios (κ_a) range from 0.488 to 2.94 for shale samples of the upper Zaonezhskaya Formation with an average ratio of 1.46.

All of the κ_a ratios are well below the model κ (3.86) for the "erosion mix" from K&T97 at 2.0 Ga. Calculating κ_a ratios using model initial Pb isotope ratios from the "erosion mix" at a younger age (e.g. 1.8 Ga) is inappropriate as the K&T97 model accommodates the oxidation of the surface environment after 2.0 Ga.

7.2.2 Sequential acid leaching

Two samples (UZF-3 and UZF-11) were selected for step-wise acid leaching and processed for Pb isotope ratio analysis (Table 7.3). The sample from drill core 207 (UZF-3) was selected on the basis of it having the highest whole rock κ_a ratio (2.94). Acid leaching of this sample resulted in isotope ratio data from all of the leaching steps with nearly equal distribution of Pb between the first three leach steps (~28%) and about half as much Pb (12.9%) liberated by the HF and HNO_3 leach step (Table 7.3). The plot of uranogenic Pb isotope ratios (Figure 7.5a) displays a field of points that are tightly clustered and show greater relative variation in $^{206}Pb/^{204}Pb$ ratios as compared to $^{207}Pb/^{204}Pb$. The slope of a best-fit line through these data corresponds to a future Pb-Pb growth age (-241 ± 5400 Ma). This age is not realistic and has no relationship to the age of sedimentary or post-depositional events, but may be indicative of homogenization of Pb isotope ratios during alteration. Pb isotope ratios from the leach steps and whole-rock define a shallow slope on a $^{206}Pb/^{204}Pb$ vs. $^{208}Pb/^{204}Pb$ plot (Figure 7.5b), indicative of potential uranium mobility without concomitant thorium mobility. It may be assumed that κ_a values are not indicative of U-Th-Pb systematics during depositional conditions, due to the nature of U-Pb behavior interpreted from the Pb-Pb age.

The step-wise acid leaching of the other sample (UZF-11; Figure 7.6) resulted in Pb isotope ratios from all of the four leach steps, with the last leach step containing lower concentrations of Pb than the first three. The leach steps and whole-rock Pb isotope composition of this sample display a positively sloped array (slope = 0.0760 ± 0.0097) on a $^{206}Pb/^{204}Pb$ vs. $^{207}Pb/^{204}Pb$ plot (Figure 7.6a). The slope corresponds to the start of radiogenic Pb isotope growth at 1094 ± 260 Ma ending at present day (MSWD = 68). Pb isotope ratios from the leach steps and whole rock also define a positively correlated array on a $^{206}Pb/^{204}Pb$ vs. $^{208}Pb/^{204}Pb$ plot (Figure 7.6b). The data correlates to various κ_a values depending upon the model initial $^{206}Pb/^{204}Pb$ and $^{208}Pb/^{204}Pb$ ratios used to calculate the κ_a ratio. The κ_a ratio varies from 0.521 to 0.893 with an average κ_a ratio of 0.693, using the model initial ratios from K&T97 at 1100 Ma. If the model initial ratios are selected from the K&T97 model at 1800 Ma, the κ_a ratios vary from 0.565 to 1.07 with an average of 0.871. The κ_a values suggest that the whole rock Pb isotope composition is in equilibrium with the leach steps because the average κ_a ratio is very close to that of the whole rock regardless of model age.

7.2.3 REE Concentrations

The REE concentrations of five samples from the upper Zaonezhskaya Formation (including the two samples selected for acid leaching) were determined by isotope dilution mass spectrometry (Table 7.4). Chondrite-normalized REE patterns of the selected samples are highly variable (Figure 7.7). Most noticeable difference is the presence of two relatively flat REE patterns (UZF-3 and UZF-12; La_N/Yb_N = 0.512 and 1.90 respectively) amongst the suite. There is no indication that these analyses are

flawed as replicate analysis of REE concentrations and interelement ratios of UZF-12 show a high degree of precision (2.25% 2σ relative error on elements and 2.85% 2σ relative error on ratios). The three remaining samples display consistent LREE and HREE fractionation ($Ce_N/Sm_N = 2.35 \pm 0.193$, 2σ; $Gd_N/Yb_N = 1.80 \pm 0.144$, 2σ) and negative Eu-anomalies ($Eu/Eu^* = 0.761 \pm 0.048$). UZF-12 is distinguishable through a lower degree of LREE and HREE fractionation ($Ce_N/Sm_N = 1.20$; $Gd_N/Yb_N = 1.23$) and the lack of an Eu-anomaly ($Eu/Eu^* = 0.961$).

Many of the interelement REE ratios are even more drastically different when considering UZF-3. The most dramatic difference between the chondrite-normalized REE pattern of UZF-3 and all other samples evaluated during the course of this study is the presence of a positive Ce- and Eu-anomaly ($Ce/Ce^* = 1.55$; $Eu/Eu^* = 1.15$). The MREE are relatively more enriched than the LREE for UZF-3 ($La_N/Sm_N = 0.473$; $Nd_N/Sm_N = 0.881$) in contrast to the typical LREE/MREE fractionation observed in shales ($La_N/Sm_N > 1$). The relative MREE enrichment of UZF-3 is also noticeable when compared to the HREE ($Gd_N/Yb_N = 1.11$), however MREE enrichment over the HREE is commonly observed in shales. The low overall REE concentration ($Nd_{UZF\text{-}3} = 6.13$ ppm) is unusually low for shales studied for this dissertation (but not the chemical sedimentary rocks of the Hotazel Formation).

7.3 Discussion

The overlap between the whole-rock Pb-Pb age (1774 ± 230 Ma) and the inferred age of deposition (2000 Ma; Melezhik et al., 1999) allows for the interpretation of κ_a ratios as an indicator of U-Th decoupling during sedimentary processes. When evaluated

as an indicator of paleoredox conditions, the highly variable κ_a ratios (0.488 to 2.94) are a strong indication that oxidative weathering had begun by 2.0 Ga, at the latest. This interpretation would agree with other data presented in this dissertation (Sections 5.4 and 6.4). In contrast, post-depositional processes may have disturbed the U-Th-Pb system shortly after deposition at or near 1774 Ma, resulting in variable κ_a ratios. This disturbance is further suggested by coincidence of the Pb-Pb age and the age of metamorphism during the ca. 1.8 Ga Svecofennian Orogeny. The variable Pb-Pb ages derived from sequential acid leaching (-241 and 1094 Ma) support the hypothesis that the U-Th-Pb geochemical system was subjected to at least one post-depositional disruption, however not all of the ages are supportive of a ca. 1.8 Ga tectonic event. The low percentages of Pb liberated in the residual leach steps (12.8% and 12.9%) are evidence that the Pb was not contained within silicate mineral phases and therefore may have been highly susceptible to metasomatic fluids. The young whole-rock Pb-Pb age, variable young leach step Pb-Pb ages, and small fraction of Pb liberated from silicate minerals, yield evidence that variable κ_a ratios may not reflect sedimentary conditions, but rather may be the result of metasomatism or source mixing.

A comparison between Gd/Er or La/Nd ratios of REE and Th/U (or κ_a) values allows for the evaluation of geochemical behavior of U and Th (Section 6.3.1). Plots of κ_a values versus Gd/Er ratios (Figure 7.8) and La/Nd ratios (Figure 7.9) provide the means for the evaluation of the effects of metamorphism and provenance heterogeneity, which may be responsible for the decoupling of U from Th. The general nature of potential provenance components can be characterized by chondrite-normalized REE patterns. The lack of LREE enrichment in UZF-3 is similar to that observed for mafic

igneous rocks. Because mafic igneous activity is known to be contemporaneous with the deposition of the Karelian sediments, the basalt-like REE pattern may be interpreted as a layer of mafic tuff. Alternatively a proximal mafic igneous source may have significantly contributed to the provenance of UZF-3 leading to chemical immaturity of this rock. If the REE patterns are the result of a proximal mafic igneous source, the REE interelement ratios and κ_a of the samples should reflect the input of this source component.

Interelement ratios of the shale samples from the upper Zaonezhskaya Formation have Gd/Er ratios that vary 39.8% (2σ) relative to the average Gd/Er value (1.75) with concomitant variability of κ_a ratios (79.8%, 2σ) relative to the average κ_a ratio of 1.90. Lithologic units that have been identified as having a homogeneous source or a well-mixed provenance (e.g. the Timeball Hill and Sengoma Argillite formations) display a low relative variation of Gd/Er ratios (<20%). The Karelian shales have twice this relative variation indicating that the source of these rocks is heterogeneous. The lack of a curvilinear relationship between these two variables makes it unlikely that bimodal source mixing explains the total variation observed in Gd/Er and κ_a ratios. A variable detrital source (the "Karelian source") can be modeled using the Gd/Er and κ_a ratios of the two samples with the highest Gd/Er ratio values. The range of interelement ratios within the samples can be modeled as mixing of the "Karelian source" with as much as 97% of a source component that is similar to Archean mafic volcanic rocks (from Taylor and McLennan, 1985).

This same concomitant variation in interelement ratios that is observed between Gd/Er and κ_a ratios is not observed between La/Nd and κ_a ratios (Figure 7.9). The geochemical character of the "Karelian source" is not completely defined by analyses, as

one sample that defines the lower κ_a limit of the source (UZF-11) does not have La concentration data. Therefore the geochemical nature of the "Karelian source" was approximated by the relative variation observed for Gd/Er ratios. Regardless of the actual value of the La/Nd ratio of UZF-11, bimodal mixing between a single homogeneous source or a "Karelian source" and Archean mafic volcanic rocks (AMv) does not explain the distribution of data points. Therefore the probability that the pattern displayed by the data is the result of bimodal mixing of diverse provenance components is greatly reduced. The hypothesis of trimodal mixing of Archean mafic volcanic rocks and a "Karelian source" requires that the third end member have unusual geochemical characteristics (La/Nd < 0.3 and κ_a < 2). The geochemistry of zircon makes it a potential end member however it is unlikely that some samples would contain the necessary additional concentration of zircon to permit this as a viable mixing end member. Furthermore, the addition of zircon would result in HREE fractionation unlike that observed for the samples of the upper Zaonezhskaya Formation. The lack of any association between La/Nd and κ_a ratios greatly reduces the likelihood that interelement ratios reflect source mixing. Similarly, the lack of covariable interelement ratios greatly reduces the probability that source mixing or variable trace element fractions are prevalent processes in controlling the geochemistry of Karelian shales.

Metasomatic alteration provides another mechanism through which the REE and Pb isotope ratios could have been altered. It has been shown that the redistribution of LREE in clastic sedimentary rocks is possible during metasomatism (Bock et al., 1994; Krogstad et al., 2004; McDaniel et al., 1994). McDaniel et al. (1994) interpreted increased Sm/Nd ratios and Ce-anomalies as the result of post-depositional alteration of

first-cycle sandstones and siltstones by oxidizing metasomatism. This metasomatic event depleted the LREE, but the rocks preferentially retained Ce in its oxidized more stable tetravalent (Ce^{4+}) form.

Similar conditions of metasomatism might result in the alteration in the Karelian shales reflected by geochemical proxies. The difficulty in modeling this scenario comes in identifying a suitable "unaltered" sample and being able to determine its stratigraphic context. If identified, this sample could then be compared to other samples to evaluate the effects of oxidizing metasomatism. The issue of stratigraphic position is too difficult to resolve using the provided drill core data and therefore the "unaltered" sample was identified as the sample having the lowest Sm/Nd concentration (UZF-11). It is possible to derive a degree of alteration experienced by the other samples, using the increase in Sm/Nd ratios as a geochemical proxy. This methodology results in UZF-11 and UZF-7 being the least altered samples. This is consistent with the premise that these two samples define the "Karelian source", but in addition to reflecting a potential provenance source they represent unaltered (or the least altered) samples. Metasomatic alteration of the type proposed by McDaniel et al. (1994) would have altered the La/Nd and Gd/Er of the Karelian samples to lower values.

Geochemical evidence of the metasomatic alteration of the Karelian shales may be observed in κ_a ratios as well. It was proposed that the metasomatic fluids were oxidizing because of the increase in Ce/Ce* of the samples. The lack of La concentration data makes a quantitative comparison of Ce-anomalies impossible, but κ_a ratios hold the potential for evaluating oxidative conditions. If the metasomatic fluids that lowered the interelement REE ratios (La/Nd and Gd/Er) were able to oxidize Ce, the fluids should

also have the potential to oxidize the U present within the samples. The oxidation of U within these samples would be reflected by elevated κ_a ratios as the U was preferentially leached resulting in Th enrichment. The observed correlated decrease in Gd/Er ratios and increase in values of κ_a ratios may be the result of U removal. Oxidative fluids may also increase the value of κ_a ratios with the unusually high concentration of organic carbon serving as a substance capable of reductive U addition to these samples. The resultant κ_a ratios would then yield no information for the interpretation of the redox conditions of the atmosphere during sedimentary processes but will constrain the redox conditions associated with the post-depositional alteration of these organic-rich shales.

7.4 Conclusions

The organic-rich shale samples of the ca. 2.0 Ga upper Zaonezhskaya Formation, Karelia, Russia do not record the sedimentary redox conditions due to the geochemical alteration of these sedimentary rocks at ca. 1.8 Ga by metasomatism during the Svecofennian Orogeny. Evidence of this alteration is observed through:

(1) A whole-rock Pb-Pb age (1774 ± 230 Ma) that is younger than that reported for the depositional age of the sampled lithologic unit (2000 Ma). The error associated with this Pb-Pb age is too high to be considered a true isochron, which is a potential indication that a disturbance to the U-Pb system occurred approximately 1.7 Ga, during the Svecofennian Orogeny, but that this disturbance did not completely reset the U-Pb isotope system.

(2) Highly variable Pb-Pb ages for sequential acid leaching (-241 Ma and 1094 Ma) that are younger than the whole-rock Pb-Pb age suggest that the

U-Pb isotope system within different samples was allowed to reach different degrees of equilibration. The low degree of variation in Pb isotope ratios in the sample with the younger age (UZF-3) may indicate a lack of U/Pb fractionation between different minerals.

(3) The high percentage of Pb liberated during non-silicate acid leaching steps (L1, L2, and L3), which are more susceptible to reestablishing equilibration of the U-Pb system during metamorphic events. The residual material remaining after HBr, HCl, HNO_3 leaching contains more radiogenic Pb (has the highest $^{206}Pb/^{204}Pb$ ratios) indicative of higher U concentrations in these (silicate) mineral phases.

(4) Interelement REE ratios decrease with increased alteration, but do not vary systematically with κ_a ratios. This lack of covariation prohibits the interpretation of the redox characteristics of the metasomatic fluid that altered the geochemistry of the samples.

Whole-rock uranogenic Pb isotope ratios and chondrite-normalized REE patterns are interpreted as recording a metasomatic event at 1.8 Ga that fractionated the trace elements (U-Th-Pb-REE) within the Zaonezhskaya Formation. It is inappropriate to interpret the highly variable values of κ_a in the context of an indicator of sedimentary paleoredox conditions. Rather it is likely that these values represent the non-systematic redistribution of U and the LREE during the 1.8 Ga Svecofennian Orogeny. Although this portion of the study fails to provide additional constraints for the rise of oxidative continental weathering, it demonstrates the effectiveness of the U-Th-Pb system at determining the appropriateness of specific stratigraphic units for use in paleoredox

studies. The alteration of the geochemistry of the shale samples from the ca. 2.0 Ga Zaonezhskaya Formation prohibits the characterization of surficial environments using model apparent time-integrated Th/U ratios (κ_a). The lack of redox significance for κ_a ratios also brings into question the interpretation of other geochemical proxies that have been determined for this and similarly altered rock units.

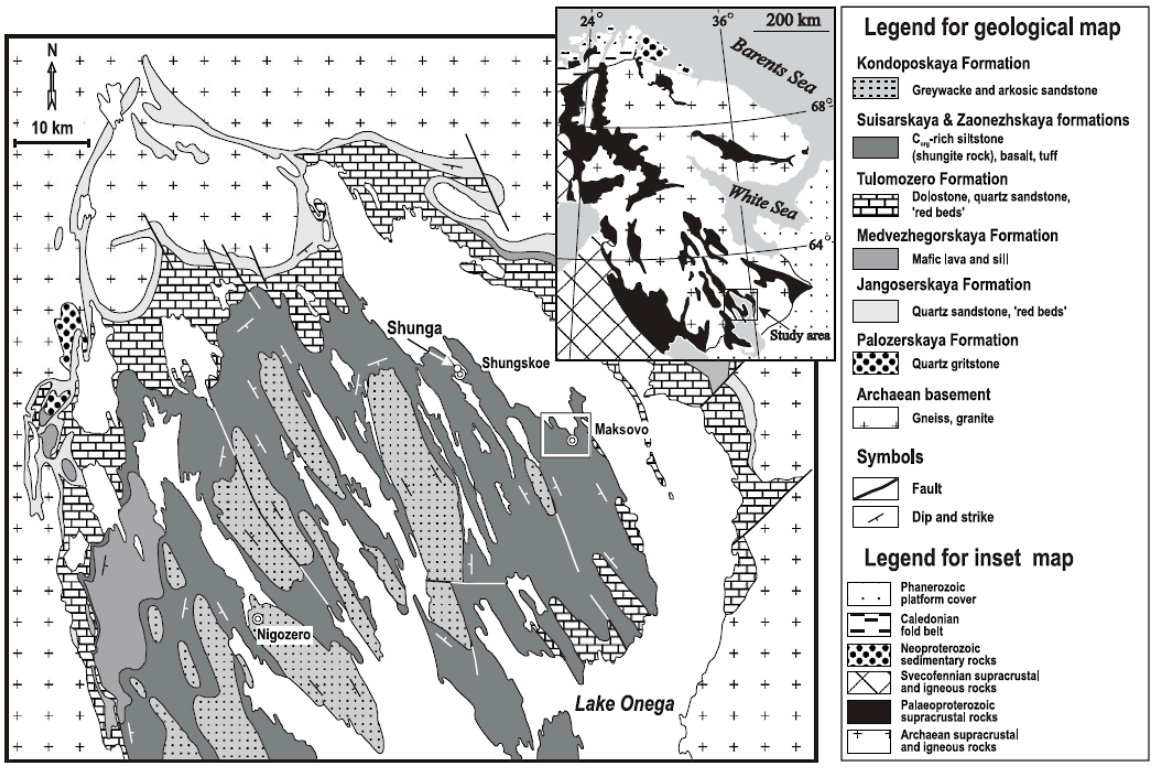

Figure 7.1 Generalized geologic map showing the distribution of the Archean and Paleoproterozoic rocks in the northern Lake Onega area, Karelia, Russia. Locations of drill core sampling are provided. Drill core C-19, C-25, C-34, and C-207 was drilled in Maksovo shungite deposit. Drill core C-5190 was drilled southeast of Padma (middle of the peninsula south of Maksovo). The northwest corner of the map is located at approximately 63°N, 33°30'E (from Melezhik et al., 1999).

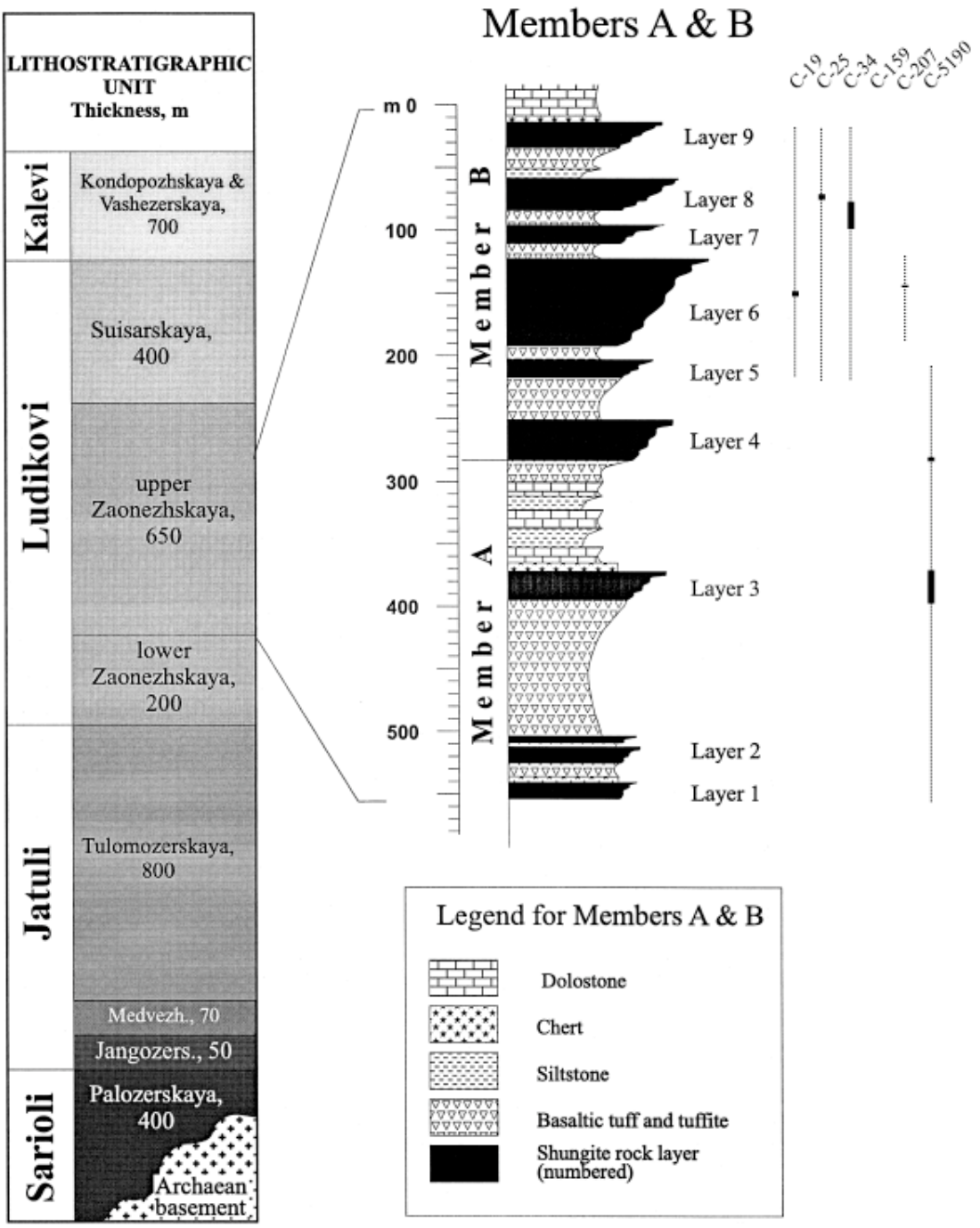

Figure 7.2 Generalized stratigraphic section of the Archean and Paleoproterozoic rocks from Karelia, Russia (adapted from Melezhik et al., 1999). Dashed lines indicate the exact portion of the upper Zaonezhskaya Formation sampled in each drill core with solid blocks indicating where samples were collected. A list of sampled "shungite rock layers" is provided in Table 7.1.

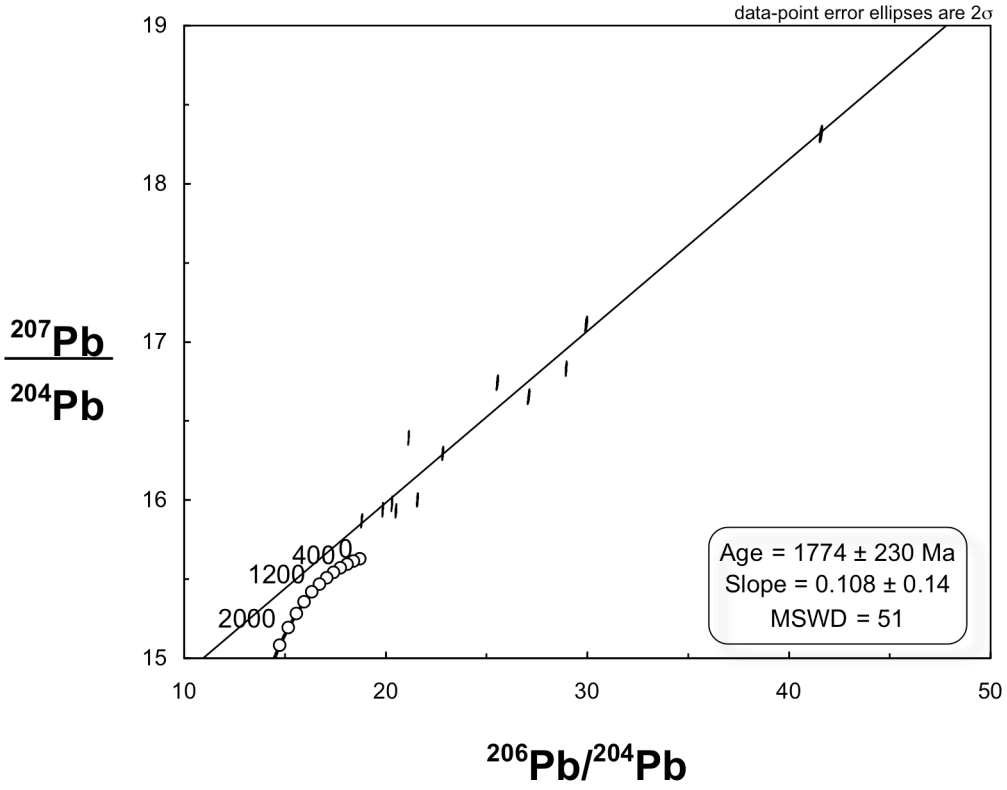

Figure 7.3 Uranogenic Pb isotope ratio ($^{206}Pb/^{204}Pb$ vs. $^{207}Pb/^{204}Pb$) plot for whole rock Karelian shale samples. A depositional age of 2000 Ma is suggested by previously determined age constraints (see text). The errors associated with the calculated Pb-Pb age allow for the interpretation that the U-Pb geochemical system is undisturbed since deposition, however it is more likely that the Pb-Pb age represents the age of regional metamorphism during the ca. 1.8 Ga Svecofennian Orogeny.

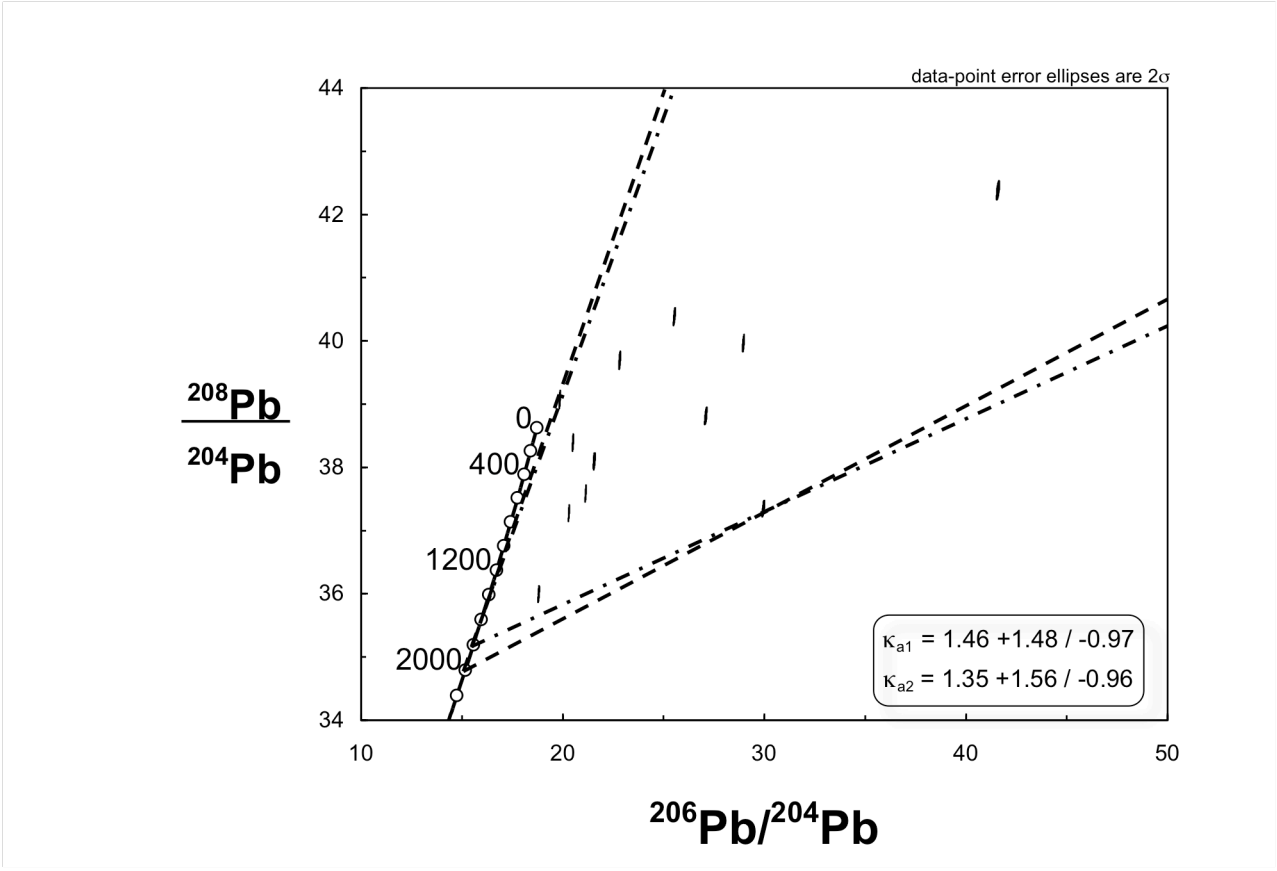

Figure 7.4 $^{206}Pb/^{204}Pb$ and $^{208}Pb/^{204}Pb$ isotope ratio diagram for the whole rock Karelian shale samples. The diagram shows the relationship between thorogenic and uranogenic Pb isotopes. The Pb isotope ratio growth curve shown in this figure represents the Pb isotope growth model of Stacey and Kramers (1975). The dashed line represents the maximum and minimum values for κ_a (κ_{a1}) if the initial Pb isotope ratios are from the 'erosion mix' at 2000 Ma (Kramers and Tolstikhin, 1997). The dash-dot line represents the range of κ_a ratio values (κ_{a2}) that are calculated using the Pb isotope ratios from the 'erosion mix' at 1800 Ma (Kramers and Tolstikhin, 1997). The observed variability results from the redistribution of U within the rocks during metasomatism associated with the ca. 1.8 Ga Svecofennian Orogeny.

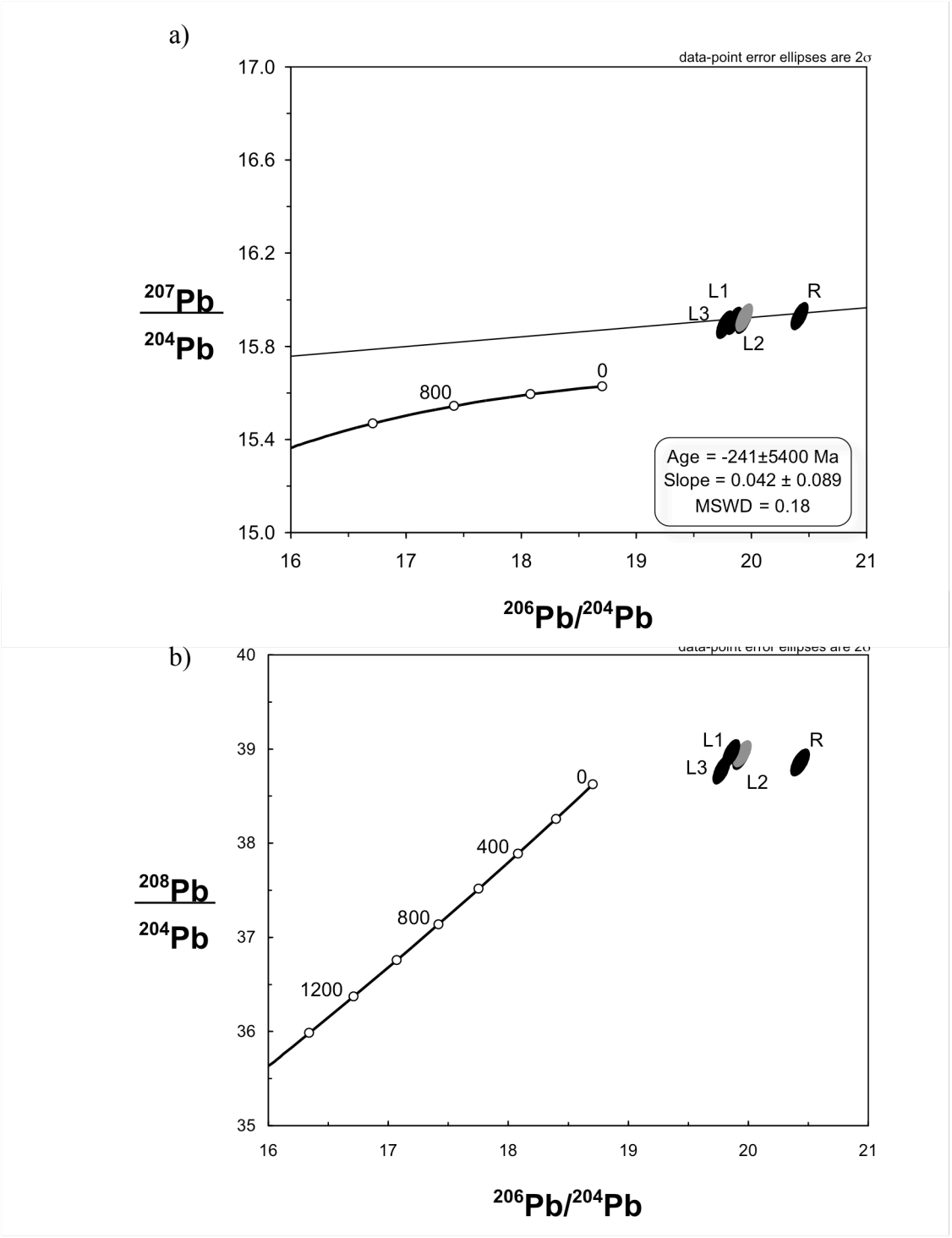

Figure 7.5 Uranogenic (a) and urano-thorogenic (b) Pb isotope ratio plots for the sequential acid leach steps of sample UZF-3. The Pb isotope compositions of the leach steps delimit the Pb isotope composition of the whole rock (gray symbol), indicative of sample homogeneity. The high percentage of Pb liberated content in the initial leach steps (L1, L2, L3) is indicative of Pb located in non-silicate mineral phases. Values of κ_a are not provided, because it is unlikely that they represent U-Th decoupling during weathering.

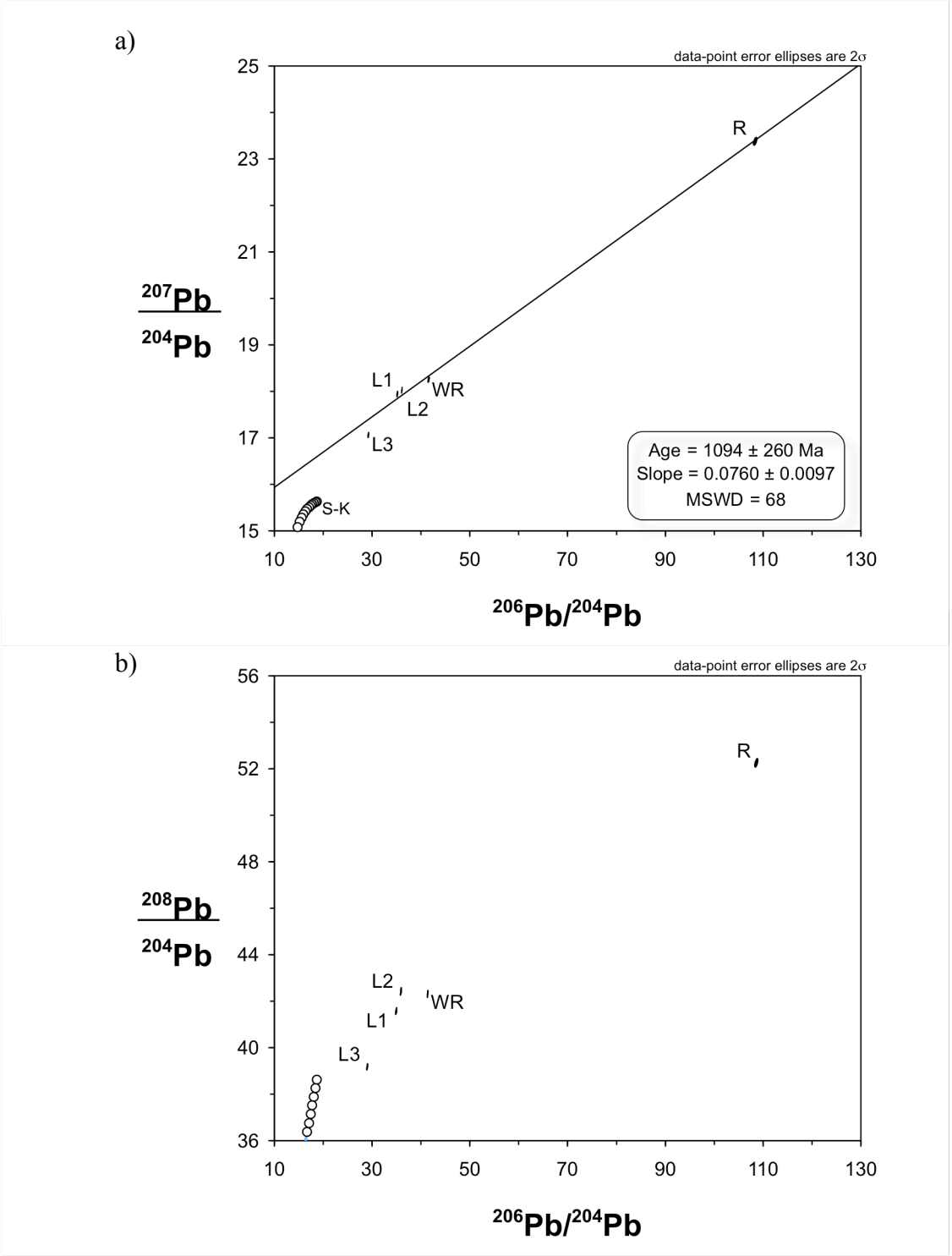

Figure 7.6 Uranogenic (a) and urano-thorogenic (b) Pb isotope ratio plots for the sequential acid leach steps of sample UZF-11. The Pb isotope compositions of the leach steps delimit the Pb isotope composition of the whole rock (WR), indicative of sample homogeneity. The high percentage of Pb liberated content in the initial leach steps (L1, L2, L3) is indicative of Pb located in non-silicate mineral phases. Values of κ_a are not provided, because it is unlikely that they represent U-Th decoupling during weathering.

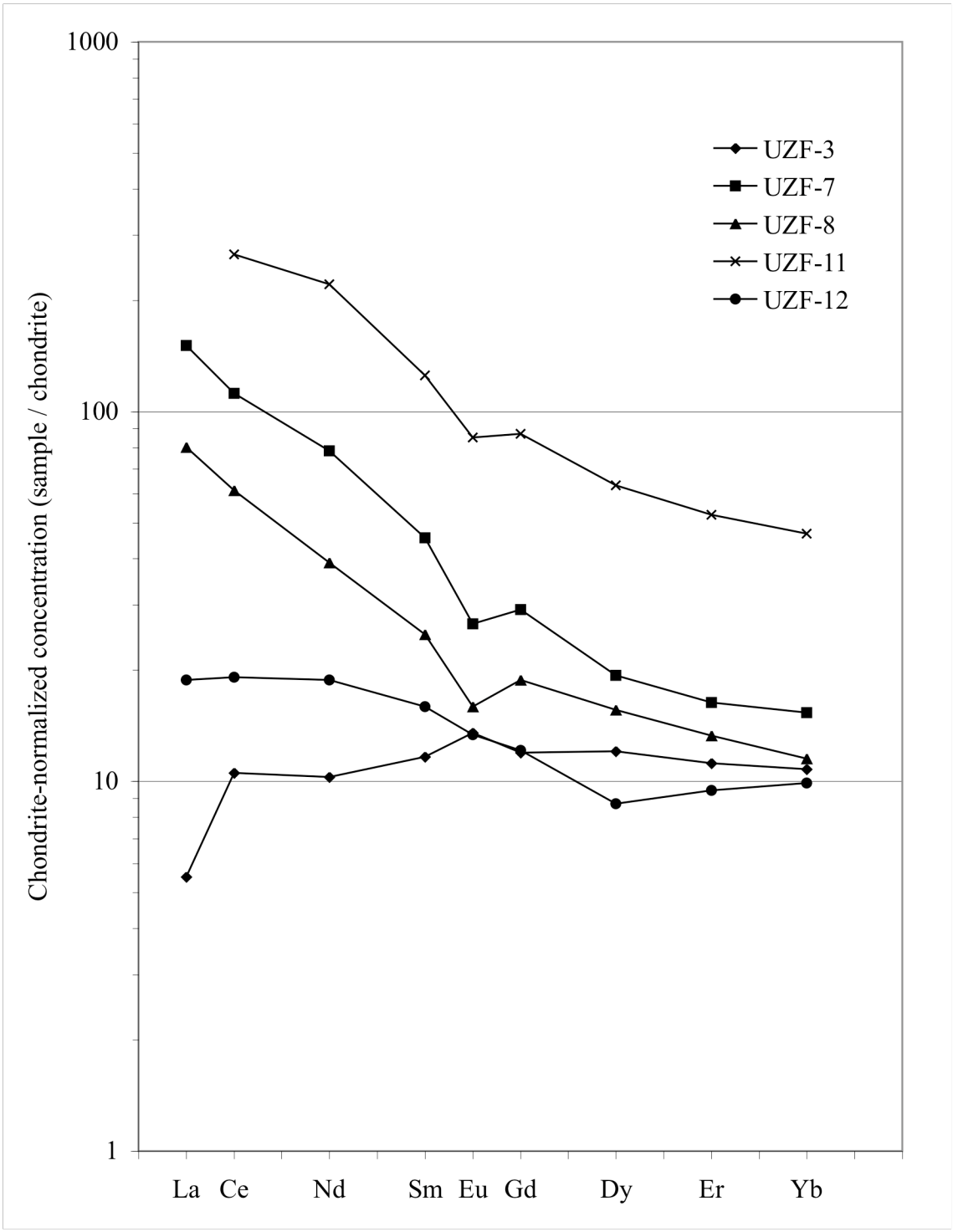

Figure 7.7 Chondrite-normalized REE patterns for the Karelian shales. These patterns are highly variable which is suggestive of multiple sources or metasomatic alteration to the geochemistry of these shales. The least REE enriched sample (UZF-3) may be better classified as a basaltic tuff based on the LREE depleted pattern and positive Eu-anomaly (similar to BIR-1; Baker et al., 2002).

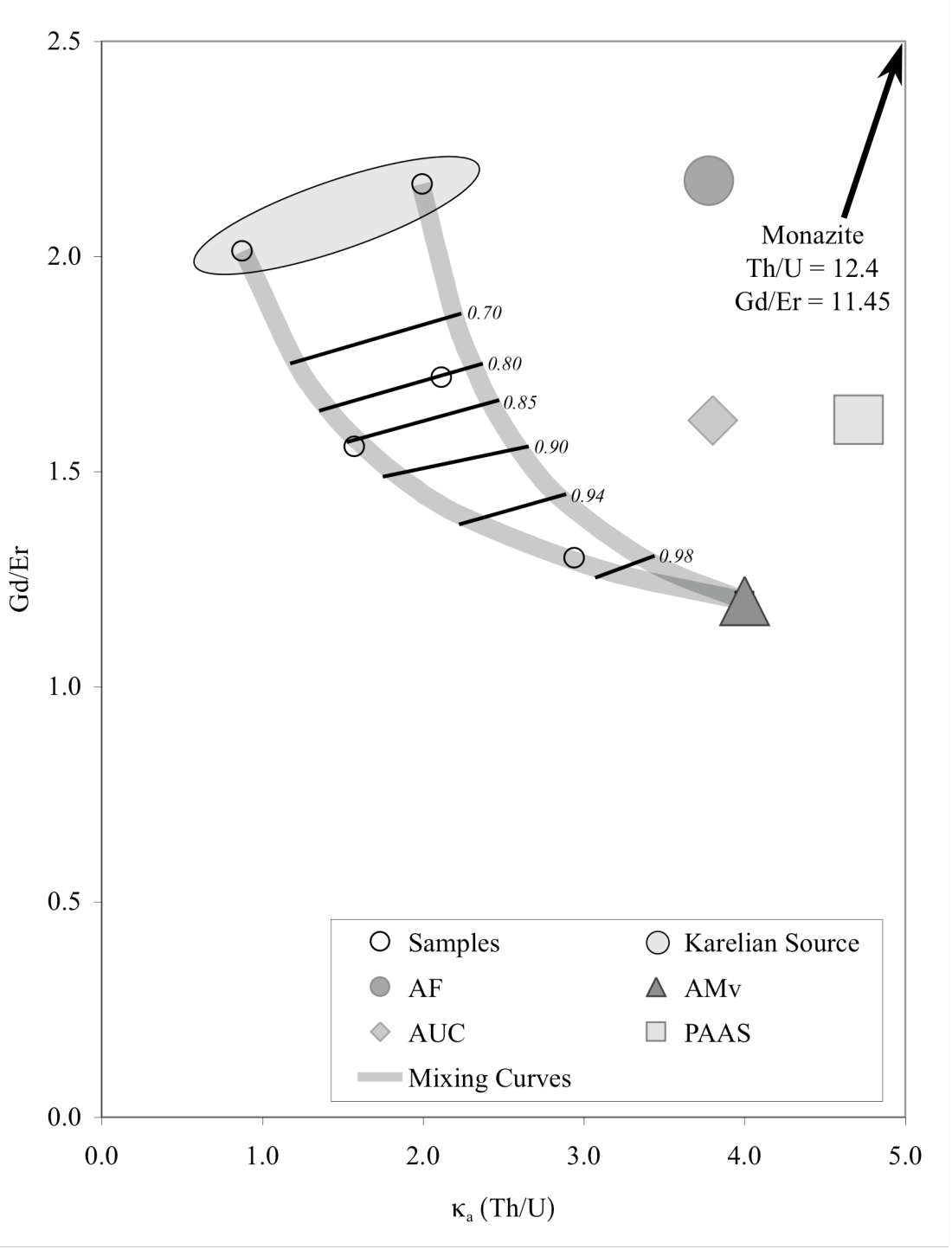

Figure 7.8 κ_a vs. Gd/Er ratios for organic-rich Karelian shales. The relationship between Gd/Er ratios and κ_a values might reflect multiple detrital sources, post-depositional alteration, or decoupling of U from Th by redox processes. The REE geochemistry of these samples supports multiple detrital sources or post-depositional alteration as an underlying factor for variations in κ_a values. The mixture of between 80 and 97% Archean mafic volcanics (AMv) and 20 to 3% shale explains all of the displayed data. Abbreviations and errors are the same as those in Figure 6.8 and 6.9.

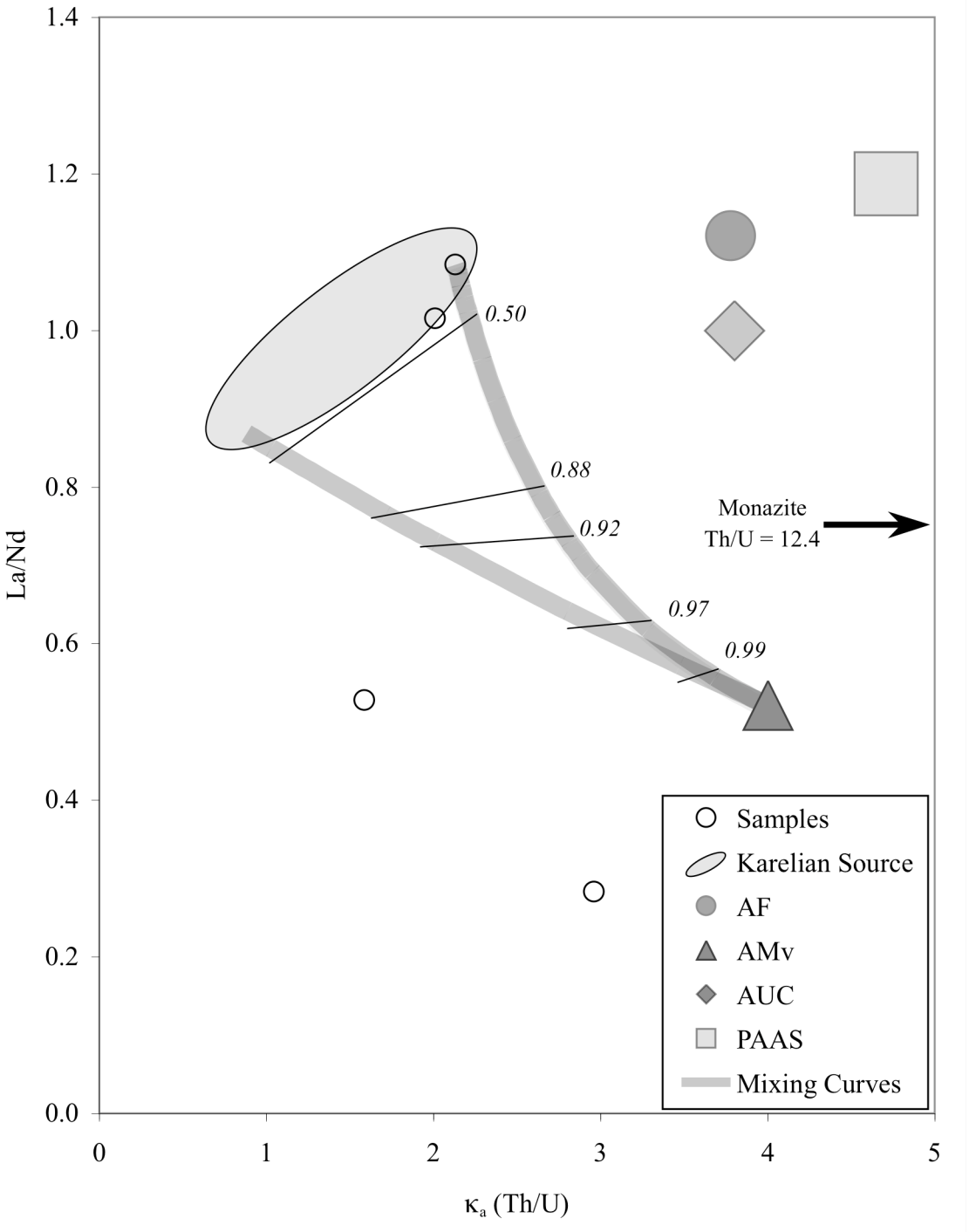

Figure 7.9 κ_a vs. La/Nd ratios for organic-rich Karelian shales. The relationship between La/Nd ratios and κ_a values might reflect multiple detrital sources, post-depositional alteration, or decoupling of U from Th by redox processes. The La/Nd geochemistry of these samples supports post-depositional alteration as an underlying factor for variations in κ_a values. The distribution of data is not explained by a mixture of Archean mafic volcanics (AMv) with the "Karelian source." Abbreviations and errors are the same as those used in Figure 7.8.

Table 7.1 List of organic-rich shale samples of the upper Zaonezhskaya Formation

Sample ID	Drill Core	Depth (m)	Sampled Layer	GSU Lab ID
UZF-1	C-19	159.0 - 159.5	6	KR-27
UZF-2	C-19	162	6	KR-32
UZF-3	C-25	137.5	8	KR-29
UZF-4	C-34	90.7	7 or 8	KR-25
UZF-5	C-34	96.5	7 or 8	KR-26
UZF-6	C-159	81.0 - 81.5		KR-34
UZF-7	C-207	111	6	KR-31
UZF-8	C-5190	85	4	KR-28
UZF-9	C-5190	146.5	3	KR-23
UZF-10	C-5190	154.8	3	KR-30
UZF-11	C-5190	199	3	KR-24
UZF-12	C-5190	204	3	KR-33

Sampled layers correspond to those “shungite rock layers” in Figure 7.2.

Table 7.2. Pb isotope compositions for the Karelian shales

Sample ID	$^{206}Pb/^{204}Pb$	$^{207}Pb/^{204}Pb$	$^{208}Pb/^{204}Pb$	κ_{a1}	κ_{a2}
UZF-1	21.27	16.41	37.64	1.41	1.26
UZF-2	25.64	16.76	40.42	1.67	1.60
UZF-3	19.98	15.96	39.10	2.94	2.91
UZF-4	20.42	16.00	37.32	1.45	1.28
UZF-5	29.07	16.85	39.99	1.13	1.07
UZF-6	21.70	16.02	38.14	1.57	1.45
UZF-7	22.94	16.32	39.73	1.99	1.92
UZF-8	20.62	15.95	38.43	2.11	2.01
UZF-9	27.20	16.67	38.84	1.01	0.922
UZF-10	18.95	15.89	36.06	0.870	0.514
UZF-11	41.69	18.31	42.39	0.873	0.835
UZF-12	30.04	17.13	37.40	0.488	0.406

The provided values of κ_a are calculated using the model initial Pb isotope composition from Kramers and Tolstikhin (1997) for the "erosion mix" at: (1) 2000 Ma and (2) 1800 Ma

Table 7.3 Pb isotope compositions from sequential acid leaching of two samples from the upper Zaonezhskaya Fm.

Leach Step	Counts per second (cps)					
	^{204}Pb	^{206}Pb	^{207}Pb	^{208}Pb	Total	Percentage
UZF-3						
L1	4.74E+07	9.40E+08	7.52E+08	1.84E+09	3.58E+09	29.7%
L2	4.57E+07	9.10E+08	7.25E+08	1.77E+09	3.45E+09	28.7%
L3	4.59E+07	9.08E+08	7.29E+08	1.78E+09	3.46E+09	28.7%
R	2.04E+07	4.16E+08	3.24E+08	7.89E+08	1.55E+09	12.9%
		$^{206}Pb/^{204}Pb$	$^{207}Pb/^{204}Pb$	$^{208}Pb/^{204}Pb$		
L1		19.87	15.92	38.95		
L2		19.95	15.92	38.93		
L3		19.79	15.90	38.78		
R		20.44	15.94	38.86		
Calculated Whole Rock		19.94	15.92	38.88		
Measured Whole Rock		19.98	15.96	39.10		
UZF-11	^{204}Pb	^{206}Pb	^{207}Pb	^{208}Pb	Total	Percentage
L1	8.06E+06	2.84E+08	1.44E+08	3.33E+08	7.69E+08	33.1%
L2	7.54E+06	2.73E+08	1.36E+08	3.19E+08	7.36E+08	31.7%
L3	6.02E+06	1.77E+08	1.03E+08	2.35E+08	5.21E+08	22.4%
R	1.63E+06	1.74E+08	3.76E+07	8.39E+07	2.97E+08	12.8%
		$^{206}Pb/^{204}Pb$	$^{207}Pb/^{204}Pb$	$^{208}Pb/^{204}Pb$		
L1		35.42	18.02	41.66		
L2		36.37	18.10	42.49		
L3		29.52	17.15	39.27		
R		108.6	23.39	52.26		
Calculated Whole Rock		43.75	18.54	42.74		
Measured Whole Rock		41.69	18.31	42.39		

Table 7.4 REE concentrations of five whole rock shale samples from the Karelian shales

Sample ID	UZF-3	UZF-7	UZF-8	UZF-11	UZF-12
Drill Core and Depth	C-25; 137.5m	C-207; 111m	C-5190; 85m	C-5190; 199m	C-5190; 204m
La	1.74	47.5	25.2	--	5.92
Ce	8.56	91.2	49.8	216	15.5
Nd	6.13	46.8	23.3	132	11.2
Sm	2.24	8.75	4.79	24.0	3.06
Eu	0.977	1.93	1.15	6.15	0.964
Gd	3.10	7.54	4.87	22.6	3.14
Dy	3.92	6.28	5.07	20.5	2.82
Er	2.38	3.48	2.84	11.2	2.02
Yb	2.24	3.19	2.39	9.71	2.06
La_N/Yb_N	0.51	9.84	6.96	--	1.90
La_N/Sm_N	0.47	3.31	3.21	--	1.18
Gd_N/Yb_N	1.11	1.90	1.64	1.86	1.23
Ce/Ce*	1.55	0.926	0.972	--	1.02
Eu/Eu*	1.15	0.733	0.734	0.816	0.961

Note: La concentration for UZF-11 was not determined

8. TIME-INTEGRATED CONSTRAINTS FOR ATMOSPHERIC OXYGEN EVOLUTION PROVIDED BY LEAD ISOTOPE RATIO AND RARE EARTH ELEMENT CONCENTRATION DATA

8.1 Discussion

The previous chapters contained within this dissertation have shown the importance of considering multiple hypotheses as the source of variable apparent model time-integrated Th/U ratios (κ_a) and interelement REE ratios. Amongst the evaluated hypotheses were:

(1) the observed variation in κ_a ratios is related to the redox decoupling of U from Th during the ancient weathering of the provenance component(s),

(2) the observed variation in κ_a ratios is a function of mixing two or more source components with different Th/U ratios during detrital transport,

(3) the observed variation in κ_a ratios is result of post-depositional mobilization of U or Pb due to metasomatic fluids,

which were evaluated using: (1) Pb-Pb ages of whole rock Pb isotope ratio analyses, (2) Pb-Pb ages of sequential acid leaching steps, (3) chondrite-normalized REE patterns, (4) sample-normalized REE patterns, (5) diagrams to compare the covariation of interelement REE and κ_a ratios.

8.1.1 Interpretation of Pb-Pb ages

The determination of Pb isotope ratios make it possible to interpret the significance of calculated apparent time-integrated Th/U ratios (κ_a) within the geochronologic context associated with the establishment of these ratios. Evaluation of the geochemical behavior and antiquity of the U-Th-Pb geochemical system is facilitated

through observation of the distribution of Pb isotope ratio data points plotted on $^{206}Pb/^{204}Pb$ vs. $^{207}Pb/^{204}Pb$ (uranogenic Pb isotope ratio) diagram and calculating Pb-Pb ages.

The geochemical behavior of the U-Th-Pb system of a lithostratigraphic unit may be interpreted as a closed system in geochemical equilibrium with its components if the data is displayed as a positively sloped array with little deviation from the best-fit line (i.e. a low MSWD) on a uranogenic Pb isotope diagram. Alternatively, this presentation of the data could be interpreted as the result of bimodal mixing of two sources with different Th/U ratios. The age associated with the establishment of the U-Th-Pb system can be determined through calculating the Pb-Pb age associated with the slope of the array of points on an uranogenic Pb isotope ratio diagram. For example, Pb-Pb age of the Sengoma Argillite Formation (2448 +260 / -450 Ma) overlaps the constraints for the depositional age for this unit (2.061 – 2.22 Ga). The consistency of the linear relationship between uranogenic isotope ratios (MSWD = 3.9) is accredited to the preservation of unaltered sedimentary geochemistry (Chapter 6). In contrast, the Pb-Pb age of the Mount McRae Shale (2402 ± 590 Ma) agrees with the 2501 ± 8.2 Ma Re-Os radiometric age for sedimentary pyrite from the same unit (Anbar et al., 2007), however the points do not represent a single array (Chapter 2). The "y-shaped" distribution and relative variation of the isotope ratio data points (MSWD = 16) is attributed to a disturbance in the U-Th-Pb system. The different interpretations can be further evaluated through Pb isotope ratios determined through sequential acid leaching.

The sequential acid leaching experiments were conducted in an effort to evaluate sample heterogeneity, the robustness of the minerals that contain Pb, and the contribution

of trace minerals to the U-Th-Pb budget. These factors were evaluated by comparing the percentage of Pb liberated during each leach step. The Pb isotope ratios of each leach step were plotted on Pb isotope ratio diagrams to evaluate the timing associated with the establishment of the U-Th-Pb system within each sample through the calculation of Pb-Pb ages. The Pb isotope ratio diagrams were also used to evaluate whether the Pb isotope ratios of the whole-rock sample lie within the area constrained by the Pb isotope ratios for the leached components. The interpretation of sample heterogeneity or disequilibrium was suggested by samples whose Pb isotope ratios of the leach steps fail to constrain the Pb isotope ratios of the whole rock. Those samples that had the majority of the Pb liberated during the first and second leach step were interpreted as having a greater probability of being altered by U and/or Pb mobilization.

The interpretation of the Pb-Pb age as an indication of the preservation of unaltered sedimentary geochemistry in the Sengoma Argillite Formation is reinforced by the Pb-Pb ages calculated for the Pb isotope ratio data from two samples that were leached by sequentially stronger acids (2180 ±450 Ma and 2136 ± 250 Ma). Most of the Pb was liberated during the second and third acid leaching steps, with over 50% of the Pb liberated during the second leach step. The distribution of Pb isotope ratios also supports the interpretation of a closed U-Th-Pb system since deposition.

The sequential acid leaching of the samples of the Mount McRae Shale reveal further lines of evidence that the U-Th-Pb geochemistry of the Mount McRae Shale was disturbed after deposition. The leached samples of the Mount McRae Shale (WLT-10; 381.0 m and WLT-02; 145.9 m) have Pb-Pb ages of 2297 ± 900 Ma and 1719 ± 9500 Ma. The sequential acid leaching of these samples results in the highest percentage of Pb

liberated in the first and second leach steps. The high degree of error and the variability of Pb-Pb ages observed for the leached samples are interpreted as further indications that the Mount McRae Shale may have experienced a post-depositional alteration to the U-Th-Pb system. Evaluating the distribution and fractionation of the REE is another geochemical tool used to evaluate the preservation of sedimentary geochemistry, due to similarities between the geochemistry of REE and that of U and Th.

8.1.2 Interpretation of REE patterns

Relative differences in REE patterns for a suite of sedimentary rocks can be quantified through interelement REE ratios. High variability of interelement REE ratios can be used to indicate differences in provenance sources or fractionation of the REE during post-depositional disturbances. In the absence of variable provenance sources or a post-depositional disturbance, REE patterns (and interelement REE ratios) should be relatively similar to one another. It is therefore through the interpretation of REE patterns and interelement ratios that we can confirm the interpretation of the Pb isotope ratio plots and evaluate the severity of post-depositional alteration. For example, the geochemical alteration of the U-Th-Pb system in the Mount McRae Shale did not alter the REE system, however evidence of geochemical alteration of the Huronian Supergroup and Karelian shales was visible in both the U-Th-Pb and REE systems.

8.1.3 Interpretation of κ_a through time

The interpretation of the time-integrated Th/U (κ_a) ratio depends heavily on the preservation of sedimentary geochemistry. This topic is addressed for units outside the

scope of this dissertation in Chapter 6 (section 6.3.2). This study illuminates the relative difficulty of finding a sedimentary unit of the appropriate age to constrain the onset of oxidative weathering (Late Archean or Early Proterozoic) that was not subjected to post-depositional geochemical alteration. From this study, only the rocks of the Timeball Hill and Sengoma Argillite formations permit the utility of calculated κ_a ratios as a paleoredox indicator of Paleoproterozoic weathering conditions. In many of the previous studies conducted to reveal the redox nature of the Precambrian atmosphere, no geochemical considerations were made to evaluate the potential alteration of the studied units.

8.2 Geochemical conclusions

The interpretation of geochemical data from the U-Th-Pb geochemical system provides geochemists with a paleoredox proxy that for the first time is integrated with geochronologic significance. The application of this radioactive geochemical system to addressing issues of variable redox conditions has been previously recognized (Faure, 1986; Krogstad, 2004; Krogstad et al., 2004), however it has not been used towards providing constraints on surficial redox conditions but in a few studies (Krogstad, 2004; Krogstad et al., 2004). Although the need for geochronologic significance to other paleoredox studies has been recognized, other studies have used Re-Os dating on sedimentary pyrite grains to establish the timing of the redox conditions recorded in the trace element geochemistry of the studied rock suites (Anbar et al., 2007; Hannah et al., 2004). Unfortunately these studies did not utilize the Re-Os system for the evaluation of paleoredox conditions bringing into question the relationship between Re-Os radiometric ages and the trace element geochemistry of the rock suites, as Mo and S are not part of

the Re-Os system. The method described within this dissertation for using the U-Th-Pb system highlights the interplay between the redox-sensitive behavior of U, the invariant behavior of Th, and their radioactive decay to different Pb isotopes making this the first use of an integrated geochronologic-redox proxy geochemical system in the attempt to better constrain the timing and the nature of the rise in atmospheric oxygen concentrations at the beginning of the Paleoproterozoic Era.

Evaluation of the overall appropriateness of using Pb isotopes and the derived quantity (κ; $^{232}Th/^{238}U$) as a geochemical paleoredox proxy as described in the chapters of this dissertation is essential to the proper use of this potentially powerful geochemical tool. The appropriateness is based largely on the preservation of the primary unaltered geochemistry of the rock suite being studied and is evaluated through the use of plots showing uranogenic Pb growth as well as chondrite-normalized and sample-normalized REE (rare earth elements) patterns. Once it has been determined that the original U-Th-Pb-REE geochemistry of the rock suite has been preserved since deposition, the variations in model time-integrated Th/U (κ_a) ratios can be interpreted as an indicator of paleoredox conditions.

8.2.1 Conclusions based on Pb isotope composition

It has been demonstrated that the application of Pb isotopic compositions to provide model time-integrated Th/U ratios (κ_a values) may be appropriate when plots of uranogenic Pb isotope ratios present themselves as linear arrays with a positive slope (greater than 0.0509; the slope of the tangent of the modeled present-day Pb isotope composition). Furthermore if the corresponding slope age is within error of the accepted

age of sedimentation for the discussed units, the geochemistry of these units may have been closed since sedimentation indicating that the κ_a value may actually represent the decoupling of U from Th during source weathering and detrital deposition. However if the Pb-Pb age differs significantly such that the slope age is older than the sedimentary age, it can be interpreted that U and Th were not equilibrated with the atmosphere or with seawater at the time of deposition. Therefore the values of κ_a determined for all of the units in this study should not interpreted as an indication of sedimentary redox conditions but rather the κ_a ratios may represent this inherited Th/U ratio. Similarly, a Pb-Pb age younger than the previously determined depositional age would yield κ_a ratios that are interpreted as being altered by post-depositional processes.

During the course of this study, most calculated Pb-Pb ages were within error of the accepted age of sedimentation. Those suites with calculated slope ages within error of the accepted sedimentary age (Timeball Hill and Sengoma Argillite Formation) were considered undisturbed (closed) with respect to the U-Th-Pb geochemical system and the calculated values of κ_a ratios from these suites are therefore considered a measure of the coherence of U and Th during sedimentary processes. In the case of slope ages being younger than sedimentary ages (Huronian Supergroup and Karelian shales), the calculated values of κ_a represent the influence of geochemical alteration on the U-Th-Pb system at the time indicated by the Pb-Pb age.

The Pb isotope compositions of leached solutions and the residue produced during sequential step-wise acid leaching of the samples were evaluated for sample heterogeneity, the robustness of the minerals that contain Pb, and the contribution of trace minerals to the U-Th-Pb budget. The samples were strategically selected from each

sample suite based on the value of its whole rock κ_a ratio and stratigraphic relationship to other samples. Pb isotope ratio plots of resultant leachates reveal that the leachates and the residue define a slope that corresponds to a Pb-Pb age for the sample. The sample Pb-Pb age is compared to the whole rock Pb-Pb and the accepted age constraints for the depositional age of the studied unit. The interpretation of the sample Pb-Pb age (from sequential acid leaching) is conducted in a similar manner to that of the whole rock Pb-Pb age, however the Pb isotope ratios for some leach steps do not vary significantly resulting in large errors and future Pb-Pb ages. The κ_a ratios of the leach steps are often evaluated using the Pb-Pb age of the whole rock, but on occasion when the whole rock Pb-Pb age of the unit does not correspond to the depositional age and the sample Pb-Pb age is not within error of the depositional age or the whole rock Pb-Pb age, the significance of the κ_a ratios is difficult to interpret.

8.2.2 Conclusions based on rare earth element concentrations

The redistribution of trace elements (i.e. U, Th, Pb) during post-depositional processes can be additionally monitored through analysis of the REE, because these elements (also called the lanthanide group elements) are generally regarded as natural analogs for the actinide group elements (see Chapter 1). Although this does not take into consideration the mobility of Pb, as Pb is not an actinide group element, it is unlikely that Pb would be mobilized due to its low solubility in most fluids and furthermore unlikely that Pb isotopes would be appreciably fractionated during post-depositional redistribution events. The well-characterized geochemical behavior of the REE under various conditions results in our ability to recognize REE fractionation patterns indicative of

sedimentary processes as well as those that have been disturbed by post-depositional processes.

In order to accommodate the natural variations observed between neighboring REE on the periodic table of the elements, concentrations are normalized to a reference material. In the choice of normalizing material is not trivial, but rather is essential to any interpretation of the resultant REE patterns (see Chapter 5). Generally, rock samples that display similar REE pattern morphologies are interpreted as a common provenance source of REE within those samples. In the case of clastic sedimentary rocks, this relates to a common provenance for the detrital fraction of the rocks (Chapters 3 and 6), whereas similar REE patterns in chemical sedimentary rocks may indicate the same process is responsible for the formation of the samples studied (Chapter 5).

When Pb isotope composition data is interpreted as evidence of disturbance to the whole-rock geochemistry by post-depositional processes (e.g., ancient weathering, tectonic, or hydrothermal event), the inconsistency of interelement REE ratios (i.e., La_N/Yb_N, La_N/Sm_N, Eu/Eu*) provides further support for alteration. The use of interelement REE ratios enables a quantitative evaluation of the overall consistency of REE patterns, a measure of potential geochemical alteration. Because the REE behave in a coherent manner, increased variability of these ratios further suggests that the geochemical system has been disturbed since deposition, making interpretations based on geochemical proxies suspicious. Interpretations based on interelement REE ratios have been used to show that shales from the Timeball Hill and Sengoma Argillite formations each have homogeneous provenance components despite their difference in geochronologic age (Chapter 3 and 5). The similarity of these REE patterns have been

used to suggest that the REE concentrations of chemical sedimentary rocks of the Hotazel Formation would be best normalized by a Sengoma Argillite Formation sample. The consistency of shale-normalized REE patterns for samples of the Hotazel Formation was interpreted such that the REE geochemistry of the unit is unaltered and that REE anomalies may represent paleoredox conditions associated with sediment deposition (Chapter 4). Also, the interelement REE ratios of samples from the Mount McRae Shale show variation are interpreted as the result of redistribution during a 465 Ma tectonic event (Chapter 2). Inconsistent REE patterns and interelement REE ratios along with whole rock Pb-Pb ages that are younger than the depositional age and sample Pb-Pb ages that do not agree with either the age are interpreted as indications of metasomatic alteration of the shales of Huronian Supergroup and the Lake Onega area (Chapters 3 and 7).

Cerium (Ce) and europium (Eu) anomalies also provide a potential quantitative measure of redox conditions as these REE have varying oxidation states depending upon the redox conditions. Although Eu-anomalies (Eu/Eu*) have long been used to determine redox conditions within magmatic systems, it appears as if they are not affected by conditions of surficial weathering and therefore are not useful for the purposes of studying surficial redox conditions. Instead Eu-anomalies are treated as an interelement ratio and used to indicate the consistency of detrital source materials (the flux of hydrothermal Eu is trivial compared to the detrital flux). In contrast, the oxidation state of Ce has been shown to be susceptible to variable surficial redox conditions and therefore Ce-anomalies (Ce/Ce*) can be used as indicators of paleoredox conditions. The presence of a Ce-anomaly is indicative of changes in the oxidation state of Ce and

therefore the environment. Ce-anomalies in chemically precipitated sedimentary rocks appear to be far more sensitive to changes in redox conditions when compared to the same variable in clastic sedimentary rocks. This is most likely due to the overwhelming lack of chemical equilibration of the REE in the detritus with river water and seawater, resulting in a preservation of pre-weathering Ce-anomalies. In samples of 2.22 Ga banded iron formation, the relative enrichment in Ce (compared to modern seawater) is indicative of different concentrations of oxygen in seawater at the time of sediment deposition (Chapter 5).

The interpretations of Ce-anomalies and Eu-anomalies have been incorporated into discussions regarding interelement REE ratios, in the previous chapters. It is only in the case of the Hotazel Formation that these ratios have proven essential to the paleoredox interpretation of the geochemistry of the whole rock samples. There it can be shown that although shale-normalized Eu-anomalies from the Hotazel Formation show little difference when compared with modern seawater, the Ce-anomalies vary greatly showing a vast difference in the cerium cycle between the middle of the Paleoproterozoic Era and today. This difference cannot be shown to exist in the europium cycle and is likely only resolved using isotope-dilution mass spectrometry (IDMS) data.

8.3 Conclusions for the onset of oxidative uranium weathering during the Great Oxidation Event

It has been established by many geochemical studies that a significant rise in the concentration of atmospheric oxygen occurred near the beginning of the Paleoproterozoic Era (between 2.45 and 2.32 Ga), which fundamentally changed the geochemical and

biogeochemical pathways of many major and trace elements. Although the timing of this unidirectional rise in atmospheric oxygen is not disputed, the timing of the resultant oxidative weathering of exposed rock units appears to be variable for each geochemical system considered. The oxidative weathering of uranium can be evaluated through the comparative geochemical behavior of U and Th effecting Th/U ratios. Because Th/U ratios are susceptible to resetting during post-depositional processes (e.g. modern and ancient weathering, metasomatism) and mixing of provenance components can result in variable Th/U ratios it is essential to evaluate multiple geochemical parameters. In the absence of post-depositional alteration, the time-integrated Th/U ratios κ_a can be used to evaluate paleoredox conditions during the sedimentary process.

A previous study has revealed that the U-Th-Pb system shows no indications of U-Th decoupling during sedimentary events associated with the deposition of the shales of the ca. 3.0 Ga Buhwa greenstone belt (Krogstad et al., 2004). This provides a baseline to which subsequent studies can be compared, as few would argue for oxygenation of the atmosphere three billion years ago. Research for this dissertation study used IDMS REE concentration data to refine the interpretations of the observed variations in κ_a for samples from the 2501 Ma Mount McRae Shale, ca. 2.4 Ga Huronian Supergroup, ca. 2.32 Ga Timeball Hill Formation, ca. 2.15 Ga Sengoma Argillite Formation, and the ca. 2.0 Ga upper Zaonezhskaya Formation.

The REE geochemistry and uranogenic Pb isotope ratios ($^{207}Pb/^{204}Pb$ and $^{206}Pb/^{204}Pb$) of the Mount McRae Shale are interpreted as resulting from a disruption to the U-Th-Pb system at 465 Ma or the presence of multiple provenance components, which renders the interpretation of all of the values of κ_a as an indicator of paleoredox

conditions inappropriate (Chapter 2). The presence of a slope defined by several samples on a uranogenic Pb isotope plot ($^{207}Pb/^{204}Pb$ vs. $^{206}Pb/^{204}Pb$) is potentially significant however no other geochemical distinction could be made to differentiate these samples from others and therefore the data were treated as one group. Although this does not provide constraints to the rise of oxidative U weathering, it demonstrates the effectiveness of the U-Th-Pb system at determining appropriate stratigraphic units for paleoredox studies. Additionally, it introduces suspicion to previous studies that have claim to have found geochemical evidence of local oxygen oases or "whiffs" of atmospheric oxygen in multiple geochemical proxies from several sedimentary units that predate Great Oxidation Event (Anbar et al., 2007; Ohmoto, 1997; Ohmoto et al., 2006).

The Pb isotope composition of the McKim and Pecors Formations of the ca. 2.4 Ga Huronian Supergroup (Chapter 3) are interpreted as indicating highly variable yet considerable enrichments of uranium compared to thorium (87 ± 74%) that were established at 1771 Ma (± 160 Ma). This date is representative of the timing of the last disruption to the U-Pb system and significantly postdates the sedimentary age of the units. The signature of oxidation should not be interpreted as a "whiff" of oxygen predating the Great Oxidation Event but as a post-depositional alteration effect associated with the 1.8 Ga Penokean Orogeny. This interpretation is supported by the REE geochemistry, which displays three distinct chondrite-normalized REE patterns indicative of redistribution of the REE during a post-depositional event or the presence of at least three distinct provenance components. This interpretation does not eliminate the possibility of oxidative weathering at 2.4 Ga but does not support it either.

The geochemistry of the Timeball Hill Formation (Chapter 4) has been the focus of other attempts to constrain the evolution of oxygen concentrations during the Paleoproterozoic Era and therefore it is important to ascertain its U-Th-Pb geochemistry. The Pb isotope composition indicates a decoupling of U from Th that occurred during sedimentary processes. The variation in values of κ_a (2.58 +0.31/-0.41) suggests an enrichment of 52% excess uranium (+26/-19) assuming that Th concentrations are conservative and that Th/U ratio of the provenance component(s) is consistent. These two assumptions are supported by consistent chondrite-normalized REE pattern morphologies and interelement REE ratios, which suggest a single provenance (or alternatively multiple well-mixed sources) of the REE (see Chapter 1). The consistency of the detrital source components and the variability of the κ_a values are interpreted as meaning that oxidative weathering reactions were active by 2.32 Ga and released dissolved hexavalent uranium (as uranyl complexes) into the oceans. The dissolved uranium was then precipitated into the sediments by reduction to the insoluble tetravalent uranium, as occurs in modern suboxic and anoxic sedimentary basins (Klinkhammer and Palmer, 1991; Yamada and Tsunogai, 1984).

The Sengoma Argillite Formation (Chapter 6) became a focus of this study because the chondrite-normalized REE patterns and interelement REE ratios were highly consistent. Furthermore the uranogenic Pb isotopes define a slope with an age within error of the sedimentary age, implying that any observed uranium enrichment is the result of sedimentary processes. The Pb isotopic composition indicates that uranium enrichments of up to 120% exist and average 55% (± 39% 1σ). The consistency of the REE data and the interpretation of the Pb isotope composition data, imply that the

oxidative part of the uranium cycle was not only established by 2.32 Ga but that it persisted through 2.15 Ga and likely beyond.

The geochemistry of Pb and the REE was determined for the ca. 2.0 Ga Zaonezhskaya Formation (Chapter 7) in an attempt to support this hypothesis of continued oxidation of uranium. The uranogenic Pb isotope ratios of the samples have a slope age of 1786 Ma (± 230 Ma), which is marginally within the stratigraphically constrained sedimentary age (2.1-2.0 Ga). Despite the near concordance in geochronology, the variability of morphologies observed for chondrite-normalized REE patterns and the lack of consistent interelement REE ratios for the rocks from this formation, eliminate the possibility that calculated time-integrated Th/U ratios could be used as a proxy for paleoredox conditions in these samples. The state of oxidation of the post-2.15 Ga atmosphere is therefore only constrained by modern conditions and other studies that have incorporated both IDMS REE data and Pb isotope compositions.

In addition to time-integrated Th/U ratios, the interpretation of REE data, particularly Ce-anomalies, has provided support for the rise of atmospheric oxygen. The ca. 2.2 Ga Hotazel Formation (Chapter 5), as preserved in the Mamatwan Mine where the samples were collected, is comprised of primary Mn ore and layers of BIF. The chondrite-normalized REE patterns of each type display LREE enrichment that is interpreted as the influence of detrital material. In an attempt to "see-through" this detrital signal, the average REE concentrations of the Hotazel Formation were normalized to those of a representative shale from the Sengoma Argillite Formation. Shale-normalized REE patterns of both groups display patterns that are very similar to shale-normalized REE patterns for modern seawater, with the exception of Ce. The

similarity is interpreted as the result of the preservation of the chemical composition of Paleoproterozoic seawater through chemical precipitation of these rocks. The amount of Ce precipitated is controlled by the presence of co-precipitating oxide mineral phases and the availability of oxygen, as Ce is found associated with ferromanganese nodules (Fe-Mn oxides) as CeO_2 in modern sediments. Because the magnitude of the Ce-anomaly is the only appreciably difference observed (both ancient and modern seawater display negative Ce-anomalies) they likely reflect lower concentrations of available oxygen in the oceans during the Paleoproterozoic Era. The results of these different portions of the study are summarized in Figure 8.1.

This study has shown that many previous studies using geochemical proxies of paleoredox conditions did not fully address the influence of post-depositional disturbances to the overall geochemistry of the sedimentary units. Additionally, these studies have not had the ability to determine an integrated radiometric age for the establishment of the geochemical proxies. This may have the undesired effect of introducing data that has been erroneously interpreted as suggesting oxygenation but might instead be indicative of inorganic or organic processes. Although this study has not had the intended effect of increasing our understanding of the timing or nature of the rise of atmospheric oxygen, it has reaffirmed our current models with time-integrated geochemical proxy data for paleoredox conditions. Additionally, it is a landmark study in choosing appropriate geochemical proxies for ancient weathering conditions and the importance of being able to determine the geologic timeframe during which the geochemical proxy was established. It also opens possibilities for studies to continue with the due diligence displayed in this work and address sedimentary units deposited at

other time periods of interest (e.g., Archean-Proterozoic boundary, pre-2.32 Ga, periods of Oceanic Anoxia Events).

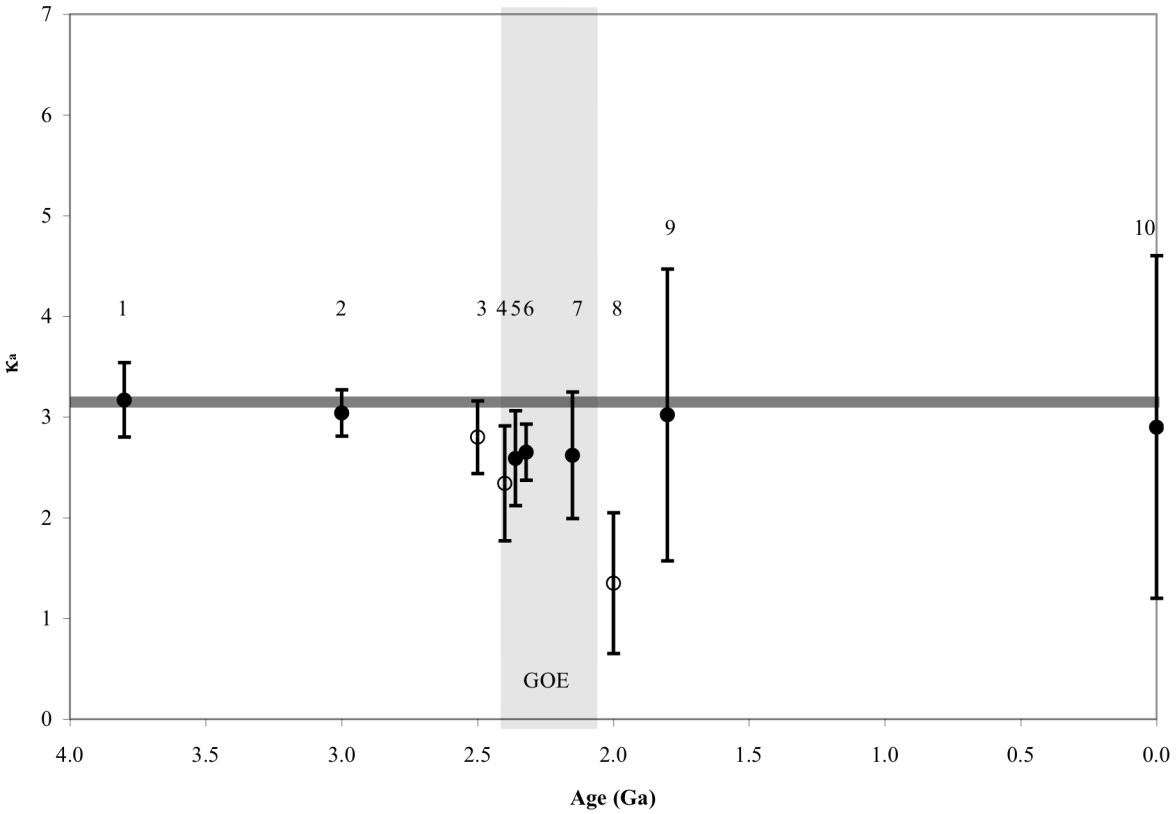

Figure 8.1 κ_a values for shale suites deposited throughout geologic time. The sample suites used in this plot come from the (1) ca. 3.8 Ga Isua Supracrustal belt, Greenland (Rosing and Frei, 2004), (2) ca. 3.05 Ga Buhwa shales, Buhwa greenstone belt, Zimbabwe (Krogstad et al., 2004), (3) 2501 Ma Mount McRae Shale, western Australia, (4) ca. 2.4 Ga Huronian Supergroup, Ontario, Canada (this study), (5) ca. 2.4 Ga Huronian Supergroup, Ontario, Canada (McLennan et al., 2000), (6) ca. 2.32 Timeball Hill Formation, South Africa (this study), (7) ca. 2.15 Ga Sengoma Argillite Formation, Botswana (this study), (8) ca. 2.0 Ga upper Zaonezhskaya Formation, Karelia, Russia, (9) ca. 1.8 Ga Hondo Group, southwestern USA (McLennan et al., 1995), and (10) modern turbiditic muds (Hemming and McLennan, 2001). The κ_a value for the average marine shale (3.2; Turekian and Wedepohl, 1961) is shown by grey horizontal line for reference. Open circles indicate κ_a ratio values for those units that appear altered (see text). The κ_a values for all suites are close to that for the average marine shale. Notably, Archean suites show little variations from this value, whereas starting as early as ca. 2.4 Ga, but definitely by ca. 2.32 Ga, shale suites show increased variation in κ_a values. This increased variation is likely due to the initiation of oxidative continental weathering by ca. 2.32 Ga, at the latest.

REFERENCES

Abdelouas, A., Lutze, W., Gong, W., Nuttall, E.H., Strietelmeier, B.A. and Travis, B.J., 2000. Biological reduction of uranium in groundwater and subsurface soil. The Science of the Total Environment, 250: 21-35.

Akagi, T., Nakai, S. and Masuda, A., 1994. The tetrad effect, a general effect in partitioning of REE between aqua and solid. Mineralogical Magazine, 58A: 7-8.

Alexander, B.W., Bau, M., Andersson, P. and Dulski, P., 2008. Continentally-derived solutes in shallow Archean seawater: Rare earth element and Nd isotope evidence in iron formation from the 2.9 Ga Pongola Supergroup, South Africa. Geochimica et Cosmochimica Acta, 72: 378-394.

Anbar, A.D., Duan, Y., Lyons, T.W., Arnold, G.L., Kendall, B., Creaser, R.A., Kaufman, A.J., Gordon, G.W., Scott, C., Garvin, J. and Buick, R., 2007. A Whiff of Oxygen Before the Great Oxidation Event? Science, 317: 1903-1906.

Anderson, R.F., Fleisher, M.Q. and LeHuray, A.P., 1989. Concentration, oxidation state, and particulate flux of uranium in the Black Sea. Geochimica et Cosmochimica Acta, 53: 2215-2224.

Anderson, R.F., LeHuray, A.P., Fleisher, M.Q. and Murray, J.W., 1989. Uranium deposition in Saanich Inlet sediments, Vancouver Island. Geochimica et Cosmochimica Acta, 53: 2205-2213.

Andrews, A.J., Masliwec, A., Morris, W.A., Owsiacki, L. and York, D., 1986. The silver deposits at Cobalt and Gowganda, Ontario. II: an experiment in age determinations employing radiometric and paleomagnetic measurements. Canadian Journal of Earth Sciences, 23: 1507-1518.

Awwiller, D.N., 1994. Geochronology and mass transfer in Gulf Coast mudrocks (south-central Texas, U.S.A.): Rb-Sr, Sm-Nd, and REE systematics. Chemical Geology, 116: 61-84.

Baker, J., Waight, T. and Ulfbeck, D., 2002. Rapid and highly reproducible analysis of rare earth elements by multiple collector inductively coupled plasma mass spectrometry. Geochimica et Cosmochimica Acta, 66: 3635-3646.

Barley, M.E., Bekker, A., and Krapez, B., 2005. Late Archean to Early Paleoproterozoic global tectonics, environmental change and the rise of atmospheric oxygen. Earth and Planetary Science Letters, 238: 156-171.

Barnes, C.E. and Cochran, J.K., 1990. Uranium removal in oceanic sediments and the oceanic U balance. Earth and Planetary Science Letters, 97: 94-101.

Barnes, C.E. and Cochran, J.K., 1993. Uranium geochemistry in estuarine sediments: Controls on removal and release processes. Geochimica et Cosmochimica Acta, 57: 555-569.

Bau, M., Beukes, N.J. and Romer, R.L., 1998. Increase of oxygen in the Earth's atmosphere and hydrosphere between ~2.5 and ~2.4 Ga B.P. Mineralogical Magazine, 62A: 127-128.

Bau, M. and Dulski, P., 1992. Small-scale variations of the rare-earth element distribution in Precambrian iron formations. European Journal of Mineralogy, 4: 1429-1433.

Bau, M. and Dulski, P., 1996. Distribution of yttrium and rare-earth elements in the Penge and Kuruman iron-formations, Transvaal Supergroup, South Africa. Precambrian Research, 79: 37-55.

Bau, M., Höhndorf, A., Dulski, P. and Beukes, N.J., 1997. Sources of rare-earth elements and iron in Paleoproterozoic iron-formations from the Transvaal Supergroup, South Africa: Evidence from neodymium isotopes. Journal of Geology, 105: 121-129.

Bau, M. and Möller, P., 1993. Rare earth element systematics of the chemically precipitated component in Early Precambrian iron formations and the evolution of the terrestrial atmosphere-hydrosphere-lithosphere system. Geochimica et Cosmochimica Acta, 57: 2239-2249.

Bau, M., Romer, R.L., Luders, V. and Beukes, N.J., 1999. Pb, O, and C isotopes in silicified Mooidraai dolomite (Transvaal Supergroup, South Africa): implications for the composition of Paleoproterozoic seawater and 'dating' the increase of oxygen in the Precambrian atmosphere. Earth and Planetary Science Letters, 174: 43-57.

Bekker, A., Beukes, N.J., Holmden, C., Kenig, F. and Eglington, B., 2008. Fractionation between inorganic and organic carbon during the Lomagundi (2.22-2.1 Ga) carbon isotope excursion. Earth and Planetary Science Letters, 271: 278-291.

Bekker, A., Holland, H.D., Wang, P.L., Rumble, D., III, Stein, H.J., Hannah, J.L., Coetzee, L.L. and Beukes, N.J., 2004. Dating the rise of atmospheric oxygen. Nature, 427: 117-120.

Bekker, A. and Kaufman, A.J., 2007. Oxidative forcing of global climate change: A biogeochemical record across the oldest Paleoproterozoic ice age in North America. Earth and Planetary Science Letters, 258: 486-499.

Bekker, A., Kaufman, A.J., Karhu, J.A., Beukes, N.J., Swart, Q.D., Coetzee, L.L. and Eriksson, K.A., 2001. Chemostratigraphy of the Paleoproterozoic Duitschland Formation, South Africa: implications for coupled climate change and carbon cycling. American Journal of Science, 301: 261-285.

Bekker, A., Kaufman, A.J., Karhu, J.A. and Eriksson, K.A., 2005. Evidence for Paleoproterozoic cap carbonates in North America. Precambrian Research, 137: 167-206.

Bertram, C.J. and Elderfield, H., 1993. The geochemical balance of the rare earth elements and neodymium isotopes in the oceans. Geochimica et Cosmochimica Acta, 57: 1957-1986.

Beukes, N.J. and Klein, C., 1990. Geochemistry and sedimentology of a facies transition - from microbanded to granular iron-formation - in the early Proterozoic Transvaal Supergroup, South Africa. Precambrian Research, 47: 99-139.

Bhatia, M.P. and Crook, K.A.W., 1986. Trace element characteristics of graywackes and tectonic setting discrimination of sedimentary basins. Contributions to Mineralogy and Petrology, 92: 181-193.

Bierlein, F.P., 1995. Rare-earth element geochemistry of clastic and chemical metasedimentary rocks associated with hydrothermal sulphide mineralisation in the Olary Block, South Australia. Chemical Geology, 122: 77-98.

Blake, T.S. (Editor), 1984. The lower Fortescue Group of the northern Pilbara Craton; stratigraphy and paleogeography. Archaean and Proterozoic basins of the Pilbara, Western Australia: Evolution and Mineralization Potential, 9, University of Western Australia, Perth.

Blake, T.S. and Barley, M.E., 1992. Tectonic evolution of the Late Archaean to Early

Proterozoic Mount Bruce Megasequence Set, Western Australia. Tectonics, 11: 1415-1425.

Bock, B., McLennan, S.M., and Hanson G.N., 1994. Rare earth element redistribution and its effects on the neodymium isotope system in the Austin Glen Member of the Normanskill Formation, New York, USA. Geochimica et Cosmochimica Acta, 58: 5245-5253.

Bolhar, R., Kamber, B.S., Moorbath, S., Fedo, C.M. and Whitehouse, M.J., 2004. Characterisation of early Archean chemical sediments by trace element signatures. Earth and Planetary Science Letters, 222: 43-60.

Brookins, D.G., 1989. Aqueous geochemistry of rare earth elements. In: B.R. Lipin and G.A. McKay (Editors), Reviews in Mineralogy - Geochemistry and Mineralogy of Rare Earth Elements. Mineralogical Society of America, pp. 201-225.

Buick, I.S., Maas, R. and Gibson, R., 2001. Precise U-Pb titanite age constraints on the emplacement of the Bushveld Complex, South Africa. Journal of the Geological Society of London, 158: 3-6.

Button, A., 1973a. Algal stromatolites of the early Proterozoic Wolkberg Group, Transvaal Sequence. Journal of Sedimentary Research, 43: 160-167.

Button, A., 1973b. The depositional history of the Wolkberg proto-basin, Transvaal. Transactions of the Geological Society of South Africa, 76: 15-25.

Button, A., 1975. A paleocurrent study of the Dwaal Heuvel Formation, Transvaal Supergroup. Transactions of the Geological Society of South Africa, 78: 173-183.

Byrne R. H. and Kim K.-H., 1990. Rare earth element scavenging in seawater. Geochimica et Cosmochimica Acta, 54: 2645-2656.

Cameron, E.M., 1982. Sulphate and sulphate reduction in early Precambrian oceans. Nature, 296: 145-148.

Canfield, D.E., 2005. The Early History of Atmospheric Oxygen: Homage to Robert M. Garrels. Annual Review of Earth and Planetary Sciences, 33: 1-36.

Canfield, D.E., Habicht, K.S. and Thamdrup, B., 2000. The Archean Sulfur Cycle and the Early History of Atmospheric Oxygen. Science, 288: 658-661.

Cantrell K. J. and Byrne R. H., 1987. Rare earth element complexation by carbonate and oxalate ions. Geochimica et Cosmochimica Acta: 51, 597-605.

Card, K.D., 1978. Metamorphism of the Middle Precambrian (Aphebian) rocks of the eastern southern province, metamorphism in the Canadian Shield. Geological Survey of Canada Paper 78-10, 269-282 pp.

Carpenter, A.B., Trout, M.L. and Pickett, E.E., 1974. Preliminary report on the origin and chemical evolution of lead- and zinc-rich oil field brines in central Mississippi. Economic Geology, 69: 1191-1206.

Christiansen, E.H., Burt, D.M., Sheridan, M.F. and Wilson, R.T., 1983. The petrogenesis of topaz rhyolites from the western United States. Contributions to Mineralogy and Petrology, 83: 16-30.

Cloud, P.E., 1968. Atmospheric and Hydrospheric Evolution on the Primitive Earth. Science, 160: 729-736.

Cocherie, A., Calvez, J.Y. and Oudin-Dunlop, E., 1994. Hydrothermal activity as recorded by Red Sea sediments; Sr-Nd isotopes and REE signatures. Marine Chemistry, 118: 291-302.

Cochran, J.K., Carey, A.E., Sholkovitz, E.R. and Surprenant, L.D., 1986. The geochemistry of uranium and thorium in coastal marine sediments and sediment

pore waters. Geochimica et Cosmochimica Acta, 50: 663-680.
Coetzee, L. L.. Genetic Stratigraphy of the Paleoproterozoic Pretoria Group in the Western Transvaal, M.Sc. Thesis, Rand Afrikaans Univ. (2001).
Condie, K.C., Dengate, J. and Cullers, R.L., 1995. Behavior of rare earth elements in a paleoweathering profile on granodiorite in the Front Range, Colorado, USA. Geochimica et Cosmochimica Acta, 59: 279-294.
Cornell, D.H., Schütte, S.S. and Eglington, B.L., 1996. The Ongeluk basaltic andesite formation in Griqualand West, South Africa: submarine alteration in a 2222 Ma Proterozoic sea. Precambrian Research, 79: 101-123.
DeBaar, H.J.W., 1991. On cerium anomalies of the Saragasso Sea. Geochimica et Cosmochimica Acta, 55: 2981-2983.
Derry, L.A. and Jacobsen, S.B., 1990. The chemical evolution of Precambrian seawater: evidence from REEs in banded iron formations. Geochimica et Cosmochimica Acta, 54: 2965-2977.
Doe, B.R., Stuckless, J.S. and Delevaux, M.H., 1983. The possible bearing of the granite of the UPH deep drill holes, northern Illinois, on the origin of Mississippi Valley ore deposits. Journal of Geophysical Research, 88: 7335-7345.
Dorland, H.C., 2004. Provenance ages and timing of sedimentation of selected Neoarchean and Paleoproterozoic successions of the Kaapvaal Craton, Rand Afrikaans University, Johannesburg, South Africa, 326 pp.
Drever, J.I., 1997. The Geochemistry of Natural Waters. Prentice Hall, Upper Saddle River, NJ, 436 pp.
Duddy, I.R., 1980. Redistribution and fractionation of rare-earth and other elements in a weathering profile. Chemical Geology, 30: 363-381.
Dymek, R.F. and Klein, C., 1988. Chemistry, petrology, and origin of banded iron-formation lithologies from the 3800 Ma Isua Supracrustal Belt, West Greenland. Precambrian Research, 39: 247-302.
Elderfield, H. and Greaves, M.J., 1982. The rare earth elements in seawater. Nature, 296: 214-219.
Elderfield, H. and Greaves, M.J., 1983. In: C.S. Wong, E. Boyle, K.W. Bruland, J.D. Burton and E.D. Goldberg (Editors), Trace Metals in Sea Water. NATO Conference Series, IV, Marine Sciences. Plenum Press, New York, pp. 920.
Elderfield, H. and Sholkovitz, E.R., 1987. Rare earth elements in the pore waters of reducing nearshore sediments. Earth and Planetary Science Letters, 82: 280-288.
Elderfield, H., Whitfield, M., Burton, J.D., Bacon, M.P. and Liss, P.S., 1988. The Oceanic Chemistry of the Rare-Earth Elements. Philosophical Transactions of the Royal Society of London, Series A, 325: 105-126.
England, G.L., Rasmussen, B., Krapez, B. and Groves, D.I., 2002. Palaeoenvironmental significance of rounded pyrite in siliciclastic sequences of the Late Archaean Witwatersrand Basin: oxygen-deficient atmosphere or hydrothermal alteration? Sedimentology, 49: 1133-1156.
Eriksson K.A., 1973. The Timeball Hill Formation – a fossil delta. Journal of Sedimentary Research, 43: 1046-1053.
Eriksson, P.G., Reczko, B.F.F., 1998. Contourites associated with pelagic mudrocks and distal delta-fed turbidites in the Lower Proterozoic Timeball Hill Formation epeiric basin (Transvaal Supergroup), South Africa. Sedimentary Geology. 120:

319– 335.
Eriksson, P.G., Hattingh, P.J. and Altermann, W., 1995. An overview of the geology of the Transvaal Sequence and Bushveld Complex, South Africa. Mineralium Deposita, 30: 98-111.
Eriksson, P.G. and Reczko, B.F.F., 1995. The sedimentary and tectonic setting of the Transvaal Supergroup floor rocks to the Bushveld Complex. Journal of African Earth Sciences, 21: 487-504.
Evans, O.C. and Hanson, G.N., 1993. Accessory-mineral fractionation of rare-earth element (REE) abundances in granitoid rocks. Chemical Geology, 110: 69-93.
Farquhar, J., Bao, H. and Thiemens, M., 2000. Atmospheric influence of Earth's earliest sulfur cycle. Science, 289: 756-758.
Faure, G., 1986. Principles of Isotope Geology. John Wiley and Sons, New York, 608 pp.
Fedo, C.M., Eriksson, K.A. and Krogstad, E.J., 1996. Geochemistry of shales from the Archean (~3.0 Ga) Buhwa Greenstone Belt, Zimbabwe: Implications for provenance and source-area weathering. Geochimica et Cosmochimica Acta, 60: 1751-1763.
Fedo, C.M., Nesbitt, H.W., Young, G.M., 1995. Unraveling the effects of potassium metasomatism in sedimentary rocks and paleosols, with implications for paleoweathering conditions and provenance. Geology, 23: 921-924.
Fralick, P.W. and Miall, A.D., 1989. Sedimentology of the Lower Huronian Supergroup (Early Proterozoic), Elliot Lake area, Ontario, Canada. Sedimentary Geology, 63: 127-153.
Fredrickson, J.K., Zachara, J.M., Kennedy, D.W., Liu, C., Duff, M.C., Hunter, D.B. and Dohnalkova, A., 2002. Influence of Mn oxides on the reduction of uranium(VI) by the metal-reducing bacterium *Shewanella putrefaciens*. Geochimica et Cosmochimica Acta, 66: 3247-3262.
Frei, R., Dahl, P.S., Duke, E.F., Frei, K.M., Hansen, T.R., Frandsson, M.M. and Jensen, L.A., 2008. Trace element and isotopic characterization of Neoarchean and Paleoproterozoic iron formations in the Black Hills (South Dakota, USA): Assessment of chemical change during 2.9-1.9 Ga deposition bracketing the 2.4-2.2 Ga first rise of atmospheric oxygen. Precambrian Research, 162: 441-474.
Frei, R. and Kamber, B.S., 1995. Single mineral Pb-Pb dating. Earth and Planetary Science Letters, 129: 261-268.
Frei, R., Nagler, T.F., Schonberg, R. and Kramers, J.D., 1998. Re-Os, Sm-Nd, U-Pb, and stepwise lead leaching isotope systematics in shear-zone hosted gold mineralization: Genetic tracing and age constraints of crustal hydrothermal activity. Geochimica et Cosmochimica Acta, 62: 1925-1936.
Fryer, B.J., 1977. Rare earth evidence in iron-formations for changing Precambrian oxidation states. Geochimica et Cosmochimica Acta, 41: 361-367.
German, C.R. and Elderfield, H., 1990. Application of the Ce anomaly as a paleoredox indicator; the ground rules. Paleoceanography, 5: 823-833.
German, C.R. and Elderfield, H., 1990. Rare earth elements in the NW Indian Ocean. Geochimica et Cosmochimica Acta, 54: 1929-1940.
German, C.R., Masuzawa, T., Greaves, M.J., Elderfield, H. and Edmond, J.M., 1995. Dissolved rare earth elements in the Southern Ocean: Cerium oxidation and the influence of hydrography. Geochimica et Cosmochimica Acta, 59: 1551-1558.

Gleason, J.D., Marikos, M.A., Barton, M.D. and Johnson, D.A., 2000. Neodymium isotopic study of rare earth element sources and mobility in hydrothermal Fe oxide (Fe-P-REE) systems. Geochimica et Cosmochimica Acta, 64: 1059-1068.

Glikson, A. and Vickers, J., 2007. Asteroid mega-impacts and Precambrian banded iron formations: 2.63 Ga and 2.56 Ga ejecta/fallout at the base of the BIF/argillite units, Hamersley Basin, Pilbara Craton, Western Australia. Earth and Planetary Science Letters, 254: 214-226.

Gao, S. and Wedepohl, K.H., 1995. The negative Eu anomaly in Archean sedimentary rocks: Implications for decomposition, age and importance of their granitic sources. Earth and Planetary Science Letters, 133: 81-94.

Greaves, M.J., Elderfield, H. and Klinkhammer, G.P., 1989. Determination of the rare earth elements in natural waters by isotope-dilution mass spectrometry. Analytica Chimica Acta, 218: 265-280.

Greaves, M.J., Rudnicki, M. and Elderfield, H., 1991. Rare earth elements in the Mediterranean Sea and mixing in the Mediterranean outflow. Earth and Planetary Science Letters, 103: 169-181.

Gromet, L.P., Haskin, L.A., Korotev, R.L. and Dymek, R.F., 1984. The "North American shale composite": Its compilation, major and trace element characteristics. Geochimica et Cosmochimica Acta, 48: 2469-2482.

Gromet, L.P. and Silver, L.T., 1983. Rare earth element distributions among minerals in a granodiorite and their petrogenetic implications. Geochimica et Cosmochimica Acta, 47: 925-939.

Gutzmer, J. and Beukes, N.J., 1997. Effects of mass transfer, compaction and secondary porosity on hydrothermal upgrading of Paleoproterozoic sedimentary manganese ore in the Kalahari manganese field, South Africa. Mineralium Deposita, 32: 250-256.

Hannah, J.L., Bekker, A., Stein, H.J., Markey, R.J. and Holland, H.D., 2004. Primitive Os and 2316 Ma age for marine shale: implications for Paleoproterozoic glacial events and the rise of atmospheric oxygen. Earth and Planetary Science Letters, 225: 43-52.

Hanson, G.N., 1980. Rare earth elements in petrogenetic studies of igneous systems. Annual Review of Earth and Planetary Sciences, 8: 371-406.

Hanson, G.N., 1989. An Approach to Trace Element Modeling Using a Simple Igneous System as an Example In: B.R. Lipin and G.A. McKay (Editors), Reviews in Mineralogy - Geochemistry and Mineralogy Of Rare Earth Elements. Mineralogical Society of America.

Hassler, S.W., 1993. Depositional history of the Main Tuff Interval of the Wittenoom Formation, late Archean-early Proterozoic Hamersley Group, Western Australia. Precambrian Research, 60: 337-359.

Hemming, S.R. and McLennan, S.M., 2001. Pb isotope compositions of modern deep sea turbidites. Earth and Planetary Science Letters, 184: 489-503.

Hogan, J.P. and Sinha, A.K., 1991. The effect of accessory minerals on the redistribution of lead isotopes during crustal anatexis: A model. Geochimica et Cosmochimica Acta, 55: 335-348.

Holland, H.D., 1984. The chemical evolution of the atmosphere and oceans. Princeton University Press, Princeton, N.J., 582 pp.

Holland, H.D., 2002. Volcanic gases, black smokers, and the Great Oxidation Event. Geochimica et Cosmochimica Acta, 66: 3811-3826.
Hudson, T. and Arth, J.G., 1983. Tin granites of Seward Peninsula, Alaska. Geological Society of America Bulletin, 94: 768-790.
Ingamells, C.O., 1970. Lithium metaborate flux in silicate analysis. Analytica Chimica Acta, 52: 323-334.
Isley, A.E., 1995. Hydrothermal plumes and the delivery of iron to banded iron formation. Journal of Geology, 103: 169-185.
Kakegawa, T., Kawai, H. and Ohmoto, H., 1999. Origins of pyrites in the ~2.5 Ga Mt. McRae Shale, the Hamersley District, Western Australia. Geochimica et Cosmochimica Acta, 62: 3205-3220.
Kamber, B.S. and Webb, G.E., 2001. The geochemistry of late Archean microbial carbonate: implications for ocean chemistry and continental erosion history. Geochimica et Cosmochimica Acta, 65: 2509-2525.
Karhu, J.A., 1993, Paleoproterozoic evolution of the carbon isotope ratios of sedimentary carbonates in the Fennoscandian Shield: Geological Survey of Finland Bulletin 371, 87 pp.
Karhu, J.A. and Holland, H.D., 1996. Carbon isotopes and the rise of atmospheric oxygen. Geology, 24: 867-870.
Kato, Y., Ohta, I., Tsunematsu, T., Watanabe, Y., Isozaki, Y., Maruyama, S. and Imai, N., 1998. Rare earth element variations in mid-Archean banded iron formations: Implications for the chemistry of ocean and continent and plate tectonics. Geochimica et Cosmochimica Acta, 62: 3475-3497.
Kaufman, A.J., Johnston, D.T., Farquhar, J., Masterson, A.L., Lyons, T.W., Bates, S., Anbar, A.D., Arnold, G.L., Garvin, J. and Buick, R., 2007. Late Archean Biospheric Oxygenation and Atmospheric Evolution. Science, 317: 1900-1903.
Key, R.M., 1983. The geology of the area around Gabarone and Lobatse, Kweneng, Kgatleng, Southern and South East Districts. Geological Survey of Botswana, District Memoir, 5. Geological Survey of Botswana, Lobatsi, Botswana, 295 pp.
Kidder, D., L., Krishnaswamy, R. and Mapes, R.H., 2003. Elemental mobility in phosphatic shales during concretion growth and implications for provenance analysis. Chemical Geology, 198: 335-353.
Klinkhammer, G.P., Elderfield, H., Edmond, J.M. and Mitra, A., 1994. Geochemical implications of rare earth element patterns in hydrothermal fluids from mid-ocean ridges. Geochimica et Cosmochimica Acta, 58: 5105-5113.
Klinkhammer, G.P. and Palmer, M.R., 1991. Uranium in the oceans: Where it goes and why. Geochimica et Cosmochimica Acta, 55: 1799-1806.
Kramers, J.D. and Tolstikhin, I.N., 1997. Two terrestrial lead isotope paradoxes, forward transport modelling, core formation and the history of the continental crust. Chemical Geology, 139: 75-110.
Krogh, T.E., 1973. A low-contamination method for hydrothermal decomposition of zircon and extraction of U and Pb for isotopic age determinations. Geochimica et Cosmochimica Acta, 37: 485-494.
Krogh, T.E., Davis, D.W. and Corfu, F., 1984. Precise U-Pb zircon and badelleyite ages for the Sudbury area. In: E.G. Pye, A.J. Naldrett and P.E. Giblin (Editors), The Geology and Ore Deposits of the Sudbury Structure. Ontario Geological Survey

Special Volume 1, pp. 431-446.
Krogh, T.E., Kamo, S.L. and Bohor, B.F., 1996. Shock metamorphosed zircons with correlated U–Pb discordance and melt rocks with concordant protolith ages indicate an impact origin for the Sudbury structure, Earth Processes: Reading the isotopic code. Geophysical Monograph 95. American Geophysical Union.
Krogstad, E.J., 2004. The Pb isotope records of Archean and Proterozoic shales limit early O-rich atmosphere. Eos, Transactions, American Geophysical Union, 85.
Krogstad, E.J., Fedo, C.M. and Eriksson, K.A., 2004. Provenance ages and alteration histories of shales from the Middle Archean Buhwa greenstone belt, Zimbabwe: Nd and Pb isotopic evidence. Geochimica et Cosmochimica Acta, 68: 319-332.
Krogstad, E.J. and Walker, R.J., 1996. Evidence of heterogeneous crustal sources: the Harney Peak Granite, South Dakota, U.S.A. Transactions of the Royal Society of Edinburgh: Earth Sciences, 87: 331-337.
Krogstad, E.J., Walker, R.J., Nabelek, P.I. and Russ-Nabelek, C., 1993. Pb isotopic evidence for mixed sources for Proterozoic granites and pegmatites, Black Hills, South Dakota, USA. Geochimica et Cosmochimica Acta, 57: 4677-4685.
Ku, T.-L., Knauss, K.G. and Mathieu, G.G., 1977. Uranium in the open ocean: concentration and isotopic composition. Deep Sea Research, 24: 1005-1017.
Kump, L.R., 2008. The rise of atmospheric oxygen. Nature, 451: 277-278.
Langmuir, D., 1978. Uranium solution-mineral equilibria at low temperatures with applications to sedimentary ore deposits. Geochimica et Cosmochimica Acta, 42: 547-569.
Langmuir, D. and Herman, J.S., 1980. The mobility of thorium in natural waters at low temperatures. Geochimica et Cosmochimica Acta, 44: 1753-1766.
Lee, J.-U., Kim, S.-M., Kim, K.-W. and Kim, I.S., 2005. Microbial removal of uranium in uranium-bearing black shale. Chemosphere, 59: 147-154.
Lee J. H. and Byrne R. H., 1993. Complexation of trivalent rare earth elements (Ce, Eu, Gd, Tb, Yb) by carbonate ions. Geochimica et Cosmochimica Acta, 57: 295-302.
Lev, S.M., McLennan, S.M. and Hanson, G.N., 1999. Mineralogic controls on REE mobility during black-shale diagenesis. Journal of Sedimentary Research, 69: 1071-1082.
Lovley, D.R., Phillips, E.J.P., Gorby, Y.A. and Landa, E.R., 1991. Biological reduction of uranium. Nature, 350: 413-416.
Ludwig, K.R., 2003. Isoplot/Ex, a geochronological toolkit for Microsoft Excel, Berkeley Geochronology Center Special Publication No. 4. Berkeley Geochronology Center.
MacGregor, A.M., 1927. The problem of the Precambrian atmosphere. South African Journal of Science, 24: 155-172.
Manhes, G., Allegre, C.J. and Provost, A., 1984. U-Th-Pb systematics of the eucrite 'Juvinas'; precise age determination and evidence for exotic lead. Geochimica et Cosmochimica Acta, 48: 2247-2264.
Manton, W.I., 1988. Separation of Pb from young zircons by single-bead ion exchange. Chemical Geology, 9: 147-152.
Masuda, A. and Ikeuchi, Y., 1979. Lanthanide tetrad effect observed in marine environment. Geochemical Journal, 13: 19-22.
Masuda, A., Kawakami, O., Dohmoto, Y. and Takenaka, T., 1987. Lanthanide tetrad

effect in nature: two mutually opposite types, W and M. Geochemical Journal, 21: 119-124.

Masuda, A., Nakamura, N. and Tanaka, T., 1973. Fine structures of mutually normalised rare-earth patterns of chondrites. Geochimica et Cosmochimica Acta, 43: 1131-1140.

McDaniel D. K., Hemming S. R., McLennan S. M., and Hanson G. N., 1994. Resetting of neodymium isotopes and redistribution of REEs during sedimentary processes: The early Proterozoic Chelmsford Formation, Sudbury Basin, Ontario, Canada. Geochimica et Cosmochimica Acta 58: 931–941.

McLennan, S.M., 1989. Rare Earth Elements in Sedimentary Rocks: Influence of Provenance and Sedimentary Processes In: B.R. Lipin and G.A. McKay (Editors), Reviews in Mineralogy - Geochemistry and Mineralogy Of Rare Earth Elements. Mineralogical Society of America, pp. 169-200.

McLennan, S.M., Hemming, S.R., Taylor, S.R. and Eriksson, K.A., 1995. Early Proterozoic crustal evolution: Geochemical and Nd-Pb isotopic evidence from metasedimentary rocks, southwestern North America. Geochimica et Cosmochimica Acta, 59: 1153-1177.

McLennan, S.M., Nance, W.B. and Taylor, S.R., 1980. Rare earth element-thorium correlations in sedimentary rocks, and the composition of the continental crust. Geochimica et Cosmochimica Acta, 44: 1833-1839.

McLennan, S.M., Simmonetti, A. and Goldstein, S.L., 2000. Nd and Pb isotopic evidence for provenance and post-depositional alteration of the Paleoproterozoic Huronian Supergroup, Canada. Precambrian Research, 102: 263-278.

McLennan, S.M. and Taylor, S.R., 1980. Th and U in sedimentary rocks: crustal evolution and sedimentary cycling. Nature, 285: 621-624.

McLennan, S.M., Fryer, B.J. and Young, G.M., 1979. Rare earth elements in Huronian (Lower Proterozoic) sedimentary rocks: crustal evolution and sedimentary recycling. Geochimica et Cosmochimica Acta, 43: 375-388.

McManus, J., Berelson, W.M., Klinkhammer, G.P., Hammond, D.E. and Holm, C., 2005. Authigenic uranium: relationship to oxygen penetration depth and organic carbon rain. Geochimica et Cosmochimica Acta, 69: 95-108.

McManus, J., Berelson, W.M., Severmann, S., Poulson, R.L., Hammond, D.E., Klinkhammer, G.P. and Holm, C., 2006. Molybdenum and uranium geochemistry in continental margin sediments: Paleoproxy potential. Geochimica et Cosmochimica Acta, 70: 4643-4662.

Melezhik, V.A., Filippov, M.M., Romashkin, A.E., 2004. A giant Palaeoproterozoic deposit of shungite in NW Russia: genesis and practical applications. Ore Geology Reviews, 24: 135-154.

Melezhik, V.A., Fallick, A.E., Filippov, M.M. and Larsen, O., 1999. Karelian shungite - an indication of 2.0-Ga-old metamorphosed oil-shale and generation of petroleum: geology, lithology, and geochemistry. Earth-Science Reviews, 47: 1-40.

Melezhik, V.A., Fallick, A.E., Clark, T., 1997. Two billion year old isotopically heavy carbon: evidence from the Labrador Trough, Canada. Canadian Journal of Earth Science, 3: 271–285.

Mills, R.A., Wells, D.M. and Roberts, S., 2001. Genesis of ferromanganese crusts from

the TAG hydrothermal field. Chemical Geology, 176: 283-293.
Mitra, A., Elderfield, H. and Greaves, M.J., 1994. Rare earth elements in submarine hydrothermal fluids and plumes from the Mid-Atlantic Ridge. Marine Chemistry, 46: 217-236.
Mo, T., Suttle, A.D. and Sackett, W.M., 1973. Uranium concentrations in marine sediments. Geochimica et Cosmochimica Acta, 37: 35-51.
Murakami, T. and Yokota, K., 2008. Atmospheric oxygen rise in the Paleoproterozoic revealed by weathering model. Geochimica et Cosmochimica Acta,72: A665.
Nel, C.J., Beukes, N.J. and De Villiers, J.P.R., 1986. The Mamatwan manganese mine of the Kalahari manganese field. In: C.R. Annhaeusser and S. Maske (Editors), Mineral deposits of Southern Africa. Geological Society of South Africa, Johannesburg, pp. 963-978.
Nesbitt, H.W. and Markovics, G., 1997. Weathering of granodioritic crust, long-term storage of elements in weathering profiles, and petrogenesis of siliciclastic sediments. Geochimica et Cosmochimica Acta, 61: 1653-1670.
Nesbitt, H.W. and Young, G.M., 1982. Early Proterozoic climates and plate motions inferred from major element chemistry of lutites. Nature, 299: 715-717.
Nozaki, Y., Horibe, Y. and Tsubota, H., 1981. The water column distributions of thorium isotopes in the western North Pacific. Earth and Planetary Science Letters, 54: 203-216.
Ohmoto, H., 1997. When did the Earth's atmosphere become oxic? Geochemical News, 93: 26-27.
Ohmoto, H., Watanabe, Y., Ikemi, H., Poulson, S.R. and Taylor, B.E., 2006. Sulphur isotope evidence for an oxic Archaean atmosphere. Nature, 442: 908-911.
Ohr, M., Halliday, A.N. and Peacor, D.R., 1994. Mobility and fractionation of rare earth elements in argillaceous sediments: Implications for dating diagenesis and low-grade metamorphism. Geochimica et Cosmochimica Acta, 58: 289-312.
Ojakangas, R.W., Marmo, J.S., Heiskanen, K.I., 2001. Basin evolution of the Paleoproterozoic Karelian Supergroup of the Fennoscandian (Baltic) Shield. Sedimentary Geology, 141-142: 255-285.
Ono, S., Beukes, N.J., Rumble, D., III and Fogel, M.L., 2006. Early evolution of atmospheric oxygen from multiple-sulfur and carbon isotope records of the 2.9 Ga Mozaan Group of the Pongola Supergroup, Southern Africa. South African Journal of Geology, 109: 97-108.
Ono, S., Eigenbrode, J.L., Pavlov, A.A., Kharecha, P., Rumble, D., III, Kasting, J.F. and Freeman, K.H., 2003. New insights into Archean sulfur cycle from the mass-independent sulfur isotope records from the Hamersley Basin, Australia. Earth and Planetary Science Letters, 213: 15-30.
Papineau, D., Mojzsis, S.J., and Schmitt, A.K., 2007. Multiple sulfur isotopes from Paleoproterozoic Huronian interglacial sediments and the rise of atmospheric oxygen. Earth and Planetary Science Letters, 255: 188-212.
Pavlov, A.A. and Kasting, J.F., 2002. Mass-Independent Fractionation of Sulfur Isotopes in Archean Sediments: Strong Evidence for an Anoxic Archean Atmosphere. Astrobiology, 2: 27-41.
Piepgras, D.J. and Jacobsen, S.B., 1992. The behavior of rare earth elements in seawater: Precise determination of variations in the North Pacific water column.

Geochimica et Cosmochimica Acta, 56: 1851-1862.
Piepgras, D.J., Wasserburg, G.J. and Dasch, E.J., 1979. The isotopic composition of Nd in different ocean masses. Earth and Planetary Science Letters, 45: 223-236.
Piper, D.Z., 1974. Rare earth elements in the sedimentary cycle: a summary. Chemical Geology, 14: 285-304.
Pukhtel, I.S., Zhuravlev, D.Z., Ashikhmina, N.A., Kulikov, V.S., Kulikova, V.V., 1992. Sm–Nd age of the Suisarian suite on the Baltic Shield. Transactions of the Russian Academy of Science, 326: 706–711, in Russian.
Rankama, K. and Sahama, T.G., 1950. Geochemistry. University of Chicago Press, Chicago, IL, 911 pp.
Rasmussen, B., Blake, T.S. and Fletcher, I.R., 2005. U-Pb zircon age constraints on the Hamersley spherule beds: Evidence for a single 2.63 Ga Jeerinah-Carawine impact ejecta layer. Geology, 33: 725-728.
Rasmussen, B., Fletcher, I.R. and Muhling, J.R., 2007. In situ U–Pb dating and element mapping of three generations of monazite: Unravelling cryptic tectonothermal events in low-grade terranes. Geochimica et Cosmochimica Acta, 71: 670-690.
Rehkämper, M. and Mezger, K., 2000. Investigation of matrix effects for Pb isotope ratio measurements by multiple collector ICP-MS: verification and application of optimized analytical protocols. Journal of Analytical Atomic Spectrometry, 15: 1451-1460.
Roscoe, S.M., 1969. Huronian rocks and uraniferous conglomerates in the Canadian Shield. Geological Survey of Canada Paper 68-40. Geological Survey of Canada, 205 pp.
Rosing, M.T. and Frei, R., 2004. U-rich Archaean sea-floor sediments from Greenland - indications of >3700 Ma oxygenic photosynthesis. Earth and Planetary Science Letters, 217: 237-244.
Rouxel, O., Bekker, A. and Edwards, K., 2005. Iron Isotope Constraints on the Archean and Paleoproterozoic Ocean Redox State. Science, 307: 1088-1091.
Roy, S., 2000. Late Archean initiation of manganese metallogenesis: its significance and environmental controls. Ore Geology Reviews, 17: 179-198.
Rudnick, R.L., McLennan, S.M. and Taylor, S.R., 1985. Large ion lithophile elements in rocks from high-pressure granulite facies terrains. Geochimica et Cosmochimica Acta, 49: 1645-1655.
Russell, A.D. and Morford, J.L., 2001. The behavior of redox-sensitive metals across a laminated-massive-laminated transition in Saanich Inlet, British Columbia. Marine Geology, 174: 341-354.
Scott, C., Lyons, T.W., Bekker, A., Shen, Y., Poulton, S.W., Chu, X. and Anbar, A.D., 2008. Tracing the stepwise oxygenation of the Proterozoic ocean. Nature, 452: 456-459.
Shannon, R.D., 1976. Revised Effective Ionic Radii and Systematic Studies of Interatomic Distances in Halides and Chalogenides. Acta Crystallographica Section A: Foundations of Crystallography, A32: 751-767.
Sherrill, R.M., Field, M. and Ravizza, G., 1999. Uptake and fractionation of rare earth elements on hydrothermal plume particles at 9°45'N, East Pacific Rise. Geochimica et Cosmochimica Acta, 63: 1709–1722.
Shields, G. and Stille, P., 2001. Diagenetic constraints on the use of cerium anomalies as

paleoseawater redox proxies: an isotopic and REE study of Cambrian phosphorites. Chemical Geology, 175: 29-48.
Sholkovitz, E.R., Landing, W.M. and Lewis, B.L., 1994. Ocean particle chemistry: The fractionation of rare earth elements between suspended particles and seawater. Geochimica et Cosmochimica Acta, 58: 1567-1579.
Sholkovitz, E.R. and Schneider, D.L., 1991. Cerium redox cycles and rare earth elements in the Sargasso Sea. Geochimica et Cosmochimica Acta, 55: 2737-2743.
Sholkovitz, E.R. and Shen, G.T., 1995. The incorporation of rare earth elements in modern coral. Geochimica et Cosmochimica Acta, 59: 2749-2756.
Smith, M.D., 2002. The timing and petrogenesis of the Creighton pluton, Ontario: an example of felsic magmatism associated with Matachewan igneous events. M.Sc. Thesis, University of Alberta, Edmonton, 123 pp.
Spier, C.A., de Oliveira, S.M.B., Sial, A.N. and Rios, F.J., 2007. Geochemistry and genesis of the banded iron formations of the Cauê Formation, Quadrilátero Ferrífero, Minas Gerais, Brazil. Precambrian Research, 152: 170-206.
Stacey, J.S. and Kramers, J.D., 1975. Approximation of terrestrial lead isotope evolution by a two-stage model. Earth and Planetary Science Letters, 26: 207-221.
Stern, R.A. and Hanson, G.N., 1991. Archean High-Mg Granodiorite: A Derivative of Light Rare Earth Element-enriched Monzodiorite of Mantle Origin. Journal of Petrology, 32: 201-238.
Strauss, H., 2002. The isotopic composition of Precambrian sulphides; seawater chemistry and biological evolution. In: W. Altermann and P.L. Corcoran (Editors), Precambrian Sedimentary; A Modern Approach to Ancient Depositional Systems. International Association of Sedimentology Special Publication 33, pp. 67-103.
Sverjensky, D., 1984. Oil field brines as ore-forming solutions. Economic Geology, 79: 23-37.
Taylor, S.R. and McLennan, S.M., 1985. The Continental Crust: Its Composition and Evolution. Blackwell, Oxford, 312 pp.
Taylor, S.R., Rudnick, R.L., McLennan, S.M. and Eriksson, K.A., 1986. Rare earth element patterns in Archean high-grade metasediments and their tectonic significance. Geochimica et Cosmochimica Acta, 50: 2267-2279.
Tomascak, P.B., Krogstad, E.J. and Walker, R.J., 1996. Nature of the crust in Maine, USA; evidence from the Sebago Batholith. Contributions to Mineralogy and Petrology, 125: 45-59.
Trendall, A.F., 1990. Precise U-Pb chronological comparison of the volcano-sedimentary sequences of the Kaapvaal and Pilbara Cartons between about 3.1 and 2.4 Ga, Third International Archaean Symposium. University of Western Australia, Department of Geology, Perth, Western Australia, pp. 81-83.
Tsikos, H. and Moore, J.M., 1998. The Kalahari manganese field: an enigmatic association of iron and manganese. South African Journal of Geology, 101: 287-290.
Veizer, J., Clayton, R.N. and Hinton, R.W., 1992. Geochemistry of Precambrian carbonates: IV. Early Paleoproterozoic (2.25 ± 0.25 Ga) seawater Geochimica et Cosmochimica Acta, 56: 875-885.
Veizer, J., Hoefs, J., Ridler, R.H., Jensen, L.S. and Lowe, D.R., 1989. Geochemistry of

Precambrian carbonates: I. Archean hydrothermal systems. Geochimica et Cosmochimica Acta, 53: 845-857.

Veizer, J., Plumb, K.A., Clayton, R.N., Hinton, R.W. and Grotzinger, J.P., 1992. Geochemistry of Precambrian carbonates: V. Late Paleoproterozoic (1.8 ± 0.25 Ga) sea water. Geochimica et Cosmochimica Acta, 56: 2487-2501.

Visser, J.N.J., 1971. The Timeball Hill Formation at Pretoria – A prograding shore-line deposit. Annual Geology Survey (South Africa), 9: 115-118.

Walraven, F., 1997. Geochronology of the Rooiberg Group, Transvaal Supergroup, South Africa. Information Circular 316, Econ. Geol. Res. Unit, University of the Witwatersrand, Johannesburg, South Africa.

Westerlund, S. and Öhman, P., 1992. Rare earth elements in the Arctic Ocean. Deep Sea Research Part A., 39: 1613-1626.

Wignall, P.B., 1994. Black Shales. Oxford Monographs on Geology and Geophysics, 30. Oxford University Press, New York, 127 pp.

Wille, M., Kramers, J.D., Nägler, T.F., Voegelin, A.R., Beukes, N.J., Schröder, S., Lacassie, J.P., and Meisel, T., 2007. Evidence for a gradual rise of oxygen between 2.6 and 2.5 Ga from Mo isotopes and Re-PGE signatures in shales. Geochimica et Cosmochimica Acta, 71: 2417-2435.

Wronkiewicz, D.J. and Condie, K.C., 1990. Geochemistry and mineralogy of sediments from the Ventersdorp and Transvaal Supergroups, South Africa: Cratonic evolution during the early Proterozoic. Geochimica et Cosmochimica Acta, 54: 343-354.

Yamada, M. and Tsunogai, S., 1984. Postdepositional enrichment of uranium in sediment from the Bering Sea. Marine Geology, 54: 263-276.

Yamamoto, K., Nobukazu, I., Matsumoto, T., Tanaka, T. and Adachi, M., 2004. Geochemistry of Precambrian carbonate intercalated in pillows and its host basalt: implications for the REE composition of circa 3.4 Ga seawater. Precambrian Research, 135: 331-344.

Yang, W., Holland, H.D. and Rye, R., 2002. Evidence for low or no oxygen in the late Archean atmosphere from the ~2.76 Ga Mt. Roe #2 paleosol, Western Australia, Part 3. Geochimica et Cosmochimica Acta, 66: 3707-3718.

Young, G.M., Long, D.G.F., Fedo, C.M. and Nesbitt, H.W., 2001. Paleoproterozoic Huronian basin: product of a Wilson cycle punctuated by glaciations and a meteorite impact. Sedimentary Geology, 141-142: 233-254.

Zheng, Y., Anderson, R.F., van Geen, A. and Fleisher, M.Q., 2002. Preservation of particulate non-lithogenic uranium in marine sediments. Geochimica et Cosmochimica Acta, 66: 3085-3092.

Zolnai, A.I., Price, R.A. and Helmstaedt, H., 1984. Regional cross section of the Southern Province adjacent to Lake Huron, Ontario: implications for the tectonic significance of the Murray Fault Zone. Canadian Journal of Earth Sciences, 21: 447-456.

APPENDIX A. ANALYTICAL METHODS

A.1. Pb Isotope Analyses

A.1.1 Whole-rock Analysis

Sample preparation of powdered organic-rich black shales were conducted under Class-100 laminar flow hoods with the objective of reducing contamination from airborne particulate matter. Samples were carefully weighed to ensure homogenization and the analysis of a representative sample. Geochemical decomposition was conducted in PFA Teflon® Savillex following the digestion technique of Krogh (1973). Isotopic ratio analyses were carried out on a Thermo FisherScientific Element2 high-resolution magnetic sector field inductively coupled plasma mass spectrometer.

The technique for the geochemical decomposition of samples involved using cleaned Teflon® vials (7 mL Savillex® vials) to ensure robustness of the vessel during digestion. Digestion vessels and caps were initially cleaned using Citranox® liquid acid cleanser and ordinary tap water. Once washed, the vessels were further rinsed twice in Milli-Q® deionized water* and placed in a 10% trace metal grade nitric acid (HNO_3) bath overnight. Next, the digestion vessels were drained of acid and rinsed thoroughly with water. Then, 1 mL of 2N Optima® Grade (ultra-pure) HNO_3 was added to each vessel, which was subsequently tightly capped and placed on a hot plate overnight for additional cleaning. The use of Optima® Grade HNO_3 is necessary to avoid lead contamination and ensure high quality data. This cleaning step requires a weakly concentrated acid to avoid the unnecessary consumption of ultra-pure reagents while maintaining the ability of the acid to dissolve all remaining lead. During this step in the cleaning procedure, it was

* All water used in cleaning and chemical separation procedures is Milli-Q® deionized water with a minimum resistivity of 18.2MΩcm unless noted.

observed that a few of the vessels were dry upon inspection the following day. In these cases, an additional milliliter of Optima® 2N HNO_3 was added to the dried vessel, which was replaced on the hot plate for two hours to dissolve the lead in the vessels. The digestion vessels were finally allowed to dry after being uncapped and the residual acid discarded after the overnight cleaning procedure. Careful attention was paid in the preparation of the digestion vessels to eliminate lead contamination, as lead is commonly found on particulate matter and prevalent in the environment. Only once the digestion vessels were properly cleaned, was sample added to ensure that accidental contamination did not occur after the final cleaning step. In situations when cleaning more vessels than immediately needed, vessels remained on the hot plate filled with acid until needed.

Sample blanks were analyzed to evaluate the efficacy of the cleaning procedure. The two cleaning blanks produced values of 177 and 13 pg respectively, which is far less Pb than is found in the sampled Pb-rich organic shales resulting in sufficient elimination of lead contamination from unclean digestion vessels. A minimum of 100 mg of powdered sample was added to each of the cleaned vessels, which were then labeled. Dropper bottles with concentrated Optima® HNO_3 (15.6M) and HF (28.9M) were previously prepared using the same cleaning technique described above before the addition of acid to the bottles. Sample vessels were tightly capped and placed on the hot plate overnight after 5 drops of Optima® HNO_3 and 25 drops of Optima® HF were added to the samples for digestion. Upon adding the concentrated nitric acid to some high sulfide-bearing samples, copious amounts of sulfur- and nitrogen-rich gases (based on odor and appearance) were released, sometimes violently. These samples were treated no differently from the others in subsequent steps. Upon returning to the laboratory the

following morning, sample vials were uncapped and allowed to dry. Once completely dry, five additional drops of Optima® HNO_3 and twenty five additional drops of Optima® HF were added to the samples to assure complete sample decomposition and release of Pb. The sample vessels were once again capped tightly and left on the hot plate overnight. These samples were then uncapped and dried as stated previously. Samples were then tested for complete sulfide decomposition using visual observance of any gases resulting from the addition of 5 drops of Optima HNO_3. If no gases were observed, the samples were once again completely dried; however if gases were observed the digestion procedure (HNO_3 and HF) was repeated until no visible gases were released. The digestion procedure resulted in a grey, white, tan, or brown crust with variable amounts of black, graphitic residue. Finally, 2M Optima® HCl was added to the vessels until they were 7/8 filled. The vessels were then capped and placed on the hot plate for an hour to assist in Pb dissolution. They were then removed from the hot plate to cool and allow the residue to settle to the bottom of the digestion vessel.

Anion resin (AG1x8) exchange columns were then prepared in order to chemically separate Pb from other similar elements that could create mass interferences during mass spectrometry. Pipette tips serve as the containers in which the anion exchange resin is deposited. A silica wool frit was used to retain the resin bed within the pipette tip columns. Once the silica wool was in place, 500 μL of the resin in suspension in 2M HCl was pipetted onto the silica wool frit in the column pipette drop wise to avoid any bubbles from forming and restricting the flow of liquid through the column. Once the resin had settled, water was added to the column until the reservoir was filled. Careful observation of the column revealed whether bubbles restricted the flow of water

through the column, as water would be transmitted very slowly or not at all. If poor transmission was observed, the columns were "floated" by quickly taking up some of the water in a transfer pipette and then squeezing it back into the column. This results in the entire quantity of resin being put into a solution with resin beads suspended in the water. Upon settling, the resin bed should be free of obstructing bubbles. This procedure was repeated as many times as necessary to eliminate all bubbles. Once all of the bubbles were removed, the columns were cleaned with two reservoir volumes of 6M Optima® HCl followed by two reservoir volumes of water to return the pH to normal.

Once the anion resin exchange columns were prepared and cleaned, they were ready for the introduction of the sample fluid (2M Optima® HCl with dissolved ions from the digested sample) for the chemical separation of lead (Krogstad et al., 1993; Krogstad and Walker, 1996). The first step in the sample introduction procedure is a 6M HCl cleaning as directed above. This was followed by two reservoir volumes of water (see above) and finally one reservoir volume of ~1.5M Optima® HBr (0.8M HBr replaced 1.5M HBr after May 9, 2006 with no difference in separation effectiveness) to convert the resin to bromide form, which will accept lead bromide complexes. One-milliliter pipettes were used to transfer one reservoir volume of sample fluid onto the columns. Since the reservoir volume was greater than 1 mL (the functional volume of the pipette used), two equal volume sample liquid aliquots were transferred. The pipette tip was twice cleaned using 2M Optima® HNO_3 prior to taking up the sample fluid to limit contamination. One reservoir volume of sample fluid was then added drop wise to the exchange column reservoir. A waste container was placed under the column to collect the waste materials produced during chemical separation. Once the sample fluid was

transmitted through the resin bed and the reservoir was empty, the reservoir was filled twice with 1.5M Optima® HBr (0.8M HBr was used after May 9, 2006), which is used to remove specific cations (namely the transition metals like Fe) from the resin (Manhes et al., 1984; Manton, 1988). Once the reservoir was empty, the reservoir was filled once with 2M Optima® HCl to remove other cations not previously removed (namely the alkali metals like K, Na). Finally, the waste container was replaced with a clean Savillex® vial (see procedure above) for Pb elution. Lead was eluted with two reservoir volumes of 6M Optima® HCl to which three drops of Optima® HNO_3 were added (Krogh, 1973). The vials were then placed on the hot plate uncapped to dry down the HCl solution. Once completely dried, a small bead containing the sample Pb remained, which was then dissolved in 2M Optima® HCl. This solution was then processed in the anion exchange resin columns an additional time to ensure lead separation. Upon completion of the second pass, the small Pb bead was dissolved in three drops of concentrated Optima® HNO_3 and 2 mL of 2% Optima® HNO_3. This nitric acid solution was then used for mass spectrometry.

Isotopic ratio analyses were conducted on a high-resolution Finnigan MAT Element 2 ICP-MS. The electron multiplier is constructed using multiple dynodes, which act to multiply the signal by releasing 2^n electrons per ion interacting with the first dynode, where n is the number of dynodes in the multiplier tube. Half way down the dynode chain, there is ground, which avoids overloading the ultimate analyzer in samples with very high ion counts. When the ground is activated the mass spectrometer switches ion-counting modes from “counting mode” to “analog mode”. Although there is no inherent advantage to either mode, it is advantageous to run all the samples on the same

mode. Since the samples being analyzed have highly variable concentrations of lead, dilution of some samples was necessary to permit all samples running without switching the ion-counting mode on the mass spectrometer. In order to calibrate the dilution, 500 mL of undiluted sample in the nitric solution was placed into small, uncovered vials, which were then placed into the auto-sampler. These samples were then run quickly to ascertain the peak intensity and rough isotope ratios. Although the data were not used in any presentations they served as the basis for sample dilution, which varied from 20:1 to 2:3 (2% Optima® HNO_3: Sample). Once the correct dilution was calculated, the diluted samples were run in triplicate to evaluate reproducibility. Mass spectrometry was controlled through a computer program that automates sample introduction. This program accesses files, which provide the method parameters (magnetic strength, analysis time, analyzed mass) necessary for the mass spectrometer to obtain the data. The data is collected and is available as a text (.TXT) file that can be imported into MS Excel. The data sets were run at three different times resulting in three subsets of the data table. Additionally, a power law mass fractionation correction (Rehkämper and Mezger, 2000) based on duplicate analyses of Standard Reference Material 981 or 982 (NIST) were used to correct the data. Sample-Standard bracketing was used to ensure accuracy in calculating a valid mass fractionation correction for each sample analysis. The average reproducibility (2σ error) was 0.130% on $^{206}Pb/^{204}Pb$ ratios, 0.181% on $^{207}Pb/^{204}Pb$ ratios, and 0.152% on $^{208}Pb/^{204}Pb$ ratios on SRM 981 or SRM 982, when appropriate. The data presented for samples from the Mount McRae Shale, Huronian Supergroup, Rooihoogte-Timeball Hill Formations, Sengoma Argillite Formation, and the upper Zaonezhskaya Formation are from several analytical runs. Data for analyses of SRM 981 and 982 are

not presented as these data are consistent throughout a specific day but may vary greatly from day to day.

A.1.2 Step-wise Acid Leaching

Powdered whole-rock samples were measured out into cleaned 7 mL Savillex® vials for step-wise digestion by 0.1M Optima® HBr, 4M Optima® HBr, 50:50 concentrated Optima® HCl:HNO_3 mixture, and concentrated Optima® HF:HNO_3 mixture (after Frei and Kamber, 1995; Krogstad et al., 2004). Sample weights were approximately 150 mg, however quantitative weight is not essential to the overall procedure and weights were not recorded. The first step (L1) involved sample leaching by adding 1000 μL of 0.1M Optima® HBr to the powdered sample, capping the vial, shaking the vial, and then allowing the subsequent reactions to occur on a hot plate at ~150°C for 1h. This solution was then centrifuged to avoid removing the fine-grained component of the sample during collection of the leachate. The leachate was decanted into a cleaned 7 mL Savillex® vial and dried to completion. The residue was dried and subsequently leached with 1000 μL of 4M Optima® HBr (L2). The procedure for this leaching step is identical to that used for the 0.1M HBr leach-step. This procedure was repeated for a third leach step (L3) with 1000 μL of a 50:50 mixture of concentrated Optima® HCl (12.1M) and HNO_3. After this third acid leaching, samples were dried and then 5 drops of concentrated Optima® HNO_3 and 25 drops of concentrated HF were added to the residual material. The resulting digestate was dried and evaluated using repeated HF:HNO_3 digestion until no sulfur gas was released. This fluid was then dried completely and all dried digestates were dissolved in 2M Optima® HCl. Chemical

separation of Pb was done in an identical manner compared to whole-rock samples, using ion exchange chromatography. All samples were diluted 1:1 with 2% Optima® HNO_3 for mass spectrometry.

A.2 Rare Earth Element Concentrations

Rare earth element concentrations were determined using isotope dilution mass spectrometry (ID-MS). The accurate and precise calibration of a multi-element rare earth element spike is essential to obtaining the best possible data from this technique. A multi-element spike was prepared at Georgia State University using metallic oxides of polyisotopic rare earth elements (La, Ce, Nd, Sm, Eu, Gd, Dy, Er, Yb, and Lu) with altered isotopic compositions. The metallic oxides were dissolved in concentrated Optima® HNO_3 with the exception of Ce, which had to be dissolved in trace element grade sulfuric acid. The two solutions were combined and then diluted to make a volume of one liter (REE #1). This spike was calibrated using REE concentrations of USGS Geologic Standard BHVO-1 and BIR-1 (Baker et al., 2002).

Samples were digested using a flux fusion method using ultra-high purity lithium metaborate flux and sample powder in a ratio of 4:1 (Ingamells, 1970). Ultra-high purity graphite crucibles were pre-fired in a furnace for 10 minutes at 1100°C and allowed to cool. Approximately 250 mg of the lithium metaborate flux was weighed in a pre-fired graphite crucible and the balance was re-zeroed. Sample powders were placed in ceramic crucibles and dried in an oven at a temperature of ~150°C overnight to evaporate all extra-structural water. The sample powders were then measured into the crucible and weighed multiple times to ensure that the recorded weight was of the highest precision.

An additional 150 mg of lithium metaborate was then added to samples creating a "flux sandwich" and an overall flux-to-sample ratio of 4:1. In samples with perceived low Fe concentrations, ~10 mg of ultra-high purity (99.999%) iron powder was added to samples (Tomascak et al., 1996). In contrast, both lithium tetraborate and metaborate were added, as flux to samples with perceived high Fe concentrations. Crucibles containing these "flux sandwiches" were then placed in an empty pipette tip box to avoid sample contamination.

Teflon griffon-style beakers (100 mL) were cleaned in a 10% trace metal grade nitric acid bath overnight and then rinsed in water. The dropper bottle containing REE#1 spike was removed from the refrigerator and allowed to achieve thermal equilibration with the atmosphere. Once rinsed, magnetic stir bars were placed in the Teflon beakers and prepared spike was added to the beaker. The amount of spike added to each beaker ranged between 8 pmoles (Ce) and 1 pmole (Yb) of each element in the spike for shale samples and between 18 pmoles and 2 pmoles for banded iron formation samples. The spike bottle was weighed carefully before and after adding the drops of spike to the beaker and the weight of the spike was calculated by subtraction. Fifty milliliters of 1M trace metal grade HNO_3 was added to the beakers, which were then covered in Parafilm® to avoid contaminating the spiked nitric acid. The spike bottle and the Teflon beakers with spiked nitric acid were placed in the refrigerator to avoid evaporation overnight.

The next day, the furnace was turned on and allowed to attain a temperature of 1100°C for 10 minutes. The samples in graphite crucibles were placed in the furnace for 15 minutes after the temperature returned to 1100°C in order to fully melt the sample and flux. The melted sample was then quenched in the corresponding stirring spiked acid and

dissolved. Coprecipitation of the REE with Fe was done once the quenched sample was completely dissolved (Rankama and Sahama, 1950; Evans and Hanson, 1993). Trace metal grade concentrated ammonium hydroxide (NH_4OH) was added to the solution until the pH was approximately 6.5 – 7. In this pH range aqueous Fe^{+2} is precipitated as iron (Fe^{+3}) oxyhydroxides with which REE are coprecipitated. The solution and precipitate are then poured into a 50 mL centrifuge tube (pre-cleaned with a rinse of 2% nitric acid), which are centrifuged for 3 minutes at 4750 rpm. The supernatant fluid is then poured out and the centrifuge tube was filled with Milli-Q® water and shaken to rinse the precipitate. This solution is then centrifuged for another 3 minutes and the supernatant fluid is decanted again. The precipitate is rinsed again and centrifuged in water as described above. When the supernatant fluid is decanted this final time, the precipitate is dissolved in 2M Optima® HCl.

During the three-minute intervals when the samples were being centrifuged, ion exchange columns (AG 50W-X8) were floated with water. These primary columns were cleaned with eight resin bed volumes using 6M trace metal grade nitric acid. The columns were then rinsed with four resin bed volumes of water. This rinse step was followed by equilibrating the columns with four resin bed volumes of 2M Optima® HCl. The sample solution (the dissolved precipitate from the centrifuge tube) was then carefully poured through a filter paper cone (11 mm diameter particle retention) to eliminate the presence of graphite particles on the columns. The filter cones were placed in a polypropylene funnel for stability, which dripped through a modified 15 mL cleaned centrifuge tube onto the resin bed within the column (the modification involved removing the closed tip of the tube with a pair of scissors). Once the sample fluid was finished

dripping through the primary columns, eight resin bed volumes of 2M Optima® HCl were used to wash the columns. The columns were further washed using six resin bed volumes of 2M trace metal grade nitric acid. Finally, the REE were eluted as a group with five resin bed volumes of 6M trace metal grade nitric acid. This solution was dried to completion on a hot plate and the columns were washed with water to reduce the acid degradation of the resin beads.

Secondary chemical separations of the REE were done using custom-made 25x1 cm PFA Teflon® columns with variable quantities and molarities of 2-methyllactic acid (also known as α-Hydroxyisobutyric acid, "alpha-HIBA"). In contrast to chemical separations previously described, the exchange resin was fully removed and the column cleaned using water in between uses. Therefore there was no need to float the resin (AG 50W-X4), but rather the resin bed was established for each separation. After the column was completely filled with resin, time was given for the resin to settle. During this time, the dried REE concentrates were dissolved in 40 µL of 1M Optima® HCl and then diluted with 360 µL of water to make a 0.1M HCl solution. Once the resin bed was fully settled, the remaining resin was washed out from the cup on top of the column and 100 µL of water was added to the column. Following this rinse step, the 0.1M HCl REE sample solution was added to the column and allowed to drip through. This was followed by another 100-µL water rinse. Cleaned Teflon vials were used to collect each of the following eluted interference free REE separates (cuts). The REE elution scheme using α-HIBA results in the elution of the heavy REE first, followed by the middle REE, and then the light REE. The first cut to be eluted was to contain only Lu, however due to an abundance of Hf in the natural samples and ineffective column calibration, the Lu-cut

contained Hf and Yb resulting in the inability to run these cuts. The natural variability of Lu concentrations in shales suggested that Lu concentrations were not essential to interpreting the REE behavior in the studied samples. The Lu-cut was eluted with 1.5 mL of 0.10M α-HIBA and typically took 80 minutes to complete. The HREE-cut (Yb, Tm, Er, Ho, Dy ± Tb) was eluted using 1.75 mL of 0.15M α-HIBA and typically took 90 minutes to complete. The absence or presence of Tb was inconsequential as Tb is monoisotopic and its concentration was not evaluated during this study. The Gd-cut (Gd ± Tb) was eluted with 1.5 mL of 0.15M α-HIBA and took approximately 75 minutes to complete. The MREE-cut (Eu, Sm, Nd ± Pr) was eluted in approximately four hours with 5.0 mL of 0.225M α-HIBA. The light REE (Ce and La) and Ba were separated from each other as ^{138}Ce (0.25% of natural Ce) and ^{138}Ba (71.7% of natural Ba) interfere with ^{138}La (0.09% of natural La) making evaluation of ^{138}La/^{139}La extremely difficult to measure even with the ^{138}La-enriched (6%) spike added. The Ce-cut (Ce ± Pr) was eluted with 1.0 mL of 0.5M α-HIBA. Lastly, the La-cut (La only) was eluted with 1.0 mL of 0.5M α-HIBA. These (multi-) elemental separates were then diluted with 2% Optima® nitric acid and analyzed by mass spectrometry. The resultant isotopic ratios were processed using a simple MS Excel spreadsheet to determine the element concentrations through the use of the isotope dilution equation.

Initially every sample was to be run however after analyzing three complete suites (Rooihoogte-Timeball Hill Formations, Hotazel Formation, and Sengoma Argillite Formation) it was determined that strategic sampling of the remaining suites would reduce the necessary laboratory time without sacrificing the integrity of the project. The samples with the highest and lowest calculated κ_2 values were selected from the suites for

REE analysis. In the case that all samples had not yet been evaluated for their whole-rock Pb isotope compositions, the samples with the highest and lowest known κ_a values were selected.